DOE-ER-0313/31
Distribution
Categories
UC-423, -424

FUSION MATERIALS
SEMIANNUAL PROGRESS REPORT
FOR THE PERIOD ENDING
December 31, 2001

Prepared for
DOE Office of Fusion Energy Sciences
(AT 60 20 10 0)

DATE PUBLISHED: MARCH 2002

Prepared for
OAK RIDGE NATIONAL LABORATORY
Oak Ridge, Tennessee 37831
Managed by
U.T.-Battelle, LLC
For the
U.S. DEPARTMENT OF ENERGY
Under Contract DE-AC05-00OR22725

FOREWORD

This is the thirty-first in a series of semiannual technical progress reports on fusion materials science activities supported by the Fusion Energy Sciences Program of the U.S. Department of Energy. This report focuses on research addressing the effects on materials properties and performance from exposure to the neutronic, thermal, and chemical environments anticipated in the chambers of fusion experiments and energy systems. This research is a major element of the national effort to establish the materials knowledge base of an economically and environmentally attractive fusion energy source. Research activities on issues related to the interaction of materials with plasmas are reported separately.

The results reported are the product of a national effort involving a number of national laboratories and universities. A large fraction of this work, particularly in relation to fission reactor irradiations, is carried out collaboratively with partners in Japan, Russia, and the European Union. The purpose of this series of reports is to provide a working technical record for the use of program participants, and to provide a means of communicating the efforts of fusion materials scientists to the broader fusion community, both nationally and worldwide.

This report has been compiled and edited under the guidance of Ron Klueh and Renetta Godfrey, Oak Ridge National Laboratory. Their efforts, and the efforts of the many persons who made technical contributions, are gratefully acknowledged.

S. E. Berk
Facilities and Enabling Technologies Division
Office of Fusion Energy Sciences

CONTENTS

1.0 VANADIUM ALLOYS 1

1.1 THERMAL CREEP OF V-4Cr-4Ti in a Li ENVIRONMENT - M. L. Grossbeck (Oak Ridge National Laboratory) 2

Tests of pressurized tube specimens of Wah Chang heat 832665 of V-4Cr-4Ti were exposed to Li at elevated temperatures and the deformation in the tubes monitored periodically by laser profilometry. It was determined that at 665°C deformations were below 0.05% for all stresses in the range of 59-117 MPa effective stress at 1105 hours and below 6% at 765°C at 1927 hours. The deformation was so small at 665°C that the temperature was increased to 700°C. Results from 700°C have not yet been obtained. At both temperatures the duration of the tests is not yet sufficient to make a valid comparison with the vacuum creep tests conducted at PNNL

1.2 OXYGEN EMBRITTLEMENT OF VANADIUM ALLOYS WITH AND WITHOUT SURFACE OXIDE FORMATION - B. A. Pint and J. R. DiStefano (Oak Ridge National Laboratory) 6

Extended Abstract

1.3 AN UPDATE ON BIAXIAL THERMAL CREEP OF VANADIUM ALLOYS – R. J. Kurtz (Pacific Northwest National Laboratory), A. M. Ermi, (COGEMA Engineering Corp.), and H. Matsui (Tohoku University). 7

A study of the thermal creep properties of two vanadium alloys was performed using pressurized tube specimens. Creep tubes nominally 4.57 mm OD by 0.25 mm wall thickness were pressurized with high-purity helium gas to mid-wall effective stresses below the effective (Von Mises) yield strength. Specimens were fabricated from V-4Cr-4Ti (Heat No. 832665) and a V-3Fe-4Ti alloy. The samples were heated to 650, 700, 725, and 800°C in an ultra-high vacuum furnace and periodically removed to measure the change in tube outer diameter with a highprecision laser profilometer. The normalized minimum creep rate was found to be power-law dependent on the modulus compensated applied stress. The value of the stress exponent varied with the applied stress. At normalized stresses ranging from 2 to $8x10^{-3}$ the stress exponent was about 4 and the activation energy was about 300 kJ/mole, which is quite close to the activation energy for self-diffusion in pure vanadium. These results suggest that the predominant mechanism of creep in this regime is climb-assisted dislocation motion. At lower stresses the value of the stress exponent is near unity suggesting that viscous creep mechanisms such as Coble creep or grain boundary sliding may be operative, but the data are too sparse to be conclusive. The reported creep rates from uniaxial tests [1] in vacuum are several times higher than the creep rates measured here. This is probably due to the larger interstitial oxygen concentration of the creep tubing (699 wppm) compared to the sheet stock (310 wppm) used for tensile specimen fabrication. Finally, the creep strength of V-4Cr-4Ti at 700 and 800°C was superior to the V-3Fe-4Ti alloy.

1.4 MICROSTRUCTURAL EXAMINATION OF V-4CR-4TI PRESSURIZED THERMAL CREEP TUBES - D. S. Gelles (Pacific Northwest National Laboratory) 17

Two further failed thermal creep pressurized tubes of V-4Cr-4Ti tested at 700 and 800°C have been examined using optical microscopy and transmission electron microscopy in order to understand failure and creep mechanisms. These conditions represent lower stress states than were previously examined. Creep deformation at lower stress is shown to be controlled by subboundary formation and mis-orientation between sub-grains arising from climb of dislocations within the boundary.

1.5 ASSESSMENT OF RECENT VANADIUM ALLOY IRRADIATION EXPERIMENTS - D. L. Smith (Argonne National Laboratory) 24

A brief assessment of the results of irradiation tests of vanadium alloys conducted in the HFIR-11J, -12J, 13J, and 10J, indicate that significant uncertainties in the data exist which affect the reliability of the data. This assessment concludes that vanadium specimens from the 12J experiment were severely oxidized, and that the irradiation data are unreliable. There is a significant uncertainty in the irradiation temperature for specimens in the 11J, 12J and 13J experiment due partially to gap conductance in the experiment. The very high irradiation creep rates obtained for the vanadium alloys in the 12J experiment are attributed to a large thermal creep component. A detailed thermal analysis of each specimen is required to provide a reliable temperature specification for the data obtained in these experiments. Similar temperature uncertainties may also exist for other materials irradiated in similar test assemblies.

1.6 CORRECTIONS AND CLARIFICATIONS ON THE EVALUATION OF THE DHCE EXPERIMENT - D. L. Smith (Argonne National Laboratory) 28

A critical issue in the development of structural materials for the fusion application involves the effects of high helium generation rates on the performance limits of neutron-irradiated materials. Since we do not have a high flux neutron source with fusion-relevant energies, we must rely on simulation techniques to obtain experimental information on these effects. The Dynamic Helium Charging Experiment (DHCE) provides a unique approach for simulating the helium production rates in vanadium alloys in fission reactor irradiations. An assessment of the DHCE-1 proof-ofprinciple experiment and a subsequent evaluation of the DHCE concept have been presented in the last two semiannual reports. This report attempt to correct and clarify several misinterpretations, incorrect statements and misleading conclusions from the evaluation, which contributed to the decision not to conduct a second DHCE experiment in the early phases of the JUPITER-II collaboration. Specific responses to statements and conclusions presented in the evaluation are presented in this report.

2.0 CERAMIC COMPOSITE MATERIALS 34

2.1 SPECIMEN SIZE EFFECT ON THE IN-PLANE SHEAR PROPERTIES OF SILICON CARBIDE/SILICON CARBIDE COMPOSITES - T. Nozawa[1], E. Lara-Curzio[2], Y. Katoh[1,3], L.L. Snead[2] and A. Kohyama[1,3] 35
[1]Institute of Advanced Energy, Kyoto University
[2]Metals and Ceramics Division, Oak Ridge National Laboratory
[3]CREST-ACE, Japan Science and Technology Corporation

Miniaturization of test specimens is often necessary to evaluate the physical and mechanical properties of materials under severe environments. The validation of these techniques requires an understanding of the role of geometric and volumetric (size) effects on the mechanical behavior of the material. Although considerable work has been dedicated to understand size and geometric effects on the off-axis tensile strength of continuous fiber-reinforced ceramic matrix composites, little work has been focused on the effect these variables on their shear properties. This paper will present the results of a study aimed at assessing the effect of notch separation and specimen thickness on the shear strength of a 2-D SiC/SiC composite by the Iosipescu test method. Provisions for mounting miniature test specimens using a fixture for standard size specimens are discussed.

2.2 TENSILE PROPERTIES OF STOICHIOMETRIC SILICON CARBIDE FIBER REINFORCED FCVI DERIVED SILICON CARBIDE MATRIX COMPOSITES - 40
T. Nozawa[1], K. Hironaka[1], T. Taguchi[2], N. Igawa[2], L.L. Snead[3], Y. Katoh[1], S. Jitsukawa[2] and A. Kohyama[1] -
[1]Institute of Advanced Energy, Kyoto University
[2]Department of Materials Science, Japan Atomic Energy Research Institute
[3]Metals and Ceramics Division, Oak Ridge National Laboratory

Recently developed SiC/SiC composites with high-crystalline, near stoichiometric SiC fiber are one of the promising materials for fusion and other high-temperature materials, because of the excellent physical and mechanical stability at high-temperature. Therefore material development has been enthusiastically carried out at ORNL as a part of US-Japan collaboration. The objective of this study is to clarify good performance of these composites at severe environment and also to identify the key issues for material development; effects of the interphase thickness, fabric orientation, and porosity on tensile properties, by using small specimen tensile test technique. It was shown that the maximum stress of Tyranno™-SA/FCVI-SiC composites was stable under high-temperature exposure up to 1300°C in mild oxidizing environment. In addition, it was revealed that Tyranno™-SA/FCVI-SiC with single PyC interphase had its maximum strength, when the thickness of PyC was around 150~200 nm.

2.3 OPTIMIZING THE FABRICATION PROCESS FOR SUPERIOR MECHANICAL PROPERTIES IN THE STOICHIOMETIRIC SiC FIBER REINFORCED FCVI SiC MATRIX COMPOSITE SYSTEM - 47
T. Taguchi[a], N. Igawa[a], T. Nozawa[b], K. Hironaka[b], L. L. Snead[c], T. Hinoki[c], Y. Katoh[b], S. Jitsukawa[a], A. Kohyama[b] and J. C. McLaughlin[c] -
[a] Japan Atomic Energy Research Institute, Tokai, Ibaraki 319-1195, Japan
[b] Kyoto University, Gokasho,Uji, Kyoto 611-0011, Japan
[c] Oak Ridge National Laboratory, PO Box 2008, Oak Ridge, TN 37831, USA

Optimization of the fabrication for SiC composites with stoichiometric SiC fibers (Hi-Nicalon Type S and Tyranno SA) by the forced thermal-gradient chemical vapor infiltration (FCVI) process was carried out. Density and mechanical properties were improved by increasing the fiber volume fraction and optimizing precursor gas flow rates. Porosity was decreased to approximately 15%. Uniformity of fiber/matrix interphase was improved by changing the upstream side and downstream side of a preform during deposition. The tensile strength was seen to slightly increase with thickness of carbon interphase in the range of 75-300 nm. From these results, a dense 300 mm diameter SiC/SiC composite

using Nicalon fiber as a trial experiment was fabricated. The density and porosity were 2.57 g/cm3 and 13.8 %, respectively.

2.4 MODELING THE TRANSVERSE THERMAL CONDUCTIVITY OF 2D-SICF/SIC COMPOSITES – G. E. Youngblood, D. J. Senor and R. H. Jones (Pacific Northwest National Laboratory) 57

A hierarchical model was developed to describe the effective transverse thermal conductivity, K_{eff}, of a 2D-SiC/SiC composite made from stacked and infiltrated woven fabric layers in terms of constituent properties and microstructural and architectural variables. The model includes the expected effects of fiber-matrix interfacial conductance as well as the effects of high fiber packing fractions within individual tows and the non-uniform nature of 2D-fabric layers that include a significant amount of interlayer porosity. Model predictions were obtained for two versions of DuPont 2D-Hi Nicalon™/PyC/ICVI-SiC composite, one with a "thin" (0.110 µm) and the other with a "thick" (1.040 µm) PyC fiber coating. The model predicts that the matrix porosity content and porosity shape factor have a major influence on $K_{eff}(T)$ for such a composite.

2.5 EFFECT OF FIBER PROPERTIES ON NEUTRON IRRADIATED SiC/SiC COMPOSITES - T. Hinoki, A. Kohyama and Y. Katoh (Kyoto University), L.L. Snead (Oak Ridge National Laboratory) 64

The use of SiC/SiC composites for nuclear application has recently been considered because of intrinsic low activation and superior high temperature mechanical properties of SiC. The property of SiC fiber is a key issue in order to improve mechanical properties of SiC/SiC composites following irradiation. SiC/SiC composites reinforced with unidirectional fibers were fabricated by chemical vapor infiltration method. Low oxygen and highly crystalline fibers or just low oxygen fibers were used in the composites. The specimens were irradiated at Japan Material Testing Reactor and High Flux Isotope Reactor. The effects of neutron irradiation on mechanical properties were examined by three points flexural test. Microstructure and fracture behavior were observed by scanning electron microscopy before and after neutron irradiation. The SiC/SiC composites reinforced with a low oxygen content, near-stoichiometric atomic composition, and highly crystalline SiC fibers showed the excellent stability to neutron irradiation. The mechanical property of the composites did not degrade, even after neutron irradiation up to 10 dpa, while the other materials reinforced with non-highly crystalline SiC fibers degraded significantly.

2.6 THE EFFECT OF HIGH DOSE/HIGH TEMPERATURE IRRADIATION ON HIGH PURITY FIBERS AND THEIR SILICON CARBIDE COMPOSITES - T. Hinoki and L. L. Snead (Oak Ridge National Laboratory), Y. Katoh, T. Nozawa and A Kohyama (Kyoto University), A. Hasegawa (Tohoku University) 74

Silicon carbide composites were fabricated by chemical vapor infiltration method with high purity fiber, Hi-Nicalon Type-S and Tyranno SA and non-high purity fiber Hi-Nicalon. SiC/SiC composites, bare fibers and CVD SiC were irradiated at 7.7 dpa and 800 °C or 6.0 dpa and 300 °C. The density of fiber and CVD SiC was measured by gradient column technique. Mechanical properties of the composites were evaluated by four-point flexural tests. Fracture surfaces were observed by SEM. Tyranno SA fiber and CVD SiC showed similar swelling behavior following irradiation at 7.7 dpa and 800 °C. Mechanical properties of Hi-

Nicalon Type-S samples and Tyranno SA samples were stable even following neutron irradiation at 7.7 dpa and 800 °C. Fracture surfaces of these samples following irradiation were similar to those of unirradiated samples with relatively short fiber pull-out.

3.0 FERRITIC/MARTENSITIC STEELS 84

3.1 EXAMINATION OF POSTIRRADIATION DEFORMATION MICROSTRUCTURES IN F82H – D. S. Gelles (Pacific Northwest National Laboratory) and R. Schäublin (EPFL-CRPP Fusion Technology, Switzerland) 85

The deformed microstructures of irradiated F82H uniaxial tensile specimens have been examined following irradiation in the High Flux Reactor (HFR) to 2.6 dpa at 327°C in order to identify controlling mechanisms. Deformation following irradiation is found to occur in poorly defined channels, causing formation of discrete steps at surfaces, similar to that in unirradiated steel. Deformation is by motion of individual σ/2<111> dislocations.

3.2 LONG-TERM HIGH TEMPERATURE OXIDATION BEHAVIOR OF ODS FERRITICS – B. A. Pint and I. G. Wright (Oak Ridge National Laboratory) 91

Extended Abstract

3.3 FERRITIC/MARTENSITIC STEELS - OVERVIEW OF RECENT RESULTS • R. L. Klueh (Oak Ridge National Laboratory), D. S. Gelles (Pacific Northwest National Laboratory), S. Jitsukawa (Japan Atomic Energy Research Institute), A. Kimura (Kyoto University), G. R. Odette (University of California at Santa Barbara), B. van der Schaaf (NRG) and M. Victoria (Paul Scherrer Institute) 92

Extended Abstract

3.4 MICROSTRUCTURAL EXAMINATION OF LOW ACTIVATION FERRITIC STEELS FOLLOWING IRRADIATION IN ORR - D. S. Gelles (Pacific Northwest National Laboratory) 94

Microstructural examinations are reported for a series of low activation steels containing Mn following irradiation in the Oak Ridge Reactor at 330 and 400°C to ~10 dpa. Alloy compositions included 2% Cr, 9% Cr and 12% Cr steels with V to 1.5% and W to 1.0%. Results include compositional changes in precipitates and microstructural changes as a function of composition and irradiation temperature. It is concluded that temperatures in ORR are on the order of 50ºC higher than anticipated.

3.5 TENSILE AND CREEP PROPERTIES OF AN OXIDE DISPERSION-STRENGTHEND FERRITIC STEEL - R. L. Klueh, P. J. Maziasz, D. T. Hoelzer, N. Hashimoto (Oak Ridge National Laboratory), I. S. Kim, and K. Miyahara (Nagoya University) 104

Extended Abstract

3.6 **IRRADIATION CREEP AND MECHANICAL PROPERTIES OF TWO FERRITICMARTENSITIC STEELS IRRADIATED IN THE BN-350 FAST REACTOR –** S .I. Porollo, Yu. Konobeev,and A. M. Dvoriashin (State Scientific Center of Russian Federation, The Institute of Physics and Power Engineering, 249020 Obninsk, Russia) N. I. Budylkin, E. G. Mironova, M. V. Leontyeva-Smirnova, and A. G. Loltukhovsky (State Scientific Center of Russian Federation, A. A. Bochvar All-Russia Research Institute of Inorganic Materials (VNIINM), Moscow, Russia) and F. A. Garner (Pacific Northwest National Laboratory) 106

Russian ferritic/martensitic steels EP-450 and EP-823 were irradiated to 20-60 dpa in the BN-350 fast reactor in the form of pressurized creep tubes and small rings used for mechanical property tests. Data derived from these steels serves to enhance our understanding of the general behavior of this class of steels. It appears that these steels exhibit behavior that is very consistent with that of Western steels. Swelling is relatively low at high neutron exposure and confined to temperatures <420°C, but may be camouflaged somewhat by precipitation-related densification. The irradiation creep studies confirm that the creep compliance of F/M steels is about one-half that of austenitic steels, and that the loss of strength at test temperatures above 500°C is a problem generic to all F/M steels. This conclusion is supported by post-irradiation measurement of short-term mechanical properties. At temperatures below 500°C both steels retain their high strength ($\sigma_{0.2}$=550-600 MPa), but at higher test temperatures a sharp decrease of strength properties occurs. However, the irradiated steels still retain high post-irradiation ductility at test temperatures in the range of 20-700°C.

3.7 **EFFECT OF CHROMIUM, TUNGSTEN, TANTALUM, AND BORON ON MECHANICAL PROPERTIES OF 5-9Cr-WVTaB STEELS** - R. L. Klueh, M. A. Sokolov (Oak Ridge National Laboratory), and D. J. Alexander (Los Alamos National Laboratory) 115

Extended Abstract

4.0 **COPPER ALLOYS** 117

4.1 **OVERAGING OF OUTOKUMPU CuCrZr AT 600°C** - D. J. Edwards (Pacific Northwest National Laboratory)* and B.N. Singh (Risø National Laboratory) 118

An attempt is being made to alter the starting microstructure of CuCrZr to produce a microstructure that is not as sensitive to overageing under irradiation as the prime aged condition. Different overageing conditions (600, 700 and 800°C for 4 hours) have been examined in an earlier report, and in this report shorter overageing times at 600°C have been examined. Overageing times of 1 and 2 hours resulted in a microstructure that is similar in overall precipitate size and density to that of the oxide dispersion in GlidCop Al25. These samples will be included in future irradiation experiments to examine the effects of irradiation on the mechanical and physical properties.

5.0 **REFRACTORY METALS AND ALLOYS** 123

No Contributions

6.0 AUSTENITIC STAINLESS STEELS 124

No Contributions

7.0 MHD INSULATORS, INSULATING CERAMICS AND OPTICAL MATERIALS 125

7.1 AN IN-SITU CALCIUM OXIDE COATING ON VANADIUM ALLOYS IN LIQUID LITHIUM-CALCIUM - J.-H. Park, K. Natesan, and D. L. Smith (Argonne National Laboratory) 126

Calcium oxide coatings were produced on oxygen-charged vanadium alloys (V, V-10Cr, V-1Ti, V-4Cr-4Ti, and V-5Cr-5Ti) by exposure to liquid Li that contained 2.8 at.% Ca. The thickness of in-situ-formed CaO layers was larger in the samples with higher oxygen charging. In the experimental conditions used, the thickness of the grown CaO films was 8-30 μm. For the CaO coating on V-4Cr-4Ti, the measured ex-situ dc-electrical conductivity was 3.0×10^{-10} to 1.0×10^{-8} $ohm^{-1}cm^{-1}$ in an Ar environment in the temperature range 200-500°C.

7.2 TEMPERATURE LIMITS ON COMPATIBILITY OF INSULATING CERAMICS IN LITHIUM - B. A. Pint, J. H. DeVan and J. R. DiStefano (Oak Ridge National Laboratory) 132

Extended Abstract

7.3 THERMAL CONDUCTIVITY OF NATURAL AND ISOTOPICALLY ENRICHED DIAMOND - EFFECT OF NEUTRON IRRADIATION - D.P. White (Merrimack College) 134

Studies on the temperature dependence of the thermal conductivity of isotopically enriched (0.1% ^{13}C) diamond [1-5] have determined the form for the intrinsic scattering phonon relaxation times in diamond. In addition, low temperature thermal conductivity measurements and infrared spectra of lightly neutron-irradiated type IIa natural diamond [6] have determined the size and concentration of extended regions of disordered carbon responsible for phonon scattering. These results have been used to model the thermal conductivity changes expected in neutron irradiated diamond at higher temperatures, from 100 to 1000K. It was found that upon irradiation to a fluence of 4.5×10^{22} neutrons m^{-2} the thermal conductivity of natural diamond went from 2200 to 370 W/mK at 300K while the thermal conductivity of diamond with a 0.1% concentration of ^{13}C went from 3000 to 370 W/mK at 300K.

8.0 BREEDING MATERIALS 139

No Contributions

9.0 RADIATION EFFECTS, MECHANISTIC STUDIES, AND EXPERIMENTAL METHODS 140

9.1 **ON THE MECHANISM OF FORMATION AND GROWTH OF <100> INTERSTITIAL LOOPS IN FERRITIC MATERIALS** – J. Marian, B. D. Wirth (Lawrence Livermore National Laboratory) and R. Schäublin (École Polytechnique Fédérale de Lausanne) 141

We propose a comprehensive mechanism for the formation and growth of <100> interstitial loops in a-Fe. This mechanism, which involves the formation of <100> junctions in the direct reaction between mobile <111> loops, reconciles long-standing experimental observations of these defects in irradiated ferritic materials with recent atomistic simulations of collision cascades and defect cluster properties in Fe, in which highly-mobile <111> clusters are seen to be the dominant feature. The <100> junctions, although metastable, grow into visible <100> loops as a consequence of the high kinetic barrier associated with rotation into <111> configurations and a very low mobility. Finally, the atomic character of <100> and 1/2 <111> loops is investigated with molecular dynamics simulations and the atomic configurations are used to calculate the defect image contrast through direct simulation of TEM images. The simulated images are subsequently compared with actual TEM micrographs of irradiated ferritic materials. Excellent agreement between the experiments and the simulations is found, allowing for a direct identification of the nature and structure of interstitial loops. Hence, this work provides one of the necessary links to unify simulation with experiments in α-Fe and ferritic alloys subject to high-energy particle irradiation.

9.2 **NEUTRON-INDUCED SWELLING AND EMBRITTLEMENT OF PURE IRON AND PURE NICKEL IRRADIATED IN THE BN-350 AND BOR-60 FAST REACTORS -** N. I. Budylkin, E**.** G. Mironova and V. M. Chernov (Bochvar Institute of Nonorganic Chemistry, Moscow, Russia), V. A. Krasnoselov (Research Institute of Atomic Reactors, Dimitrovgrad, Russia), S. I. Porollo (Institute of Physics and Power Engineering, Obninsk, Russia), and F. A. Garner (Pacific Northwest National Laboratory) 153

Pure iron and nickel were irradiated to very high exposures in two fast reactors, BOR-60 and BN-350. It appears that both nickel and iron exhibit a transient-dominated swelling behavior in the range of 2 to 15×10^{-7} dpa/sec, with the shortest transient at ~500°C in nickel, but at <350°C for iron. It also appears that the duration of the transient regime may be dependent on the dpa rate. When the two metals are irradiated at 345-355°C, it is possible to obtain essentially the same swelling level, but the evolution of mechanical properties is quite different. The differences reflect the fact that iron is subject to a low-temperature embrittlement arising from a shift in ductile-brittle transition temperature, while nickel is not. Nickel, however, exhibits high temperature embrittlement, thought to arise from the collection of helium gas at the grain boundaries. Iron generates much less helium during equivalent irradiation.

9.3 **THE EFFECTS OF ONE-DIMENSIONAL MIGRATION OF SELF-INTERSTITIAL CLUSTERS ON THE FORMATION OF VOID LATTICES –** H. L. Heinisch (Pacific Northwest National Laboratory) and B. N. Singh (Risø National Laboratory, Denmark) 161

Extended Abstract

9.4 **THE EFFECT OF FREE SURFACES ON CASCADE DAMAGE PRODUCTION IN IRON –** R. E. Stoller (Oak Ridge National Laboratory) 164

Extended Abstract

9.5 **DISPLACEMENT DAMAGE CROSS SECTIONS FOR NEUTRON-RRADIATED SILICON CARBIDE** - H. L. Heinisch, L. R. Greenwood, W. J. Weber and R. E. Williford (Pacific Northwest National Laboratory) 169

Extended Abstract

10.0 **DOSIMETRY, DAMAGE PARAMETERS, AND ACTIVATION CALCULATIONS** 170

No Contributions

11.0 **MATERIALS ENGINEERING AND DESIGN REQUIREMENTS** 171

No Contributions

12.0 **IRRADIATION FACILITIES AND TEST MATRICES** 172

12.1 **ASSESSMENT OF OPERATIONAL DIFFICULTIES EXPERIENCED IN RECENT HFIR INSTRUMENTED MATERIALS IRRADIATION EXPERIMENTS -** K. R. Thoms (Oak Ridge National Laboratory) 173

Operational difficulties were experienced with some instrumented materials irradiation experiments performed in HFIR during the two-year period preceding the outage for the beryllium changeout and reactor upgrades. This paper provides a detailed description of the operational problems, the investigations into the cause, and the proposed changes to prevent recurrence of the problems.

1.0 VANADIUM ALLOYS

THERMAL CREEP OF V-4Cr-4Ti in a Li ENVIRONMENT

M. L. Grossbeck (Oak Ridge National Laboratory)

Objective

This investigation is being conducted to evaluate thermal creep behavior under conditions where the oxygen concentration is not increased during the life of the test. This will allow thermal creep to be separated from irradiation and helium effects in DHCE (Dynamic Helium Charging Experiments) experiments and will aid in interpretation of the vacuum thermal creep experiments now being performed.

Summary

Tests of pressurized tube specimens of Wah Chang heat 832665 of V-4Cr-4Ti were exposed to Li at elevated temperatures and the deformation in the tubes monitored periodically by laser profilometry. It was determined that at 665°C deformations were below 0.05% for all stresses in the range of 59-117 MPa effective stress at 1105 hours and below 6% at 765°C at 1927 hours. The deformation was so small at 665°C that the temperature was increased to 700°C. Results from 700 C have not yet been obtained. At both temperatures the duration of the tests is not yet sufficient to make a valid comparison with the vacuum creep tests conducted at PNNL.1

Experimental Modifications

Temperature measurements using a sheathed thermocouple directly in the molten lithium determined that the lithium was about 35°C lower than the temperature measured on the thermocouples placed on the outside of the quartz tube surrounding the retorts. Although a temperature gradient was expected, a difference this great was not anticipated. Temperatures were corrected from 700 to 665 and from 800 to 765°C and stresses corrected as appropriate. The retorts have been redesigned to accommodate a thermocouple well in the liquid lithium to obtain a more accurate temperature measurement. Results from the newly designed retorts will described in the next reporting period.

The c-ring type vanadium gaskets originally used on the retorts were found to be unreliable. Internal pressures were monitored so that a leaking gasket could be replaced prior to reaching operating temperature, but numerous delays were experienced. A newer design uses Conflat type flanges with Nb-1Zr gaskets. The newer flange design is much more reliable. However, difficulties are still being experienced in welding flanges to the molybdenum retorts.

Results and Discussion

Table 1 provides results of creep deformation in terms of effective uniaxial strain. For 765°C, effective strain is plotted as a function of stress in Fig. 1. The power law stress behavior is expected, and the stress exponent is found to be in the range of 1-5. Values greater than one are indicative of diffusion-controlled dislocation climb creep.

Table 1. Creep data in terms of effective stress and strain

Specimen	Eff. Stress (MPa)	Effective Strain, %		
765°C				
		200 Hrs	**1064 Hrs**	**1927 Hrs**
V5	25	-.0037	-.017	-.016
V8	42	.017	.016	.078
V3	59	.027	.039	.38
V10	59	.0007	-.016	.36
V7	75	.033	.13	2.5
V4	84	.031	.30	5.9
665°C				
		242 Hrs	**1105 Hrs**	
V12	59	.023	.034	
V2	75	.025	.031	
V11	75	.0074	.0022	
V9	83	.027	.040	
V6	100	.022	leaked	
V1	117	-.010	.0044	
V13	133	.014	leaked	

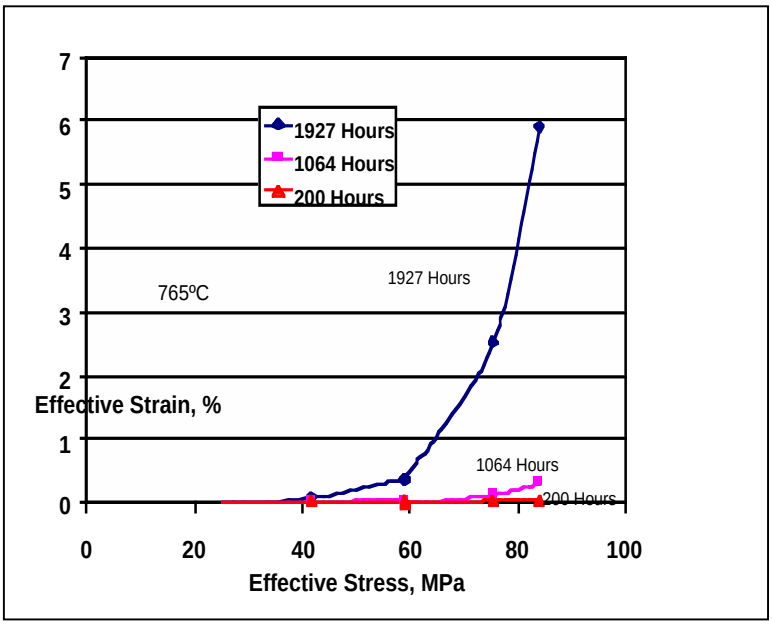

Comparison of 665°C data with results for 700°C in a vacuum, from tests at PNNL, shows larger deformations in the 665°C specimens. This is an unexpected result, but there are large errors associated with the small strains. Longer tests will enable better comparisons to be made. At 765°C the Li exposed specimens show creep deformation similar to the 800°C vacuum tests, allowing for the difference in temperature.

No creep ruptures have been observed at either temperature. A Larson-Miller parameter plot as shown in Fig. 2 compares the creep rupture data from PNNL with the Larson-Miller parameters, $P=T(\log t_r + 20)/1000$ (T is the absolute temperature and t_r is the time to rupture in hours), for Li-exposed specimens that have not yet failed.[2] It can be seen from Fig. 2 that the Li-exposed specimens would not yet be expected to fail.

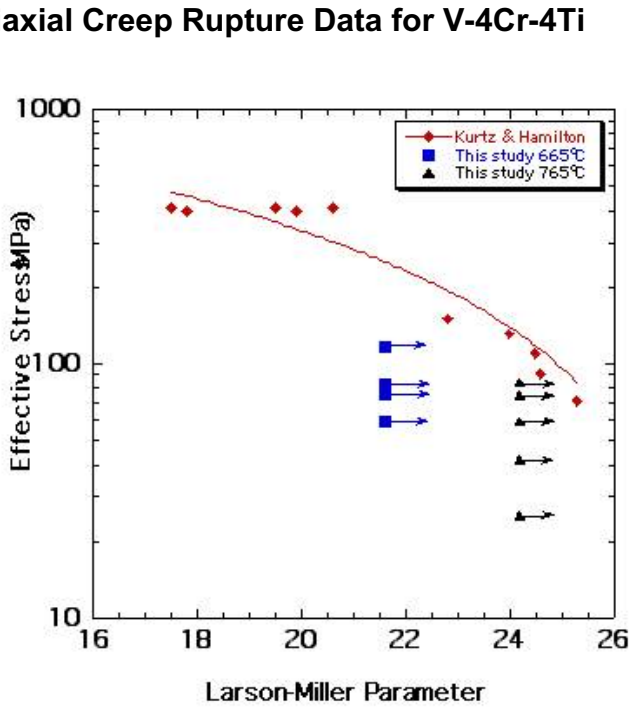

Fig. 2 Larson-Miller type plot comparing creep rupture data from PNNL with tests in progress in the present study.

The activation energy is compared with that of other studies in Table 2. The observed value of 2.8 eV is in close agreement with the value measured in the vacuum experiment of 3.1 eV. It is also in rather close agreement to the value of 2.3 eV observed by Bohm and Schirra in the V-5Ti alloy.[3]

Table 2. Activation energy for creep and self-diffusion

Stress State	Laboratory	Act. Energy, eV
Biaxial	Present Study	2.8
Biaxial	PNNL	3.1
Uniaxial	ANL	5.7
Uniaxial	Bohm and Schirra	2.3
Self-diffusion[4]		3.2

Conclusions

1. An experimental apparatus has been developed for handling liquid lithium for creep testing of pressurized tubes. All metals in contact with Li are refractory metal, including gaskets. It was concluded that a thermocouple well protruding into the liquid lithium is necessary and will be incorporated. Operating experience was also obtained for using a retort with a tritium barrier in anticipation of the next series of experiments.
2. The creep rates observed are consistent with those obtained from specimens in a vacuum environment, with the exception of 665°C where creep rates are higher for the lithium environment. Longer exposures will have to be achieved before confidence can be gained in this observation.
3. At 765°C, no creep failures were observed after an exposure of 1927 hours at effective stress levels up to 87 MPa.
4. Tertiary creep initiates early, with a short region of steady-state creep.
5. The observed activation energy of 2.8 eV is consistent with other measurements and with the activation energy for self-diffusion within experimental error.

References

[1] R.J. Kurtz and M.L. Hamilton, J. Nucl. Mater. 283-287 (2000) 628.
[2] F.R. Larson and J. Miller, Trans. ASME 74 (1952) 765.
[3] H. Bohm and M. Schirra, J. Less Comm. Metals 12 (1967) 280.
[4] R.F. Peart, *Diffusion in Body-Centered Cubic Metals*, Chapter 16, ASM, Metals Park, OH (1965) p. 235.

OXYGEN EMBRITTLEMENT OF VANADIUM ALLOYS WITH AND WITHOUT SURFACE OXIDE FORMATION -- B. A. Pint and J. R. DiStefano (Oak Ridge National Laboratory)

To be published in the Journal of Nuclear Materials as Proceedings of the 10th International Conference on Fusion Reactor Materials, October 2001, Baden-Baden, Germany.

EXTENDED ABSTRACT

Specimens of V-4Cr-4Ti were exposed to low pressure oxygen and high purity He environments from 1atm down to 10^{-4}atm in order to determine oxidation kinetics at 600°-700°C and effects on mechanical properties at 25° and 600°C. At lower oxygen pressures ($P_{O_2} \leq 10^{-5}$Pa), linear reaction kinetics were measured for exposures up to 2000h and the data was used to develop a mathematical expression for the oxidation rate (r in units of mg/cm^2) under these conditions as a function of temperature (T in K) and oxygen pressure (in Pa):

$$r = 4.7 \times 10^{2} \bullet e^{-821/T} \bullet P_{O_2}$$

At higher oxygen pressures, linear-parabolic reaction kinetics were associated with high oxygen uptake and the formation of an external oxide layer. Room-temperature and 600°C tensile ductility was reduced by these exposures, but specimens which formed an external oxide retained some tensile ductility after exposure even though the total oxygen uptake was relatively large. However, when similar specimens with an external oxide were subsequently annealed for 2000h at 700°C the oxide layer disappeared and the specimens were severely embrittled, Figure 1. These results suggest that a surface oxide on V-4Cr-4Ti can be a source of oxygen for subsequent internal dissolution and, therefore, does not prevent embrittlement in extended exposures at 700°C.

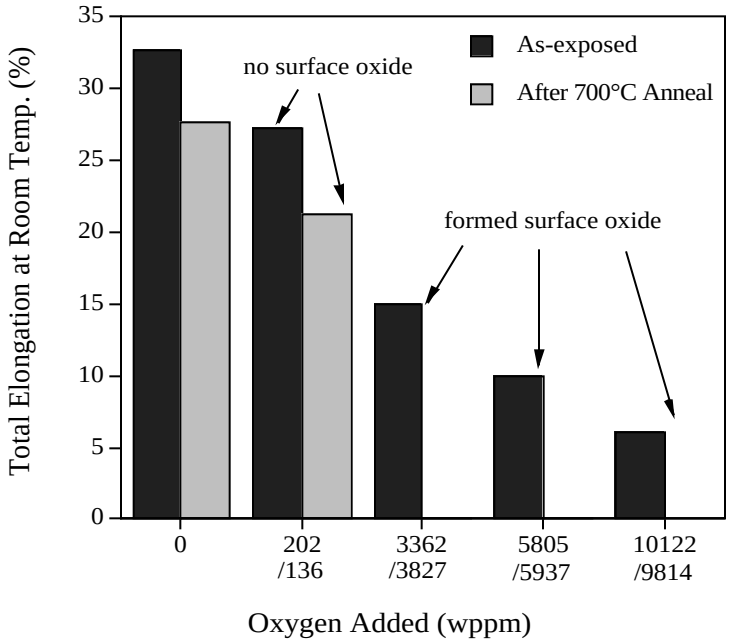

Figure 1. Total elongation at room temperature as a function of added oxygen with and without annealing for 2000h at 700°C. V-4Cr-4Ti specimens which formed a surface oxide and were annealed (3827, 5937 and 9814ppm O) were severely embrittled and had zero ductility.

AN UPDATE ON BIAXIAL THERMAL CREEP OF VANADIUM ALLOYS – R. J. Kurtz (Pacific Northwest National Laboratory)*, A. M. Ermi, (COGEMA Engineering Corp.), and H. Matsui (Tohoku University).

OBJECTIVE

To determine the biaxial thermal creep characteristics of V-4Cr-4Ti and V-3Fe-4Ti over the temperature range 650 to 800°C at realistic stress levels. The results will be compared with uniaxial creep tests in vacuum being carried out at Argonne National Laboratory [1] and biaxial creep experiments in lithium being performed at Oak Ridge National Laboratory [2] to determine the effect of interstitial oxygen on creep properties.

SUMMARY

A study of the thermal creep properties of two vanadium alloys was performed using pressurized tube specimens. Creep tubes nominally 4.57 mm OD by 0.25 mm wall thickness were pressurized with high-purity helium gas to mid-wall effective stresses below the effective (Von Mises) yield strength. Specimens were fabricated from V-4Cr-4Ti (Heat No. 832665) and a V-3Fe-4Ti alloy. The samples were heated to 650, 700, 725, and 800°C in an ultra-high vacuum furnace and periodically removed to measure the change in tube outer diameter with a high-precision laser profilometer. The normalized minimum creep rate $(\dot{\varepsilon}kT/DGb)$ was found to be power-law dependent on the modulus compensated applied stress (σ/G). The value of the stress exponent varied with the applied stress. At normalized stresses ranging from 2 to $8\text{x}10^{-3}$ the stress exponent was about 4 and the activation energy was about 300 kJ/mole, which is quite close to the activation energy for self-diffusion in pure vanadium. These results suggest that the predominant mechanism of creep in this regime is climb-assisted dislocation motion. At lower stresses the value of the stress exponent is near unity suggesting that viscous creep mechanisms such as Coble creep or grain boundary sliding may be operative, but the data are too sparse to be conclusive. The reported creep rates from uniaxial tests [1] in vacuum are several times higher than the creep rates measured here. This is probably due to the larger interstitial oxygen concentration of the creep tubing (699 wppm) compared to the sheet stock (310 wppm) used for tensile specimen fabrication. Finally, the creep strength of V-4Cr-4Ti at 700 and 800°C was superior to the V-3Fe-4Ti alloy.

PROGRESS AND STATUS

The procedure for specimen preparation and testing has been described in detail previously [3]. Since the most recent report [4] considerable additional data has been obtained on the creep characteristics of V-4Cr-4Ti, and an additional vanadium alloy, V-3Fe-4Ti. The matrix of materials, test temperatures and stress levels that has been explored is shown in Table 1. All testing has been completed at 700 and 800°C. Only specimens at 650 and 725°C are currently under test.

Results and Discussion

The effective strain-time data for the 650 and 725°C specimens are listed in Table 2. Tables 3 and 4 give the same type of data for pressurized tubes tested at 700 and 800°C, respectively. The time dependence of the effective mid-wall strain is plotted in Figures 1 – 4 for V-4Cr-4Ti

---

* Pacific Northwest National Laboratory (PNNL) is operated for the U.S. Department of Energy by Battelle Memorial Institute under contract DE-AC06-76RLO-1830.

Table 1. Unpressurized creep tube dimensions, fill pressures and mid-wall effective stress levels.

Test Temperature, °C	Alloy	Specimen Code	Specimen OD, mm	Specimen Wall, mm	Fill Pressure, MPa	Mid-Wall Effective Stress, MPa
650	V-4Cr-4Ti	AR01	4.5665	0.2504	7.922	175.0
		AR02	4.5686	0.2560	9.308	200.1
		AR03	4.5668	0.2530	11.556	250.0
		AR04	4.5690	0.2550	13.093	279.9
		AR06	4.5669	0.2520	13.886	300.1
		AR07	4.5651	0.2560	15.884	335.1
700	V-4Cr-4Ti	AR11	4.5674	0.2601	2.896	66.5
		AR12	4.5662	0.2532	3.909	91.4
		AR13	4.5672	0.2456	4.937	118.5
		AR14	4.5657	0.2499	5.930	138.9
		AR15	4.5659	0.2553	6.964	158.8
	V-3Fe-4Ti	NB01	4.5712	0.2146	3.268	91.8
		NB02	4.5700	0.1753	3.730	129.2
		NB03	4.5789	0.2073	5.592	160.6
725	V-4Cr-4Ti	AR08	4.5646	0.2477	6.205	150.0
		AR09	4.5667	0.2586	7.846	180.0
		AR10	4.5677	0.2428	8.156	200.0
800	V-4Cr-4Ti	AR16	4.5684	0.2477	2.654	70.6
		AR17	4.5667	0.2507	3.571	92.6
		AR18	4.5664	0.2461	4.482	117.7
		AR19	4.5667	0.2543	5.419	136.8
		AR20	4.5659	0.2527	1.793	47.6
		AR21	4.5679	0.2454	0.910	26.4
	V-3Fe-4Ti	NB05	4.5692	0.1882	2.055	74.0
		NB06	4.5669	0.2139	2.979	92.2

Table 2. Time dependence of effective mid-wall creep strain for 650 and 725°C tests.

	Specimen Code								
	650°C						725°C		
Time, h	AR01	AR02	AR03	AR04	AR06	AR07	AR08	AR09	AR10
144	-	-	-	1.8425	-	-	-	-	-
190	0.0151	0.0223	1.2427	-	2.2417	3.7172	0.0694	0.4905	0.6075
313	-	-	-	1.8729	-	-	-	-	-
330	-	-	-	-	-	-	-	-	3.4775
334	0.0172	0.0275	1.2531	-	2.2883	4.0141	0.1560	2.8212	
385	-	-	-	-	-	-	-	3.8558	
483	-	-	-	1.9031	-	-	-		
503	0.0187	0.0169	1.2592	-	2.3590	4.6455	0.3027		
651	-	-	-	1.9916	-		-		
673	0.0193	0.0406	1.2879	-	2.8959		0.5310		
820	-	-	-	2.0396	-		-		
841	0.0262	0.0567	1.3069	-	3.2688		1.6045		
988	-	-	-	2.1186	-		-		
1010	0.0367	0.0697	1.3182	-	3.7093		3.0028		
1178	0.0317	0.0732	1.3447	-	4.8321		4.3460		

Table 3. Time dependence of effective mid-wall creep strain for 700°C tests.

	Specimen Code							
Time, h	AR11	AR12	AR13	AR14	AR15	NB01	NB02	NB03
101	-	-	-	-	-	0.0650	0.0578	0.3314
168	0.0072	0.0000	0.0072	0.0072	0.0217	-	-	-
242	0.0072	0.0000	0.0072	0.0145	0.0361	-	-	-
357	0.0072	0.0072	0.0072	0.0289	0.0795	-	-	-
478	-	-	-	-	-	0.4546	0.3826	5.6911
585	-	-	-	-	-	0.6278	0.5486	12.165
598	0.0072	0.0217	0.0145	0.0578	0.2096	-	-	
752	-	-	-	-	-	0.9884	0.9382	
919	-	-	-	-	-	1.3921	1.3204	
1110	-	-	-	-	-	1.8605	1.8178	
1277	-	-	-	-	-	2.3791	2.2357	
1375	0.0072	0.0145	0.0217	0.1229	0.9246	-	-	
1523	0.0072	0.0000	0.0361	0.1373	1.2783	-	-	
1661	-	-	-	-	-	3.6456	3.6395	
1997	-	-	-	-	-	5.7723	5.3574	
2157	0.0361	0.0289	0.0578	0.3468	4.5424	-	-	
2362	-	-	-	-	-	7.5867	6.9435	
2780	0.0289	0.0217	0.0578	0.8596	10.247	-	-	
2804	-	-	-	-	12.956	-	-	
2842	-	-	-	-		10.585	9.3220	
2881	0.0289	0.0361	0.0867	0.9896		-	-	
3258	0.0289	0.0217	0.0867	1.5309		-	-	
3273	-	-	-	-		13.533	11.760	
3365	0.0361	0.0289	0.0939	1.6896				
3418	-	-	-	-		-	-	
3532	0.0289	0.0289	0.0939	2.1008		17.040	12.688	
3653	-	-	-	-			14.414	
3699	0.0289	0.0361	0.1011	2.3676			-	
3827	-	-	-	-			15.885	
3887	-	-	-	-			17.269	
3890	0.0217	0.0361	0.1445	2.7712				
4057	0.0217	0.0361	0.1300	3.1820				
4441	0.0289	0.0506	0.1806	4.1036				
4777	0.0361	0.0578	0.2312	5.4847				
5142	0.0506	0.0650	0.2817	6.6126				
5622	0.0361	0.0650	0.3756	8.3490				
6053	0.0506	0.0650	0.4623	9.9534				
6198	0.0795	0.0723	0.5200	10.763				
6433	0.0433	0.1228	0.5922	12.564				
6607	0.0361	0.0723	0.6716	14.199				
6667	0.0650	0.0867	0.6933	14.798				
7267	0.0578	0.1012	0.9604					
8029	0.0578	0.1156	1.3428					
8772	0.0722	0.1301	1.7756					
9663	0.0650	0.1445	2.3019					

Table 4. Time dependence of effective mid-wall creep strain for 800°C tests.

Time, h	Specimen Code							
	AR21	AR20	AR16	AR17	AR18	AR19	NB05	NB06
101	-	-	-	-	-	-	-	20.024
144	-	-	-	-	-	-	1.3495	
167	0.0072	0.0000	-	-	-	-	-	
168	-	-	0.0289	0.0650	0.1445	3.5917	-	
242	-	-	0.0361	0.1156	0.6212	14.709	-	
358	0.0217	0.0217	-	-	-		-	
412	-	-	0.1156	0.8089	5.7999		-	
427	-	-	-	-	-		6.8442	
488	-	-	0.1806	1.5306	10.832			
516	0.0217	0.0434	-	-	-			
578	-	-	0.3466	2.9363	24.141			
727	-	-	0.8375	6.4173				
864	-	-	1.5156	13.561				
900	0.0578	0.2312	-					
1031	-	-	2.6327					
1236	0.0795	0.5202	-					
1343	-	-	5.4454					
1491	-	-	7.1108					
1601	0.1300	1.0329	-					
1784	-	-	10.835					
2081	0.2095	1.8483	-					
2125	-	-	16.000					
2333	0.2311	2.3458	-					
2460	-	-	21.295					
2668	0.3033	3.1025	-					
2812	-	-	26.827					
2903	0.3539	3.6787	-					
2956	-	-	29.201					
3077	0.3683	4.0818	-					
3137	0.3972	4.2545	-					
3239	-	-	33.912					
3346	-	-	35.806					
3513	-	-	38.907					
3680	-	-	42.279					
3737	0.5199	5.9371	-					
3871	-	-	46.557					
4029	-	-	51.885					
4499	0.6860	8.0689						
5242	0.8736	10.304						
6052	1.0613	12.735						

specimens tested at 650, 700, 725 and 800°C, respectively. Figure 5 gives a plot of the strain-time data for V-3Fe-4Ti at 700°C. It is interesting that the 650°C creep curves all display "classical" features in that a distinct primary creep regime is found, followed by a steady-state creep region, and finally an accelerating creep rate to failure. In contrast, the creep curves at 700, 725 and 800°C show an accelerating creep rate almost from the beginning of the test. No primary creep was observed and the duration of the steady-state regime was very brief. Similar results have been found for biaxial creep tests in lithium [5] but not for the uniaxial tests in vacuum [4]. The occurrence of a continuously accelerating creep rate almost from the onset of testing is not due to specimen geometry effects. Wheeler [6] found an accelerating creep curve for ultrahigh vacuum tests of pure vanadium at temperatures below 925°C but not at higher

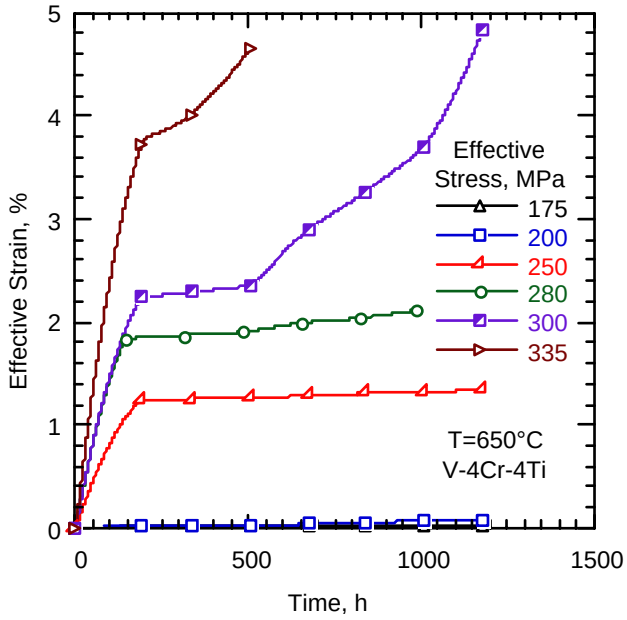

Figure 1. Time dependence of the normalized effective mid-wall creep strain at 650°C for unirradiated V-4Cr-4Ti.

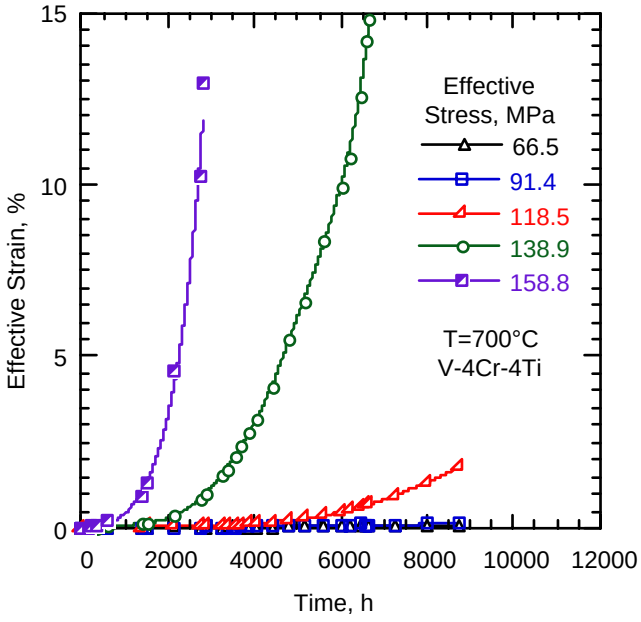

Figure 2. Time dependence of the normalized effective mid-wall creep strain at 700°C for unirradiated V-4Cr-4Ti.

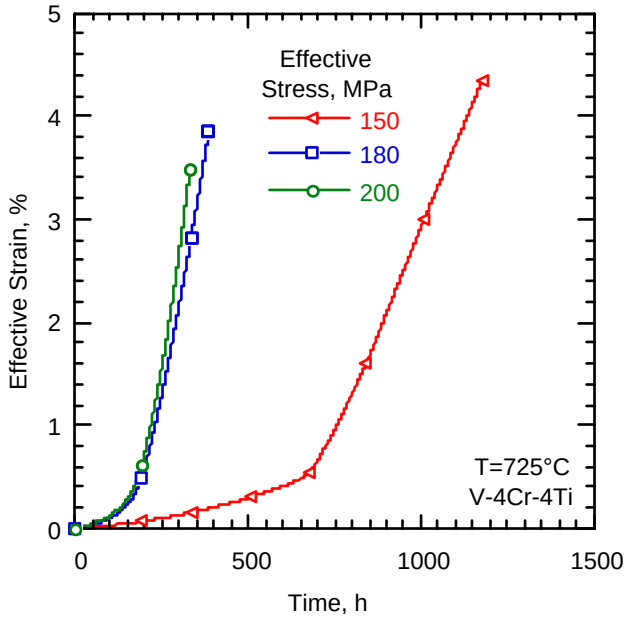

Figure 3. Time dependence of the normalized effective mid-wall creep strain at 725°C for unirradiated V-4Cr-4Ti.

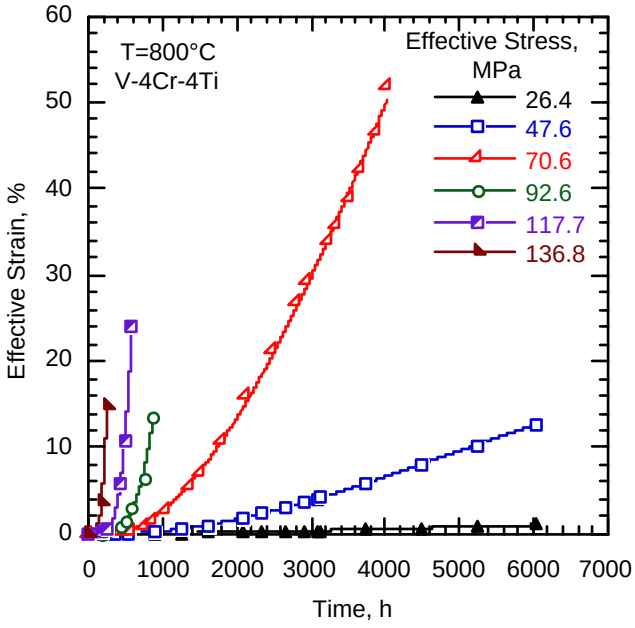

Figure 4. Time dependence of the normalized effective mid-wall creep strain at 800°C for unirradiated V-4Cr-4Ti.

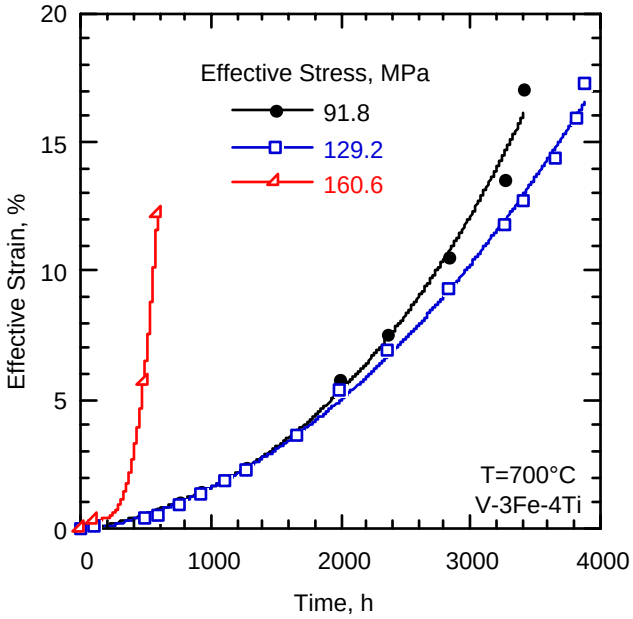

Figure 5. Time dependence of the normalized effective mid-wall creep strain at 700°C for unirradiated V-3Fe-4Ti.

temperatures. Accelerating creep curves are not uncommon and can be observed in most metals and alloys [7].

Effective minimum creep rates were obtained from the strain-time data taking care to exclude the portions of the curves that showed primary or tertiary creep behavior. Typically the effective minimum creep rates were determined at effective strain levels less than about 0.2%. Normalized effective creep rates were then calculated from:

$$\dot{\varepsilon}_N = \frac{\dot{\varepsilon} kT}{DGb} \qquad (1)$$

where $\dot{\varepsilon}$ is the effective minimum creep rate, k is Boltzmann's constant, T is the absolute temperature, D is the self-diffusion coefficient, G is the elastic shear modulus and b is the Burgers vector. The normalized effective creep rates were plotted against the normalized stress, which was obtained by dividing the applied stress by the shear modulus. Values of the shear modulus as a function of temperature were determined from [8]:

$$G = \left(0.488 - 8.43x10^{-5}\,T\right)x10^{11} \qquad (2)$$

where T is the absolute temperature. Equation 2 is valid only for pure vanadium but recent research [9] on the elastic properties of V-5Cr-5Ti indicates that the shear modulus of this particular alloy differs from pure vanadium by less than 1% at 300K. The temperature dependence of the self-diffusion coefficient was computed from [7]:

$$D = D_o \exp\left[\frac{-Q}{RT}\right] \qquad (3)$$

where the pre-exponential term, D_o, was assumed to be $1x10^{-6}$ and the activation energy, Q, was taken as 270 kJ/mole.

A log-log plot of the normalized effective minimum strain rate against the normalized stress is given in Figure 6 for the biaxial and uniaxial [1] creep experiments performed in vacuum. The data clearly shows that the stress dependence of the creep rate (and therefore the predominant creep mechanism) varies with stress. At low stresses ($<2x10^{-3}$) the stress exponent is near unity which is indicative of a viscous creep mechanism such as Coble creep or grain boundary sliding. The data are too few to reach a firm estimate at what stress these mechanisms become operative. At intermediate stresses (2 to $8x10^{-3}$) the stress exponent is around 4 which suggests that a climb-assisted dislocation glide mechanism dominates the creep process. Finally, at high stresses ($>8x10^{-3}$) the stress exponent is very large (>10) which is representative of the power-law breakdown regime.

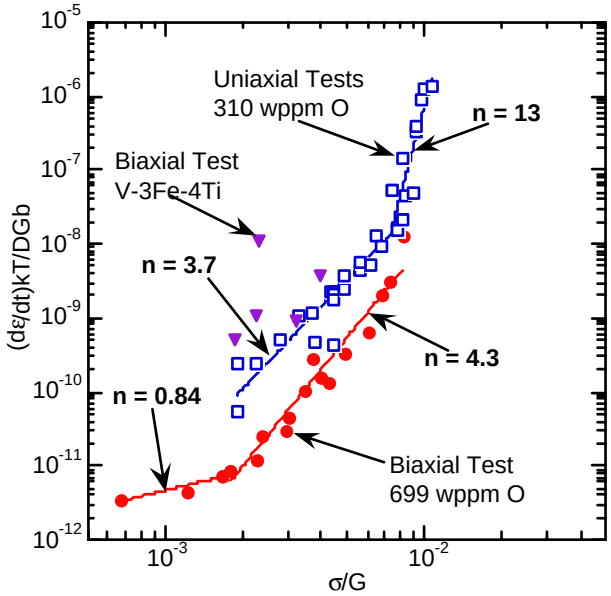

Figure 6. Stress dependence of the normalized effective mid-wall creep strain for unirradiated vanadium alloys.

It is evident from Figure 6 that the creep rate of the uniaxial specimens is substantially greater than the biaxial specimens. Part of this difference may be due to texture effects associated with the tube microstructure compared to sheet tensile specimens. While such an effect could account for some of the difference it is not known if the creep tubing exhibits any significant texture. A more likely source of the difference is the different interstitial oxygen concentration of the creep tubes versus the tensile specimens. The sheet stock used to make the uniaxial creep specimens had a starting interstitial oxygen concentration of 310 wppm, whereas the initial creep tube oxygen level is much higher at 699 wppm. Since the steady-state creep regime is very short duration in these tests it is expected that oxygen pickup during the test is not a concern. Such differences in interstitial oxygen can produce dramatic changes in the creep rate of pure vanadium. Schirra [10] has shown that increasing the oxygen concentration from 220 to 750 wppm decreased the creep rate by five orders of magnitude. The effect of interstitial oxygen on creep of V-Ti alloys was smaller than pure vanadium, but on the same order as the findings reported here [10].

Also shown in Figure 6 are creep data for V-3Fe-4Ti pressurized creep tubes. With the exception of one data point the stress dependence of the creep rate is similar to V-4Cr-4Ti, but there is far too few data to reliably compute a meaningful stress exponent. The data clearly show that the creep rate of this alloy is significantly greater than that of V-4Cr-4Ti.

A comparison of the creep-rupture performance of various vanadium alloys is presented in Figure 7 which shows a Larsen-Miller parameter plot of the available data. The Larsen-Miller parameter was computed from:

$$P = \frac{T(\log t_r + 20)}{1000} \qquad (4)$$

where T is the absolute temperature and t_r is the time-to-rupture in hours. V-Cr-Ti alloys containing 10 to 15% Cr are included in Figure 7 to illustrate the superior creep-rupture resistance of vanadium alloys with chromium levels greater than 4 to 5% [11]. There is generally good correlation between the uniaxial test results of Chung et al., [12] and Natesan et al. [1] and the biaxial creep results generated in this study. Evidently differences in interstitial oxygen concentration did not significantly influence the time-to-rupture. The good correlation may be fortuitous since oxygen pickup during the course of a long term test is expected to affect creep ductility and, therefore, time-to-rupture. In addition, the uniaxial tests employed constant loading so the gauge section stress increases during the experiment as the specimen cross-section decreases. In contrast, as a pressurized tube expands the gas pressure decreases yielding a roughly constant effective stress for mid-wall strains up to about 20%. Note the creep-rupture performance of V-3Fe-4Ti is generally inferior to the V-Cr-Ti alloys.

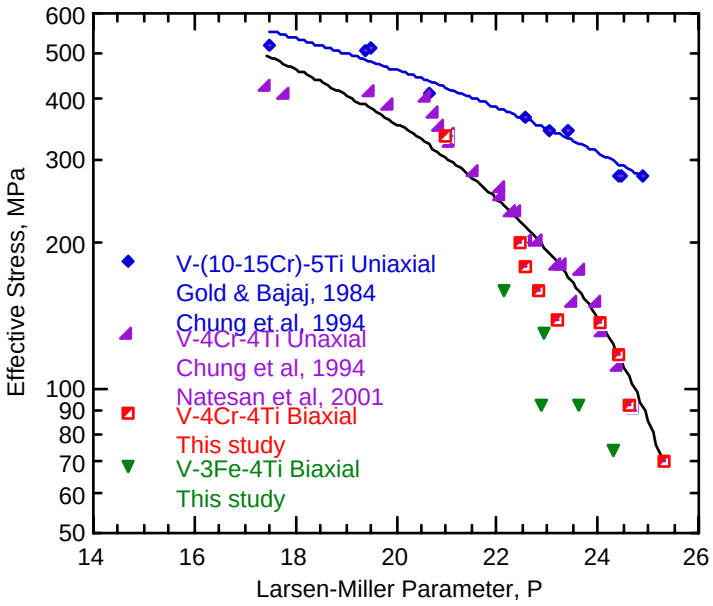

Figure 7. Larsen-Miller parameter plot for creep rupture of unirradiated vanadium alloys.

Conclusions

An on-going study of the thermal creep properties of V-4Cr-4Ti is being performed using pressurized tube specimens. The normalized minimum creep rate was found to be power-law dependent on the modulus compensated applied stress. The value of the stress exponent varied

with the applied stress. At normalized stresses ranging from 2 to $8x10^{-3}$ the stress exponent was about 4 and the activation energy was about 300 kJ/mole, which is quite close to the activation energy for self-diffusion in pure vanadium. These results suggest that the predominant mechanism of creep in this regime is climb-assisted dislocation motion. At lower stresses the value of the stress exponent is near unity suggesting that viscous creep mechanisms such as Coble creep or grain boundary sliding may be operative. The reported creep rates from uniaxial tests are several times higher than the creep rates measured here. This is probably due to differences in interstitial oxygen concentration at the beginning of the test. Finally, the creep strength of V-4Cr-4Ti at 700 and 800°C was superior to the V-3Fe-4Ti alloy.

ACKNOWLEDGEMENTS

We acknowledge the significant efforts of L. K. Fetrow and R. M. Ermi in performing the experiments described in this report.

REFERENCES

[1] K. Natesan, W. K. Soppet and D. L. Rink, "Uniaxial Creep Behavior of V-4Cr-4Ti Alloy," in Fusion Materials: Semiannual Progress Report for Period Ending December 31, 2000, DOE/ER-0313/29 (2001) 37.

[2] M. L. Grossbeck, "Biaxial Thermal Creep of V-4Cr-4Ti in a Lithium Environment," in Fusion Materials: Semiannual Progress Report for Period Ending June 30, 2001, DOE/ER-0313/30 (2001) 8.

[3] R. J. Kurtz and M. L. Hamilton, “Biaxial Thermal Creep of V-4Cr-4Ti at 700°C and 800°C,” in Fusion Materials: Semiannual Progress Report for Period Ending December 31, 1998, DOE/ER-0313/25 (1999) 7.

[4] R. J. Kurtz and M. L. Hamilton, "Biaxial Thermal Creep of V-4Cr-4Ti at 700°C and 800°C," *J. of Nuc. Matls*. 283-287 (2000) 628.

[5] M. L. Grossbeck, "Biaxial Creep of V-4Cr-4Ti in a Lithium Environment," submitted for publication in the proceedings of the 10th International Conference on Fusion Reactor Materials.

[6] R. K. Wheeler, E. R. Gilbert, F. L. Yaggee and S. A. Duran, *Acta Metal*. Vol. 19 (1971) 21.

[7] D. L. Harrod and R. E. Gold, *Int. Metals Rev.* 4 (1980) 163.

[8] R. J. Farraro and R. B. McLellan, “High Temperature Elastic Properties of Polycrystalline Niobium, Tantalum and Vanadium,” *Met. Trans.* 10A (1979) 1699.

[9] W. D. Porter, R. B. Dinwiddie, W. A. Simpson, and M. L. Grossbeck, “Determination of the Thermophysical Properties of V-5Cr-5Ti,” ANL/FPP/TM-287 (1994) 41.

[10] M. Schirra, “Das Zeitstandfestigkeits und Kriechverhalten von Vanad-Basis Legierungen,” KFK Report 2440, Kernforschungszentrum Karlsruhe (1989).

[11] R. E. Gold and R. Bajaj, *J. of Nucl. Mater*. 122-123 (1984) 759.

[12] H. M. Chung, B. A. Loomis and D. L. Smith, *J. of Nucl. Mater*. 212-215 (1994) 772.

MICROSTRUCTURAL EXAMINATION OF V-4CR-4TI PRESSURIZED THERMAL CREEP TUBES - D. S. Gelles (Pacific Northwest National Laboratory)*

OBJECTIVE

The objective of this effort is to provide further understanding of processes controlling thermal creep in vanadium alloys.

SUMMARY

Two further failed thermal creep pressurized tubes of V-4Cr-4Ti tested at 700 and 800°C have been examined using optical microscopy and transmission electron microscopy in order to understand failure and creep mechanisms. These conditions represent lower stress states than were previously examined. Creep deformation at lower stress is shown to be controlled by sub-boundary formation and mis-orientation between sub-grains arising from climb of dislocations within the boundary.

PROGRESS AND STATUS

Introduction

Biaxial thermal creep microstructural response for V-4Cr-4Ti at 700 and 800°C was recently reported.[1] The present effort describes examination using optical microscopy (OM) and transmission electron microscopy (TEM) techniques of specimens at lower stress states that failed more recently. The OM examinations were intended to locate the failure sites and to begin evaluating the failure mechanism and the TEM microstructural examinations were intended to verify the controlling deformation mechanisms. The previous microstructural examinations had shown failure due to high local thinning with microstructures containing high densities of individual dislocations. Creep was therefore expected to be controlled by dislocation climb, in agreement with the high values for the stress dependence of secondary creep found.[2] Evidence for a well-defined dislocation cell structure was not found. The present results indicate a change in creep mechanism occurs for lower stress conditions.

Experimental Procedure

Details for the pressurized tubes examined in this and the previous study are provided in Table 1. Ring sections of specimens AR14 and AR16 were sectioned and punched to produce 3 mm curved disks in a manner similar to that done previously. Disks were thinned by grinding but evidence of the curvature was retained in order to be able to orient the microstructure relative to the stress state. Disks were then electropolished at low temperature using standard techniques to produce thin foils. Each disk was mounted in the microscope so that images could be related to the tube orientation and therefore the state of stress could be related to the microstructure. Dislocation imaging involved procedures that allowed identification of all $\frac{a}{2}$<111> Burgers vectors present.[3]

* Pacific Northwest National Laboratory (PNNL) is operated for the U.S. Department of Energy by Battelle Memorial Institute under contract DE-AC06-76RLO-1830.

Table 1. Test conditions for selected failed pressurized tube specimens of V-4Cr-4Ti (heat 832665).

Specimen ID	Temp. (°C)	Effective Stress (MPa)	Time to failure (hrs)	Effective mid-wall failure strain (%)
AR14	700	138.9	6667	14.8
AR15	700	158.8	2804	13.0
AR16	800	70.6	4029	51.9
AR17	800	92.6	864	13.6
AR18	800	117.7	578	24.1
AR19	800	136.8	242	14.7

Results

Macroscopic features

Photographs of tubes AR14 and AR16 using OM are shown in Figures 1a) and b), and c) and d), respectively. The tubes have been oriented to show the likely failure sites in the center of the tube. Tubes are 27.4 mm in length. In both cases failure appears to be due to formation of a longitudinal crack but the crack is shorter following testing at the higher temperature.

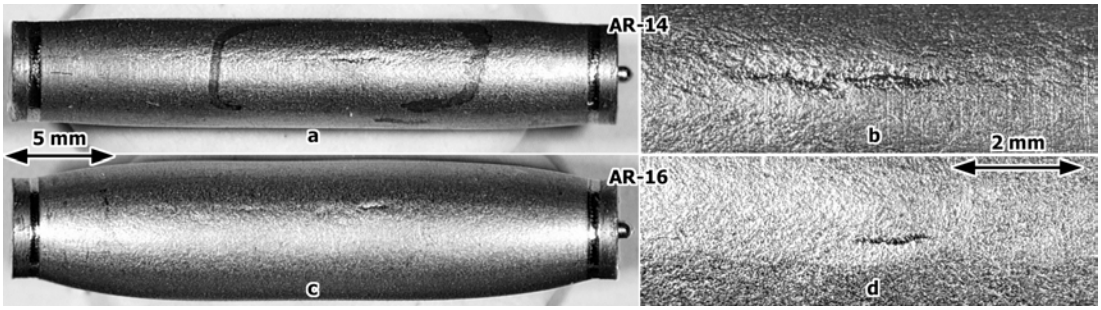

Figure 1. Failed pressurized tubes AR14 in a) and b) and AR16 in c) and d) shown with the likely failure sites face-on at low and intermediated magnifications.

The tubes were then sectioned in order to examine the failure sites from the inside of the tube. Failure features appeared similar to those in Figures 1b) and 1d).

Metallographic sections were then prepared in order to locate through-thickness cracks, Examples are provided in Figure 2 showing regions in specimens AR14 and AR16 that contain areas that have been reduced in wall thickness to the point of failure. From Figure 2, examples of grain elongation can be identified in each of the thinned sections, indicating that strain within grains reached high levels in comparison to grains in unthinned regions, where grains remained equiaxed, despite strains up to 50% as in specimen AR16. Therefore, local plasticity was very high prior to failure and failure was a result of that thinning.

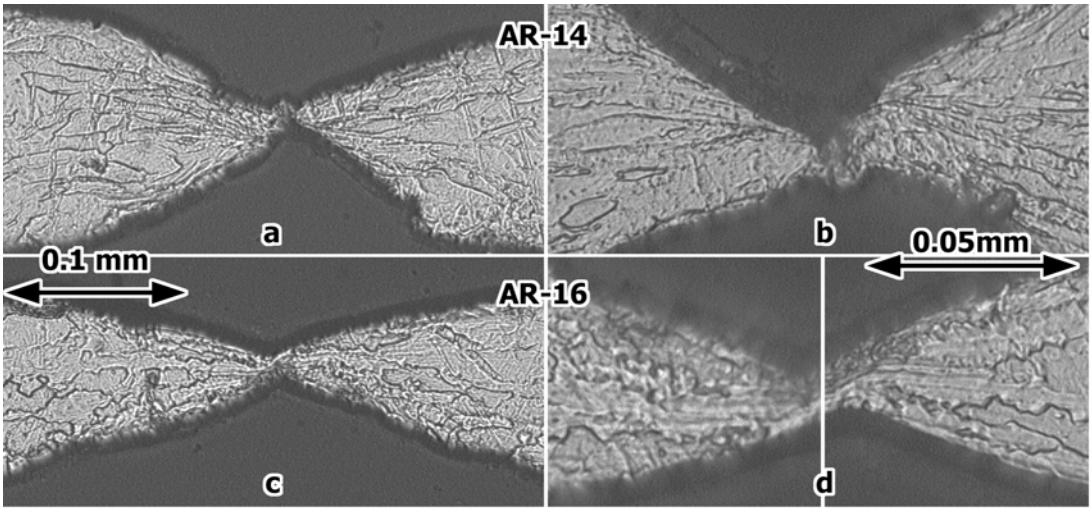

Figure 2. Optical metallography examples of thinned sections of specimens AR14 and AR16.

Microstructure

Specimens for TEM were successfully prepared from specimens AR14 and AR16 but thin area was limited. However, microstructures in these samples were quite different from those previously examined. Well defined sub-grain boundaries were found in each condition, with low dislocation densities between sub-grain boundary walls. Examples were found where the sub-grain boundary was connected to dislocations within sub-cells, perhaps indicating that these boundaries were beginning to break down. (Tests were continued for some time after failure, so the final stress state was reduced to zero before microstructural development was stopped.) However, the cells formed by these boundaries were often of very unusual shape. Examples at low magnification are provided in Figure 3 showing sub-grain boundary structures in AR-16 following creep at 800ºC. Although some sub-grains are equiaxed, many are unusually shaped such as one at the top of Figure 3a) and another on the upper left of Figure 3c. Initially the nature of the dislocations within sub-grains suggested that they were formed during preparation. Three vertical traces in Figure 3c) towards the upper left are indicative of dislocation migration within the foil. However, it is now understood that these dislocations were probably present following creep deformation.

Comparison of imaging conditions across a given sub-grain boundary demonstrated that the boundaries defined changes in tilt between adjacent sub-grains. Also, it was apparent that the dislocation structure within the sub-boundaries developed interesting patterns that clearly delineated the dislocations that made up the boundary. It appeared possible to analyze the dislocation arrays within a given sub-boundary in order to determine the character of the dislocations within the boundary, assuming that the Burgers vectors present were restricted to those that existed in the matrix. Therefore, several boundaries were imaged according to procedures previously described that allow determination of all Burgers vectors in a given area.[1,3]

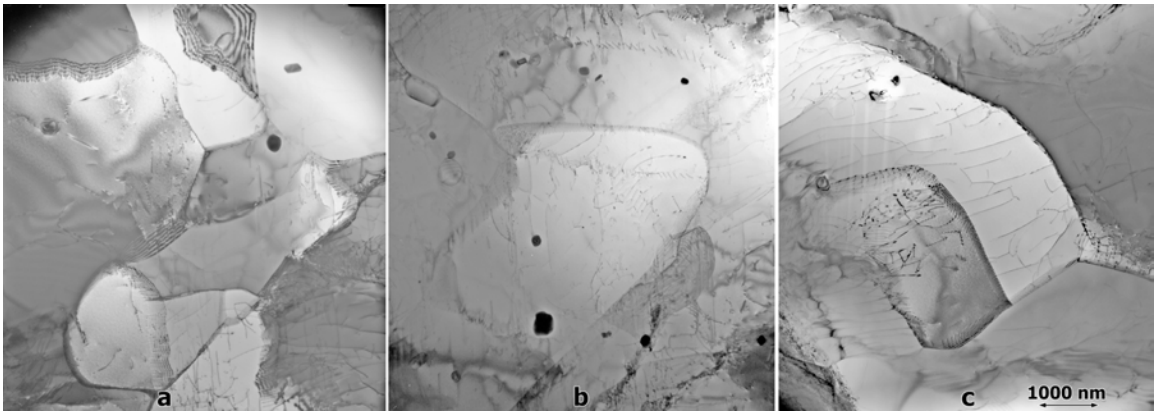

Figure 3. Examples of sub-grain boundaries in AR-16.

Examples of sub-grain microstructures are provided in Figures 4 to 7, 4 for condition AR-14 and 5 to 7 for AR-16. However, it should be noted that Figures 6 and 7 show the same sub-boundary but along two different sections. The figures have been prepared to allow identification of all $\frac{a}{2}$<111> Burgers vectors present, so three views of the same area are given, one in $01\bar{1}$ contrast and one in 200 contrast, both taken near a (011) orientation, and the third in either $\bar{1}10$ or $\bar{1}01$ contrast taken after a large tilt of the foil. Stronger contrast has been used in Figures 6c) and 7c) in order to emphasize that few dislocations appear in the boundary under this imaging condition. In each case, the foil orientation was determined at zero tilt and the microstructure could be related to the cylindrical axis of the pressurized tube, thereby allowing definition of the stress state. The mis-orientation across the sub-boundary is estimated for Figure 4 at 0.09° with the grain orientation near (001) for zero tilt. The mis-orientation across the sub-boundary for Figure 5 is 0.13° with the grain oriented near (133) for zero tilt and for Figures 6 and 7 the mis-orientation is estimated at 0.16° with the grain orientation near (001) for zero tilt. Note that rotational misorientation could not be determined to this degree of precision based on film records of the Kikuchi patterns. A stereographic triangle is inset for each figure sequence with a black dot to define zero tilt and an arrow to define the circumferential stress direction from that point. In all cases the tilt direction corresponded to the circumferential stress direction. In each of these figures, imaging with $\bar{g}$ = 200 as in b) should show all four of the possible $\frac{a}{2}$<111> Burgers vectors, whereas the other imaging conditions will only show two of the possibilities. With $\bar{g}$ = $01\bar{1}$ as in all a) figures, $\frac{a}{2}[1\bar{1}1]$ and $\frac{a}{2}[11\bar{1}]$ should be visible, whereas with $\bar{g}$ = $\bar{1}10$ as in the 4c), 6c) and 7c) figures, $\frac{a}{2}[\bar{1}11]$ and $\frac{a}{2}[1\bar{1}1]$ should be visible and with $\bar{g}$ = $\bar{1}01$ as in the 5c) figure, $\frac{a}{2}[\bar{1}11]$ and $\frac{a}{2}[11\bar{1}]$ should be visible. From these relationships, all Burgers vectors for dislocations present can be defined. However, it can be noted that fine dislocation arrays, such as in Figures 5, 6 and 7 have much weaker contrast using 200 contrast. See for example, Figures 5b), 6b) and 7b) where all dislocations should be equally visible.

Applying this Burgers vector analysis to Figure 4 through 7 provides several useful observations. In both the a) and b) figures for each of these micrograph series, a fine array of dislocations can be seen on each sub-boundary, having Burgers vector $\frac{a}{2}[\bar{1}11]$ in Figures 4, 6 and 7 and $\frac{a}{2}[1\bar{1}1]$ in Figure 5. But the closely spaced dislocations in Figure 4 (at the upper right) are oriented differently than those in Figures 6 and 7. A second array of more coarsely spaced dislocations appears in all images of Figures 6 and 7 indicating a Burgers vector of $\frac{a}{2}[1\bar{1}1]$. Some dislocations appear curved In Figure 7, showing that the screw verses edge component may be changing for a single dislocation in a sub-grain boundary. This change in character is probably associated

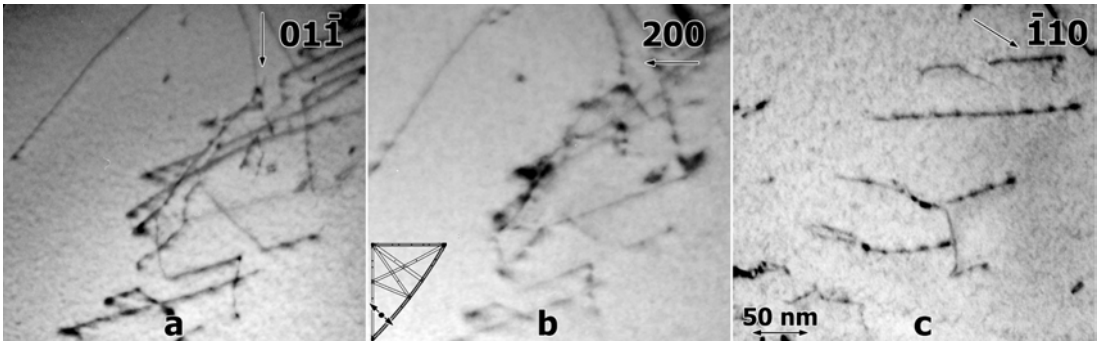

Figure 4. A sub-grain boundary in specimen AR-14 at 700ºC and 152 MPa.

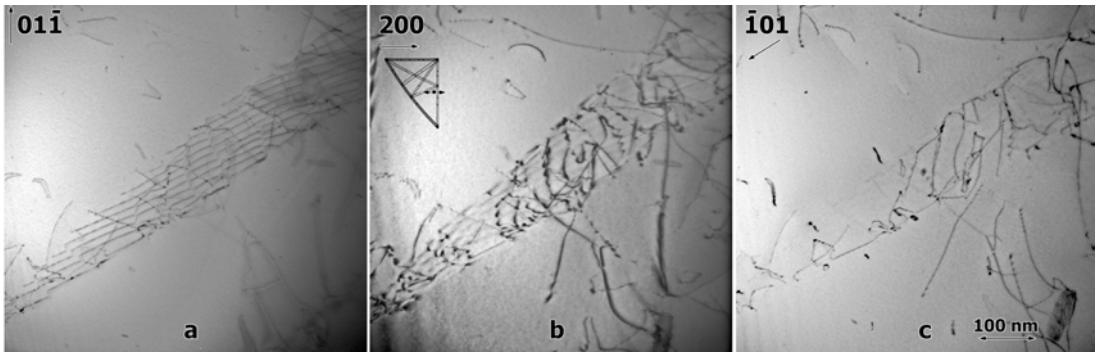

Figure 5. A sub-grain boundary region in specimen AR-16.

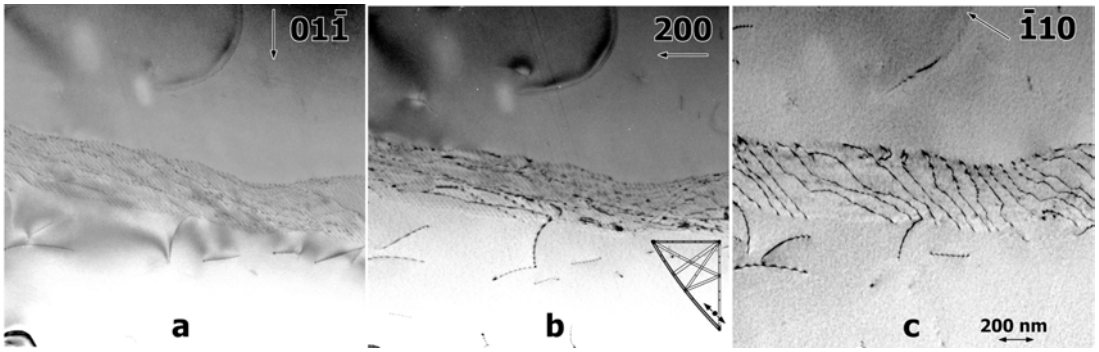

Figure 6. A sub-grain boundary in condition AR-16 at 800ºC and 77 MPa.

with the curvature of the boundary. Many coarsely spaced dislocations in subgrain boundaries exhibit zig-zag imaging. As these oscillations are not as apparent in matrix dislocation images, it is expected that the zig-zag behavior demonstrates network behavior with at least two different Burgers vectors represented, so that care must be taken interpreting the Burgers vector type and character of each zig or zag.

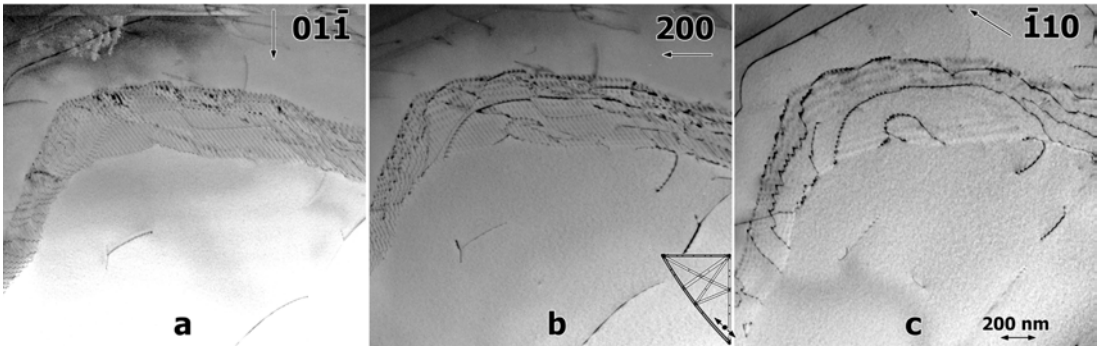

Figure 7. An adjacent sub-grain boundary in condition AR-16 at 800ºC and 77 MPa.

Discussion

The results of microstructural examinations of these V-4Cr-4Ti pressurized thermal creep tubes provide insight into the deformation mechanisms controlling creep behavior at high temperatures. Although higher stress samples showed that the motion of individual dislocations caused the deformation, at lower stresses, deformation arises from flow within grains that is largely restricted to sub-grain boundaries.

The stress dependence of the sub-grain size is often found to vary according to the relation

$$\frac{d_s}{b} = K\left(\frac{G}{\sigma}\right)^m$$

where d_s is the subgrain diameter, b is the Burgers vector, in this case $\frac{a}{2}$<111>, σ is the applied stress, G is the shear modulus and K and m are constants. For pure vanadium, m was estimated at 0.26 and K at 705 for d_s/b in the range 8.4 x 10^3 to 3.0 x 10^3,[4,5] whereas K is very often assumed to be a universal constant of the order of 20 and m approximately 1.[6]

An estimate for K for V-4Cr-4Ti can be made based on the present work. For AR-16 at 800ºC and 70.6 MPa, based on Figure 3, d_s is estimated at 1000nm. Then G can be estimated at 39.4 GPa based on [7], and b at 0.262 nm based on pure vanadium, allowing estimate of K at 6.8 if m = 1, or 735 if m = 0.26. The latter agreement with values for pure vanadium is perhaps remarkable.

Conclusions

Thermal creep at 700 and 800ºC is controlled by dislocation climb. At higher stresses, dislocations move individually and motion may be affected by precipitation. At lower stress, dislocations form sub-grain boundary arrays with mis-orientation developed across the boundary. Therefore, the deformation at lower stresses is expected to be controlled by climb of dislocations into and within the sub-grain boundaries. The present results are shown to agree well with those for pure vanadium regarding the expected stress dependence of the sub-grain size.

FUTURE WORK

This work will be continued when more specimens are available for testing. Specimens irradiated in HFIR at 500°C would be appropriate.

REFERENCES

[1] D. S. Gelles, M. L. Hamilton and R. J. Kurtz, DOE/ER-0313/26 (1999) 11.

[2] R. J. Kurtz and M. L. Hamilton, DOE/ER-0313/26 (1999) 11.

[3] D. S. Gelles, A. Kimura and R. J. Puigh, DOE/ER-0313/25 (1999) 7.

[4] V. V. Levitin, Phys. Stat. Sol., (a) 62 (1980) 557.

[5] S. V. Raj and G. M. Pharr, Mater. Sci. Eng., 81 (1986) 217.

[6] L.P. Kubin, *Dislocation patterning.* Mater. Sci. Technol., 6 **(**1993) 137.

[7] W. E. Porter, R. B. Dinwiddie, W. A. Simpson and M. L. Grossbeck, ANL/FPP/TM-287 (1994) 41.

ASSESSMENT OF RECENT VANADIUM ALLOY IRRADIATION EXPERIMENTS - D.L. Smith (Argonne National Laboratory)

OBJECTIVE

The objective of this task is to review and assess the status of the database obtained from recent vanadium alloy irradiation experiments.

SUMARY

A brief assessment of the results of irradiation tests of vanadium alloys conducted in the HFIR-11J, -12J, 13J, and 10J, indicate that significant uncertainties in the data exist which affect the reliability of the data. This assessment concludes that vanadium specimens from the 12J experiment were severely oxidized, and that the irradiation data are unreliable. There is a significant uncertainty in the irradiation temperature for specimens in the 11J, 12J and 13J experiment due partially to gap conductance in the experiment. The very high irradiation creep rates obtained for the vanadium alloys in the 12J experiment are attributed to a large thermal creep component. A detailed thermal analysis of each specimen is required to provide a reliable temperature specification for the data obtained in these experiments. Similar temperature uncertainties may also exist for other materials irradiated in similar test assemblies.

PROGRESS AND STATUS

Background

The purpose of this document is to provide a brief assessment of the status and results obtained from recent irradiation experiments on vanadium alloys in order to provide a basis for developing priorities for future irradiation testing of vanadium alloys. Early irradiation testing of vanadium alloys conducted primarily in FFTF focused on higher damage levels and temperatures projected for fusion power applications, viz., 15 - 100 dpa and 400 - 600^{o}C. These experiments, which demonstrated that vanadium alloys containing titanium were highly resistant to irradiation-induced swelling and alloys with less than ~ 10% (Cr + Ti) exhibited favorable mechanical properties after irradiation, provided the basis for proposing V-4Cr-4Ti as a reference composition for Li-cooled fusion power systems. In the early phases of ITER, the possibility of using the vanadium/lithium system was also explored, leading to the conduct of low temperature irradiation experiments (T < 400^{o}C) to identify candidate compositions for this application. Since the ITER application was rejected, the primary interest for vanadium alloys is for high performance lithium-cooled systems at higher temperatures (400 - 750^{o}C). The primary uncertainty for this application involves the effects of fusion-relevant helium generation rates with displacement damage on the properties of vanadium alloys.

This assessment is limited to the irradiation experiments on vanadium alloys that have been conducted during the last five years at temperatures in the range of primary interest for fusion power applications, viz., > 400^{o}C. Primary issues associated with these recent irradiation experiments relate to oxygen contamination of the specimens during irradiation, uncertainties in the specimen temperatures during irradiation, and limited damage levels attained. Severe oxidation of vanadium alloy specimens was observed in the HFIR-12J experiment, thermal analyses indicate that the specimen temperatures exceeded the reported temperatures in HFIR 11J, 12J and 13J, and the displacement damage in HFIR-10 J was only a few tenths of a dpa, since the experiment was terminated prematurely.

Vanadium irradiation experiments

HFIR-12J experiment

The HFIR-12J experiment was inserted into the HFIR on February 7, 1997 and was removed on July 17, 1998 for a total of 224 days of irradiation, which corresponds to a damage level of ~7 dpa. The specimen temperature for this experiment was reported to be ~ 500^{o}C. This experiment contained irradiation creep specimens in addition to tensile and TEM specimens. In reviewing various aspects of this experiment, there are two issues which indicate that much of the data obtained from this experiment is not reliable. The two issues relate to severe oxidation of the vanadium alloy specimens exposed to the helium purge gas during irradiation and uncertainties in the actual specimen temperature during the irradiation. Both issues can have a significant effect on the results. In this experiment, the tensile specimens were exposed to low-pressure helium gas during the irradiation. The creep specimens and the TEM specimens were contained in sealed capsules.

Vanadium alloy tensile specimens examined during PIE indicated severe oxidation of the alloy. The surfaces of specimens from this irradiation were covered with a heavy black scale that appears to be similar to the VO_2 oxide observed on vanadium alloy specimens obtained from oxidation studies in high purity helium, which contained low oxygen concentrations. Although the oxygen content of the helium purge in this experiment was not measured, it is expected to be similar to the oxygen levels used for some of the oxidation experiments. A few parts-per-million of oxygen in helium is sufficient to oxidize the vanadium alloys. Although the tensile specimens were wrapped with zirconium foil, the gettering capacity for this material is limited at ~500^{o}C. Based on thermodynamic and kinetic data on oxygen interactions with vanadium and vanadium alloys, large amounts of oxygen are predicted to diffuse into the thin (typically 0.25 mm thick) tensile specimens during the relatively long irradiation time (~ 5000 hr). The observations from this experiment certainly confirm this. A major fraction of the reduction in ductility observed in these specimens after irradiation in the HFIR-12J experiment can be attributed to the oxidation rather than the irradiation.

There also appears to be a substantial uncertainty in the temperature of the vanadium alloy specimens in this experiment. This is particularly important since the temperature uncertainty would also exist in other similarly designed experiments. The primary source of the temperature uncertainty relates to the temperature rise across multiple gas gaps in the experiment design. This explains the unexpectedly high radiation creep measurements reported for the specimens irradiated in this experiment. In this case there is a significant gas gap between the pressurized creep tube (PCT) specimen and the zirconium capsule. This gap was necessary to avoid any constraint in the creep of the specimen, but the gap is sufficient to contribute a significant temperature increase in the specimen. In addition, differential thermal expansion between the zirconium capsule and the aluminum holder plus the required assembly tolerances creates a second gap that would provide additional temperature rise. A thermal analysis based on the specified dimensions indicates that the temperatures of the PCT's were significantly higher than the design reported temperature of 500^{o}C. Most of the measured creep in this experiment can be attributed to thermal creep and not to irradiation creep. This conclusion regarding temperature uncertainties is further supported by the recent results obtained from the flux monitors reported by L. Greenwood [1]. Although the explanation provided by Greenwood for the mechanism of the melting process is questionable since some melting would provide a good contact and thus lower the temperature, the flux monitors were obviously at a significantly higher temperature than the design temperature. This can be partially attributed to the gap outside the flux monitor capsule. A similar conclusion is reached for the vanadium tensile specimens in this experiment. These specimens also involved a double gap design with the zirconium foil and the differential expansion with the aluminum capsule. The tensile specimens were not only severely oxidized, but the actual temperature is uncertain. This temperature uncertainty also exists for the steel specimens irradiated in this experiment, although to a lessor degree since they were not wrapped

with zirconium. As a result of these considerations, the results obtained on the mechanical properties of vanadium alloys irradiated in this experiment are not considered reliable.

HFIR-11J experiment

The HFIR-11J experiment was conducted simultaneously with the HFIR-12J experiment, except the reported specimen temperatures for the HFIR-11J experiment are ~300^{o}C. This temperature is below the range of primary interest for fusion power applications. However, similar to the case for the HFIR-12J experiment discussed above, the temperatures are uncertain but appear to be significantly above the reported temperatures. The oxidation problem associated with the HFIR-12J experiment should not be severe at the temperatures of the HFIR-11J experiment. Consistent with the oxidation experiments, specimens from this experiment did not exhibit the heavy surface oxide that was observed on the HFIR-12J specimens.

HFIR-10J experiment

The vanadium alloy specimens from the HFIR-10J experiment were contained in lithium- bonded capsules, which eliminates any oxidation problem. The measured specimen temperatures for this experiment should also be more reliable. However, the damage level achieved was extremely low because of leaks encountered in the gas system during irradiation. Since details of the second insertion of this experiment have not been reported in the semiannual reports, exact values cannot be given. However, since the damage levels are so low, results from this experiment are of limited value.

HFIR-13J experiment

The HFIR-13J experiment was inserted into the reactor on July 22, 1998 and was removed on May 16, 1999 after an irradiation of 195 effective full power days, which corresponds to a predicted damage level of ~ 5.4 dpa for vanadium specimens. In this experiment the regions of the vanadium alloy test specimens were sealed with static helium so oxidation, even at the higher temperatures of this experiment, should not be an issue. We have not observed the specimens to verify this conclusion. However, as in the previous experiments, there is a significant uncertainty in the temperature of the specimens during irradiation. The design temperatures for the HFIR-13J experiment ranged from 200 - 500^{o}C. However, as indicated in reference [2], the thermocouple temperatures in many cases varied from the design temperatures by as much as 50^{o}C. The temperatures also varied significantly from cycle-to-cycle because of the rotation of the subassembly, which was rotated 180 degrees each cycle to obtain a more uniform average damage level. This capsule also contained multiple gas gaps between the specimens and the bulk specimen holder where the temperature was measured. In addition, tensile specimens were contained in stacks of ~ 15 which were loosely held in the specimen holder. Significant temperature gradients are predicted through the stack of loosely packed specimens, which would result in significantly higher temperatures for specimens located in the center of the stacks. For the HFIR-13J irradiation, the measured temperatures were generally higher than the design temperatures, significant variations in the recorded temperatures were obtained during the irradiation, and significant temperature differences between the actual specimen temperatures and the measured temperatures are predicted because of gaps/contact resistances. This leads to a conclusion that there are significant uncertainties in the actual specimen temperatures for this irradiation experiment. For any case where the effects of irradiation are sensitive to the irradiation temperature, a careful review of the thermal history of the test specimens is required to provide a reliable evaluation of the data.

CONCLUSIONS

A review of the experimental conditions for vanadium alloy irradiations in three of the four recent HFIR irradiation experiments (11J, 12J and 13J) indicate that much of the reported mechanical property data, particularly tensile and irradiation creep data, are questionable. Vanadium alloys

irradiated in HFIR-12J were severely oxidized, which would have a major impact on the properties of the thin specimens. The effects on the thicker specimens such as Charpy specimens and bend bars is less certain. Actual temperatures of the vanadium specimens in all three experiments are subject to significant uncertainties produced by multiple gap thermal-conductance considerations. This temperature uncertainty also extends to other materials irradiated in the same experiments. The damage level accrued in the fourth experiment, HFIR-10J, was so low as to be of limited value. A detailed evaluation of these problems should be conducted before additional irradiation experiments using similar capsule designs are initiated.

REFERENCES

1. L.R. Greenwood and C.A. Baldwin, Fusion Materials Semiannual report DOE/ER-0313/30, p. 214, October 2001.
2. A.L. Qualls and T. Muroga, Fusion Materials Semiannual report DOE/ER-0313/28, p. 266, September 2000.

CORRECTIONS AND CLARIFICATIONS ON THE EVALUATION OF THE DHCE EXPERIMENT - D. L. Smith (Argonne National Laboratory)

OBJECTIVE

The objective of this task is to provide a viable simulation for investigating the effects of neutron irradiation damage with fusion-relevant helium generation rates on the properties of vanadium-base alloys.

SUMMARY

A critical issue in the development of structural materials for the fusion application involves the effects of high helium generation rates on the performance limits of neutron irradiated materials. Since we do not have a high flux neutron source with fusion-relevant energies, we must rely on simulation techniques to obtain experimental information on these effects. The Dynamic Helium Charging Experiment (DHCE) provides a unique approach for simulating the helium production rates in vanadium alloys in fission reactor irradiations. An assessment of the DHCE-1 proof-of-principle experiment and a subsequent evaluation of the DHCE concept have been presented in the last two semiannual reports. This report attempt to correct and clarify several misinterpretations, incorrect statements and misleading conclusions from the evaluation, which contributed to the decision not to conduct a second DHCE experiment in the early phases of the JUPITER-II collaboration. Specific responses to statements and conclusions presented in the evaluation are presented in this report.

PROGRESS AND STATUS

Background

The Dynamic Helium Charging Experiment (DHCE) was developed to simulate the effects of fusion-relevant helium generation rates in vanadium alloys on the properties of neutron irradiated alloys during fission-reactor irradiations [1]. A proof-of-principle experiment (DHCE-1) was conducted in the FFTF reactor and the results reported in several publications (see ICFRM conference proceedings 1996-date). A detailed assessment of the DHCE concept was distributed in June 1999 and updated condensed versions were reported in the Fusion Materials Semiannual report [2] and presented as a selected oral presentation at the ICFRM-10 in Baden Baden, Germany in October 2001. The results of these assessments suggest that the DHCE provides a viable simulation for simultaneously producing fusion-relevant helium generation rates during fission-reactor irradiations of vanadium-base alloys.

An evaluation of the results from the first Dynamic Helium Charging Experiment (DHCE-1) and an assessment of the readiness to conduct a future DHCE (referred to as the evaluation) was also conducted by L.R. Greenwood, D.L. Baldwin, G.W. Hollenberg, and R.J. Kurtz and reported in the Fusion Materials Semiannual report [3]. This evaluation contains several misinterpretations, incorrect statements, and misleading conclusions, which contributed to the decision not to conduct a second DHCE experiment in the early phases of the JUPITER-II collaboration. The purpose of this report is to correct and clarify the major inaccuracies presented in the evaluation by Greenwood, et al., in order to provide a technically correct assessment of the status of the DHCE technique. For convenience, the specific issues are presented below in the order they are contained in the evaluation report and are not necessarily in the order of importance.

Unfortunately, we did not take advantage of an opportunity to conduct a DHCE as part of the JUPITER-II collaboration. A future experiment of this type will be much more expensive since the ANL program on vanadium alloy research has been terminated and the unique facilities developed for disassembly of the tritium-containing capsules will be dismantled. Replacement of

the ANL facilities used for tritium charging and capsule disassembly for the DHCE-1 would cost $500-1000 K, which now will make a DHCE-type experiment significantly more expensive.

Corrections and Clarifications on the DHCE Evaluation

Post test prediction of helium levels

Based on results from analyses of specimens from two of the seven test capsules (4D1 and 4D2) in DHCE-1, the evaluation states [3](pg. 16, par 2) that "up to 35% of the ^{3}He in the samples in these positions may have been generated from tritium decay after the irradiation". This statement is highly misleading and inaccurate. The evaluation fails to point out that analyses obtained from the other five capsules indicate that much smaller fractions of the ^{3}He was generated after termination of the irradiation. For example, specimens from the other capsule (5E2) irradiated at the same temperature as the two capsules mentioned above actually indicated more tritium in the later analysis than in the earlier analysis, which would indicate a negative contribution to the ^{3}He content. This certainly cannot be attributed to tritium decay. Specimens from the 500^{o}C capsules indicated only a variation of 3.8 and 3.9% increase in the ^{3}He content. Specimens from one of the 600^{o}C capsules indicated an additional contribution to the ^{3}He of only ~10%; however, this was based on a very high analysis, most likely due to a mix-up of specimens as discussed in previous assessments [2]. Results from the other 600^{o}C capsule indicated so much variation in the helium analyses that a meaningful correlation is not possible. Helium measurements on this specimen were made at three different times. Analyses of two of these time periods indicate a large depletion of ^{3}He which would indicate a large negative effect (impossible), while analysis of the third condition would indicate an unreasonably large (~180 %) increase in ^{3}He. The average calculated tritium from this capsule was listed as 20 ± 66 appm, which is not very meaningful. The only plausible explanation for these results is an anomaly in the chemical analyses since they were all conducted on samples from the same specimen. The contribution of ^{3}He after termination of the irradiation for the 4D1 and 4D2 capsules are also significantly lower than the values reported in the evaluation, ~23% for 4D2. One might also point out that the differences in the average analyses of the ^{3}He for the different times is only ~1.4% which is quite small. In any case, the results indicate that the contribution to the ^{3}He after termination of the irradiation is very small in most of the specimens analyzed. Based on calculations of the hydrogen distribution in the V/Li system using recent data, one also predicts very low contributions to the ^{3}He concentration after termination of the irradiation. It is grossly misleading to convey that the ^{3}He generated after termination of the irradiation is as high as stated in the evaluation.

The evaluation also states that "most of the samples were degassed sometime in 1994 prior to the ^{3}He measurements in 1995". All specimens included in the analysis discussed above were not degassed as indicated by the specimen ID numbers, which contain "ND" in the ID. Furthermore, the He and tritium analyses relevant to this discussion were analyzed during the period June-August, 1994, and not 1995, and mechanical properties data on the V-4Cr-4Ti alloys from this experiment were conducted and reported in 1994.

The high uncertainty in the ^{3}He generation after termination of the irradiation, which is stated in the review, is very misleading.

Tritium trapping and correlation with stainless steel data

The suggestion that the high ^{3}He content of the V-1Si and V-5Fe specimens is possibly due to tritium trapping similar to that observed in irradiated stainless steels (pg 18, par 2) is not well founded. Extensive experience and experimental results indicate that this is not the case. There are major differences in the solubility and mobility of hydrogen in vanadium and hydrogen in steel. One only needs to compare the vast differences associated with hydrogen or tritium charging and hydrogen permeation results for the two metal systems to conclude that hydrogen trapping is very different. Several simple examples follow. Hydrogen solubility measurements for vanadium (and

alloys) are difficult because the hydrogen migrates into or out of the alloy so fast that quenching in the hydrogen is almost impossible (see H-solubility data). This also shows up in the hydrogen adsorption/desorption experiments. In the early irradiation experiments, specimens were normally degassed to assure that hydrogen did not affect the measurements of the radiation effects. Experience showed that degassing of irradiated specimens was typically easier than non-irradiated specimens. This was not attributed to the irradiation effects, but demonstrates that tritium trapping has not been observed in a large number of alloy compositions tested. Results from tests in sodium also confirm this conclusion. In contrast, it is well documented that hydrogen trapping can occur in steels and that hydrogen charging is very difficult. Correlations of hydrogen effects observed in steels with those in vanadium are not supported by extensive data.

High helium generation in some alloys

The suggested correlation of tritium trapping with the high helium content (pg 20, par 1) does not hold up even for the V-5Cr alloy discussed. Although Nakajima's data for V-5Cr might suggest this, other data on V-5Cr, including Garner, et al. in same proceedings, indicate high swelling at both 500 and 600^{o}C. Swelling data for V-5Fe also do not correlate with the helium concentrations. Very high swelling of the V-Fe alloys are observed both with and without helium. In some cases the swelling is lower in this alloy with higher helium concentrations. As discussed in the previous paragraph, a substantial database indicates that significant trapping of tritium in vanadium alloys does not occur at the temperatures of interest.

Tritium permeation losses through TZM capsules

The suggestion that tritium leakage from the TZM capsules at 600^{o}C appears to be lower than the ideal leakage rate based on pure molybdenum data (pg 20, par 2) is consistent with the previous assessments provided for the DHCE. Recent data presented in the assessments indicate that tritium permeation through TZM is significantly lower than that for pure molybdenum. It has also been suggested that some surface contamination, e.g., oxide, on the capsule walls may also reduce the tritium permeation rates. Calculated values for both Mo and TZM have been presented previously [2].

Consideration of hydrogen solubility limits in lithium.

The evaluation states that when the original DHCE calculations were performed, the solubility limits for H in lithium were not considered (pg 20, par 3). This is not the case. Based on the predicted hydrogen distribution coefficients at that time, the predicted tritium concentrations attainable in the vanadium at ~425^{o}C was close to the level needed for the desired He generation rate in vanadium. The original distribution coefficients were biased because of experimental measurements, which were based on measured H concentrations in V at levels at or below the limits of the analysis.

Uncertainties in the solubility of H in Li

The evaluation concludes that there are still relatively large uncertainties in the data for the solubility of H in lithium and the LiH equilibrium (pg 21, par 2). This is true in the original calculations for the DHCE and in the references cited in the evaluation. However, these uncertainties have been largely resolved by the references we have used in the recent assessment. Veleckis, et al. [4] have published in 1986 a summary report that includes an updated evaluation of the hydrogen solubility data. This appears to be the most reliable assessment of all of the relevant data and is recommended. This assessment has significantly reduced the uncertainties in the hydrogen solubility in lithium. The points made in the evaluation regarding the equilibrium related to the saturation pressure of hydrogen in lithium, and hence in the capsule, are completely correct. An earlier concern expressed by others suggesting that the formation of LiT could lead to higher tritium partial pressures is not valid.

Limits of He generation in a future experiment

Values presented in the evaluation of the He generation limits (pg 23, par 1 and Table 2) are underestimated since the most recent hydrogen solubility data were not used. The proposed temperatures for the next vanadium alloy irradiation test have been either 450/600/750^{o}C or 500/600/700^{o}C. Calculations based on the recent data indicate a maximum He generation rate of 22 and 45 appm ^{3}He/yr in V4Cr4Ti in tritium saturated lithium at 450 and 500^{o}C, respectively. This corresponds to about half the desired rate at 450^{o}C and approximately the desired rate at 500^{o}C, assuming a damage rate of ~12 dpa/fpy, which is typical of the ATR peak damage rate. Although the spectrum in a fusion device varies some with the blanket composition, the more recent neutronic analyses indicate a He/dpa rate for V in a Li/V blanket is ~4.5 appm He/dpa. The ORNL data indicate a value of 4 appm/He/dpa for V-15Cr-5Ti; however, I do not know what blanket system they assumed. Since we have carried V-5Ti alloys in most irradiation tests, these alloys, which have a higher tritium solubility, would generate somewhat higher helium concentrations in the same lithium/tritium exposure. Certain other alloys exhibit even higher H solubilities and would provide higher He concentrations. Since our primary objective is to develop an improved understanding of He effects in irradiated materials, a judicious selection of vanadium alloys would provide range of He concentrations for investigation. At temperatures above 500^{o}C, He concentrations higher than values corresponding to projected He/dpa ratios for vanadium alloys in a fusion spectrum can be obtained in most alloys.

Leakage of tritium from capsules at 600^{o}C and higher

As stated in the fourth item above, recent data that we referenced in the recent assessment [2] indicate that the hydrogen permeation rate through TZM is lower than that of pure vanadium. We also suggest that surface films may also contribute to lower tritium permeation rates. However, at higher temperatures of interest, viz., ~750^{o}C, tritium permeation losses would be excessive for a single-walled capsule. The proposed solution is the use of a double-walled capsule, with the outer capsule at a temperature low enough (~ 400^{o}C) to contain the tritium. This appears to be a straightforward solution since one also needs a significant thermal gap to attain the higher test temperatures in water-cooled reactors. One would not need the high ^{6}Li suggested in the evaluation in this case (pg 24, par 1 and Table 2) and the ^{4}He generation rate would be much smaller and not a serious problem.

Issue of testing alloys that produce high He concentrations

The comment is made that the future DHCE experiment is more complicated since separate capsules would be required to test the alloys that generate higher helium concentrations (pg 24, par 3). This does not appear to be any more complicated than the requirement to have different capsules to test at different temperatures. In the DHCE-I we used multiple capsules at each temperature, typically with different tritium concentrations in order to investigate the effects of different He concentrations. In this case one only needs to decide on priorities for the test as all conditions, whether they be temperature, fluence, alloy composition or helium content, cannot be accommodated in a single experiment. The current objective of the program is to develop an improved understanding of helium effects on irradiated alloys. It is not clear that one must accommodate all alloys of interest in this particular part of an experiment. It might be more important to emphasize different variables in one or only a few alloys to provide a better understanding of helium effects..

Correlation of post-test tritium measurements in test capsules

A question is raised regarding the poor correlation of the post-test tritium measurement obtained during opening of the capsules with the amount of tritium in the precharge (pg 25, par 2). It should be pointed out that only the tritium released in the gas phase during specimen retrieval was measured. It is certainly assumed, and partially indicated that a significant fraction of the tritium in the capsule remained in the condensed phases after dissolution of the lithium to remove

the specimens. As indicated in the report on the specimen retrieval, the ratio of tritium measured in the off-gas to the tritium precharge was relatively constant for all capsules, typically 40 - 60 %. The variations observed appear to be fairly consistent with the inconsistencies in the He measurements, which have been attributed partially to observed tritium losses during capsule filling and welding. This conclusion is considered a much more likely explanation than the suggestion that tritium leaked from the 430^{o}C capsule. The alternate explanation suggested in the evaluation relates to He produced in the specimens after termination of the irradiation. As stated above, this is not a likely explanation and is not consistent with results from the other capsules.

Tritium transport in Na or NaK which have low solubilities

The evaluation states that it is essential that the Sieverts' constant for tritium solubility in the liquid metal must exceed that of vanadium (pg 26, par 1). This is completely incorrect. Extensive data exist that demonstrate that mass transport of trace elements in liquid metals occurs even though the solubility of these trace elements have a very low solubility in the liquid metal. Extensive experience in the sodium systems shows that hydrogen transport occurs effectively in sodium at much lower concentrations than are proposed here. Even carbon transfer in sodium/steel systems, which has been the subject of extensive investigations because of its importance, readily occurs even though the solubility of carbon in sodium is orders of magnitude lower than even that of hydrogen. Tritium transport from a mother alloy in the capsule through the sodium to the test specimens is not a constraint for the conditions of interest. The primary reason this alternative has not been recommended, even though we suggested it as a possibility, relates to the redistribution of tritium at the end of the irradiation. In this case, significant helium would be generated in the vanadium after termination of the irradiation unless the specimens were removed and degassed in a short period of time. The comment on this issue in the evaluation is not correct. A concern is also raised that the He/dpa ratio for this case would decline during the irradiation. This is true but the magnitude is very small since the tritium decay is only ~5%/yr. This is not considered to be a significant issue.

Required work to conduct a future DHCE experiment

The evaluation concludes that although a future DHCE experiment is feasible, a great deal more effort is required to design such an experiment (pg 27, par 5). I believe all of the critical technical issues associated with a DHCE experiment in the ATR reactor have been resolved to the extent that an effective irradiation experiment could be conducted on the most critical issue associated with the viability of structural materials for fusion applications. A detailed design is still required, but the critical issues have been addressed. The most critical issue relates to the burnout of ^{3}He from thermal neutrons. This requires a highly effective thermal neutron shield and a reactor with a higher fast/thermal neutron ratio is much preferred. This is the main reason that use of the HFIR reactor for a DHCE experiment is questionable. If alloys with high hydrogen solubility such as those that contain yttrium are to be included in the experiment, they should be contained in separate capsules.

CONCLUSIONS

The greatest uncertainty related to the performance limitations of candidate structural materials in a fusion environment involves the effects of the high-helium generation rate characteristic of a fusion neutron spectrum on the properties of neutron-irradiated materials. The Dynamic Helium Charging Experiment (DHCE) with vanadium-base alloys provides the most viable simulation for investigating these effects without a high-flux, high-energy neutron source. A detailed review of the proof-of-principle DHCE-1 indicates that, with lessons learned from DHCE-1, this approach provides a validated method for obtaining essentially constant values of He/dpa ratios in vanadium alloys during fission-reactor irradiations for a wide range of fusion-relevant parameters.

REFERENCES

1. D.L. Smith, et al., J. Nucl. Mater. 155-157(1988)1359.
2. D.L. Smith, "Helium Analysis from the DHCE-1 Simulation Experiment", Fusion Materials Semiannual Report DOE/ER-0313/29, p. 26, April 2001.
3. L.R. Greeenwood, et al., "Evaluation of the DHCE Experiment", Fusion Materials Semiannual Report DOE/ER-0313/30, p. 15, October 2001.
4. E. Veleckis, R.M. Yonco and V.A. Maroni, "The Current Status of Fusion Reactor Blanket Thermodynamics", IAEA Report IAEA-SM-236/56(1986) p. 3.

2.0 CERAMIC COMPOSITE MATERIALS

SPECIMEN SIZE EFFECT ON THE IN-PLANE SHEAR PROPERTIES OF SILICON CARBIDE/SILICON CARBIDE COMPOSITES

T. Nozawa[1], E. Lara-Curzio[2], Y. Katoh[1, 3], L.L. Snead[2] and A. Kohyama[1, 3]
[1]Institute of Advanced Energy, Kyoto University
[2]Metals and Ceramics Division, Oak Ridge National Laboratory
[3]CREST-ACE, Japan Science and Technology Corporation

OBJECTIVE

The objective in this study is to investigate the size dependency of in-plane shear strength, which a significantly influences the on off-axial tension. A further objective is to distinguish the volumetric effect and geometric effect on shear properties. Also, in further investigation, relationships between tensile and shear properties were evaluated.

SUMMARY

Miniaturization of test specimens is often necessary to evaluate the physical and mechanical properties of materials under severe environments. The validation of these techniques requires an understanding of the role of geometric and volumetric (size) effects on the mechanical behavior of the material. Although considerable work has been dedicated to understand size and geometric effects on the off-axis tensile strength of continuous fiber-reinforced ceramic matrix composites, little work has been focused on the effect these variables on their shear properties. This paper will present the results of a study aimed at assessing the effect of notch separation and specimen thickness on the shear strength of a 2-D SiC/SiC composite by the Iosipescu test method. Provisions for mounting miniature test specimens using a fixture for standard size specimens are discussed.

PROGRESS AND STATUS

1. INTRODUCTION

Small specimen test technique (SSTT) for tensile testing has been developed to meet several demands [1]. First of all, in the field of fusion research, SSTT has been considered one of the effective methods to evaluate irradiated materials because of possibility to reduce radiological waste. SSTT also has an advantage to make distribution of defects uniform in composites. This is very important to evaluate composites with complex fracture behavior. In addition, statistical analysis will be available as the number of specimens increases. And what is most important is to make it possible to evaluate mechanical properties of extremely small materials for practical use.

It is noted that fusion stuctural components have finite size, so miniaturization of specimen size, given intrinsic size effects associated with composites, is problematic[2, 3]. The weakest link theory is often mentioned to discuss this problem [4]. This says that quasi-brittle materials like monolithic ceramics lose strength as specimen volume increases. The size effect is also closely dependent on fracture mode, fabric architecture, loading directions, environments and other variables [5, 6]. So it is very important to identify key factors governing size effect.

Composite strength is significantly dependent on the properties of reinforcing fibers. It has been shown experimentally and theoretically that maximum strength was roughly proportional to volume fraction of fibers aligned with the tensile axis [7]. However it is also well known that composite strength decreased a lot because of the anisotropy due to its characteristic architecture, once the loading direction changed from the longitudinal direction of fibers [8]. This is because a change in fracture mode occurs from tension of fibers to shear or detachment at fiber/matrix interface. What is most important is that the change of fracture mode made size dependency on tensile properties quite different.

According to our previous research [9], [0º/90º] SiC/SiC composites had a size effect, dependent on architecture. Tensile strength of 3-D SiC/SiC was determined by the fiber strength itself and hence it had a length effect following the weakest link theory. The fiber volume fraction for 3-D configuration was different in gauge width due to the structural limitation and hence tensile properties, which had a close relation to fiber properties, had also specific size dependency related to axial fiber volume fraction. On the contrary, 2-D SiC/SiC had nearly no size dependency. However tensile properties in off-axis tension had quite different size dependency from that of [0º/90º] SiC/SiC. Tensile strength reduced as gauge width decreased for both architectures, once the loading direction came apart from longitudinal direction of fiber [8]. This is due to the change of fracture mode from tension of fiber to shear strength between bundles or debonding strength at F/M interface, as mentioned before. In this study, more detailed discussion about the former effect, i.e. size effect of in-plane shear, has been carried out.

2. EXPERIMENTAL

Material

A plane-weave (P/W) SiC/SiC composite was prepared by Ube Industries, Ltd., Japan. This composite has stitching fibers in the transthick direction. First of all, Si-Ti-C-O fiber bundles (Tyranno™-LoxM, Ube Industries, Ltd., Japan) used as reinforcements had undergone a surface modification before weaving in order to optimize the fiber-matrix interface. Due to this treatment, composition gradient interphase with excess carbon was formed close to the fiber surfaces [10]. Then, these composites were synthesized by polymer impregnation and pyrolysis (PIP) process. This composite had relatively high porosity above 10 % after the PIP sequences and especially inter-bundle porosities near stitching fibers were characteristic. Hence, this made the bulk density quite lower, about 2.2 Mg/m^3.

Iosipescu Test

In order to evaluate size effect on the in-plane shear strength, Iosipescu shear test was conducted. Schematic illustrations of test specimens and test fixture were as shown in Fig. 1. Distance between notches and specimen thickness were varied in each specimen. Specimens for the evaluation of volumetric effect were designed as possessing the same aspect ratio, i.e. notch separation to thickness, but different volume, respectively. On the contrary, specimens for the evaluation of geometric effect had the same volume but different aspect ratio. All the tests were carried out on the guideline of ASTM C1292. Crosshead speed was chosen 0.6 mm/min. Shear stress was calculated as load divided by the effective area, which means fracture area measured after testing. After the tests,

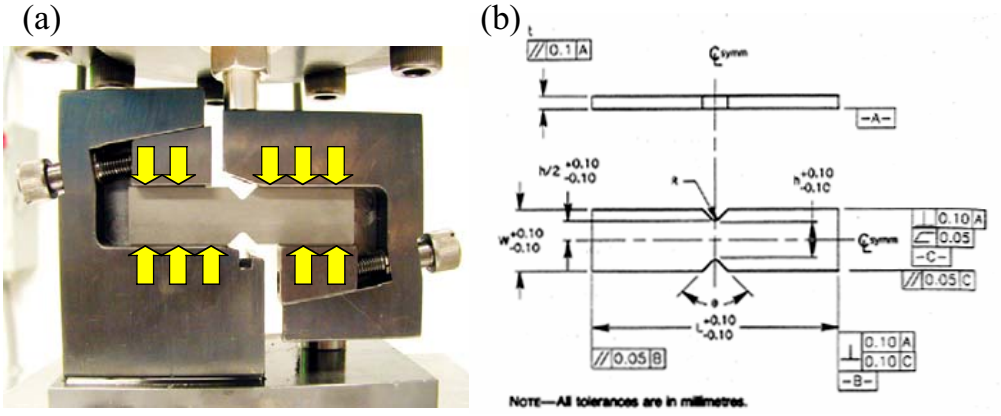

Fig. 1. Schematic illustration of (a) test fixture and (b) Iosipescu specimen.

fracture surfaces were observed by optical microscopy and scanning electron microscopy (SEM).

3. RESULTS AND DISSCUSSION

In-Plane Shear Behaviors

Typical stress-displacement relations in Iosipescu tests were shown in Fig. 2. All the curves had proportional behaviors in the beginning. Just beyond proportional limit, it became non-linear due to the accumulation of matrix cracks. At the maximum, large stress drops occurred due to the failures of fibers by tension in the transverse-loading direction. At this time, visible large cracks were observed between notches. Beyond this point, the friction of pullout fibers and fiber bundles maintained all the applied loads. After the period of gradual decreases of loads, stress dropped again. This means complete failures of pullout fibers by shear.

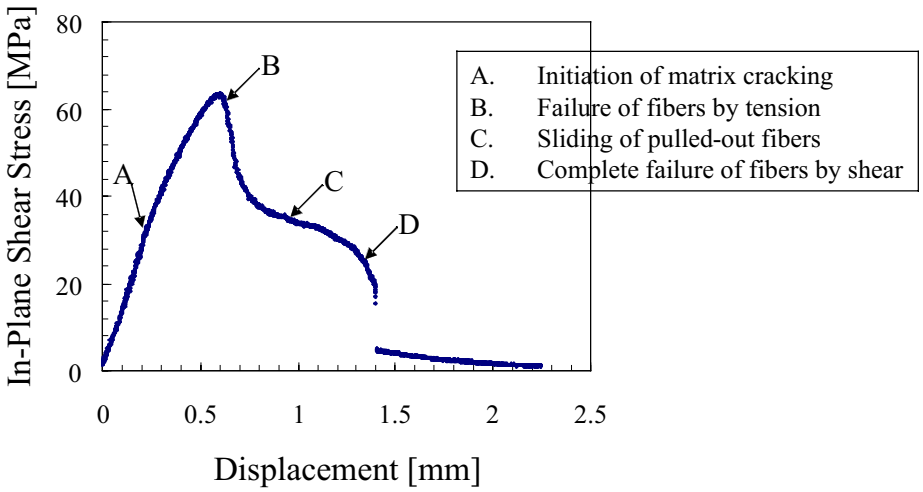

Fig. 2. Typical stress-displacement curve of Iosipescu test for SiC/SiC.

According to fracture surface (Fig. 3), main crack propagated between fiber bundles not in intra bundles. Pullouts of fibers were very numerous and long. These fracture appearances were very similar to those of tension.

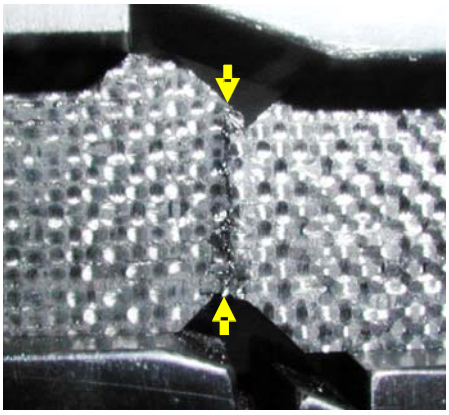

Fig. 3. Crack propagation between inter bundles.

Specimen Size Effect on In-Plane Shear Properties

Fig. 4 shows the size dependency of the maximum in-plane shear strength. This showed gradual increase of maximum shear strength for reduced gauge width. In particular, it was clearly significant that strength increases for the specimen with reduced aspect ratio, in case of the constant volume in the gauge section. With increasing aspect ratio, shear strength tended to converge into some constant value (Fig. 4 (a)). On the contrary, in case of the constant aspect ratio, there was no clear difference in specimen size (Fig. 4 (b)). This meant that size dependency of the in-plane shear strength was considered due to the geometric effect. Therefore composites with small aspect ratio might have a strength increase regardless of specimen size. However it is necessary to investigate the mechanism of the strength increase and also to discuss the relationships with the stress drop observed in the off-

axis tension in case of the small aspect ratio.

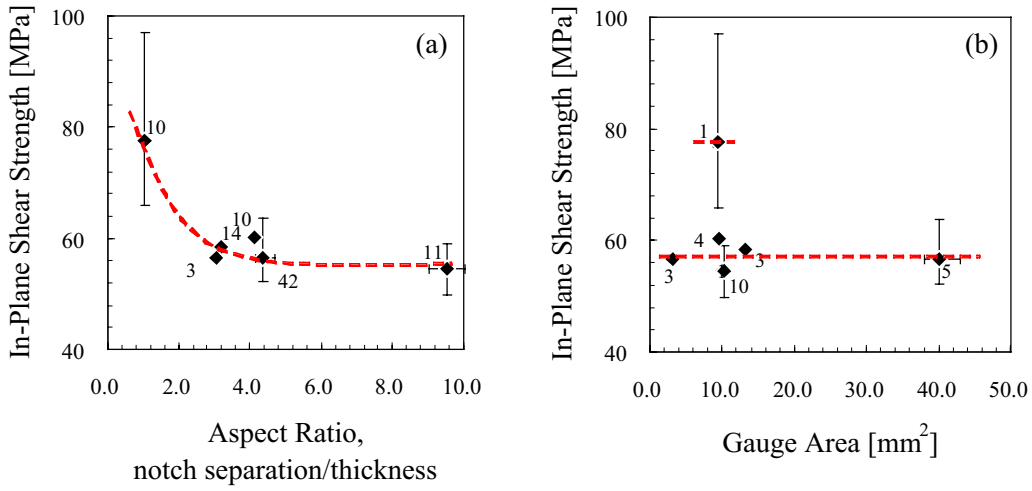

Fig. 4. Specimen size dependencies on in-plane shear strength; (a) geometric and (b) volumetric effects. (Note: numbers in figures (a) and (b) mean gauge area and aspect ratio, respectively.).

Relationships between Tensile and Shear Properties

Fig. 5 shows the width dependency of tensile strength compared to that of shear. Some reasons were considered for the reduction of off-axis tensile strength in the short gauge width and in this study in-plane shear was mentioned. However, this research on the size dependency of the in-plane shear strength showed opposite tendency to that of off-axis tension. In fact, tensile strength in off-axis tension might be determined by the weak debonding strength at the fiber/matrix interface not the in-plane shear, since there was no complex cross of weaving in shorter gauge width and each fiber was easy to detach with no special restriction by weaving architecture. Further investigation is necessary for complete understanding.

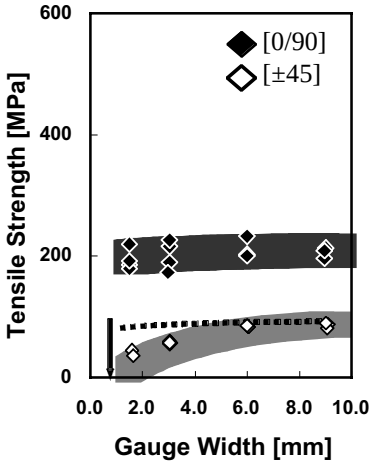

Fig. 5. Width effect on tensile strength for 2-D SiC/SiC.

4. CONCLUSIONS

In order to investigate the size effect of the in-plane shear strength of SiC/SiC composites and to discuss the relationship between tensile and shear properties, Iosipescu test was performed. Key conclusions were summarized as follows.

1. In-plane shear strength by Iosipescu test showed a specimen geometric dependency. Maximum shear stress was nearly constant with no relation to the specimen gauge area. However, it tended to increase as the aspect ratio, width to thickness, decreased.
2. Size effect on the in-plane shear strength was quite opposite to that on the off-axis tensile strength. This indicated that in-plane shear was not the critical fracture factor in off-axis tension. Other mechanisms like the detachment strength at the F/M interface might make an effect on the stress reduction in small sized material. Further investigation about this is strongly required.

ACKNOWLEDGMENTS

The authors would like to express their sincere appreciation to Dr. M. Sato (Ube Industries Ltd., Japan) for providing the materials. This work is performed as a part of 'R&D of Composite Materials for Advanced Energy Systems' research project supported by Core Research for Evolutional Science and Technology (CREST) and supported by collaboration at Japan-US Program for Irradiation Test of Fusion Materials (JUPITER-II).

REFERENCES

[1] T. Nozawa, K. Hironaka, Y. Katoh, A. Kohyama and E. Lara-Curzio, *J. Nucl. Mater.*, to be published.
[2] L.S. Sutherland, R.A. Shenoi and S.M. Lewis, *Comp. Sci. and Tech.*, 59, (1999) 209.
[3] L.S. Sutherland, R.A. Shenoi and S.M. Lewis, *Comp. Sci. and Tech.*, 59, (1999) 221.
[4] W.A. Curtin, *J. Am. Ceram. Soc.*, 74 (1991) 2837.
[5] M. Ibnabdeljalil and W.A. Curtin, *Int. J. Solids and Structures*, 34 (1997) 2649.
[6] M.R. Wisnom, *Comp. Sci. and Tech.*, 59, 1937-1957 (1999).
[7] T. Nozawa, T. Hinoki, Y. Katoh, A. Kohyama, E. Lara-Curzio, M. Sato, *Ad. in Ceram. Comp. VI*, 124 (2001) 351.
[8] T. Nozawa, Y. Katoh, A. Kohyama and E. Lara-Curzio, *Ceram. Eng. and Sci. Proc.*, to be published.
[9] T. Nozawa, T. Hinoki, Y. Katoh, A. Kohyama and E. Lara-Curzio, *ASTM STP 1418*, to be published.
[10] T. Ishikawa, K. Bansaku, N. Watanabe, Y. Nomura, M. Shibuya and T. Hirokawa, *Comp. Sci. and Tech.*, 58, (1998) 51.

TENSILE PROPERTIES OF STOICHIOMETRIC SILICON CARBIDE FIBER REINFORCED FCVI DERIVED SILICON CARBIDE MATRIX COMPOSITES

T. Nozawa[1], K. Hironaka[1], T. Taguchi[2], N. Igawa[2], L.L. Snead[3], Y. Katoh[1], S. Jitsukawa[2] and A. Kohyama[1]
[1]Institute of Advanced Energy, Kyoto University
[2]Department of Materials Science, Japan Atomic Energy Research Institute
[3]Metals and Ceramics Division, Oak Ridge National Laboratory

OBJECTIVE

The objective of this study is to investigate mechanical performance of recently developed stoichiometric SiC fiber reinforced FCVI SiC matrix composites and also to identify the key implementation for the improvement of FCVI technique. High-temperature tensile properties and the effects of fabric configurations and interfacial conditions on them were investigated using small specimen test technique for tensile testing.

SUMMARY

Recently developed SiC/SiC composites with high-crystalline, near stoichiometric SiC fiber are one of the promising materials for fusion and other high-temperature materials, because of the excellent physical and mechanical stability at high-temperature. Therefore material development has been enthusiastically carried out at ORNL as a part of US-Japan collaboration. The objective of this study is to clarify good performance of these composites at severe environment and also to identify the key issues for material development; effects of the interphase thickness, fabric orientation, and porosity on tensile properties, by using small specimen tensile test technique. It was shown that the maximum stress of Tyranno™-SA/FCVI-SiC composites was stable under high-temperature exposure up to 1300°C in mild oxidizing environment. In addition, it was revealed that Tyranno™-SA/FCVI-SiC with single PyC interphase had its maximum strength, when the thickness of PyC was around 150~200 nm.

PROGRESS AND STATUS

1. INTRODUCTION

SiC/SiC composites are considered one of the promising materials for fusion and other applications in advanced energy industries, because silicon carbide (SiC) has inherently superior stability of mechanical properties at high-temperature, low-induced activation and after heat, and excellent corrosion resistance [1, 2]. High-crystalline and stoichiometric SiC fibers like Hi-Nicalon™ Type-S and Tyranno™-SA are, in particular, stable to oxidation at high-temperature and severe neutron exposure because of less impurities like oxygen and good structural order [3, 4]. Similarly, b-SiC matrix derived by forced-flow/thermal-gradient chemical vapor infiltration (F-CVI) process, which has also high-crystalline structure, would show good stability of strength against neutron [5-7]. From these reasons, SiC/SiC composites with high-crystalline and stoichiometric SiC fiber and matrix are considered to have excellent physical and mechanical properties under these severe conditions. Therefore many researches on F-CVI process have long been enthusiastically carried out at Oak Ridge National Laboratory (ORNL), as a part of Japan-US collaborations. This study focused on tensile properties of SiC/SiC composites with recently developed new SiC fibers, for the optimization of F-CVI process.

Several advantages are focused on to discuss CVI process; less residual stress due to the fabrication at relatively low temperature (<1200°C), good infiltration of high-purity and stoichiometric b-SiC within extremely small spaces among fiber bundles [3, 8]. In addition, high-accuracy of controlling fiber/matrix (F/M) interface is characteristic in CVI method. On the contrary, CVI method has several disadvantages; gradients of gas concentration, temperature, and gas pressure due to the

presence of thermal-gradient. These gradients make an effect on uniformity of formed SiC matrix. Most composites fabricated by CVI method, in spite of high-crystalline SiC matrix, have relatively large gradients of density and porosity in bulk materials. This has been pointed out and need to be improved.

For the evaluation of these composites, conventionally flexural test was often used because of its simplicity to conduct. However, contrary to this simplicity, two opposite fracture modes such as compression and tension made it very difficult to do analysis. In some cases, inter-laminar shear fracture also made it more difficult. Therefore effect of each fracture mode on composite strength is required to evaluate separately for further discussion. On the while, tensile test is possibly useful to meet these demands because of its simplicity of fracture mode. This helps us to analyze composite strength easier and to identify fracture behavior more clearly. Tensile test also gives us the most fundamental information for practical applications.

Small specimen test technique (SSTT) for ceramic matrix composites (CMCs) has been developed as one of the effective means for the evaluation of mechanical properties for neutron irradiation [9, 10]. Miniaturization of test specimen has also been considered to be very effective in economical use and statistical analysis. Moreover, this technique, which is based on specimen size effects, will be very useful for the estimation of the mechanical properties of both large-sized materials and extremely small specimens used in practical applications. In this study, possibility and usefulness of this technique were also evaluated.

2. EXPERIMENTAL

Materials

All the composite disks with 3-inch diameter and half-inch thickness were fabricated by FCVI method at ORNL. Plane-woven (P/W) sheets of Tyranno™-SA fiber (Ube Industries), which were stacked in [-30°/0°/30°] or [0°/90°] directions, were used as reinforcements (Table 1). In order to reduce porosity and to obtain high density, fiber volume fraction of all the [0°/90°] composites (ID: 1264, 1265 and 1266) was designed to be higher than that of previous series; [-30°/0°/30°] composites (ID: 1256, 1260 and 1261). This is because it was revealed that composite porosity decreased proportionally as fiber volume fraction increasing. Fiber volume fraction plays an important role in decreasing open porosities, most of which are distributed among lay-up fabric sheets, although closed pores might be still remained. Less than 20 % of porosity was attained in each composite fabricated in recent activities after complete infiltration, by using methyltrichlorosilane (MTS) carried by hydrogen. These porosities were uniformly distributed especially in inner parts of composites.

Pyrolytic carbon (PyC) interphase was deposited on the surface of each fiber before FCVI densification. Three kinds of thickness of PyC interphase; 75, 150 and 300 nm, were chosen for the evaluation of influences of their thickness on tensile properties. In order to fabricate the uniform

Table 1 Materials

	Fabric Information			Fabrication of Interphase			Material Properties		
Sample ID	Fiber	Weave	Orientation	Material	Thickness of Interphase [nm]		Estimated Fiber Volume Fraction [vol%]	Estimated Density [Mg/m^3]	Estimated Porosity [%]
					Aimed	Measured Average			
1256	Tyranno SA	P/W	[-30°/0°/30°]	PyC	150	107.1	37	2.76	10.8
1260	Tyranno SA	P/W	[-30°/0°/30°]	PyC	300	168.5	30.2	2.28	28
1261	Tyranno SA	P/W	[-30°/0°/30°]	PyC	75	70.5	33.3	2.54	19.7
1264	Tyranno SA	P/W	[0°/90°]	PyC	150	116.4	35.4	2.61	17.7
1265	Tyranno SA	P/W	[0°/90°]	PyC	300	225.5	35.3	2.72	14.2
1266	Tyranno SA	P/W	[0°/90°]	PyC	75	42.3	35.2	2.62	17.4

interphase in F/M interface, deposition of PyC was carried out at two times separately with gas either flowing first from top and then the bottom. All the composites had a small gradient in interfacial thickness and it had a maximum at the center of upstream side. Unfortunately, these interphases were formed 20~30 % thinner than desired. More details were discussed elsewhere [11, 12].

Small Specimen Test Technique for Tensile Testing

Several miniature specimens were designed from our ongoing research on specimen size effects on tensile properties of SiC/SiC composites (Fig. 1, 2) [10]. In particular, for the high-temperature tensile test, edge-loaded miniature specimen were selected for this study. The main features of this specimen are described as follows.

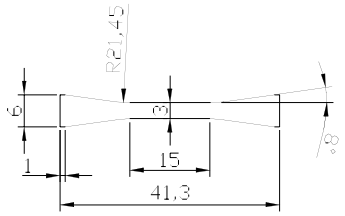

thickness: 2.3 mm

Fig. 1 Schematic illustration of miniature tensile specimen

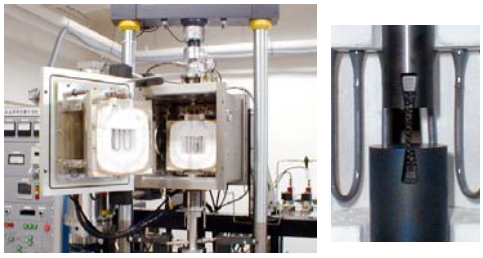

Fig. 2 High-temperature tensile testing machine

Total specimen length was determined by the dimensional constraints of the irradiation capsule, about 50 mm or less. The gage length was 15-20 mm in order to leave enough gripping area and for easy comparison with previous results [9, 10]. Gage width was designed to have more than one tow (1.5 mm) in width within the specimen total width to reduce influences of the presences surface flaws induced by machining. Especially for the case of shorter gage widths, stress concentration at the root became the most critical factor for failure and in such a case composites fail at lower stress. Gage thickness was taken as 2.3 mm. Moreover, the reduced thickness made it easy to decrease composite strength due to the local load sharing theory [13, 14]. Transition between gage section and edge section was curved in order to reduce stress concentration and this radius was determined by finite element method analysis.

Measurements

Tensile tests were conducted by electromechanical testing machine (Instron Japan Co. Ltd.) on the basis of ASTM C1275 and C1359. All tests were conducted at a rate of 0.5 mm/min crosshead speed. The step-loading tests were performed for room-temperature tension in air for the precise evaluation of damage accumulation near proportional limit [15]. Monotonic tests were conducted for high-temperature tension at 1300°C in a flow of commercial argon with about 0.1 Pa of oxygen in partial pressure. High temperature tests were carried out following a 20 min ramp to the test temperature and a subsequent equilibration time of about 10 min. More details are provided elsewhere [16].

After the tensile tests, fracture behaviors of all the specimens were examined by using scanning electron microscopy (SEM). Besides, porosity, fiber volume fraction and thickness of PyC interphase near fracture plane were also measured.

Analysis

Mechanical properties were analyzed using normalized stress as below, on considering large scatter in porosity among the materials. In this equation, stress was calculated as applied force divided by real area of cross-section excluding the area of pores.

$$\text{Normalized Stress} = \frac{\text{Applied Force}}{\text{Cross Sectional Area} \times (1 - \text{Porosity})}$$

It is noted that, in this analysis, it was assumed that porosity was distributed equally in any cross-section.

3. RESULTS

It was revealed that maximum strength had no clear relationships in porosity, although elastic modulus was proportional to porosity. Elastic modulus increased as the porosity decreased (Fig. 3).

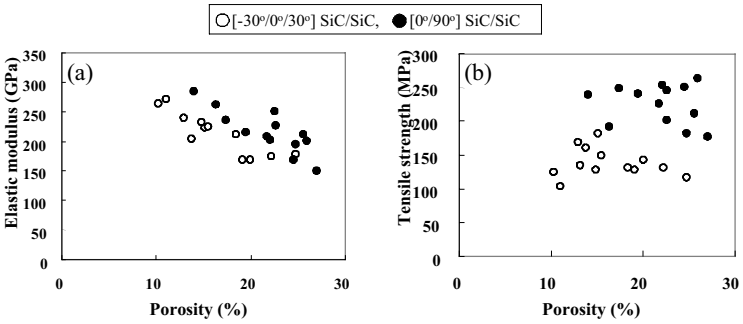

Fig. 3 Porosity dependencies on tensile properties; (a) tensile modulus and (b) maximum stress

Fig. 4 shows the stress-strain behaviors of [0º/90º] and [-30º/0º/30º] SiC/SiC composites at room temperature. Before the proportional limit, both curves were quite similar and slope of initial proportional region and this limit was almost the same. However, tensile behaviors in non-linear region were different. [-30º/0º/30º] SiC/SiC had larger accumulation of strain. The large reduction of slope of hysteresis in [-30º/0º/30º] SiC/SiC also explained this. Due to the accumulation of damage at lower stress, tensile strength of [-30º/0º/30º] SiC/SiC was reduced into about 60 % for [0º/90º] SiC/SiC (Fig. 5).

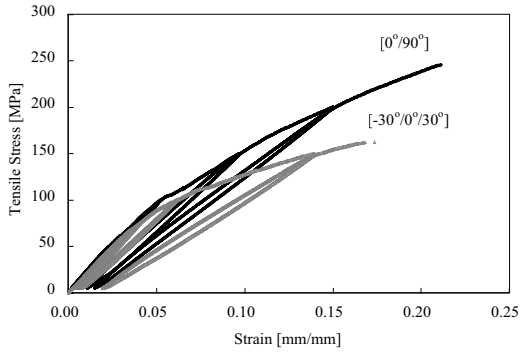

Fig. 4 Typical tensile behaviors of [-30º/0º/30º] and [0º/90º] SiC/SiC composites

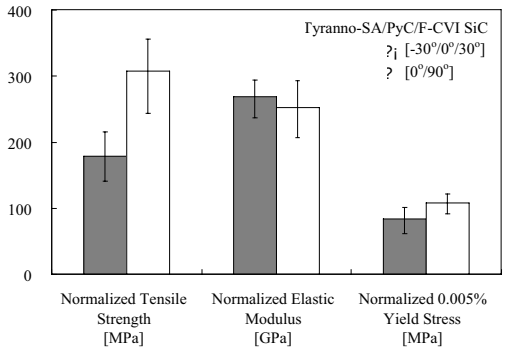

Fig. 5 Tensile properties of [-30º/0º/30º] and [0º/90º] SiC/SiC composites

According to fracture images (Fig. 6), fracture surface was nearly flat. However, there were a lot of pullouts of fibers, although they were relatively short.

Tensile strength of SiC/SiC with single PyC interface showed its maximum stress when the thickness of interphase was 150~200 nm (Fig. 7). However in this range, composite strength tended to maintain some constant value. This result was a little different from that of flexural strength. In flexure, Tyranno™-SA fiber reinforced composites with 200 nm thick PyC showed apparent its maximum strength [17].

Tyranno™-SA/PyC/FCVI-SiC had a good stability in mechanical properties under high-temperature exposure (Fig. 8). There was no significant degradation of tensile strength at 1300°C in mild oxidizing environment.

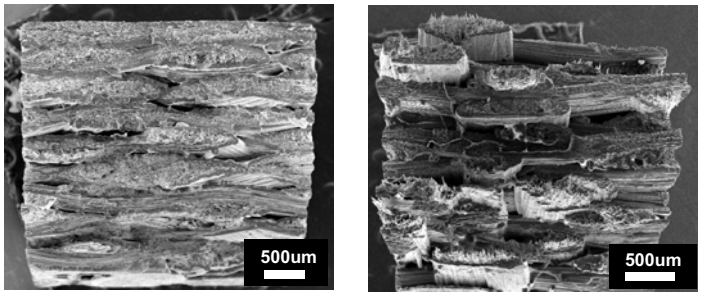

(a) (b)

Fig. 6 Typical fracture surfaces of (a) [-30º/0º/30º] and (b) [0º/90º] SiC/SiC composites

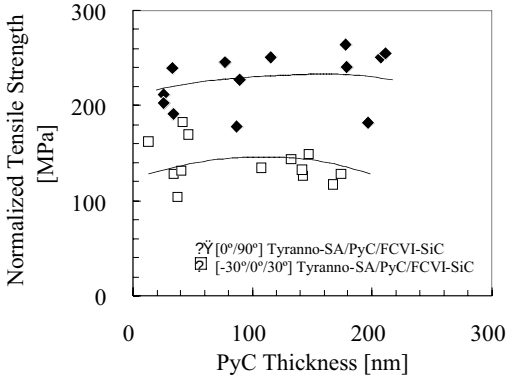

Fig. 7 Carbon interphase effect on tensile strength at room temperature

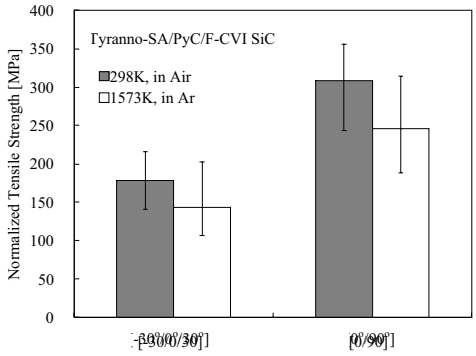

Fig. 8 High-temperature tensile properties of [-30º/0º/30º] and [0º/90º] SiC/SiC composites

4. DISCUSSION

Effect of Porosity on Tensile Properties

The SiC matrix fabricated by FCVI method grows radially from the fiber surface and traps tiny spaces in the developed matrix. Most pores were formed by the presence of the one-way flow of resource gas. Hence this made porosity (density) gradient in composites. Stress calculated as applied force divided by gauge area including pores, was usually used for the analysis, but this is not realistic for such high-porosity composites. This is one reason to apply normalized stress in this study.

It is well known that maximum stress significantly depends on axial fiber volume fraction [9, 18]. So tensile strength may not change if the quantity of fibers is constant in each specimen. In this case, most pores were induced by less matrix densification, with not relation to fibers. Hence, composite strength, which was governed by fiber strength, did not have any relation to porosity. In flexure, there was a clear relationship between maximum strength and porosity, and flexural strength was nearly proportional to density. This is due to the difference of key fracture mode that works on composite fracture. In tension, delamination, characteristic in flexure, did not make a significant effect on fracture behavior at maximum stress. In general, tensile strength was almostly determined by the fiber strength itself.

The mixture of the modulus of each component determines tensile modulus, and therefore tensile modulus is strongly affected by the occupation of all the components, i.e. porosity. PLS is often considered to be equivalent to matrix cracking stress. On considering most cracks emerged at the pores and sharp edges of the specimen, PLS might change by the presence of randomly distributed pores.

Effect of Fabric Orientation on Tensile Properties at Room Temperature

Maximum strength was dependent on fabric orientation due to the change of key fracture mode. Supposing that fiber strength aligned in the tensile axis made most significant effect on composite strength, then [0º/90º] SiC/SiC, with higher volume fraction of fibers in tensile axis, showed higher tensile strength than [-30º/0º/30º] SiC/SiC. Of course, there were some other contributions to maximum strength such as off-axis tension, macroscopic in-plane shear between fiber bundles and microscopic interfacial shear between fiber and matrix. However, it seems very difficult to identify them only by tensile test.

Effect of Interlayer Thickness on Tensile Properties at Room Temperature

Tyranno™-SA/SiC composite had maximum tensile and flexural strength at the 200 nm in thickness of PyC. However, in tension, there was not clear difference in PyC thickness. In particular in flexure, it was sifted 50 nm thicker than that of Hi-Nicalon™/SiC [17]. One of the reasons is the difference of surface roughness of fibers. Tyranno™-SA is composed of high-crystalline, large (>20 nm) grains and hence the fiber surface is so rough. Rough surface needs much interfacial material to obtain good bonding condition. From this reason, high-efficiency interfacial function was performed, even if the relatively thick PyC interphase was formed. Additionally, there was an advantage that friction along the F/M interface after debonding was higher. It is noted that smooth surface like Hi-Nicalon™ made bonding strength and also friction after debonding lower, and most cracks easily propagated at the F/M interface. However, what was the most important was that almost of all the cracks developed between fiber and interfacial material, even if the bonding strength improved like Tyranno-SA/SiC [19]. Therefore there are still some issues to be improved and now many researches on multi-layer SiC/PyC interface are going on.

Tensile Behavior at High Temperature

SiC formed easily into SiO_2 in air by oxidation and, even if in inert environment, SiC is oxidized due to the reaction with oxygen included in as impurity [20, 21]. The former is well known as passive oxidation and also the latter is referred as active oxidation. SiC fiber and matrix used in this study were near-stoichiometric composition and hence there were few impurities. Indeed, it is reported that there was no significant degradation of tensile strength in Tyranno™-SA fiber itself below 1300°C in inert environment [3, 22]. On the while, it was afraid that PyC might be easily burned out by oxidation. However, in the non-oxidized environment like this study, this seemed quite small, not zero. These good stabilities of each component made tensile strength of composites much stable to the oxidizing attack. Hence, [-30º/0º/30º] SiC/SiC showed no degradation in oxidizing environments. While, [0º/90º] SiC/SiC slightly degraded at high-temperature but hopefully there seems little degradation in tensile properties. Otherwise, active oxidation to fiber and/or PyC might be performed in significant order. Anyway, further investigations are necessary to conclude this because of the shortage of test results.

5. CONCLUSIONS

In order to identify mechanical performance of recently developed SiC/SiC composites with high-crystalline, stoichiometric SiC fiber (Tyranno™-SA), several composites were fabricated by FCVI method at ORNL and ambient/high-temperature tensile tests were performed by small specimen test technique. Key conclusions were summarized as follows.

1. Maximum tensile stress of Tyranno™-SA/FCVI-SiC composites was significantly stable to high-temperature exposure up to 1300°C in mild oxidizing environment.
2. Tyranno™-SA/FCVI-SiC composite with single PyC interphase had its maximum strength when the thickness of PyC was about 200 nm.
3. Tensile strength was nearly no dependent on porosity. On the contrary, elastic modulus increases proportionally by improving composite density.

ACKNOWLEDGEMENTS

The authors would like to express their sincere appreciation to Mr. J.C. McLaughlin and Dr. T.M. Besmann, Oak Ridge National Laboratory for the fabrication of materials. This work was performed as a part of collaborations at Japan-US Program for Irradiation Test of Fusion Materials (JUPITER-II) and US-DOE/JAERI Collaborative Program on FWB Structural Materials in Mixed-Spectrum Fission Reactors, Phase IV. This study was also supported by Core Research for Evolutional Science and Technology (CREST).

REFERENCES

[1] R.H. Jones, L.L. Snead, A. Kohyama, P. Fenici, Fusion Engineering and Design 41 (1998) 15.
[2] L.L. Snead, R.H. Jones, A. Kohyama, P. Fenici, J. Nucl. Mater. 233-237 (1996) 23.
[3] Y. Katoh, T. Hinoki, W. Yang, W. Zhang and A. Kohyama, Proceedings of the 24th Annual Conference on Composites and Advanced Ceramic Materials-A, 21 (2000) 399.
[4] L.L. Snead, Y. Katoh, A. Kohyama, J.L. Bailey, N.L. Vaughm, R.A. Lowden, J. Nucl. Mater. 283-287 (2000) 551.
[5] R.J. Price, J. Nucl. Mater. 33 (1969) 17.
[6] R.J. Price, G.R. Hopkins, J. Nucl. Mater. 108-109 (1982) 732.
[7] M.C. Osborne, J.C. Hay, L.L. Snead, D. Steiner, J. Am. Ceram. Soc. 82 (1999) 2490.
[8] E. Lara-Curzio, Comprehensive Composites Encyclopedia, (2000) 533.
[9] T. Nozawa, T. Hinoki, Y. Katoh, A. Kohyama, E. Lara-Curzio, ASTM STP 1418 (2002), to be published
[10] T. Nozawa, K. Hironaka, Y. Katoh, A. Kohyama, E. Lara-Curzio, J. Nucl. Mater. to be published.
[11] T. Taguchi, et al., ORNL semiannual report, to be published.
[12] T.M. Besmann, J.C. McLaughlin, Hua-Tay Lin, J. Nuci. Mater. 219 (1995) 31.
[13] M. Ibanabdeljalil, W.A. Curtin, Int. J. Solids and Structuers, 34 (1997) 2649.
[14] W.A. Curtin, Composites Sci. Technol. 60 (2000) 543.
[15] M. Steen and J.L Valles, ASTM STP 1309, (1997) 49.
[16] K. Hironaka, T. Nozawa, T. Hinoki, N. Igawa, Y. Katoh, L.L. Snead, A. Kohyama, J. Nucl. Mater. to be published.
[17] Wen Yang, H. Araki, T. Noda, J. Y. Park, Y. Katoh, T. Hinoki, J. Yu, A. Kohyama, Submitted to J. Am. Ceram. Soc.
[18] W.A. Curtin, J. Am. Ceram. Soc. 74 (1991) 2837.
[19] T. Hinoki, W. Yang, T. Nozawa, T. Shibayama, Y. Katoh, A. Kohyama, J. Nucl. Mater. 289 (2001) 23.
[20] C. Labrugere, A. Guette, R. Naslain, J. Euro. Ceram. Soc. 17 (1997) 623.
[21] C. Labrugere, L. Guillaumat, A. Guette, R. Naslain, J. Euro. Ceram. Soc. 17 (1997) 641.
[22] R.E. Tressler, Composites A30 (1999) 429.

OPTIMIZING THE FABRICATION PROCESS FOR SUPERIOR MECHANICAL PROPERTIES IN THE STOICHIOMETIRIC SiC FIBER REINFORCED FCVI SiC MATRIX COMPOSITE SYSTEM

T. Taguchi[a], N. Igawa[a], T. Nozawa[b], K. Hironaka[b], L. L. Snead[c], T. Hinoki[c], Y. Katoh[b], S. Jitsukawa[a], A. Kohyama[b] and J. C. McLaughlin[c]

[a] Japan Atomic Energy Research Institute, Tokai, Ibaraki 319-1195, Japan

[b] Kyoto University, Gokasho,Uji, Kyoto 611-0011, Japan

[c] Oak Ridge National Laboratory, P.O. Box 2008, Oak Ridge, TN 37831, USA

Objective

The purpose of this work is the fabrication of the 300 mm diameter SiC/SiC composite using new stoichiometric SiC fibers, such as Tyranno SA and Hi-Nicalon Type S fiber, of low porosity and high tensile strength. Before these large size composite are fabricated, the fabrication process of smaller size (75 mm diameter) SiC/SiC composite using the new SiC fibers by FCVI process required optimization. In addition, the effect of the interphase between fiber and matrix on the mechanical properties of composites was also investigated

Summary

Optimization of the fabrication for SiC composites with stoichiometric SiC fibers (Hi-Nicalon Type S and Tyranno SA) by the forced thermal-gradient chemical vapor infiltration (FCVI) process was carried out. Density and mechanical properties were improved by increasing the fiber volume fraction and optimizing precursor gas flow rates. Porosity was decreased to approximately 15%. Uniformity of fiber/matrix interphase was improved by changing the upstream side and down-stream side of a preform during deposition. The tensile strength was seen to slightly increase with thickness of carbon interphase in the range of 75-300 nm. From these results, a dense 300 mm diameter SiC/SiC composite using Nicalon fiber as a trial experiment was fabricated. The density and porosity were 2.57 g/cm^3 and 13.8 %, respectively.

Progress and status

1. Introduction

Ceramic matrix composites show excellent mechanical properties at high temperature and non-catastrophic failure behavior. These materials are therefore attractive candidates for structural applications at high temperature. For these reasons and their low residual radioactivity following the neutron irradiation, the continuous SiC-fiber reinforced SiC-matrix (SiC/SiC) composites are being actively investigated for first wall and blanket components in power fusion reactors [1-4].

Among the various fabrication processes, the chemical vapor infiltration(CVI) is one of the best techniques to fabricate the SiC/SiC because of the high purity and minimizal fibers damage during the composite fabrication[5]. Whereas the isothermal CVI(I-CVI) can efficiently produce thin-wall and complex shape parts, it requires a significantly long time to produce thicker-wall materials. It takes high cost to produce the thick-wall materials by I-CVI. On the other hand, the forced-thermal gradient CVI(FCVI) of thicker parts can be effected at sufficiently high rates to only require tens of hours or less[5]. It can improve the cost to produce thick parts. We, therefore, adopted the FCVI process to make SiC/SiC composites in this study.

The large size composite is required to perform the variant thermal and mechanical properties for the both of un-irradiated and neutron irradiated specimens at the almost same microstructural property in each specimen, which includes the interphase structure and porosity. It is, therefore, very important

to fabricate the large size SiC/SiC composite with the uniform microstructural property. The definitive purpose in this study is the fabrication of the 300 mm diameter size SiC/SiC composite with the uniform microstructural properties.

Recently, high crystalline and stoichiometric SiC fibers have been produced including Hi-Nicalon Type S[6] and Tyranno SA[7], which possess superior mechanical and thermal properties as well as superior performance under neutron irradiation compared with their SiC-based predecessors. Because the properties of these advanced fibers, e.g. thermal conductivity, waviness, tensile modulus and fiber diameter, are very different from their predecessors, optimization of composite fabrication and interphase should be now being focused on their application. Before the 300 mm diameter size composite will be fabricated, it is important to optimize the fabrication process and the interphase by making the smaller size composite (75 mm diameter) in order to economize the cost. This study has also included general process optimization of properties such as through-thickness densification and interphase uniformity.

We adopted two kinds of advanced SiC fabrics as preforms: 2D-plain weave Tyranno SA and Hi-Nicalon Type S. Boron Nitride shows the excellent interphase for mechanical properties. Boron Nitride, however, is undesirable for fusion applications because nitrogen transmutes into ^{14}C that has a very long half-life of beta emitter by fusion neutrons, and also boron simultaneously produces helium and enhances radiation damage through recoil interaction. Therefore, the fusion community has limited the potential interphase materials to carbon, porous-SiC and multilayer-carbon/SiC are being studied for fusion applications [8]. Carbon interphase were selected for this study in the thickness range from 75 nm to 300 nm. Room temperature tensile properties were measured and optical and SEM observations of cross-sections and fracture surfaces in SiC/SiC were carried out in order to evaluate the thickness of interphase layer and investigate the effect of interphase on the mechanical properties of the composites.

2. Experimental procedure

Two kinds of advanced SiC fabric as performs was adopted: 2D-plain Tyranno SA (Ube Industries, Ube, Japan) and Hi-Nicalon Type S (Nippon Carbon Co., Ltd., Tokyo, Japan).

The precursor for carbon deposition was 99% purity propylene (C_3H_6, Matheson, Morrow, GA, USA)

Table 1. Fiber fabrics information of FCVI SiC/SiC composites

Specimen ID	Fiber	Weave type	Fiber orientation	Number of layers	Fiber as a spacer	Number of spacer layers
CVI1256	Tyranno SA	plane weave	[-30/0/+30]	55	P/W Nicalon	11
CVI1257	Hi-Nicalon Type S	plane weave	[-30/0+30]	55	P/W Nicalon	8
CVI1258	Hi-Nicalon Type S	plane weave	[-30/0/+30]	45	P/W Nicalon	20
CVI1259	Hi-Nicalon Type S	plane weave	[-30/0/+30]	45	P/W Nicalon	20
CVI1260	Tyranno SA	plane weave	[-30/0/+30]	55	Tyranno SA grade 1	11
CVI1261	Tyranno SA	plane weave	[-30/0/+30]	58	Tyranno SA grade 1	13
CVI1264	Tyranno SA	plane weave	[0/90]	60	P/W Nicalon	11
CVI1265	Tyranno SA	plane weave	[0/90]	60	P/W Nicalon	11
CVI1266	Tyranno SA	plane weave	[0/90]	60	P/W Nicalon	11

and for SiC infiltration, technical grade methyltrichlorosilane (MTS, CH_3SiCl_3,Gelest Inc., Tullytown, PA, USA) was used.

Table 2. Fabrication parameter of interpahse

Specimen ID	Interface material	Thickness / nm	Source of interphase		Carrier gas		Temperature / C	Time / min
		Nominal	Material	Flow rate / cm^3/min	Material	Flow rate / l/min		
CVI1256	carbon	150	C_3H_6	50	Ar	1.0	1100	60
CVI1257	carbon	150	C_3H_6	50	Ar	1.0	1100	30+30
CVI1258	carbon	75	C_3H_6	50	Ar	1.0	1100	15+15
CVI1259	carbon	300	C_3H_6	50	Ar	1.0	1100	60+60
CVI1260	carbon	300	C_3H_6	50	Ar	1.0	1100	60+60
CVI1261	carbon	75	C_3H_6	50	Ar	1.0	1100	15+15
CVI1264	carbon	150	C_3H_6	50	Ar	1.0	1100	40+40
CVI1265	carbon	300	C_3H_6	50	Ar	1.0	1100	90+90
CVI1266	carbon	75	C_3H_6	50	Ar	1.0	1100	15+15

Table 3. fabrication parameters of F-CVI process

Specimen ID	Source of material		Carrier gas		Temperature / C	Run time / hours
	Material	Flow rate / g/min	Material	Flow rate / dm^3/min		
CVI1256	MTS	0.5	H_2	0.75	1200	66
CVI1257	MTS	0.5	H_2	0.75	1200	31
CVI1258	MTS	0.5 0.33	H_2	0.75 0.75	1200	21.5 3.5
CVI1259	MTS	0.5 0.33	H_2	0.75 0.75	1100	25.9 4.5
CVI1260	MTS	0.5 0.17	H_2	0.75 0.35	1200	16 6
CVI1261	MTS	0.17	H_2	0.35	1200	66
CVI1264	MTS	0.3	H_2	0.45	1100	61.5
CVI1265	MTS	0.3	H_2	0.45	1050	70.5
CVI1266	MTS	0.3	H_2	0.45	1000	90.2

The SiC fabric layers with a fabric layer orientation of [-30˚/0˚/30˚] or [0˚/90˚] were restrained in a graphite fixture. The fiber volume fraction range was 30 to 39 vol%. The size of preform was 75 mm in diameter and 12.5 mm thickness. The fiber fabric parameters of the fabricated SiC/SiC in this study are shown in Table 1. The carbon interphase was deposited at 1100 ˚C and at 5 Pa. The condition of carbon deposition is flow rates of 50 cm^3/min C_3H_6 and 1000 cm^3/min Ar. The fabrication parameters of the interpahses are shown in Table 2. After the interphase layer was deposited, the preforms were infiltrated at 1000-1200 ˚C at atmospheric pressure with MTS flow rate of 0.2-0.5 g/min carried by 450-750 cm^3/min of H_2. The back-pressure was monitored and the FCVI process was automatically finished after the back pressure reached 6.9X10^4 Pa. The infiltration conditions are shown in Table 3.

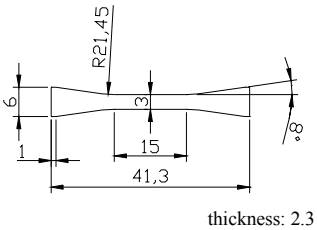

Fig. 1 Schematic illustration of tensile test specimen

To determine the distribution of porosity and carbon interphase thickness, the plate was cut into nine sections as shown in Fig. 2. The density of each section was calculated from the dimensions and the mass of the plate to determine the distribution of the porosity in the composite. The microstructure of the composites was observed by optical microscopy and scanning electron microscopy(SEM).

Tensile testing was carried out at room temperature with a cross-head speed of 0.5 mm/min. The

shape and size of the specimen was shown in Fig. 1. The strain of the specimen was measured with bonded strain gauges. The fracture surfaces were observed by SEM in order to investigate the effect of interphase on the mechanical properties.

3. Results and discussion

3.1 Fabrication of the 75 mm diameter composite

3.1.1 Densification process

The distributions of the porosity in the fabricated SiC/SiC in this study are shown in Fig. 2. The characterization of SiC/SiC is also shown Table 4. The porosity in the ID 1257 specimen was relatively large (23.5 %) and depending on position: we found that the lower and outer position in the composite had the highest porosity. Much better uniform porosity in the composites (for example ID 1259 specimen) was obtained by decreasing the MTS and H_2 gas flow rates at the latter part of the FCVI process. Presently, the porosity in the composite was decreased. Because the termination of the FCVI process was controlled by the back-pressure that was decreased with decreasing the gas flow rate, the FCVI process was extended by the decrease in the flow rate.

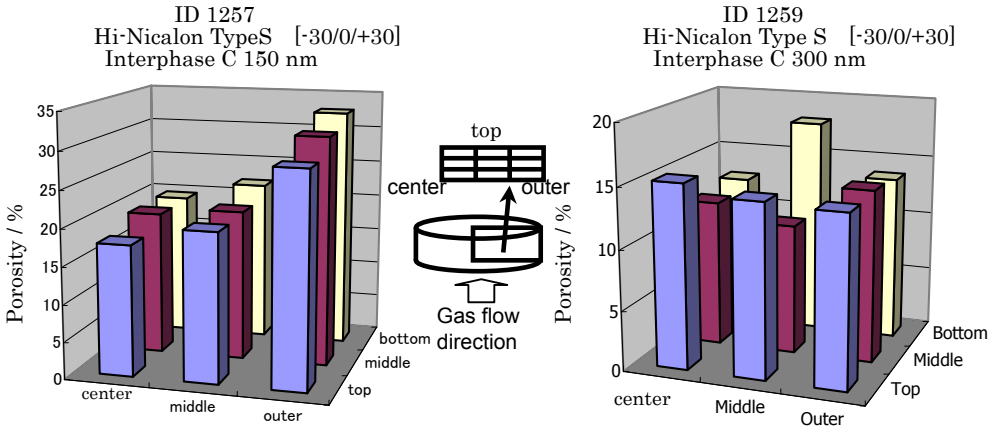

Fig.2 Typical distribution of the porosity of the fabricated SiC/SiC composite.

Table 4. Characterization of F-CVI SiC/SiC composites

Specimen ID	Fiber volume fraction / %	Density / g/cm^3	Porosity / %
CVI1256	37.0	2.67 ± 0.12	15.1 ± 4.0
CVI1257	33.0	2.43 ± 0.18	23.5 ± 5.7
CVI1258	36.1	----------	----------
CVI1259	35.0	2.73 ± 0.07	13.9 ± 2.1
CVI1260	30.2	2.41 ± 0.09	24.2 ± 2.8
CVI1261	33.3	2.53 ± 0.13	20.4 ± 4.2
CVI1264	35.4	2.43 ± 0.12	23.3 ± 3.7
CVI1265	35.3	2.60 ± 0.14	18.0 ± 4.5
CVI1266	35.2	2.60 ± 0.17	18.1 ± 5.3

The average porosity as a function of fiber volume fraction was shown in Fig. 3. The fiber volume fraction is very effective in decreasing the porosity; the average porosity is decreased to 15 % by increasing the fiber volume fraction to 39 vol%, but seems independence of fiber type and infiltration parameter.

The typical cross-sections of SiC/SiC are shown in Fig. 4. Even in the specimen that had smallest porosity (15.1 %), we could observe the two kinds of pores; the one is the inter-bundle large pores and

the another is the intra-bundle small pores. The porosity in the composite depends on the amount of inter-bundle pore more efficiently than that of intra-bundle pore because the total amount of inter-bundle pore is much larger than that of intra-bundle pore. From the cross-sections microphotographs, it was found that the size of inter-bundle pores was smaller with the shorter distance between the fiber bundles in the specimen. The distance between fiber bundles is shorter when fiber volume fraction is higher, which mean each space between bundles with higher fiber volume fraction is smaller than those with lower fiber volume fraction; therefore the size of inter-bundle pore at higher fiber volume fractions is smaller than those of lower fiber volume fraction.

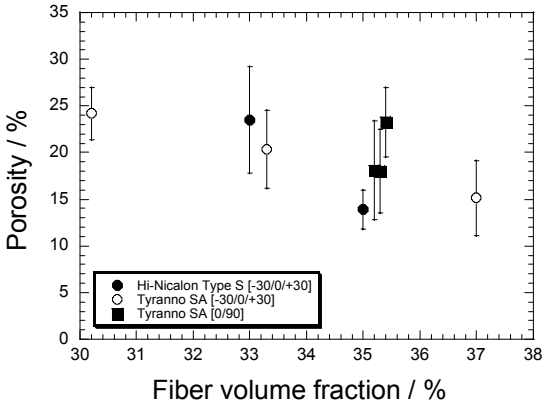

Fig.3 Effect of fiber volume fraction on the porosity.

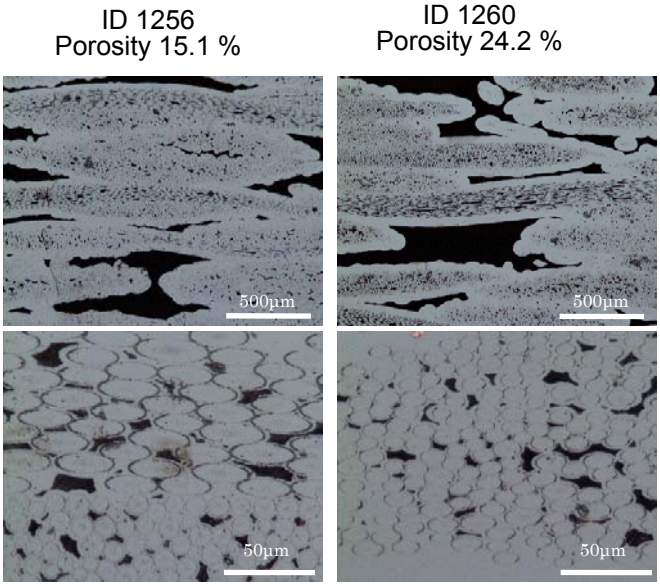

Fig.4 Cross-sections photographs of SiC/SiC composites.

3.1.2 Interphase fabrication process

Figure 5 shows the distribution of the thickness of carbon interphase between SiC fiber and SiC matrix in the composites estimated from cross-section SEM images. The results of the thickness of carbon are shown in Table. 5. In ID1256 specimen, we found that the lower position in the composite had the thicker carbon interphase: the average thickness of carbon interphase at bottom is about 145 nm whereas that

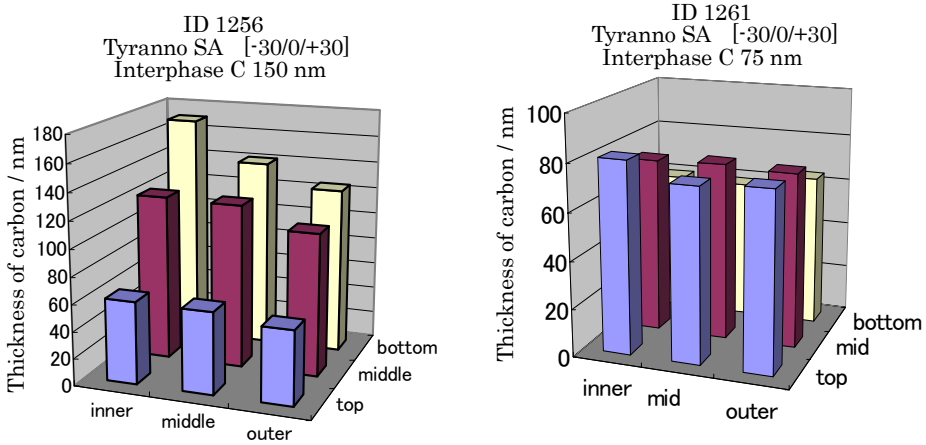

Fig.5 Typical distribution of the carbon thickness in the SiC/SiC composite

at top 60 nm. This tendency was attributed to a concentration gradient in the C_3H_6 gas. This material gas traveled from the bottom surface to top of the specimen, and the thickness of specimen was so large that the concentration of C_3H_6 gas was decreased due to its consumption at the lower part of the specimen. To mitigate this problem the preform was flipped midway through the interphase infiltration. The distribution of carbon interphase thickness was remarkably improved and we obtained the specimens with near uniform through-thickness carbon interphase thickness (see ID1261 specimen in Fig.5).

Table 5. Interphase thickness of F-CVI SiC/SiC composites

Specimen ID	material	Thickness of interphase / nm				
		nominal	Measured average	Minimum	Maximum	Statistical scatter
CVI1256	carbon	150	107.1	54.8	170.1	40.1
CVI1257	carbon	150	159.5	141.9	172.7	10.8
CVI1258	carbon	75	----------	----------	----------	----------
CVI1259	carbon	300	407.3	266.4	612.2	121.3
CVI1260	carbon	300	168.5	138.2	206.9	22.1
CVI1261	carbon	75	70.5	58.8	81.1	7.8
CVI1264	carbon	150	116.4	86.1	154.5	20.5
CVI1265	carbon	300	225.5	168.0	256.3	29.4
CVI1266	carbon	75	42.3	28.5	54.2	7.2

The relationship between the average thickness of carbon interphase and deposition time is shown in Fig.6. The thickness of carbon interphase increased linearly with increasing the deposition time. The carbon deposition rate of the composite using Hi-Nicalon Type S fiber is, however, larger than that of the composite using Tyranno SA fiber. In the case of the same fiber volume fraction, the total superficies of fibers of the composite using Hi-Nicalon Type S is smaller than that of the composite using Tyranno SA fiber because the diameter of Hi-Nicalon Type S fiber is larger than that of Tyranno SA fiber. It is, therefore, considered that the carbon deposition rate of the composite using Hi-Nicalon Type S was larger than that of the composite using Tyranno SA. The relationship between the thickness of carbon and the standardized deposition time (the deposition time divided by the total superficies of fibers) is shown in Fig.7. The average thickness of carbon in all composites increased as one linear series with increasing the standardized deposition time. Therefore we can estimate the carbon thickness from the standardized deposition time, even if any kinds of fiber are used in the

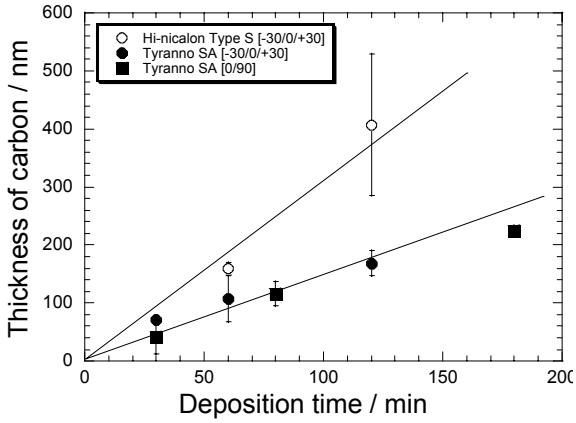

Fig.6 Relationship between deposition time and carbon thickness.

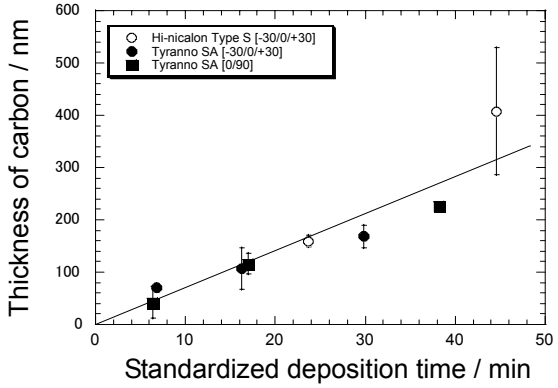

Fig.7 Relationship between standardized deposition time and carbon thickness.

composite.

3.1.3 Mechanical properties

Typical stress-strain curves during the tensile testing are seen in Fig. 8. The summaries of tensile strength testing in the composites with carbon layer as the interphase layer are shown in Table 6. In tensile testing, each specimen exhibited nonlinear stress-strain behavior, which means noncatastrophic failure behavior.

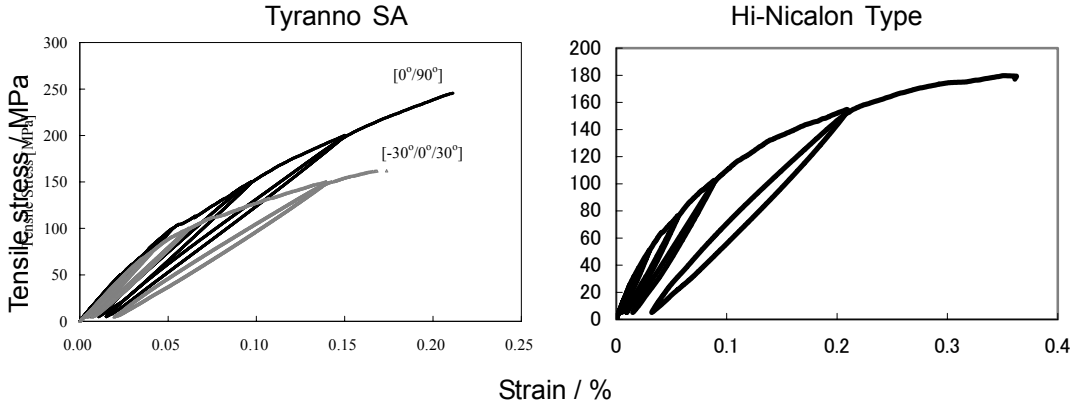

Fig. 8 Typical tensile behaviors of [-30º/0º/30º] and [0º/90º] SiC/SiC composites

Table 6. Mechanical properties of F-CVI SiC/SiC composites

Specimen ID	Tensile strength /MPa	Normalized tensile strength / MPa	Strain at fracture / %
CVI1256	155 ± 24	144 ± 22	0.126 ± 0.07
CVI1257	165 ± 23	164 ± 27	0.256 ± 0.15
CVI1258	164 ± 19	158 ± 18	0.204 ± 0.11
CVI1259	203 ± 10	201 ± 10	0.361 ± 0.05
CVI1260	131 ± 11	149 ± 12	0.173 ± 0.05
CVI1261	128 ± 19	133 ± 19	0.135 ± 0.03
CVI1264	233 ± 52	226 ± 33	0.253 ± 0.11
CVI1265	232 ± 34	226 ± 33	0.235 ± 0.03
CVI1266	211 ± 20	206 ± 20	0.175 ± 0.03

The composites fabricated by this study each have different density and fiber volume fraction. The relationship between the density of composite and the tensile strength is shown in Fig.9. No tendency can be, however, observed in this relationship. Because the load is mainly maintained by unfractured fibers and friction between fractured fiber and interphase above the proportional limit stress, the tensile strengths were, therefore, normalized by the fiber volume fraction of each composite in order to compare to them each other. Optimization of the interphase is one of the important factors to improve the mechanical properties of SiC/SiC composites. The effect of carbon thickness on normalized tensile strength of SiC/SiC composites was shown in Fig.10. For the bend strength, the

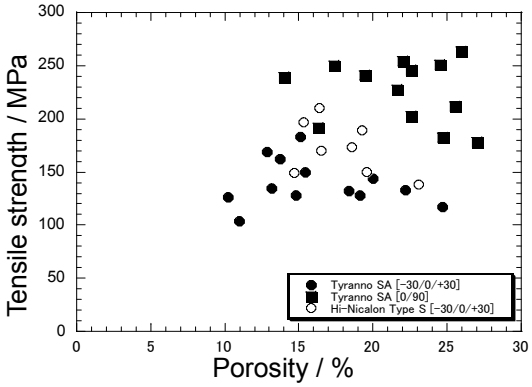

Fig.9 Effect of porosity on the tensile strength.

optimum carbon interphase thickness is in the range of 170-1000nm[9]. In both [0˚/90˚] and [-30˚/0˚/30˚] composites using Tyranno SA fiber, it seems that normalized tensile strength is slightly increased with the thickness of carbon interphase in the range of 75-150 nm and then almost constant in the range of 150-300 nm. And in the composite using Hi-Nicalon Type S fiber, the normalized tensile strength was slightly increased with the thickness of carbon interphase in the range of 75-300 nm. The thick carbon layer as an interphase layer may cause the reduction of the strength in the composite following the neutron irradiation due to the irradiation-assisted oxidation and dimensional changes of the carbon [10,11]. The thinner carbon should be used as an interphase layer. From these results, the best thickness of carbon as an interphase layer may be about 150 nm.

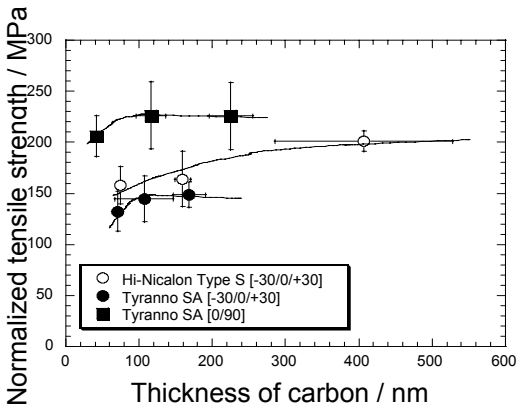

Fig.10 Effect of carbon thickness on the normalized tensile strength.

The tensile strength of the composite with the fabric orientation of [0/90] using Tyranno SA fiber is larger than that of [-30˚/0˚/30˚]. The tensile fracture surfaces of the composites were shown in Fig.11. For the excellent tensile strength, a large number of fibers retained at a maximum load are required as well as the fiber strength itself[12]. In Fig.11 the fiber pull-out was observed in the tensile fracture surface of all specimens. It seems that the pull-out length of the fibes angled to the tensile axis is shorter than that of the aligned fiber with the tensile axis in the [-30˚/0˚/30˚] composite. So the angled fibers might be unable to keep the strength. It is considered that the tensile strength depends on the strength of the aligned fiber with the tensile axis efficiently. The aligned fiber volume fraction with the tensile axis in the [0˚/90˚] composite is higher than that of [-30˚/0˚/30˚] composite. The tensile strength of [0˚/90˚] composite was, therefore, larger than that of [-30˚/0˚/30˚] composite.

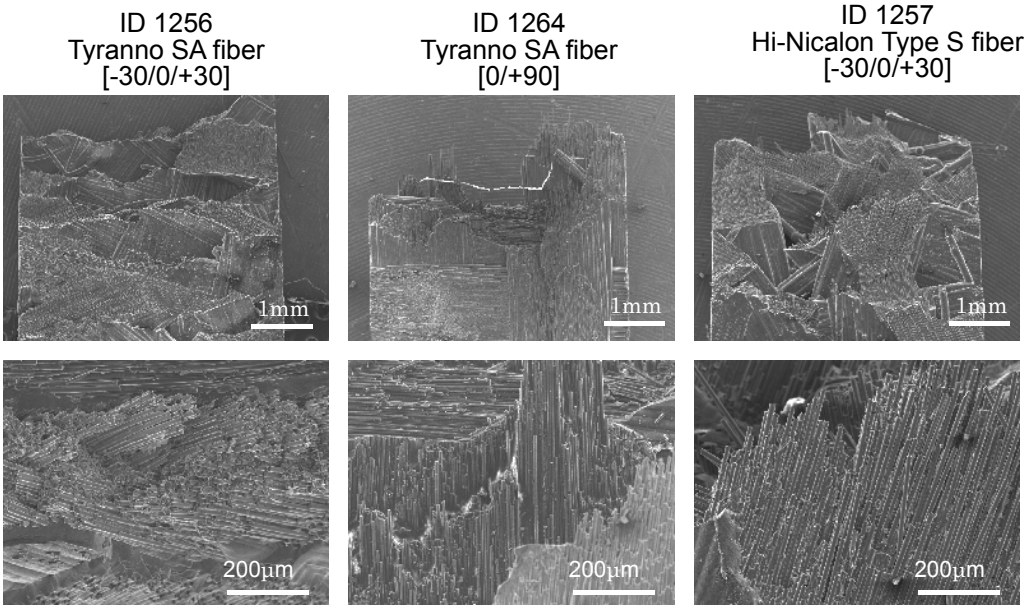

Fig.11 Fracture surface of tensile tested SiC/SiC composites with 150 nm carbon as an interphase layer.

In the case of fabric orientation of [-30˚/0˚/30˚], the strength of the composite using Hi-Nicalon Type S is larger than that of Tyranno SA. From the result of the fracture surface observation (see Fig.11), it is found that the pull-out length of the composite using Hi-Nicalon Type S is longer than that of Tyranno SA. Especially the angled fibers with respect to the tensile axis also caused the long pull-out as well as the aligned fibers. It is considered that the angled fibers in the composite using Hi-Nicalon Type S could retain their strength. Therefore the strength of the composite using Hi-Nicalon Type S is larger than that of Tyranno SA.

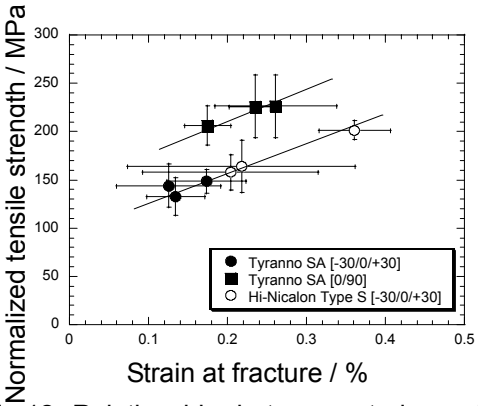

Fig.12 Relationship between strain and normalized tensile strength.

The normalized tensile strength as a function of the strain at tensile strength is shown in Fig.12. The normalized tensile strength increased linearly with increasing the strain. They depended on the fabric layer orientation but did not depend on the SiC fiber type. In the case of using Tyranno SA fiber, the strain of the composite with the fabric layer orientation of [0˚/90˚] was larger than that of [-30˚/0˚/30˚]. The reason is that the aligned fiber volume fraction with the tensile axis in the [0˚/90˚] composite is higher than that of [-30˚/0˚/30˚] composite. In the case of fabric orientation of [-30˚/0˚/30˚], the strain of the composite using Hi-Nicalon Type S is larger than that of Tyranno SA. As mentioned above, the reason is that the angled fibers also could cause the pull-out of composites using Hi-Nicalon Type S.

3.2 Fabrication of the 300 mm diameter composite

The 300 mm diameter size composites using the new SiC fiber with the optimized interphase will be fabricated. We fabricated the 300 mm diameter size composite using Nicalon fibers in order to estimate the carbon deposition rate on the new SiC fiber. The reason is that we can estimate the carbon deposition rate by that of other fiber type as mentioned in the previous section. The photograph of 300 mm diameter size SiC/SiC composite was shown in Fig.13. The fiber volume fracture is about 34.7 %. The density and porosity of this composite were about 2.57 g/cm^3 and 13.8 %, respectively. We are observing the cross-sections of this specimen by SEM to evaluate the thickness of carbon and SiC layer as the interphase.

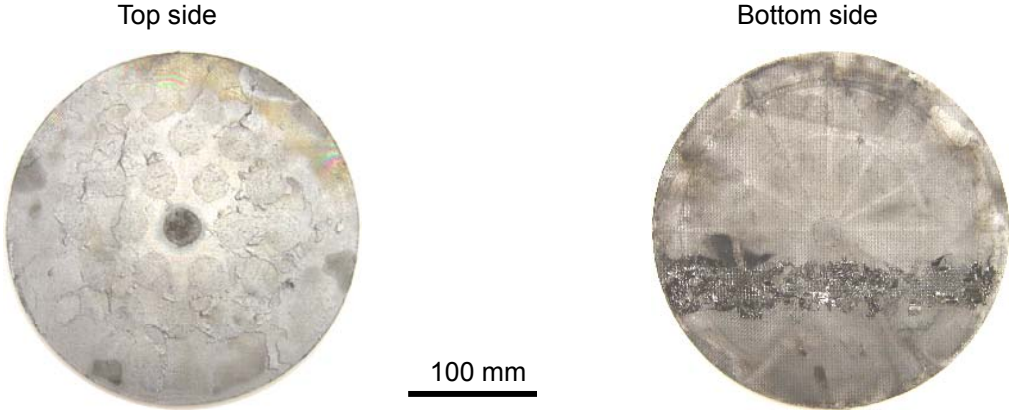

Fig.13 Photographs of the 300 mm diameter SiC/SiC composite using Nicalon fibers.

4. Conclusion

Process optimization for FCVI fabrication of 75 mm diameter SiC composites with new SiC fibers, Hi-Nicalon Type S and Tyranno SA, was carried out. The SiC/SiC composites fabricated by FCVI exhibited significant improvement reduction in porosity (15.1%) and more uniform pore distribution by decreasing in the MTS and H_2 gases flow rates at the latter part of the FCVI process. Uniform carbon interphase between advanced SiC fibers and FCVI-SiC matrix could be obtained by reversing the gas-flow direction mid-way through the coating process. The tensile strength was slightly increased with thickness of carbon interphase in the range of 75-300 nm.

From these results, the dense 300 mm diameter SiC/SiC composite using Nicalon fiber as a trial experiment was fabricated. The density and porosity were 2.57 g/cm^3 and 13.8 %, respectively.

Acknowledgements

The authors would like to thank Dr. T. M. Besmann at ORNL for useful discussion. This study has been carried out under the US-DOE/ JAERI Collaborative Program on FWB Structural materials in Mixed-Spectrum Fission Reactors, Phase IV. This study is also supported by CREST-ACE(Core Research for Evolutional Science and Technology/Advanced material Systems for Energy Conversion) program sponsored by Japan Science and Technology Corporation.

References

[1] L.L. Snead, R.H. Jones, A. Kohyama, P. Fenici, J. Nucl. Mater. 233-237(1996)26.
[2] R.H. Jones, D. Steiner, H.L. Heinisch, G.A. Newsome, H.M. Kerch, J. Nucl. Mater.,245(1997)87.
[3] P. Fenici, A.J. Frias Rebelo, R. H.Jones, A. Kohyama, L.L. Snead, J. Nucl. Mater. 258-263(1998)215.
[4] A. Hasegawa, A. Kohyama, R.H. Jones, L.L. Snead, B. Riccardi, P. Fenici, J. Nucl. Mater. 283-287(2000)128.
[5] T.M. Besmann, J.C. McLaughlin, H-T. Lin, J. Nucl. Mater. 219(1995)31.
[6] M. Takeda, A. Urano, J. Sakamoto, Y. Imai, J. Nucl. Mater. 258-263(1998)1594.
[7] T.Ishikawa, Y. Kohtoku, K. Kumagawa, T Yamamura, T. Nagasawa, Nature 391(1998)773..
[8] W.S. Stefier, Ceram. Eng. Sci. Proc. 14(1993)1045.
[9] A. Kohyama, H. Hinoki, H. Serizawa, S. Sato, Proc. of 11th Inter. Conf. on Composites Mater. 1997.
[10] L.L.Snead, M.C.Osborne and K.L.More, J. Nucl. Mater., 231 (1996) 245-248.
[11] J.H.W.Simmons, Radiation Damage in Graphite, Pergamon Press, (1965).
[12] T. Hinoki, W. Yang, T. Nozawa, T. Shibayama, Y. Katoh, A. Kohyama, J. Nucl. Mater. 289(2001)23.

MODELING THE TRANSVERSE THERMAL CONDUCTIVITY OF 2D-SIC$_F$/SIC COMPOSITES

– G. E. Youngblood, D. J. Senor and R. H. Jones (Pacific Northwest National Laboratory)*

OBJECTIVE

The primary objective of this task is to assess the thermal conductivity of SiC/SiC composites made from SiC fibers (with various SiC-type matrices, fiber coatings and architectures) before and after irradiation and to develop analytic models that describe the transverse and in-plane thermal conductivity of these composites as a function of constituent properties and geometry as well as temperature and dose.

SUMMARY

A hierarchical model was developed to describe the effective transverse thermal conductivity, K_{eff}, of a 2D-SiC/SiC composite made from stacked and infiltrated woven fabric layers in terms of constituent properties and microstructural and architectural variables. The model includes the expected effects of fiber-matrix interfacial conductance as well as the effects of high fiber packing fractions within individual tows and the non-uniform nature of 2D-fabric layers that include a significant amount of interlayer porosity. Model predictions were obtained for two versions of DuPont 2D-Hi Nicalon™/PyC/ICVI-SiC composite, one with a "thin" (0.110 μm) and the other with a "thick" (1.040 μm) PyC fiber coating. The model predicts that the matrix porosity content and porosity shape factor have a major influence on $K_{eff}(T)$ for such a composite.

PROGRESS AND STATUS

Introduction

In previous work, the Hasselman-Johnson (H-J) model for the effective transverse thermal conductivity (K_{eff}) of 2D-SiC/SiC was used to predict K_{eff} for a hypothetical composite made with high conductivity fiber and matrix components [1,2]. The H-J model includes the effect of the interfacial conductance, which in a composite with numerous fiber/matrix (f/m) interfaces can have a profound influence on K_{eff}. The model itself shows that for a composite with dispersed fibers the most important factor needed to achieve high K_{eff} is high thermal conductivity of the continuous matrix phase. Nevertheless, both high fiber and high interface conductivity also will be necessary.

The H-J model was derived for an ideal f/m geometry consisting of dispersed uniaxial fibers with relatively low volume fractions in a uniform matrix so that fiber-fiber interactions could be neglected. The model should especially be useful to describe the effects of f/m separation or debonding [3], which might occur during irradiation as a result of differential fiber-matrix swelling or fiber densification. A second model, the Markworth "3-Cylinder" model, was developed to examine the detailed contribution of a fiber coating characterized by the thickness of the coating and its thermal conductivity [4]. The 3-cylinder model proved to be most useful to describe K_{eff} for a composite with an f/m interface consisting of a well-bonded, uniform isotropic pyrocarbon (PyC) fiber coating [5]. Apparent agreement between Markworth model predictions and measured K_{eff}-values as a function of temperature for two different versions of a commercial, plain-woven 2D-SiC/SiC composite suggested that the Markworth model (and the H-J model) describe the general behavior of K_{eff} as a function of constituent thermal properties.

* Pacific Northwest National Laboratory (PNNL) is operated for the U.S. Department of Energy by Battelle Memorial Institute under contract DE-AC06-76RLO-1830.

Furthermore, depending on conditions each model should be useful to critically assess degradation mechanisms in these type composites [6].

Two versions of 2D-SiC/SiC were similarly fabricated by DuPont Lanxide (now Honeywell Advanced Composites) using fabric layers of Hi-Nicalon™ SiC fiber stacked in 0-90 sequence. Each version contained a nominal fiber volume fraction f = 0.4. The SiC matrix was applied by isothermal chemical vapor infiltration (ICVI). The only major difference between the two versions was that in one version the PyC fiber coating was "thin" (nominally 150 nm) while in the other the coating was "thick" (nominally 1.2 μm). The fiber thermal conductivity (K_f) and K_{eff} were separately determined from thermal diffusivity measurements as a function of temperature over the RT-1000°C range by methods described previously [7,8]. By using these data and the Markworth model, preliminary values of thermal conductivity for the matrix and coating constituents (K_m = 22-25 W/mK for an ICVI-SiC matrix and K_c = 25 W/mK for a PyC fiber coating at RT, respectively) were estimated [5]. The effective interfacial conductance (h) for the composite with the thin PyC coating also was estimated by $h \sim K_c/t = 24 \times 10^6$ W/m^{2}K. Typical SEM micrographs of composite cross-sections for the two DuPont 2D-SiC$_f$/SiC composite versions with different coating thickness are given in Figs. 1(a-d).

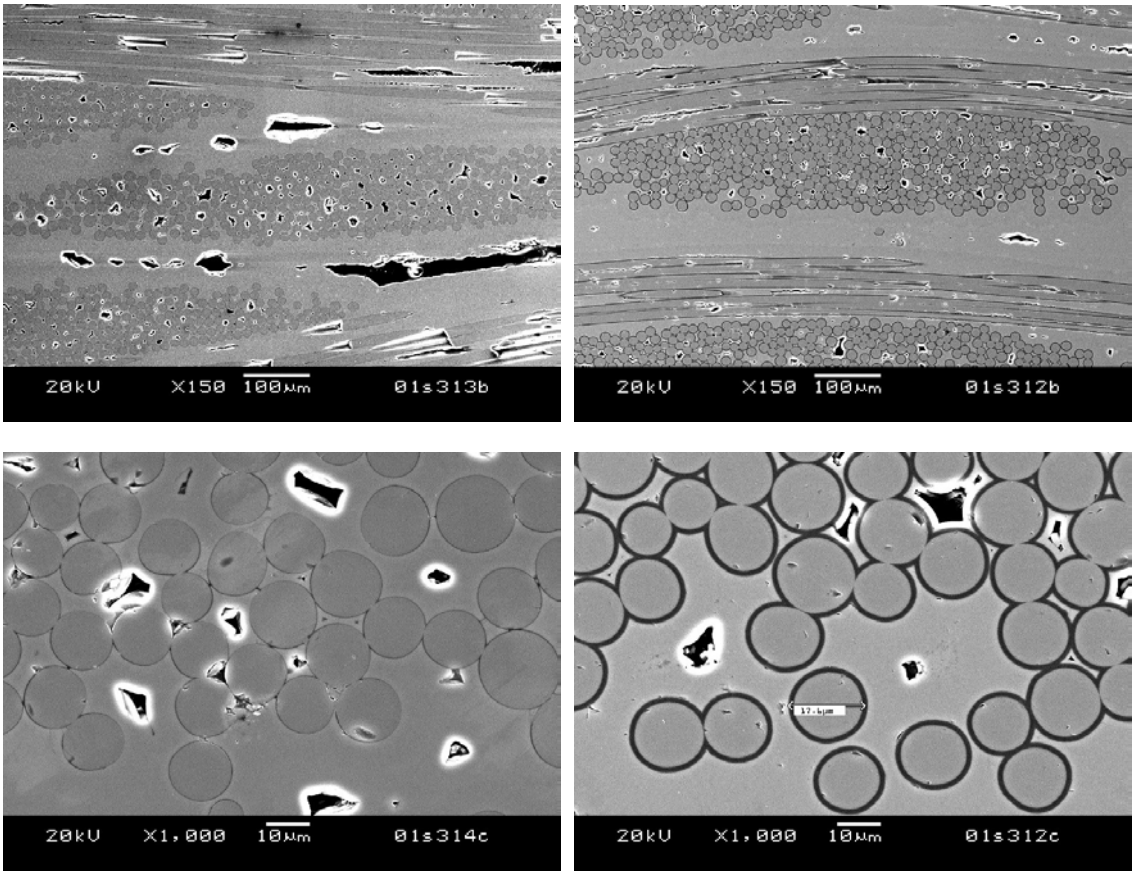

Figure 1. SEM micrographs of polished DuPont 2D-SiC/SiC cross-sections showing typical porosity and good infiltration of ICVI-SiC matrix within plain-woven Hi-Nicalon™ bundles for (lhs) "thin" (0.110 μm) and (rhs) "thick" (1.040 μm) PyC fiber coating versions. The higher magnification views (lower) illustrate good f/m bonding through the PyC fiber coating for each version of the as-received composite.

The 2D-woven pattern and the microstructures appear to be quite similar for each version. As observed in Figures 1(a-d), the CVI-SiC infiltration was fairly uniform with only a few needle-like pores running parallel to the fiber axis contained within the 0-90 bundles. The apparently tight f/m bonding through either the thin or thick PyC fiber coatings suggests that the fibers were thermally well-coupled to the matrix. However, a number of rather large laminar-shaped pores, characteristic of composite fabricated by CVI infiltration of stacks of woven fabric layers, were observed typically in the interlayer region between the fabric layers. Although each version of the composite had a nominal fiber packing fraction of 0.4, the localized fiber packing within the individual tows obviously is much higher. Also, rather thick regions of single phase ICVI-SiC matrix exist around each fiber tow and also existed as a seal coat on the outer surfaces of the composite plates.

Neither the H-J nor the Markworth models account for the non-homogeneous nature of a composite with 2D plain-woven fabric layers. A refined model based on the actual architectural design is needed to reliably examine irradiation degradation mechanisms in detail for such a composite. For instance, due to expected high fiber packing fractions within individual fiber tows, the effects on K_{eff} of potential fiber-fiber interaction, and even direct fiber or fiber coating connectivity, needs to be considered. Furthermore, the non-uniform nature of the 2D fabric layers separated by dense matrix layers, but which typically contain numerous, relatively large laminar-shaped pores, needs to be included in a realistic model. Such a model, based on a hierarchical approach, is presented below.

The hierarchical model approach

The hierarchical model approach is based on the schematic representation of the 2D-SiC/SiC architecture for a typical composite made from stacked and infiltrated fabric layers, as illustrated in Figures 2(a-b). A major consideration is to include the effects of the dense CVD-SiC layers that separate the infiltrated 2D-fabric layers and of the numerous laminar-shaped pores contained in the interlayer between the dense CVD layers. In the schematic representation the composite is divided into two layers, an infiltrated 2D-fabric layer and a dense CVD-SiC layer of relative thickness f_F and f_M, respectively. The layers are aligned perpendicular to the heat flux.

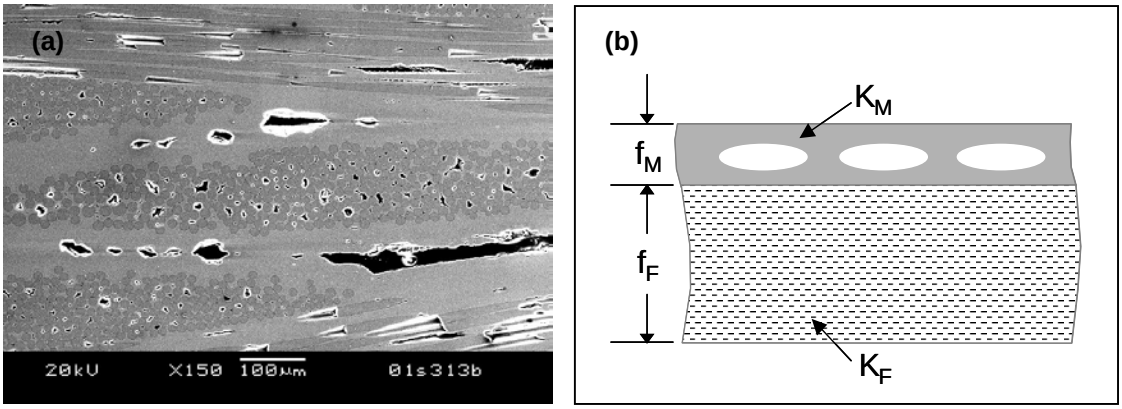

Figure 2. (a) SEM micrograph of a polished DuPont 2D-SiC/CVI-SiC cross-section showing the typical fabric and matrix layer pattern. Most of the laminar-shaped porosity is contained within the interlayer region between the fabric layers. (b) Schematic depiction of the composite two-layer architecture.

The average composite porosity (P_{avg}) can be estimated from the values of the overall fiber volume fraction (f) and composite bulk density (ρ_b), the fiber density (ρ_f), and the theoretical composite density (ρ_o) by

$$P_{avg} = 1 - f - (\rho_b - f\rho_f)/\rho_o \quad (1)$$

Since most of the porosity is assumed to be contained within the dense CVI-SiC layer, P_{avg} must be adjusted to give the volume fraction porosity (P) contained within this layer by $P = P_{avg}/f_M$. Then the effective thermal conductivity in the CVI-layer (K_M) is estimated by the Maxwell-Eucken expression

$$K_M = K_m(1 - P)/(1 + \beta P) \quad (2)$$

where β is a pore shape factor (e.g., $\beta = 0$ for needle-shaped pores parallel to the heat flux, $\beta = 1/2$ for isolated spherical pores, $\beta = 2/3$ for randomly dispersed cylindrical pores, and $\beta > 2/3$ for oblate spherical-shaped pores aligned perpendicular to the heat flux) [9,10].

The effective thermal conductivity in the 2D-fabric layer (K_F) is approximated by the H-J equation

$$K_F = K_m[1 - (B/A)p]/[1 + (B/A)p] \quad (3)$$

where p, the actual packing fraction of the fibers within the fabric layers, has been substituted for f as the representative fiber volume fraction. As developed in Reference [1], $A = 1 + x + r$ and $B = 1 + x - r$, where $r = K_f/K_m$ and $x = K_f/ah$, and x is the reciprocal Biot number for heat transfer at the f/m interface with interfacial conductance (h) and fiber radius (a). In Equations (2) and (3), K_m now becomes the intrinsic ICVI-SiC matrix thermal conductivity. The effective transverse thermal conductivity of this two-layer composite model is then simply given by the expression for a fabric and matrix layer in series with thermal conductivities K_F and K_M, respectively:

$$1/K_{eff} = f_F/K_F + f_M/K_M \quad (4)$$

As was discovered later, the H-J equation does not adequately treat thermal conduction in a composite with a rather thick, well-bonded fiber coating since the coating itself can contribute to the overall conduction. For a composite with a thin fiber coating, the substitution $h \sim K_c/t$ (where K_c and t are the fiber coating thermal conductivity and thickness, respectively) in the H-J equation gives representative results for K_F. For a composite with a well-bonded, "thick" fiber coating the somewhat more complex Markworth or "3-cylinder" model is used to describe K_F. For this latter case,

$$K_F = K_m\{f(K_f, K_m, K_c; p, t, a)/g(K_f, K_m, K_c; p, t, a)\} \quad (5)$$

where the functions f and g are given by

$$f = 2c(r + c)[1 + p(1 + u)^2] + [(c - 1) + p(1 + u)^2(c + 1)]\{ (r - c)/(1 + u)^2 - (r + c)\} \quad (6)$$

$$g = 2c(r + c)[1 - p(1 + u)^2] + [(c - 1) - p(1 + u)^2(c + 1)]\{ (r - c)/(1 + u)^2 - (r + c)\} \quad (7)$$

In Equations (6) and (7), $u = t/a$ and $c = K_c/K_m$. As before, $r = K_f/K_m$ and p is the actual fiber packing fraction within a fabric layer.

Results

The temperature dependent thermal conductivity data $K_f(T)$ and the bulk density and average radius of Hi-Nicalon™ fiber (ρ_f = 2.74 g/cc and a = 7.0 ± 0.6 μm, respectively) were obtained in a separate experiment [8]. Other measured or calculated microstructural quantities used in the model descriptions for the "thin" and "thick" versions of the DuPont 2D Hi-Nic/PyC/ICVI-SiC composite are listed in Table 1.

Table 1. Microstructural data for "thin" and "thick" versions of DuPont 2D Hi-Nic/PyC/ICVI-SiC composite.

Version	t (μm)	ρ_o (g/cc)	ρ_b (g/cc)	P_{avg}	f_M	f_F	p	P	β
"thin"	0.110 (0.020)*	3.106	2.597 (0.030)	0.117	0.294 (0.07)	0.706 (0.08)	0.65 (0.02)	0.36 (0.10)	2.3 (1.3)
"thick"	1.044 (0.020)	2.991	2.627 (0.027)	0.088	0.314 (0.07)	0.686 (0.08)	0.67 (0.02)	0.25 (0.06)	2.3 (1.3)

* Numbers in parenthesis indicate approximate range of values based on repeated measurements at different locations.

In Table 1, ρ_o was calculated from a rule of mixtures based on the composition of Hi-Nicalon™ fiber and the dimensions and an assumed density of 1.90 g/cc for the PyC fiber coating. The bulk density of the composite (ρ_b) was determined by weighing and dimensioning the individual samples used for thermal diffusivity measurements. The values for f_M and f_F were approximated by scaling from a number of SEM views of composite cross-sections similar to Figure 1. Likewise, p and β were estimated in this manner. In particular, an approximation (β ~ 1/2 a/c for an oblate spheroid with large and small axes, a and c, respectively) was used to represent the interlayer pores having elliptically shaped cross-sections as depicted in Figure 2(b). Using the appropriate f_F-factor, P_{avg} was calculated from Equation (1) and adjusted to give P.

The model results based on the measured values of $K_{eff}(T)$ and $K_f(T)$ and on the microstructural data given in Table 1 are depicted in Figures 3 (a,b) for the "thin" and "thick" versions of the DuPont composite, respectively. In Figures 3(a,b), the large difference between the intrinsic $K_m(T)$ and $K_M(T)$ curves is due to the large influence of the porosity content within the matrix layer (P) and its shape factor (β). The "thin" version of the DuPont composite had a slightly higher ρ_o-value (due to a lower PyC content) and a lower ρ_b-value compared to the "thick" version. Since both versions were fabricated by the same CVI-process, the $K_m(T)$-values and the fiber coating thermal conductivity $K_c(T)$-values were required to be approximately the same during the model curve fitting. The coating $K_c(T)$-values ranged from 24 (@27°C) up to 40 (@200°C) and down to 32.5 W/mK (@1000°C). Then the major difference between the two versions is the significantly smaller $K_M(T)$-values for the "thin" version, with a larger difference occurring at lower temperatures. The fabric layer $K_F(T)$-values were about the same for each version, although the thicker PyC coating contributes more to the overall $K_{eff}(T)$ than the thinner coating. Finally, note that the $K_{eff}(T)$ curve lies between the $K_F(T)$ and $K_M(T)$ curves due to the layer configuration being in series.

The quantitative measurement of the microstructural features in 2D-woven composite generally exhibit a wide variation, as indicated by the relatively large uncertainties listed for these quantities in Table 1. In Figure 3(a), the sensitivity of $K_m(T)$ to a range of β-values from 1-4 (equivalent to an ellipse aspect ratio range 2-8) is examined. The basic difference between

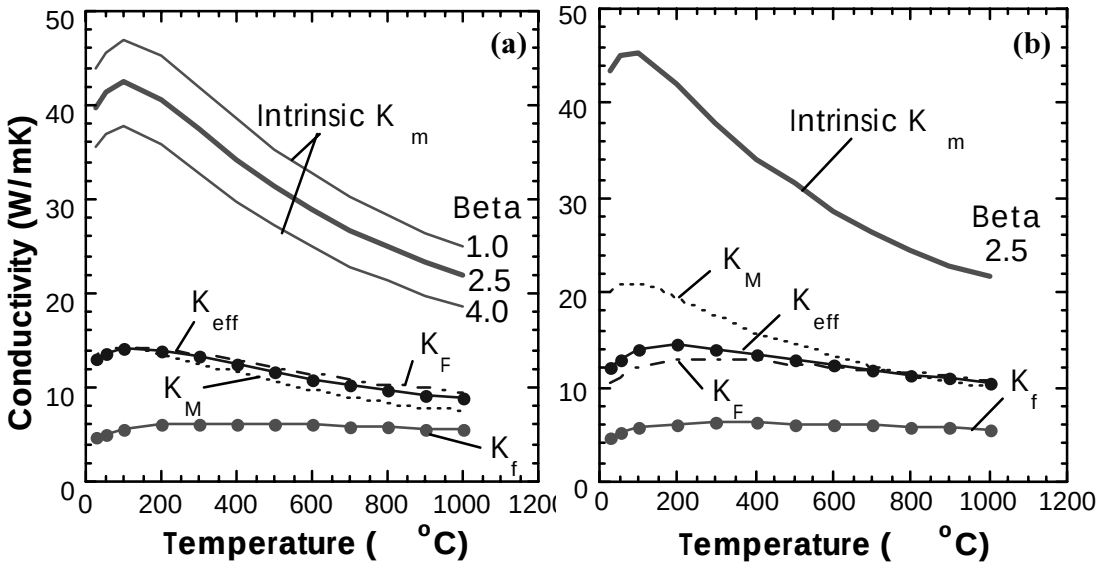

Figure 3. Hierarchical model predictions based on measured values of $K_{eff}(T)$, $K_f(T)$ and the porosity shape factor β for DuPont 2D-Hi Nic/PyC/ICVI-SiC composite versions with (a) "thin" and (b) "thick" PyC fiber coatings. The quantities derived from model fitting are the intrinsic ICVI-SiC matrix conductivity, K_m, and the effective fabric and matrix layer conductivities, K_F and K_M, respectively, as well as $K_c(T)$ that is not shown.

$K_m(T)$ and $K_M(T)$ is relatively unchanged for the range of β-values examined.

The large impact of the matrix porosity content and shape factor is not unexpected, but the hierarchical model is the first time that porosity has realistically been represented in a model for 2D-woven composite. The much smaller intra-bundle, needle-shaped pore content is not expected to exert much influence on $K_{eff}(T)$. Irradiation is expected to affect $K_m(T)$ by the introduction of point defects, but will have little affect on the porosity factor. At the same time, $K_F(T)$ will be affected primarily by thermal f/m decoupling (decrease in h).

FUTURE WORK

Using the hierarchical model, sensitivity studies will be performed to examine other composite systems. In particular, systems made with other SiC fibers (such as Tyranno™ SA with higher $K_f(T)$-values than Hi-Nicalon™) and other SiC-matrices (such as PIP with lower $K_m(T)$-values and different P and β-factors) will be examined. Expected irradiation effects then will be examined for these systems.

ACKNOWLEDGMENTS

The experimental work was funded by the U.S. DOE Fusion Energy Materials program. The model development work was funded by the U.S. DOE Nuclear Energy Research Initiative (NERI) program.

REFERENCES

[1] G. E. Youngblood and R. H. Jones, "The transverse thermal conductivity of 2D-SiC/SiC composites," p. 140 in the 4th IEA workshop on SiC/SiC ceramic matrix composites for fusion structural applications, Eds. B. Riccardi, R. H. Jones and A. Kohyama, October 12-13, 2000, Frascati, Italy.

[2] D. P. H. Hasselman and Lloyd F. Johnson, "Effective thermal conductivity of composites with interfacial thermal barrier resistance," J. Comp. Mater., 21 (1987) 508.

[3] D. P. H. Hasselman, A. Venkateswaran, M. Yu and H. Tawil, "Role of interfacial debonding and matrix cracking in the effective thermal diffusivity of SiC fibre-reinforced chemical vapour deposited SiC matrix composites," J. of Mater. Sci. Lett., 10 (1991) 1037.

[4] A. J. Markworth, "The effective thermal conductivity of a unidirectional fibre composite with fibre-matrix debonding: a calculation based on effective-medium theory," J. Mater. Sci. Lett., 12 (1993) 1497.

[5] G. E. Youngblood, D. J. Senor, R.H. Jones and Witold Kowbel, "Optimizing the transverse thermal conductivity of 2D-SiC/SiC composites, II. Experimental," paper 07A.O3.3 presented at the 10th International Conference on Fusion Reactor Materials, 14-19 October 2001, Baden-Baden, Germany.

[6] Samuel Graham, David L. McDowell, Edgar Lara-Curzio, Ralph B. Dinwiddie and Hsin Wang, "The effects of microstructural damage on the thermal diffusivity of continuous fiber-reinforced ceramic matrix composites," ASTM STP 1392, M.G. Jenkins, E. Lara-Curzio and S.T. Gonczy, Eds., American Society for Testing and Materials, West Conshohocken, PA, 2000.

[7] D. J. Senor, G. E. Youngblood, D. V. Archer and C. E. Chamberlin, "Recent progress in thermal diffusivity testing of SiC-based materials for fusion reactor applications," p. 102 in the 3rd IEA workshop on SiC/SiC ceramic matrix composites for fusion structural applications, Eds. R. H. Jones and A. Kohyama, January 29-30, 1999, Cocoa Beach, Florida.

[8] G. E. Youngblood, D. J. Senor, W. Kowbel, J. Webb and Akira Kohyama, "Thermal conductivity of SiC and C fibers," p. 113 in Fusion Materials Semiannual Progress Report (FMSPR) for period ending December 31, 1999 (DOE/ER-031327).

[9] S. K. Rhee, "Porosity – Thermal conductivity correlations for ceramic materials," Mater. Sci. and Eng., 20 (1975) 89.

[10] G. P. Marino, "The porosity correction factor for the thermal conductivity of ceramic fuels," J. Nucl. Mater., 38 (1971) 178.

EFFECT OF FIBER PROPERTIES ON NEUTRON IRRADIATED SiC/SiC COMPOSITES

T. Hinoki*, A. Kohyama and Y. Katoh (Kyoto University), L.L. Snead (Oak Ridge National Laboratory)

OBJECTIVE

Several kinds of SiC fibers have been developed recently. The objective of this work is to understand the effect of fiber properties on neutron irradiated SiC/SiC composites.

SUMMARY

The use of SiC/SiC composites for nuclear application has recently been considered because of intrinsic low activation and superior high temperature mechanical properties of SiC. The property of SiC fiber is a key issue in order to improve mechanical properties of SiC/SiC composites following irradiation. SiC/SiC composites reinforced with unidirectional fibers were fabricated by chemical vapor infiltration method. Low oxygen and highly crystalline fibers or just low oxygen fibers were used in the composites. The specimens were irradiated at Japan Material Testing Reactor and High Flux Isotope Reactor. The effects of neutron irradiation on mechanical properties were examined by three points flexural test. Microstructure and fracture behavior were observed by scanning electron microscopy before and after neutron irradiation. The SiC/SiC composites reinforced with a low oxygen content, near-stoichiometric atomic composition, and highly crystalline SiC fibers showed the excellent stability to neutron irradiation. The mechanical property of the composites did not degrade, even after neutron irradiation up to 10 dpa, while the other materials reinforced with non-highly crystalline SiC fibers degraded significantly.

PROGRESS AND STATUS

Introduction

The superior high-temperature mechanical properties and low induced radioactivity of SiC/SiC composite make them very attractive as fission and fusion reactor structural materials. [1,2] In fusion reactor environment, nuclear collision and reaction with high-energy neutrons and particles from fusion plasma strongly affect on material properties through the production of displacement damage and transmutation products. [3,4] Degradations of material performance such as mechanical properties, thermal properties etc. are important issues and extensive effort has been conducted. [5]

Interfacial properties between the fiber and matrix of neutron-irradiated SiC/SiC composite influence mechanical performance. [6] This is attributed primarily to shrinkage in the SiC-based fibers due to irradiation-induced recrystallization of microcrystalline fibers [7,8], irradiation-assisted oxidation [9], and potential dimensional changes of carbon [10] interphase applied to the fibers, while matrix swells slightly by irradiation-induced point defect. Fiber shrinkage leads to fiber/matrix debonding as being reported by Snead [11] so that elastic modulus and fracture strength are decreased. Therefore, it is needed to optimize the microstructure of SiC/SiC composite (i.e. fiber, fiber/matrix interphase and matrix) in order to retain interfacial shear strength between fiber and matrix. In order to mitigate radiation effects, development of SiC fiber with lower oxygen content, reduced free carbon and enhanced crystallization is the recent trend. The development of SiC composite with radiation-resistance is based on the use of near stoichiometric SiC fibers with lower oxygen and

* Current affiliation: Oak Ridge National Laboratory

SiC-based interphase. Recently, stoichiometric SiC fibers have been developed such as Hi-Nicalon™ Type-S, [12] Sylramic™ [13] and Tyranno™ SA. [14]

The objective of this work is to understand the effect of fiber properties on neutron irradiated SiC/SiC composite and to improve the stability of SiC/SiC composite under fusion environment. The effects of neutron irradiation on microstructure and mechanical properties were studied.

Experimental

The SiC/SiC composites used in this work were fabricated at the National Research Institute for Metals using Hi-Nicalon™ SiC fibers, Hi-Nicalon™ Type-S advanced SiC fibers, Tyranno™ TE and Tyranno™ ZE. The Type-S fiber contains a reduced amount of oxygen and has near-stoichiometric chemical composition. Representative properties and chemical compositions of the fibers have been compiled in Table 1. The matrix of a unidirectional fiber-reinforced composite was formed by chemical vapor infiltration (CVI). A pyrolitic C interphase was applied to the fibers by CVI prior to the matrix CVI processing. The nominal thickness of the C interphase was 200 nm. The plate size was 40 (diameter) × 2 (thick) mm. The composites were square-cut into 25 (long) × 4 (wide) × 2 (thick) mm bar for the bend bars irradiated at Japan Material Testing Reactor (JMTR) [15], and 15 (long) × 1.5 (wide) × 1.5 (thick) mm bar for the bend bars irradiated at High Flux Isotope Reactor (HFIR) [16]. The composites prepared for JMTR irradiation had an extra SiC layer with approximately 300 μm in thickness, which deposited on the infiltrated SiC/SiC composites.

Table1: Properties of SiC fibers used in this work

SiC Fiber	C/Si Atomic Ratio	Oxygen Content (mass%)	Tensile Strength (GPa)	Tensile Modulus (GPa)	Elongation (%)	Density (Mg/m^3)	Diameter (μm)
Hi-Nicalon	1.39	0.5	2.8	270	1	2.74	14
Hi-Nicalon Type-S	1.05	0.2	2.6	420	0.6	3.1	12
Tyranno TE	1.59	5	3.4	206	1.7	2.55	11
Tyranno ZE	1.52	2	3.5	233	1.5	2.55	11

Neutron irradiations were carried out in the 97M-33U capsule at JMTR, Oarai Research Establishment of Japan Atomic Energy Research Institute, Japan, and in the HFIR 13J capsule at Oak Ridge National Laboratory, USA. In the 97M-33U capsule, a dose equivalent of 1.0×10^{25} nm^{-2} (E>0.1 MeV) = 1.0 dpa was used. The sample temperature was controlled by the combination of gas gap conduction of the nuclear heat and electric heaters. The samples were irradiated at 400 °C. In the HFIR 13J capsule, a dose equivalent of 1.0×10^{26} nm^{-2} (E>0.1 MeV) = 10 dpa was used. The sample temperature was controlled by electric heaters. The samples were irradiated at a constant temperature of 350 °C or 500 °C or in periodically-variable temperature of 300 °C and 500 °C or 200 °C and 350 °C. After irradiation, the capsule was cooled to enough low activation level, and then the capsules were moved to the hotcell and disassembled by the manipulators. Fig. 1 shows the disassembly of the HFIR 13 capsule at the hotcell of ORNL. The samples were then shipped to ORNL LAMDA for observation of the microstructure and flexural tests.

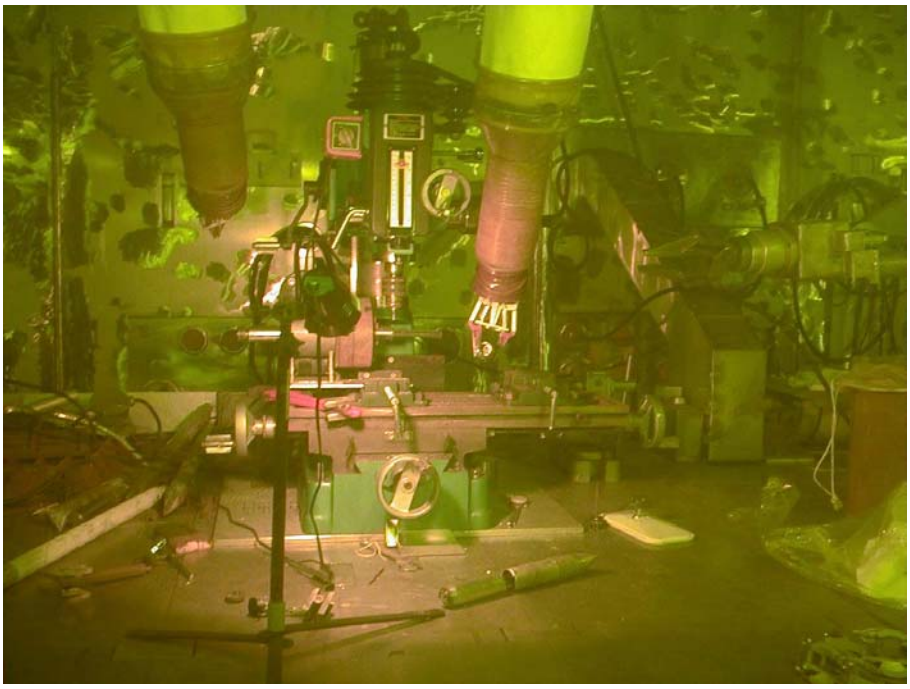

Fig. 1: The disassembly of the HFIR 13J capsule at hotcell of ORNL

Three-point flexural tests were carried out at ambient temperature after the irradiations. The support spans were 18 mm and the crosshead speed was 0.03 mm/sec for the sample irradiated at JMTR 97M-33U. The support spans were 16 mm and the crosshead speed was 0.02 mm/sec for the sample irradiated at HFIR 13J. The size of the bend bar used at JMTR 97M-33U irradiation was

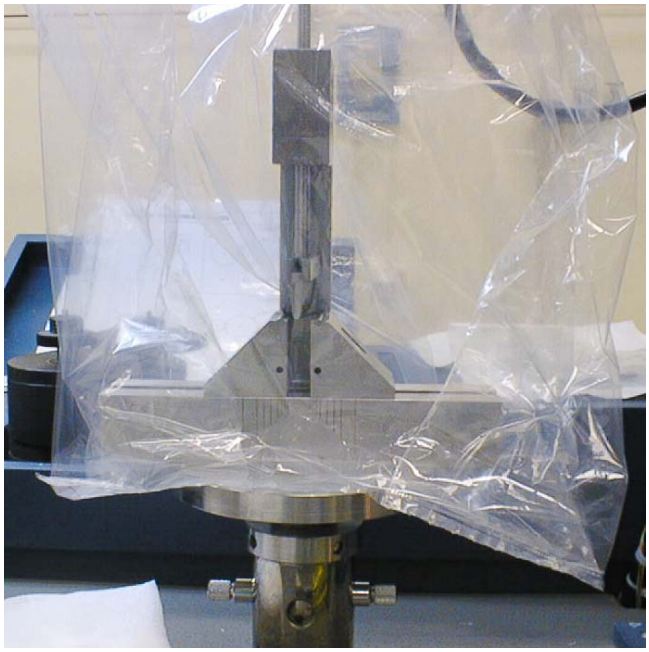

Fig. 2: The flexural test of SiC/SiC composites after neutron irradiation

different from that used at HFIR 13J irradiation because of limitation of each capsule. And different experimental conditions were applied. One of the serious problems to carry out the mechanical tests of SiC/SiC composites after neutron irradiation is the diffusion of the dust during the fracture. The flexural tests were carried out within a plastic bag as shown in Fig. 2.

Effect of neutron irradiation of 97M-33U

Four kinds of the SiC/SiC composites were irradiated. However, three kinds of composites reinforced with Hi-Nicalon, Tyranno TE and Tyranno ZE fibers could not keep their shape following the irradiation as shown in Fig. 3. In marked contrast to the deformed samples, any deformation after

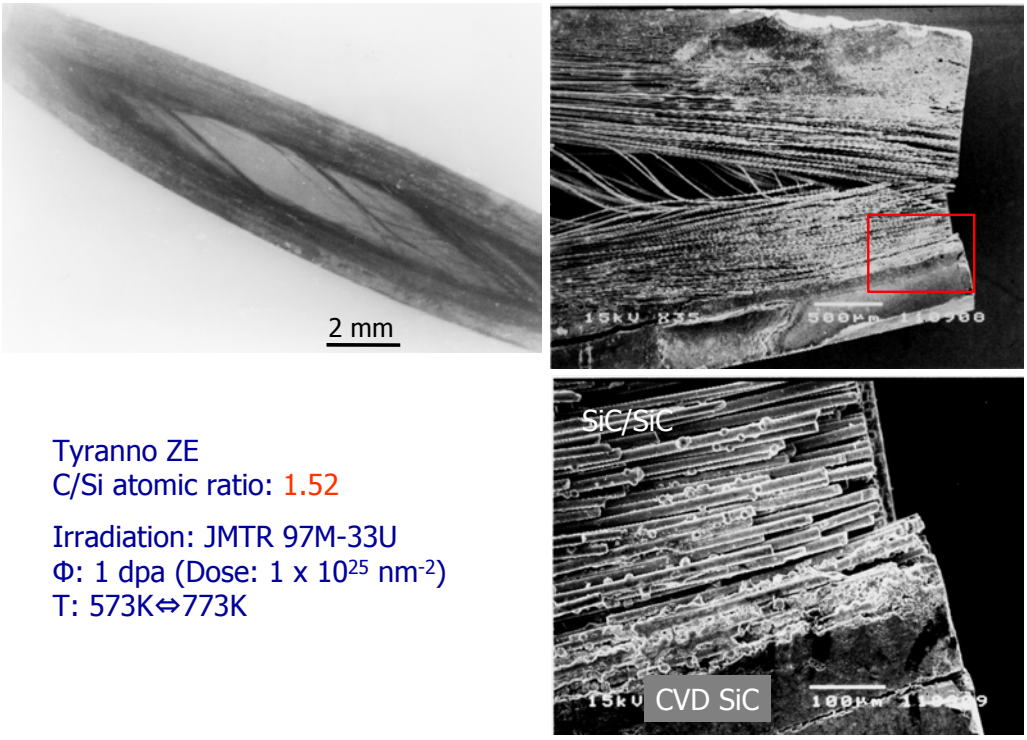

Fig. 3: Effect of neutron irradiation on Tyranno ZE/C/SiC

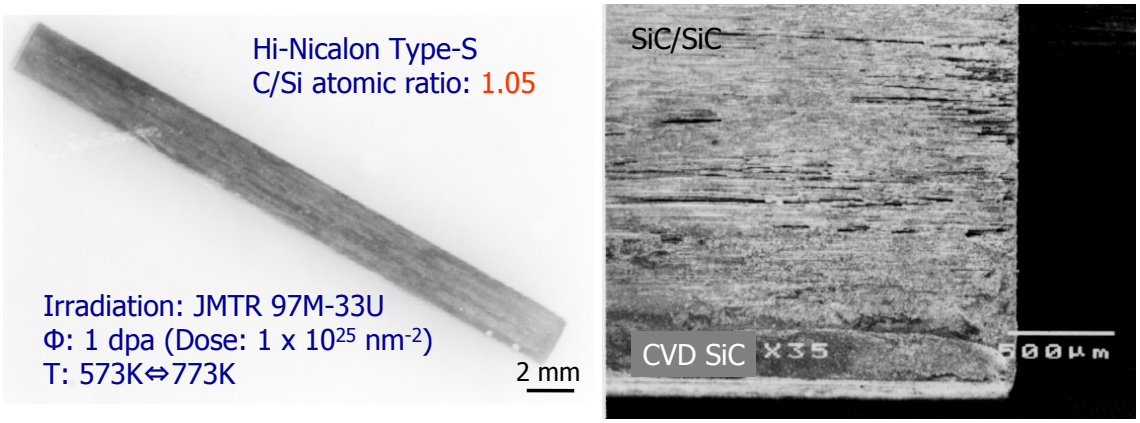

Fig. 4: Effect of Neutron Irradiation on Hi-Nicalon Type-S/C/SiC

the irradiation could not be observed in the SiC/SiC composites reinforced with Hi-Nicalon Type-S fibers as shown in Fig. 4. The composites used in this work had an extra thick SiC layer at one side. The three kinds of fibers used for the deformed composites dose not have near-stoichiometric SiC composition, although they are low oxygen content fibers. The shrinkage of the non-crystalline SiC fiber [9] due to recrystallization [17] and the swelling of β-SiC by neutron irradiation [18] have been reported. So, this deformation was attributed to the mismatch between the fiber shrinkage and β-SiC swelling as illustrated in Fig. 5.

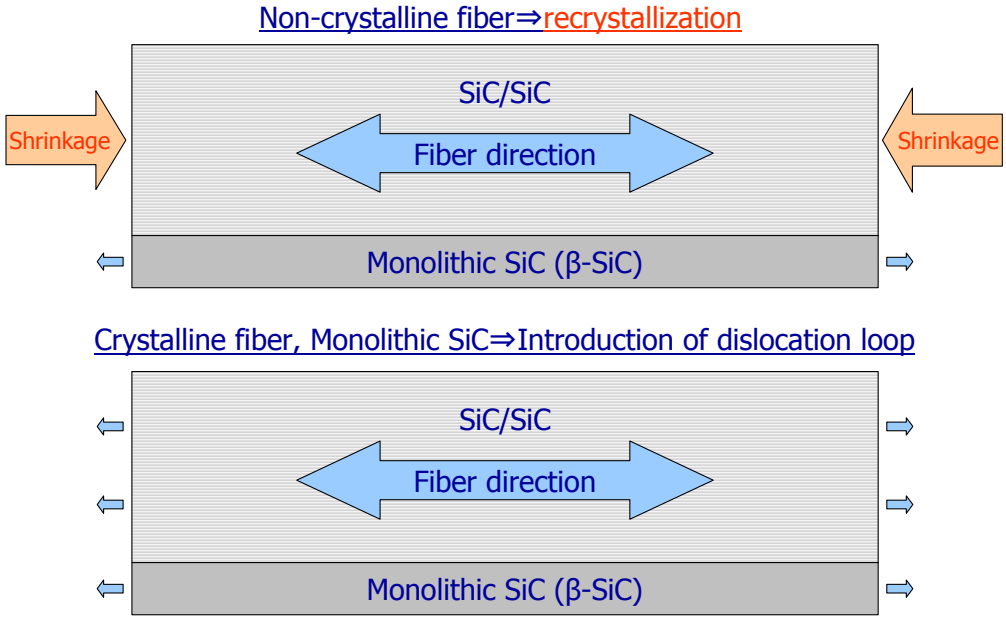

Fig. 5: Deformation mechanism of SiC/SiC composites after neutron irradiation

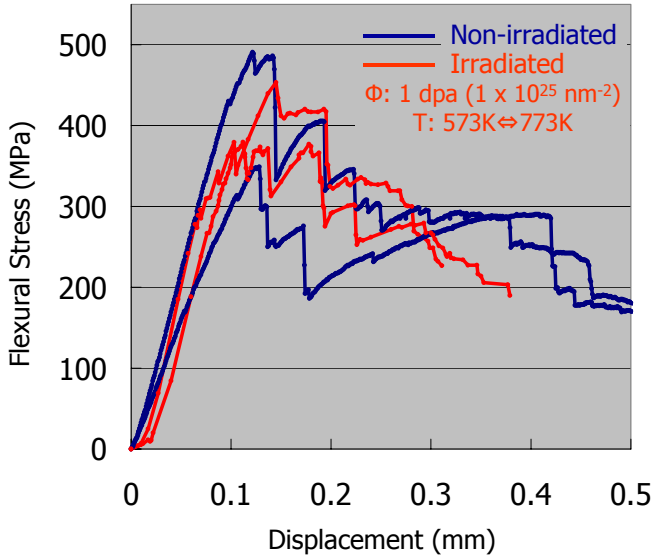

Fig. 6: Effect of Neutron Irradiation on flexural Properties of Hi-Nicalon Type-S/C/SiC

Only the composites reinforced with Hi-Nicalon Type-S fibers were evaluated by flexural tests due to the deformation of the other samples. Fig. 6 shows the effect of the neutron irradiation on the flexural properties of the composites reinforced with Hi-Nicalon Type-S fibers. Clear degradations due to the neutron irradiation were not seen in modulus, proportional limit stress (PLS) and flexural strength. However most of pull-out fibers in the fracture surface of the irradiated composites were separated, respectively, while most of pull-out fibers of the non-irradiated composites were gathering as shown in Fig. 7. And pull-out length of the irradiated sample was longer than that of the non-irradiated sample. The similar results regarding the effect of the neutron irradiation on the mechanical properties of composites reinforced with Hi-Nicalon Type-S were reported in the Ref. 19.

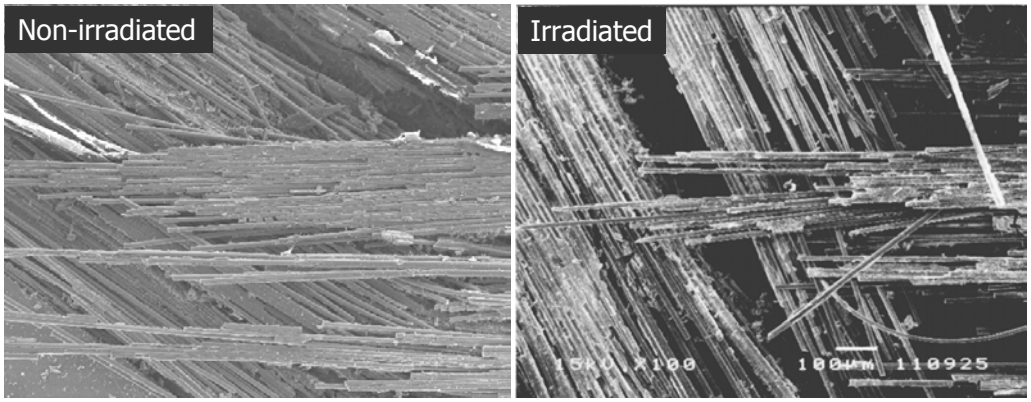

Fig. 7: Comparison of the fracture surface
of the non-irradiated and the irradiated sample with Hi-Nicalon Type-S

Effect of neutron irradiation of HFIR 13J

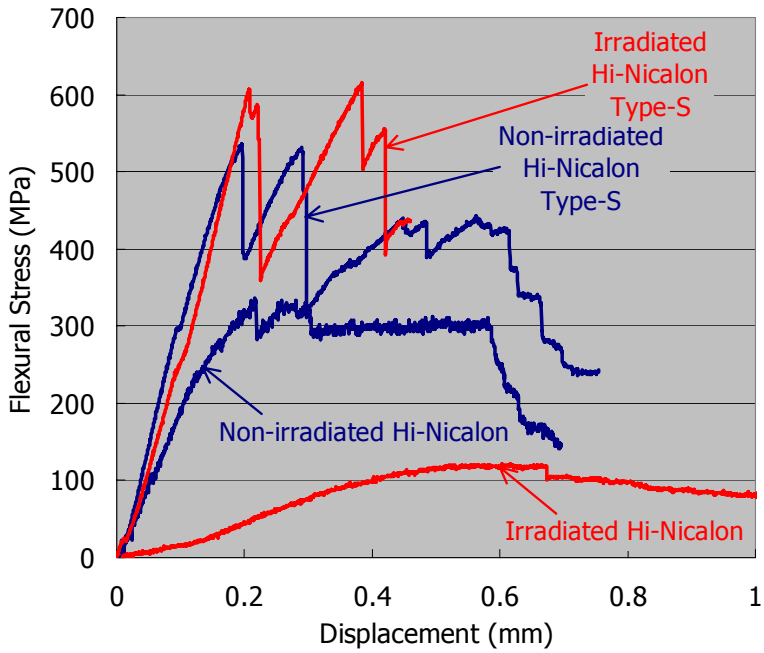

Fig. 8: Effect of neutron irradiation on flexural curves
of SiC/SiC composites with Hi-Nicalon and with Hi-Nicalon Type-S

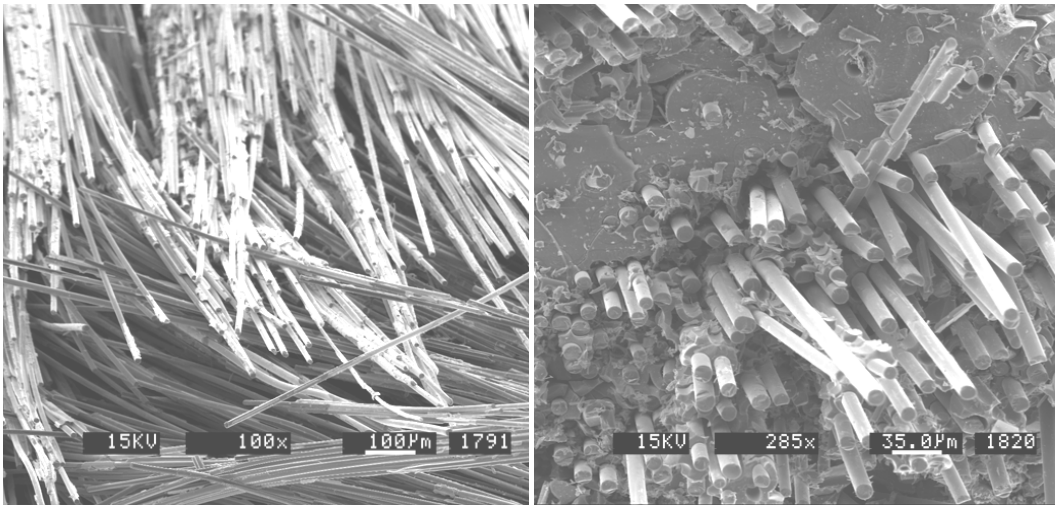

Irradiated Hi-Nicalon sample Irradiated Hi-Nicalon Type-S sample

Fig. 9: Comparison of fracture surface of the irradiated Hi-Nicalon sample and the irradiated Hi-Nicalon Type-S sample

The SiC/SiC composites reinforced with Hi-Nicalon and Hi-Nicalon Type-S fibers were used in this experiment. Effect of the fiber properties on flexural properties of neutron irradiated SiC/SiC composites were evaluated, while some of the composites were deformed or delaminated during the irradiation. Fig. 8 shows a typical example of the effect of neutron irradiation on the flexural curve of SiC/SiC composites. This figure shows that composites reinforced with Hi-Nicalon Type-S fibers was very stable to the neutron irradiation, while composites reinforced with Hi-Nicalon fibers degraded significantly after the neutron irradiation of 10 dpa. The fiber pull-out length of the irradiated composites reinforced with Hi-Nicalon fibers was much longer than that of the irradiated composites

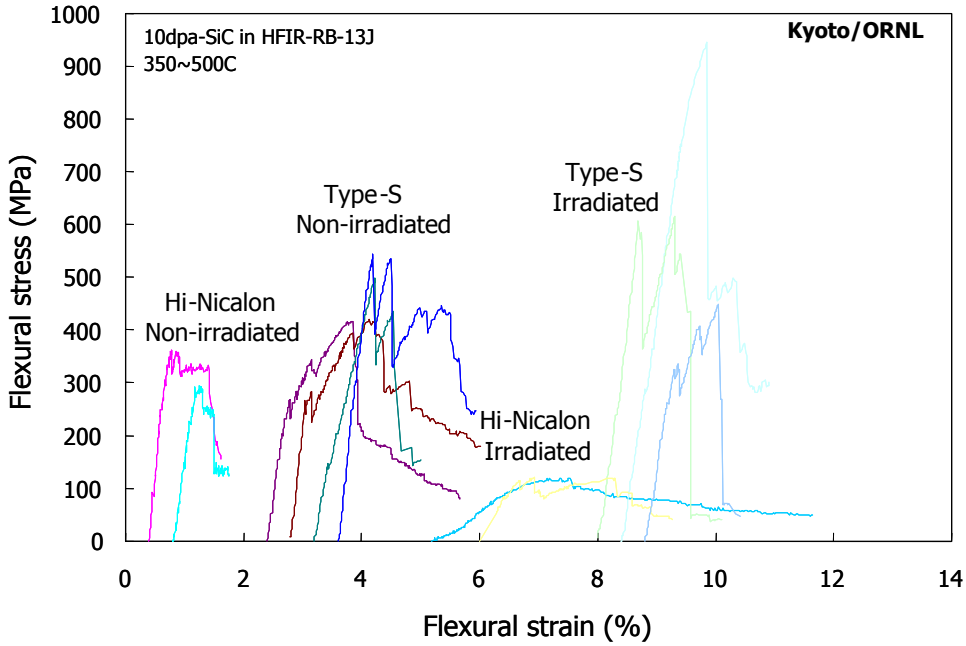

Fig. 10: The entire flexural curve of Hi-Nicalon and Hi-Nicalon Type-S samples prior to and after neutron irradiation

reinforced with Hi-Nicalon Type-S fibers as shown in Fig 9. The entire flexural curves obtained in this work are shown in Fig. 10. A lot of data scatter were seen in this experiment, since the composites used in this work were relatively small, and the composites were prepared three years ago and the quality of the composites were not as high as the present composites. However the obvious neutron irradiation effect was obtained from these data as shown in Fig. 11. In the composites reinforced with Hi-Nicalon fibers, the flexural properties, modulus, PLS and flexural strength were significantly degraded. In marked contrast to the composites reinforced with Hi-Nicalon fibers, the composites reinforced with Hi-Nicalon Type-S fibers showed stable behavior to the neutron irradiation. The average flexural strength improved, while PLS showed a slight degradation.

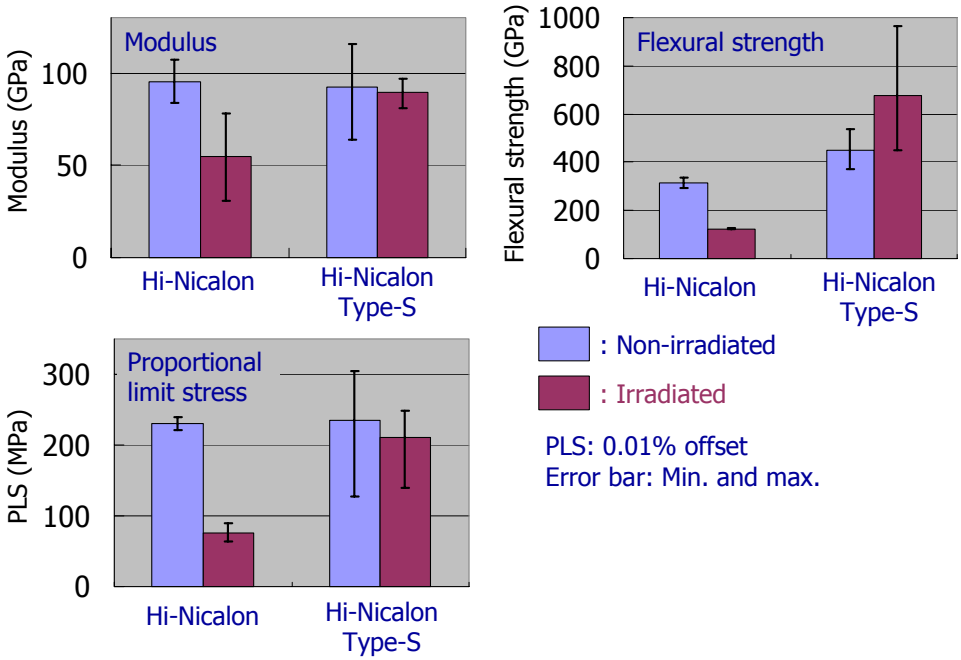

Fig. 11: Summary of the effect of neutron irradiation on flexural properties

Discussions

SiC/SiC composites reinforced with low oxygen SiC fibers which are not near stoichiometric such as Hi-Nicalon and Tyranno TE are anticipated for nuclear application, since it was reported that the low oxygen content fibers showed stability to neutron irradiation compared with commercial grade SiC fiber such as Nicalon and Tyranno Lox M [20]. Even the composites reinforced with these low oxygen content fibers degraded mechanical performance due to mismatch of swelling behavior of the fiber and matrix β-SiC. This mismatch reduced interfacial shear strength significantly. Degradation of interfacial shear strength is also explained by following Eq. (1) and (2) [21,22],

$$\sigma_m = \left(\frac{6\tau G_m V_f^{\,2} E_f E_{cl}^{\,2}}{(1-V_f) E_m^{\,2} r} \right)^{1/3} - \sigma_r \qquad (1)$$

$$h = \frac{\sigma_m^{\,2} r}{2\tau} \qquad (2)$$

where σ_m is the matrix cracking stress, τ is the interfacial shear strength, G_m is the critical mode I

energy release rate, V_f is the volume fraction of the fiber, E_f, E_{cl} and E_m is the modulus of the fiber, the composites and the matrix, r is the fiber radius, σ_r is the residual stress and h is the pull-out length. The matrix cracking stress depends on the proportional limit stress (PLS) and the PLS of the composites reinforced with Hi-Nicalon fibers decreased significantly. And it is reported that the Hi-Nicalon fiber modulus slightly increased and the fiber radius of Hi-Nicalon decreases by the densification after the irradiation [9]. The modulus of CVD SiC is seen to decrease by the irradiation [18,23]. The pull-out length increased a lot by the irradiation. These results mean the significant reduction of the interfacial shear strength of the composites reinforced with Hi-Nicalon fibers.

In the case of the SiC/SiC composites reinforced with Hi-Nicalon Type-S fibers, which are low oxygen content, near stoichiometric atomic composition and highly crystalline, the flexural strength was not decreased by the neutron irradiation. Most of the reasons of the excellent stability to the neutron irradiation are attributed to the similar swelling behavior of the fiber and β-SiC matrix to the neutron irradiation. The significant reduction of the interfacial shear strength as shown in the composites reinforced with Hi-Nicalon fibers was not observed in these composites. The slight degradation of PLS was obtained in the composites reinforced with Hi-Nicalon Type-S fibers, while pull-out length did not change by the neutron irradiation. These results and Eq. (2) suggests the degradation of the interfacial shear strength. The SiC/SiC composites irradiated in this work had C interphase. So alternative interphase which is stable to the irradiation is required.

CONCLUSIONS

The SiC/SiC composites were developed with the newly developed fibers. The effect of the irradiation on mechanical properties was evaluated following the neutron irradiation in several fusion reactors.

The conclusions are;

(1) In the SiC/SiC composites reinforced with low oxygen SiC fiber which is not near stoichiometric SiC, the deformation and the delamination due to the shrinkage of the fibers were observed and the mechanical performance degraded significantly with poor fiber/matrix interfacial properties.
(2) The SiC/SiC composites reinforced with a low oxygen content, near-stoichiometric and highly crystalline SiC fibers showed the excellent stability to neutron irradiation. The mechanical performance of the composites did not degrade, even following the neutron irradiation of 10 dpa.

ACKNOWLEDGEMENT

The authors would like to thank Dr. Noda and Mr. Araki at NRIM for their assistance of material fabrication. Authors also wish to thank Dr. Narui, the other members of IMR Oarai branch of Tohoku University, Mr. Bailey and Dr. Qualls of ORNL for their assistance of post irradiation experiments. This work was supported by Japan-USA Program of Irradiation Test for Fusion Research (JUPITER).

REFERENCES

[1] P. Fenici, A.J. Frias Rebelo, R.H. Jones, A. Kohyama and L.L. Snead, J. Nucl. Mater., 258-263 (1998) 215.
[2] A. Hasegawa, A. Kohyama, R.H. Jones, L.L. Snead, B. Riccardi and P. Fenici, J. Nucl. Mater., 283-287 (2000) 128-137.
[3] L. Giancarli, J.P. Bonal, A. Caso, G. Le Marois, N.B. Morley and J.F. Salavy, Fusion Engineering and Design, 41 (1998) 165-171.
[4] A. Kohyama, M. Seki, K. Abe, T. Muroga, H. Matsui, S. Jitsukawa and S. Matsuda, J. Nucl. Mater., 283-287 (2000) 20-27.
[5] L.L. Snead, R.H. Jones, A. Kohyama and P. Fenici, J. Nucl. Mater., 233-237 (1996) 26-36.
[6] L.L. Snead, M.C. Osborne, R.A. Lowden, J. Strizak, R.J. Shinavski, K.L. More, W.S. Eatherly, J. Bailey and A.M. Williams, J. Nucl. Mater., 253 (1998) 20-30.
[7] A. Hasegawa, G. E. Youngblood and R.H. Jones, J. Nucl. Mater., 231 (1996) 245-248.
[8] M.C. Osborne, C.R. Hubbard, L.L. Snead and D. Steiner, J. Nucl. Mater., 253 (1998) 67-77.
[9] L.L. Snead, M.C. Osborne and K.L. More, J. Mater. Res. 10(3) (1995) 736.
[10] J.H.W. Simmons, Radiation Damage in Graphite, Pergamon Press, (1965).
[11] L.L. Snead, D. Steiner and S.J. Zinkle, J. Nucl. Mater., 191-194 (1992) 566-570.
[12] M. Takeda, A. Urano, J. Sakamoto and Y. Imai, J. Nucl. Mater., 258-263 (1998) 1594-1599.
[13] R.E. Jones, D. Petrak, J. Rabe and A. Szweda, J. Nucl. Mater., 283-287 (2000) 556-559.
[14] T. Ishikawa, Y. Kohtoku, K. Kumagawa, T. Yamamura and T. Nagasawa, Nature, 391 (1998) 773-775.
[15] M. Narui, H. Kurishita, H. Kayano, T. Sagawa, N. Yoshida and M. Kiritani, J. Nucl. Mater., 212-215 (1994) 1665-1670.
[16] A.L. Qualls and T. Muroga, J. Nucl. Mater., 258-263 (1998) 407-412.
[17] Y. Katoh, T. Hinoki, A. Kohyama, T. Shibayama and H. Takahashi, Ceram. Eng. Sci. Proc. 20 [4] (1999) 325-332.
[18] M.C. Osborne, J.C. Hay, L.L. Snead and D. Steiner, J. Am. Ceram. Soc. 82 [9] (1999) 2490-2496.
[19] L.L. Snead, Y. Katoh, A. Kohyama, J.L. Bailey, N.L. Vaughn and R.A. Lowden, J. Nucl. Mater., 283-287 (2000) 551-555.
[20] L.L. Snead and E. Lara-Curzio, Mat. Res. Soc. Symp. Proc., 540 (1999) 273-278.
[21] B. Budiansky, J.W. Hutchinson and A.G. Evans, J. Mech. Phys. Solids, 34 (1986) 167.
[22] R.W. Davidge, in: K. Friedrich (Ed.), Applications of Fracture Mechanics to Composite Materials, Elsevier, New York, (1989) 547.
[23] L.L. Snead, S.J. Zinkle and D. Steiner, J. Nucl. Mater., 191-194 (1992) 560-565.

THE EFFECT OF HIGH DOSE/HIGH TEMPERATURE IRRADIATION ON HIGH PURITY FIBERS AND THEIR SILICON CARBIDE COMPOSITES -

T. Hinoki and L.L. Snead (Oak Ridge National Laboratory), Y. Katoh, T. Nozawa and A Kohyama (Kyoto University), A. Hasegawa (Tohoku University)

OBJECTIVE

The objective of this work is to understand the effect of high dose/high temperature neutron irradiation on high purity silicon carbide fiber and their silicon carbide composites.

SUMMARY

Silicon carbide composites were fabricated by chemical vapor infiltration method with high purity fiber, Hi-Nicalon Type-S and Tyranno SA and non-high purity fiber Hi-Nicalon. SiC/SiC composites, bare fibers and CVD SiC were irradiated at 7.7 dpa and 800 °C or 6.0 dpa and 300 °C. The density of fiber and CVD SiC was measured by gradient column technique. Mechanical properties of the composites were evaluated by four-point flexural tests. Fracture surfaces were observed by SEM. Tyranno SA fiber and CVD SiC showed similar swelling behavior following irradiation at 7.7 dpa and 800 °C. Mechanical properties of Hi-Nicalon Type-S samples and Tyranno SA samples were stable even following neutron irradiation at 7.7 dpa and 800 °C. Fracture surfaces of these samples following irradiation were similar to those of unirradiated samples with relatively short fiber pull-out.

PROGRESS AND STATUS

Introduction

The superior high temperature mechanical properties and low activation make SiC/SiC composites very attractive as fission and fusion reactor materials [1,2]. The higher thermal efficiency associated with gas-cooled solid blanket, where potential plant efficiency is 50 %, can be available in the fusion blanket using SiC/SiC composites [3]. In fusion reactor environment, nuclear collisions and reactions with high-energy neutrons and particles from fusion plasma have strong impacts on materials through the production of displacement damage and transmutation effects [4]. Degradation of material performance such as mechanical properties, thermal properties and so on has been recognized as the key issues and extensive efforts have been conducted [5].

Up to this point, interfacial properties between the fiber and matrix of neutron-irradiated SiC/SiC composites limited mechanical performance [6] This limitation has been attributed primarily to shrinkage in the SiC-based fibers due to irradiation-induced recrystallization of microcrystalline fibers [7,8], irradiation-assisted oxidation [9], and potentially large dimensional changes of the graphite [10] interphase applied to the fibers, while matrix swells a little by irradiation-induced point defect. Fiber shrinkage leads to fiber/matrix debonding as reported by Snead [11] and a decrease in elastic modulus and fracture strength. Therefore, there is a critical need to optimize the microstructure of SiC/SiC composites (i.e. fiber, fiber/matrix interphase and matrix) to retain the interfacial shear strength between the fiber and matrix. To mitigate radiation effects, the recent trend in SiC fiber development is toward lower oxygen content, reduced free carbon and enhanced crystallinity. The development of more radiation-resistant SiC composites is based on the use of near stoichiometric SiC fibers with lower oxygen and SiC-based interphases. Recently, near stoichiometric SiC fibers have been developed including Hi-Nicalon™ Type-S [12], Sylramic™ [13]

and Tyranno™ SA [14]. However the effect of high dose and high temperature irradiation, in which void driven swelling may occur, on the SiC/SiC composites with highly crystalline fibers was not revealed yet.

The objective of this work is to improve the stability of SiC/SiC composites under fusion environment. For this purpose, the effects of high dose and high temperature neutron irradiation on mechanical properties of SiC/SiC composites with high purity fiber were evaluated.

Experimental procedure

The fibers used in this work were Tyranno™ SA (Ube Industries Ltd., Ube, Japan), Hi-Nicalon Type-S, and Hi-Nicalon™ SiC fibers (Nippon Carbon Co., Tokyo, Japan). Both satin woven and plain woven fibers were used to fabricate composites with orientation of 0/90°±30°. Tyranno SA and Hi-Nicalon Type-S fibers contain a reduced amount of oxygen and a near-stoichiometric chemical composition and consist of β -SiC polycrystalline structures while another low oxygen fiber, Hi-Nicalon has excess carbon and does not have highly crystalline structure compared with Tyranno SA and Type-S. Representative properties and chemical compositions of the fibers [12,15] reported by the manufactures are compiled in Table 1. Note Tyranno SA fiber used in this work was the first trial piece. Tyranno SA fiber has been improved and the mechanical properties of a current fiber are different from those of the Tyranno SA fiber used in this work. The matrix of composite was formed by forced-flow thermal-gradient chemical vapor infiltration (FCVI) method [16] at Oak Ridge National Laboratory. A pyrolitic carbon interphase was applied to the fibers by CVI prior to the matrix processing. The nominal thickness of the interphase was 150 nm and 500 nm. The properties of materials used in this work are summarized in Table 2.

Table1: The properties of fibers used in this work

SiC Fiber	C/Si Atomic Ratio	Oxygen Content (wt%)	Tensile Strength (GPa)	Tensile Modulus (Gpa)	Elongation (%)	Density (g/cm3)	Diameter (μm)
Tyranno SA	1.07	<0.5	1.8	320	0.7	3.02	10
Hi-Nicalon Type-S	1.05	0.2	2.6	420	0.6	3.1	12
Hi-Nicalon	1.39	0.5	2.8	270	1.0	2.74	14

Neutron irradiation was carried out in the HFIR 14J capsule at Oak Ridge National Laboratory, USA. The fluence and temperature of the irradiation were 7.7×10^{25} nm^{-2} (E>0.1 MeV) at 800 °C and 6.0×10^{25} nm^{-2} (E>0.1 MeV) at 300 °C. The sample temperature was controlled by electric heaters.

Density was measured using density gradient column as shown in Fig. 1 and chemicals were mixed to generate a column. The column with a density range between 2.90 and 3.10 g/cm^3 was mixed with bromoform and diiodomethane. Following a HF bath at room temperature to remove any surface silica, Samples were dropped into the column. When the sample position was stable, accurate density was measured.

Table2: The properties of samples used in this work

Fiber	Woven type	C thickness (nm)	Irra. temp. (°C)
Tyranno SA	Plain woven	150	800
Tyranno SA	Satin woven	150	300, 800
Hi-Nicalon Type-S	Plain woven	150	300, 800
Hi-Nicalon Type-S	Satin woven	150	300, 800
Hi-Nicalon Type-S	Satin woven	500	300
Hi-Nicalon	Plain woven	150	800

The composites were square-cut into 30 (long) × 6.0 (wide) × 2.2 (thick) mm bar for the flexural tests. Four-point flexural tests were carried out at ambient temperature prior to and after the irradiations. The support span and the loading span were 20 mm and 5 mm. The crosshead speed was 0.51 mm/min. Fracture surfaces were observed by SEM following the flexural tests.

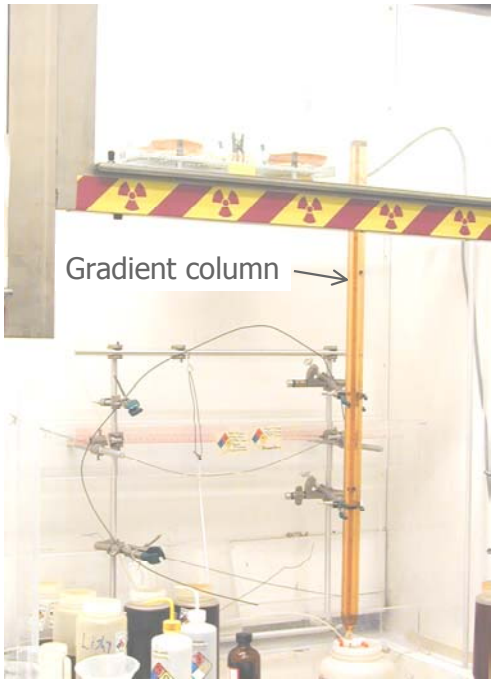

Fig. 1: Gradient column

Results

Figs 2~4 show the effect of neutron irradiation on strain-stress behavior of the four point flexural tests of SiC/SiC composites with plain woven fibers. Both composites reinforced with Hi-Nicalon Type-S fibers and Tyranno SA fibers were stable to neutron irradiations compared with composites

reinforced with Hi-Nicalon fibers although the composites reinforced with Tyranno SA fibers had a large scatter in the non-irradiated composites. As mentioned in previous section the Tyranno SA fiber used in this work was the first trial piece, so there was scatter in grain size and mechanical properties. The non-irradiated strength of composites reinforced with Tyranno SA fibers used in this work was less than the recent composites reinforced with Tyranno SA fibers. However the average proportional limit stress and average flexural strength of Tyranno SA samples were almost same in between the non-irradiated samples and the irradiated samples. It was obvious that mechanical properties of composites reinforced with Hi-Nicalon fibers degraded following neutron irradiation and composites reinforced with Hi-Nicalon Type-S fibers were very stable to neutron irradiation.

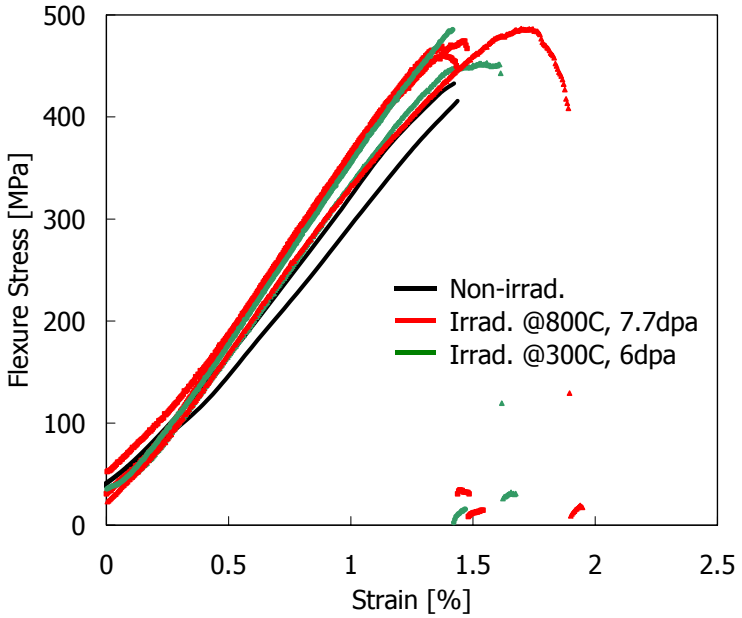

Fig. 2: Effect of irradiation on flexural behavior of Hi-Nicalon Type-S (P/W) samples

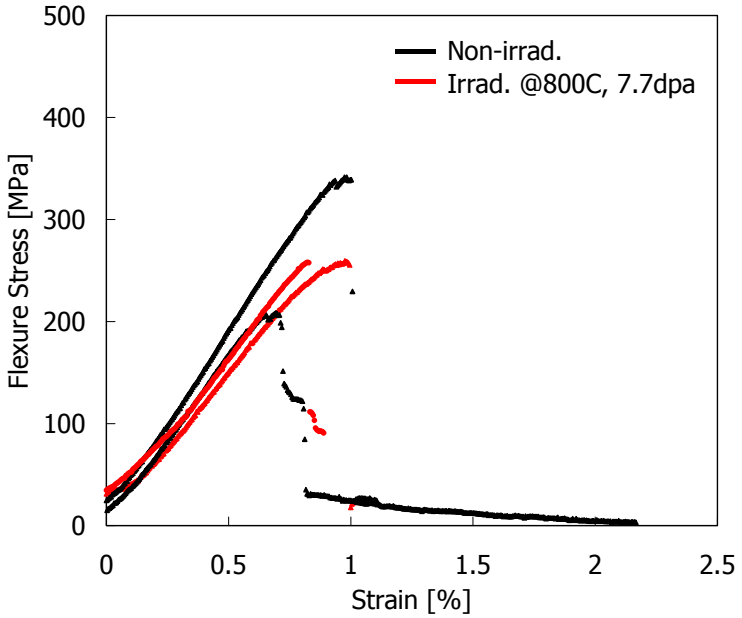

Fig. 3: Effect of irradiation on flexural behavior of Tyranno SA (P/W) samples

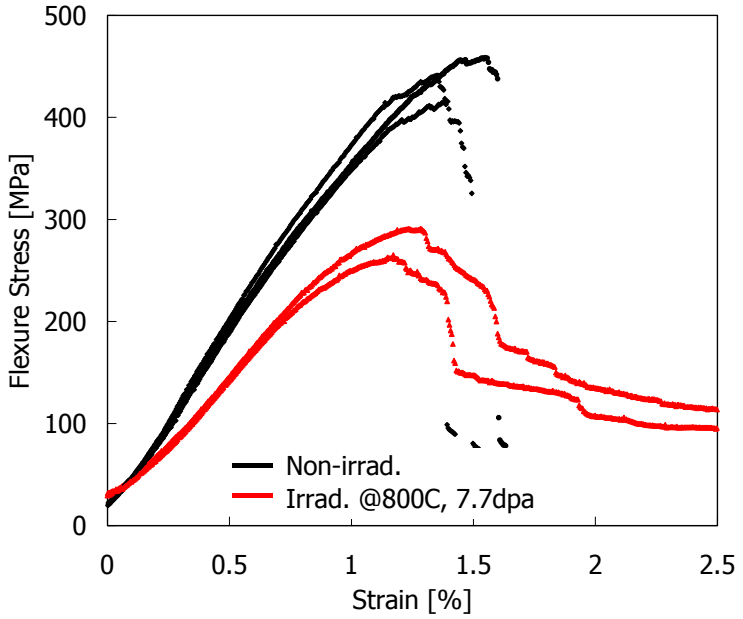

Fig. 4: Effect of irradiation on flexural behavior of Hi-Nicalon (P/W) samples

Figs. 5 show the fracture surface of composites reinforced with Hi-Nicalon Type-S and Tyranno SA fibers following irradiation at 800 °C. In the previous composites containing off-stoichiometric SiC fibers such as Nicalon, Tyranno Lox M and Hi-Nicalon, significantly long fiber pull-out with more than several hundred μm length was seen following irradiation [6,17]. However in the composites reinforced with Hi-Nicalon Type-S fibers, fiber pull-out was relatively short and seemed almost same with non-irradiated composites even following 10 dpa irradiation. Composites reinforced with Tyranno SA fibers showed brittle fracture surface and seemed almost same with the non-irradiated composites, too.

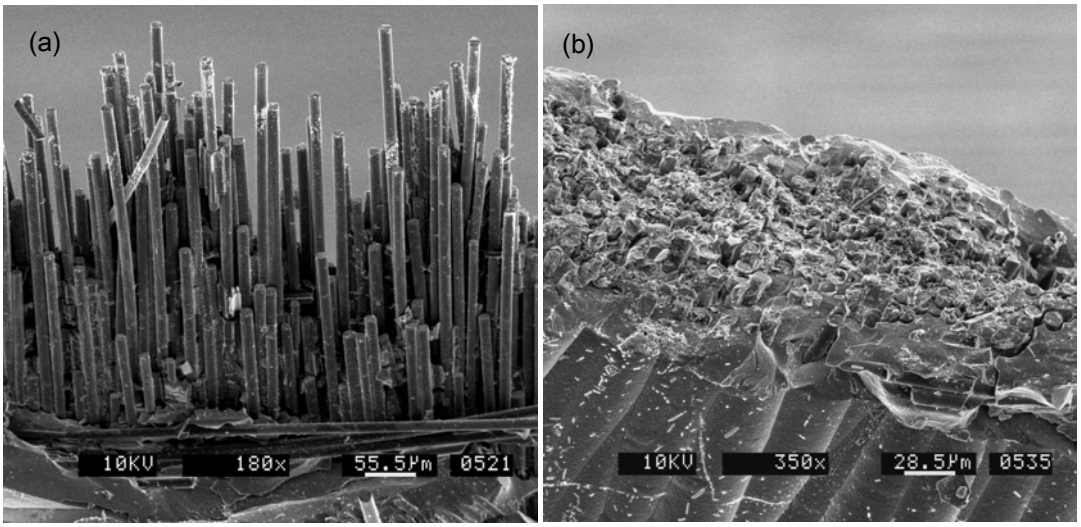

Fig. 5: Fracture surface of Hi-Nicalon Type-S sample (a) and Tyranno SA sample (b) following the irradiation at 800 °C

Mechanical properties of SiC/SiC composites following irradiation at 800 °C and at 300 °C are compared with those prior to the irradiation in Figs. 6 and 7. The Figs show the relative values, i.e. the value after irradiation/the value prior to irradiation, of modulus, proportional limit stress (PLS) obtained from 0.01% strain offset and flexural strength. Error bars show maximum and minimum values. The composites reinforced with Type-S fibers and Tyranno SA fibers with plain weave fabric kept their flexural strength following irradiation, while the composites reinforced with Hi-Nicalon fibers decreased. Most of PLS decreased following the irradiation at 800 °C, while they are increased following the irradiation at 300 °C. In all composites, the elastic modulus was decreased following the irradiation with the exception of the composites reinforced with Hi-Nicalon Type-S plain weave fabric.

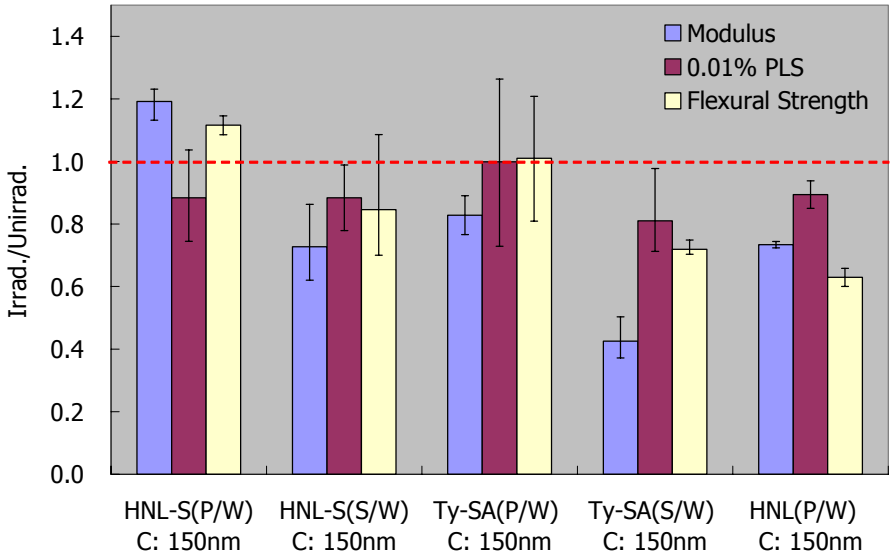

Fig. 6: Effect of irradiation at 7.7 dpa and 800 °C on mechanical properties

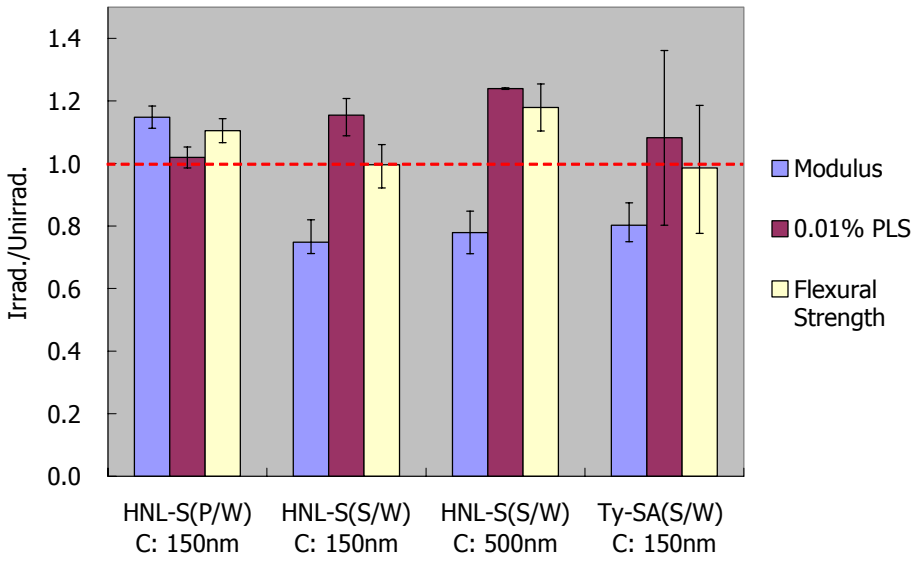

Fig. 7: Effect of irradiation at 6.0 dpa and 300 C on mechanical properties

Normalized density change of Tyranno SA fiber and CVD SiC irradiated at 7.7 dpa and 800 °C are shown in Fig. 8 with those of previous fibers, Nicalon and Hi-Nicalon and CVD SiC irradiated at 150 °C. Tyranno SA fiber swelled slightly following irradiation, while the other fibers underwent radiation-induced densification. The normalized density change of Tyranno SA was very similar to that of CVD SiC irradiated at same condition.

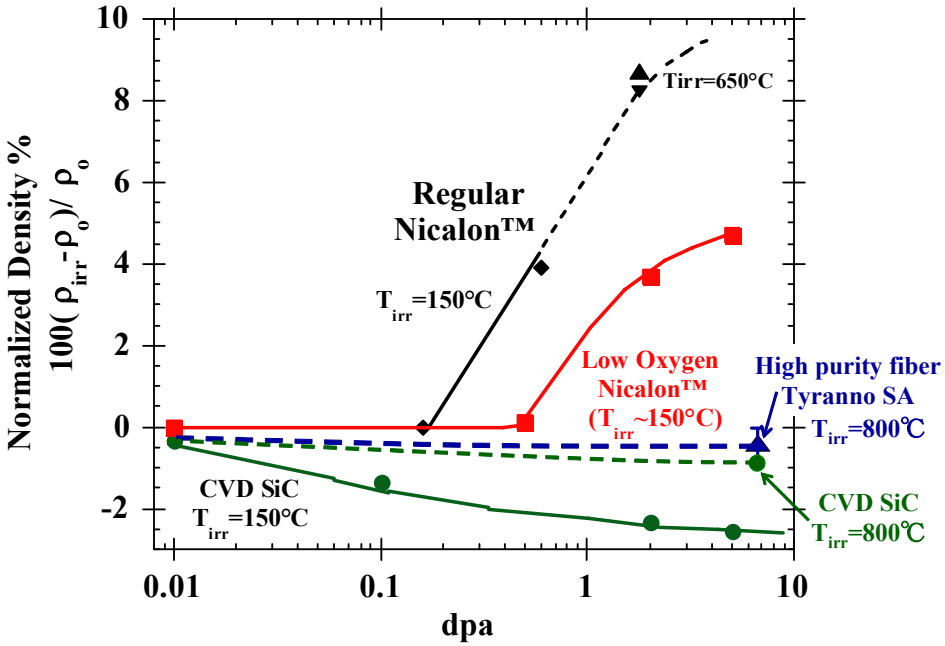

Fig. 8: Relative density change of SiC fibers and CVD SiC by neutron irradiation

Discussions

Both composites reinforced with Hi-Nicalon Type-S and Tyranno SA fibers showed stable mechanical properties to even high dose and high temperature irradiation. Of particular note, the fracture behavior was completely different from previous composites reinforced with non-high purity fiber. In composites reinforced with previous fibers, the samples fractured with long fiber pull-out following irradiation due to debonding of fiber/matrix interface. However, composites reinforced with Hi-Nicalon Type-S and Tyranno SA fibers fractured with relatively short fiber pull-out, and the fracture behavior of the composites following irradiation was similar with that of non-irradiated composites. Composites reinforced with Tyranno SA fibers showed brittle fracture behavior even following irradiation. This fracture behavior is not ideal for composite materials. However, it was completely different from previous composites after irradiation. It is not difficult to reduce interfacial shear strength to improve mechanical properties. And composites reinforced with Tyranno SA fibers have a good potential to be improved by optimum condition of fiber/matrix interphase.

Similar fracture behavior between irradiated composites and unirradiated composites with relatively short fiber pull-out is attributed to similar swelling behavior between the fiber and matrix. As shown in Fig. 8, there was a large mismatch of swelling between previous fiber such as Nicalon and Hi-Nicalon and CVD SiC. This mismatch caused fiber/matrix interfacial debonding and reduced mechanical properties with long fiber pull-out. Normalized density of Tyranno SA is quite similar to

CVD SiC irradiated at same condition. That is the reason that both composites reinforced with Hi-Nicalon Type-S and Tyranno SA fibers retain their fiber/matrix integrity and mechanical properties.

Another advantage of composites reinforced with high purity fibers is that the swelling of CVD SiC saturates at less than irradiation of 10 dpa at irradiation temperature <1000 °C [18,19] while the displacement damage of saturation depends on the irradiation temperature. At temperatures lower than 1000 °C, SiC swells by accumulation of point defects in the lattice. This swelling phenomenon saturates at lower damage levels and the total swelling decreases with increasing temperature. It was showed that void driven swelling, which would not saturate but increase monotonically with irradiation damage, does not occur below about 1000 °C [20]. These results suggest that the SiC/SiC composites reinforced with reduced oxygen contents and near stoichiometric atomic composition fibers might be stable to higher neutron irradiation above 10 dpa. The stability to neutron irradiation of the SiC/SiC composites reinforced with various SiC fibers is summarized in Fig. 9. Error bars show maximum and minimum values. It is obvious that SiC/SiC composites reinforced with high purity fibers were significantly improved for irradiation resistance compared with previous composites reinforced with non-high purity fibers.

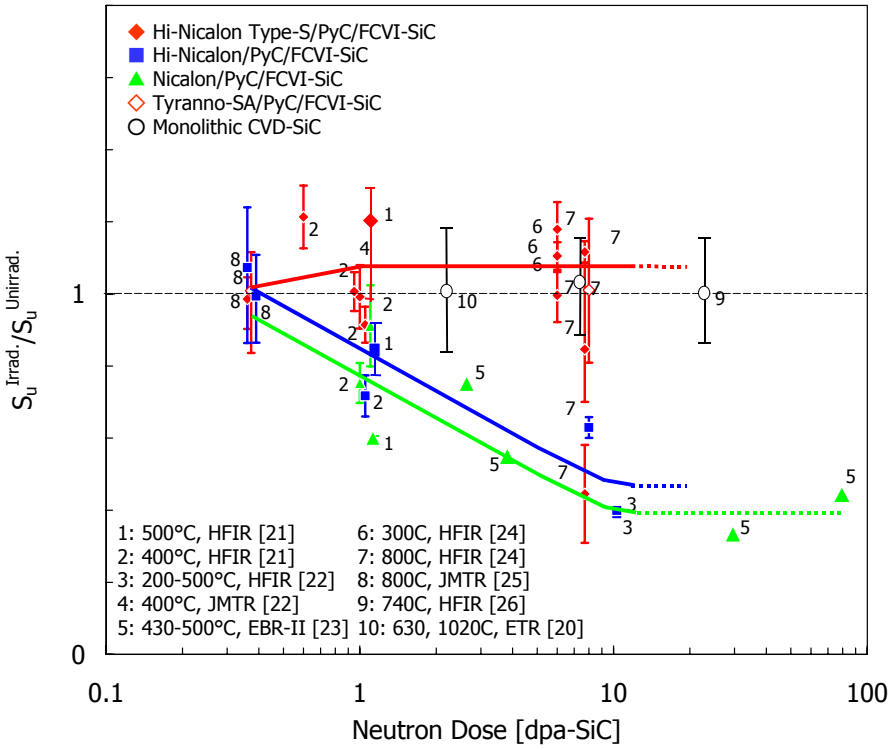

Fig. 9: Irradiation Effect on Flexural Strength of SiC/SiC

In most of samples, degradation of modulus was seen, while proportional limit stress and flexural strength were retained following irradiation. The degradation of modulus of CVD SiC following irradiation has been reported [27,28] and considered that the degradation is inversely proportional to the amount of swelling. In the samples used in this work, it is considered that both fiber and matrix swelled and the modulus of both fiber and matrix decreased.

CONCLUSIONS

1. Stoichiometric fibers are dimensionally stable to doses and temperatures of this study like CVD SiC.
2. The SiC/SiC composites with high purity fiber showed stable mechanical properties to high dose (7.7 dpa)/high temperature(800 °C) irradiation.

Typically, mechanical properties of ceramics saturate by a few dpa. Perhaps this indicates that composite will be stable to much higher dpa.

ACKNOWLEDGEMENT

The authors would like to thank Lou Qualls and Jeff Bailey for assistance with the irradiation. This work was supported by Japan-USA Program of Irradiation Test for Fusion Research (JUPITER).

REFERENCES

[1] P. Fenici, A.J. Frias Rebelo, R.H. Jones, A. Kohyama and L.L. Snead, J. Nucl. Mater., 258-263 (1998) 215.
[2] A. Hasegawa, A. Kohyama, R.H. Jones, L.L. Snead, B. Riccardi and P. Fenici, J. Nucl. Mater., 283-287 (2000) 128-137.
[3] A. Kohyama, M. Seki, K. Abe, T. Muroga, H. Matsui, S. Jitsukawa and S. Matsuda, J. Nucl. Mater., 283-287 (2000) 20-27.
[4] L. Giancarli, J.P. Bonai, A. Caso, G. Le Marois, N.B. Morley and J.F. Salavy, Fusion Engineering and Design, 41 (1998) 165-171.
[5] L.L. Snead, R.H. Jones, A. Kohyama and P. Fenici, J. Nucl. Mater., 233-237 (1996) 26-36.
[6] L.L. Snead, M.C. Osborne, R.A. Lowden, J. Strizak, R.J. Shinavski, K.L. More, W.S. Eatherly, J. Bailey and A.M. Williams, J. Nucl. Mater., 253 (1998) 20-30.
[7] A. Hasegawa, G. E. Youngblood and R.H. Jones, J. Nucl. Mater., 231 (1996) 245-248.
[8] Y. Katoh, T. Hinoki, A. Kohyama, T. Shibayama and H. Takahashi, Ceram. Eng. Sci. Proc., 20 [4] (1999) 325-332.
[9] L.L. Snead M.C. Osborne and K.L. More, J. Mater. Res. 10(3) (1995) 736.
[10] J.H.W. Simmons, Radiation Damage in Graphite, Pergamon Press, (1965).
[11] L.L. Snead, D. Steiner and S.J. Zinkle, J. Nucl. Mater., 191-194 (1992) 566-570.
[12] M. Takeda, A. Urano, J. Sakamoto and Y. Imai, J. Nucl. Mater., 258-263 (1998) 1594-1599.
[13] R.E. Jones, D. Petrak, J. Rabe and A. Szweda, J. Nucl. Mater., 283-287 (2000) 556-559.
[14] T. Ishikawa, Y. Kohtoku, K. Kumagawa, T. Yamamura and T. Nagasawa, Nature, 391 (1998) 773-775.
[15] K. Kumagawa, H. Yamaoka, M. Shibuya and T. Yamamura, Ceram. Eng. Sci. Proc., 18 [3] (1997) 113-118.
[16] T.M. Besmann, E.R. Kupp, E. Lara-Curzio and K.L. More, J. Am. Ceram. Soc., 83 [12] (2000) 3014-20.
[17] T. Hinoki, Y. Katoh and A. Kohyama, Proc. PRICM4, (2001) in press.
[18] L.L. Snead and J.C. Hay, J. Nucl. Mater., 273 (1999) 213-220.
[19] H. Kishimoto, Y. Katoh, A. Kohyama, M. Ando, H. Tanigawa and K. Jimbo, Proc. 4th IEA workshop on SiC/SiC Ceramic Matrix Composites for Fusion Structural Applications, Oct., 2000, Frascati, Italy, (2000) 59-66.
[20] R.J. Price, J. Nucl. Mater. 33 (1969) 17-22.

[21] L.L. Snead, Y. Katoh, A. Kohyama, J.L. Bailey, N.L. Vaughn and R.A. Lowden, J. Nucl. Mater., 283-287 (2000) 551-555.
[22] T. Hinoki, Y. Katoh and A. Kohyama, Mater. Trans., (2002) to be published.
[23] R.H. Jones, et al., 1st IEA-SiC/SiC (1996).
[24] T. Hinoki, L.L. Snead, Y. Katoh, A. Hasegawa, T. Nozawa and A Kohyama, J. Nucl. Mater., (2002) to be published.
[25] T. Nozawa, T. Hinoki, Y. Katoh and A. Kohyama, J. Nucl. Mater., (2002) to be published.
[26] R.J. Price, et al., J. Nucl. Mater., 108-109 (1982) 732-738.
[27] L.L. Snead, S.J. Zinkle and D. Steiner, J. Nucl. Mater., 191-194 (1992) 560-565.
[28] M.C. Osborne, J.C. Hay, L.L. Snead and D. Steiner, J. Am. Ceram. Soc., 82 [9] (1999) 2490-2496.

3.0 FERRITIC/MARTENSITIC STEELS

EXAMINATION OF POSTIRRADIATION DEFORMATION MICROSTRUCTURES IN F82H –
D. S. Gelles (Pacific Northwest National Laboratory)* and R. Schäublin (EPFL-CRPP Fusion Technology, Switzerland)

OBJECTIVE

The objective of this effort is to provide further understanding of postirradiation deformation mechanisms controlling in ferritic/martensitic steels.

SUMMARY

The deformed microstructures of irradiated F82H uniaxial tensile specimens have been examined following irradiation in the High Flux Reactor (HFR) to 2.6 dpa at 327ºC in order to identify controlling mechanisms. Deformation following irradiation is found to occur in poorly defined channels, causing formation of discrete steps at surfaces, similar to that in unirradiated steel. Deformation is by motion of individual $\frac{a}{2}$<111> dislocations.

PROGRESS AND STATUS

Introduction

In a previous report on post-irradiation deformation behavior in ferritic/martensitic steels, results were obtained for an Fe-9Cr binary alloy irradiated in the FFTF at 370 and 400ºC to 10 and 40 dpa, respectively.[1] Behavior was compared to that in the unirradiated control material. It was found in both cases that deformation following irradiation occurred in poorly defined channels, causing formation of discrete steps at surfaces and delineated by nonuniformly distributed highly elongated voids. Deformation was by motion of $\frac{a}{2}$<111> dislocations, which interacted with and decomposed irradiation-induced a<100> loops. The structure formed after extensive deformation consists of highly complex cell walls and moderate densities of individual slip dislocations. In comparison, behavior for unirradiated samples gave surface steps that were poorly delineated and dislocation tangles with no obvious evidence of channeling.

The present effort is intended to extend those results to more complex steels. The work is based on F82H miniature tensile specimens recently irradiated in HFR in Petten, The Netherlands.

Experimental Procedure

Miniature sheet tensile specimens of F82H with nominal gauge dimensions of 5.1 mm x 0.25 mm x 1.0 mm were irradiated in the HFR up to a calculated dose level of ~2.6 dpa, and were tested to provide understanding of postirradiation deformation response in reduced activation steels.[2] Composition details are provided in Table 1.

Table 1. Chemical composition of F82H heat 9741.

C	Si	Mn	P	S	Cr	Ni	Mo	N
0.09	0.11	0.16	0.002	0.002	7.71	0.02	0.003	0.006
Cu	Co	Ta	B	Ti	Nb	V	Al	W
0.01	0.005	0.02	0.0002	0.01	0.0001	0.16	0.003	1.95

Irradiation details are as follows: irradiation vehicle: CHARIOT-2, a basket-type sample holder; target dpa: 2.5; actual dpa: 2.57; Thermal fluence; 1.53 dpa; Fast Fluence: 1.85 $x10^{25}$ n/m^2;

*Pacific Northwest National Laboratory (PNNL) is operated for the U.S. Department of Energy by Battelle Memorial Institute under contract DE-AC06-76RLO-1830.

Target temperature: 300°C; Actual temperature estimated: 320-335°C; for 150 full power days ending March, 1997. (TEM disks were also included and underwent the following irradiation details: actual dpa: 2.84; Thermal fluence: 1.77 dpa; Fast Fluence: 2.05 x10^{25}n/m^2; Target temperature:300°C; Actual temperature estimated: 324-340 °C.)

Flat surfaces of sheet tensile specimens were mechanically polished to Linde 600 grit and then deformed at room temperature either to failure on the first test or to about 3% for the remaining specimens. Testing details are provided in Table 2 with elongation estimated from test traces. However, the test trace for specimen II was unusual, probably a result of slipping in the grips, and the test trace was so interpreted.

Table 2. Test Details for Deformed Tensile Specimens.

Specimen ID	Condition (°C)	Yield (MPa)	Max. load (MPa)	Elongation (%)
I	2.57 dpa at 327	626	653	0.6 UE, 5.8 TE
II	"	621	637	0.4 UE, 4?
III	"	609	634	0.6 UE, 2.8

UE: uniform elongation, TE: total elongation.

Following deformation, specimens were examined by SEM to identify regions that were deformed. Disks 1 mm in diameter were then punched from promising areas so that the edge of the specimen was retained on one side to allow determination of the stress axis. Each disk was then mounted in a 3 mm stainless steel disk using recently developed procedures [3] and prepared using normal polishing procedures. Microscopy was performed on a JEOL 1200EX transmission electron microscope operating at 120 KeV and using a double tilting ±45° goniometer stage. Imaging included procedures for identifying each of the a<100> and $\frac{a}{2}$<111> Burgers vectors in a field of view.[4] All micrographs have been digitized and some stereo images were prepared as anaglyphs, available on request.

Results

Surface Features

SEM revealed that surfaces of the irradiated specimens had developed poorly defined steps. The vertical surfaces of these steps were not flat, but instead showed fine slip traces. Examples are provided in Figures 1 and 2. Figure 1, containing montages at low magnification, compares the specimen taken to fracture (# I) with two specimens deformed to about half the strain to failure (#'s II & III). Areas in specimens II and III that show deformation are marked with arrows. From this figure, it is apparent that deformation is very localized and appears to emanate from an edge notch, in both cases. Figure 2 shows examples of specimen surfaces at higher magnifications with examples of unirradiated and irradiated Fe-9Cr for comparison. From Figure 2, it is apparent that irradiated F82H is behaving like unirradiated Fe-9Cr.

Microstructural Examination

The microstructure found in all irradiated specimens of F82H on a coarse scale was typical of martensitic steels. Lath boundaries were decorated with $M_{23}C_6$ carbides. Effects of irradiation and postirradiation deformation are on a finer scale than lath boundary dimensions. Examples of the microstructure at low magnification are provided in Figure 3. Specimen IA is shown on the left and IIA in the center and on the right. Careful examination reveals some differences; IA contains significantly less dislocation structure within martensite laths than does IIA.

The dislocation structure in specimen IA is shown in greater detail in Figure 4. The same area in bright and dark field contrast is shown for three different imaging conditions. From this figure, it is apparent that most of the structure is in the vicinity of the lath sub-grain boundaries. However,

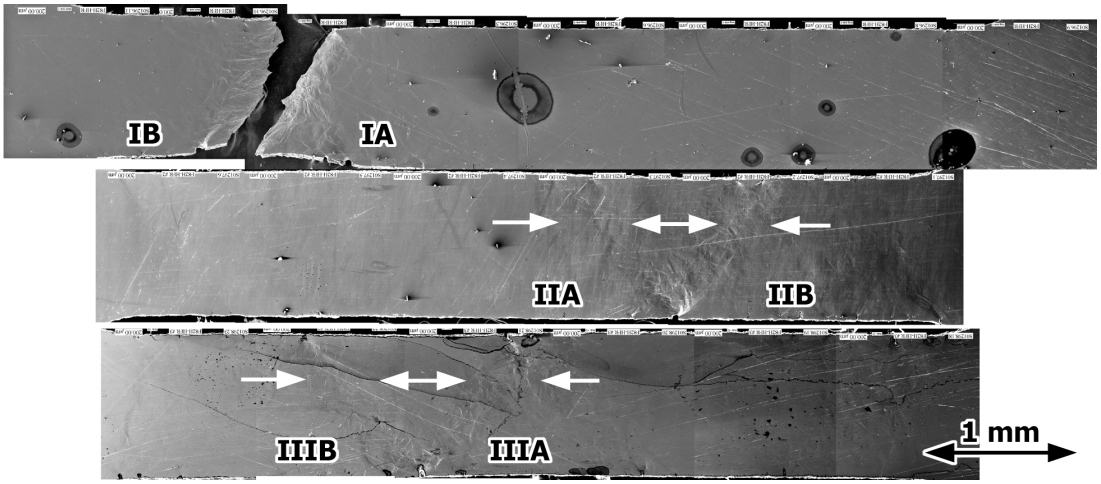

Figure 1. Low magnification examples of deformed F82H tensile specimens. Labels correspond to descriptions in the text.

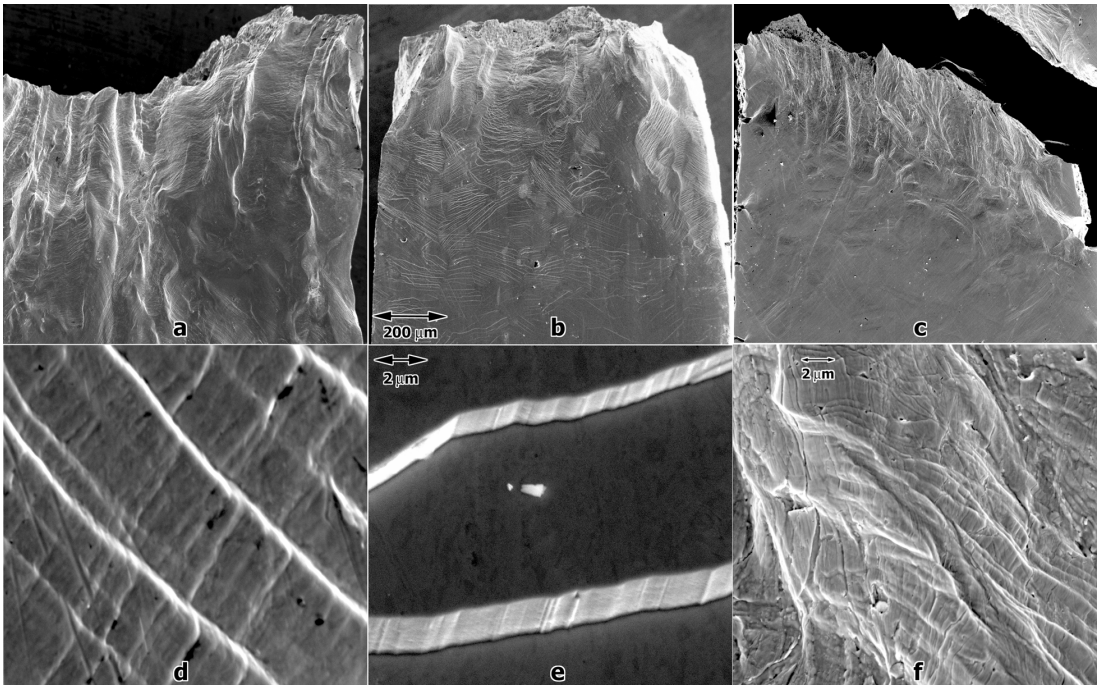

Figure 2. Higher magnification examples of the fracture surfaces and slip steps, with the unirradiated Fe-9Cr condition on the left, irradiated Fe-9Cr in the center and irradiated F82H on the right.

although it is not clear with bright field imaging, the boundary regions are decorated with fine structure, similar to loop structures that can be nucleated during irradiation near dislocations present prior to irradiation. Therefore, it is likely that this structure represents undeformed material. Apparently deformation only occurred less than about 0.5 mm from the failure site, and preparation of a thinned region 1 mm in diameter near the failure site therefore did not show deformation.

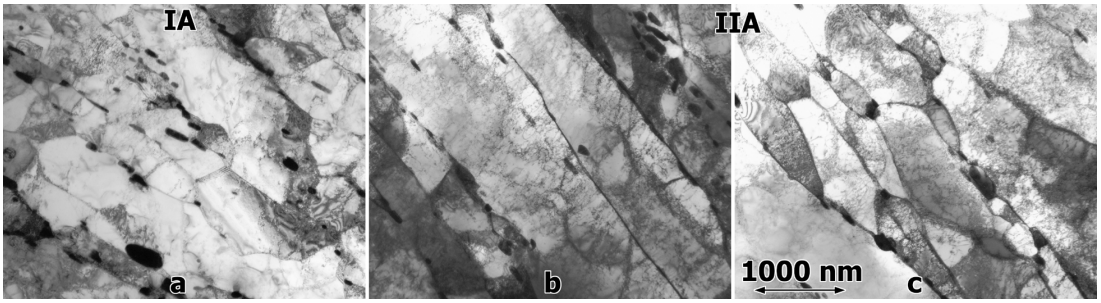

Figure 3. Martensite lath structure in specimens IA and IIA

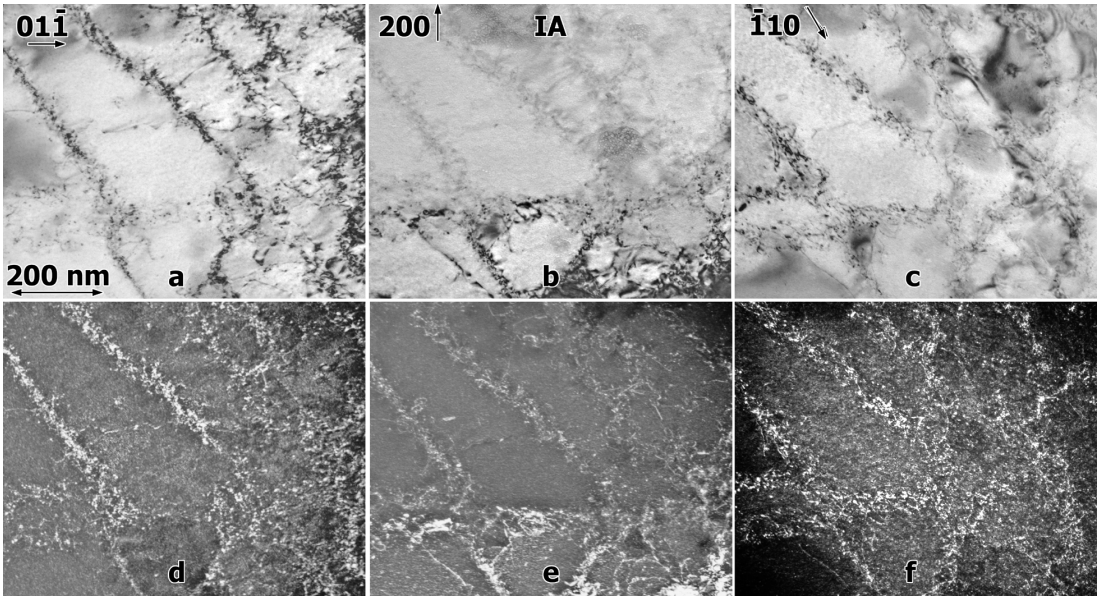

Figure 4. Microstructures in apparently undeformed regions of specimen IA shown in bright field a) to c) and dark field d) to f) contrast.

Figures 5 and 6 show dislocation structure in specimen II. An area in specimen IIA is shown in bright and dark field contrast for three different imaging conditions. Two significant differences can be identified in comparison to Figure 4. Many more individual dislocation lines are present between lath boundaries and the density of fine structure near lath boundaries appears to have been reduced. Figure 6 has been prepared to show two further regions in dark field contrast, one in specimen IIA and the other in specimen IIB.

Discussion

Postirradiation microstructural examination has shown that deformation in F82H to 2.7 dpa at 327ºC does not occur by channel deformation. Effects of irradiation are demonstrated. Fine structure typical of small dislocation loops has formed near dislocations in subgrain boundaries, and this may explain the increase in hardening observed. Companion specimens in the Chariot experiments have shown that unirradiated F82H gives ~540 MPa for the unirradiated condition yield strength, 610-660 MPa following irradiation to ~2.7 dpa (in agreement with the present results) and ~820 MPa following irradiation to doses of 5 dpa and above.[4] Therefore, it can be suggested that hardening is at least in part due to development of small loops in the vicinity of dislocations present prior to irradiation. For example, if the loops were of type a<100>, glide dislocations could react with the loop according to the relation:

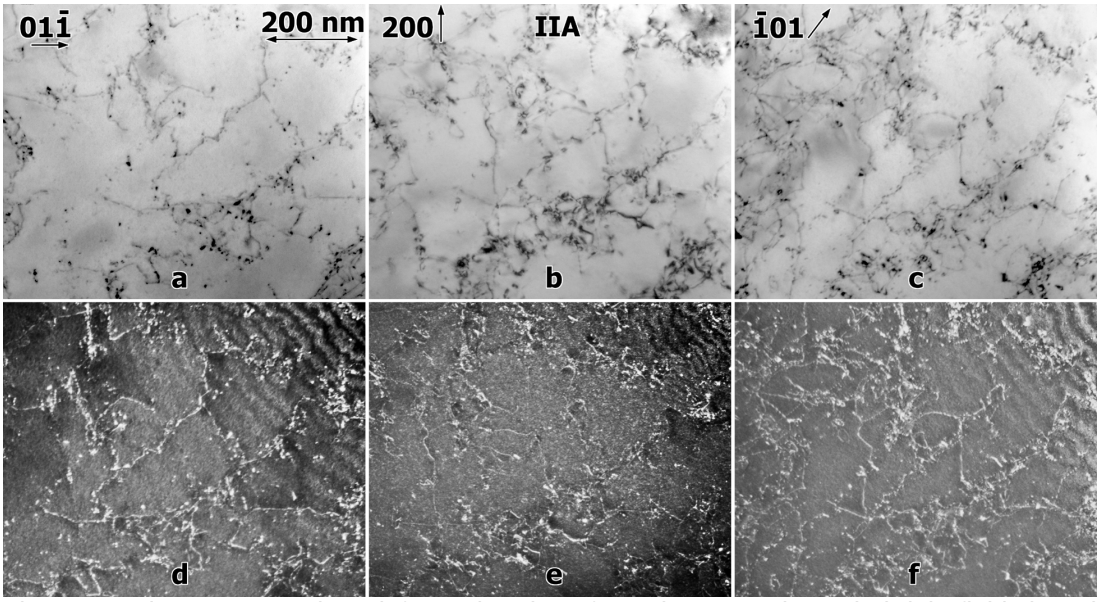

Figure 5. Microstructures in a deformed region of specimen IIA shown in bright field a) to c) and dark field d) to f) contrast.

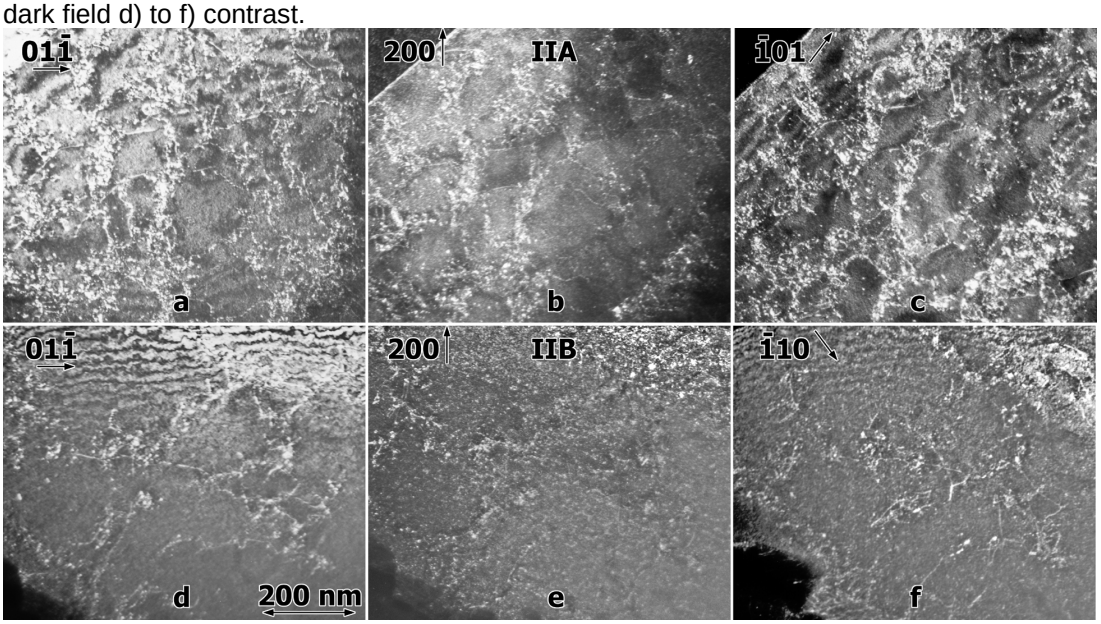

Figure 6. Microstructures in specimens IIA and IIB shown in dark field contrast.

$$\tfrac{a}{2}[\bar{1}11] + a[100] = \tfrac{a}{2}[111]$$

and leave a different loop and the original $\frac{a}{2}[\bar{1}11]$ dislocation unaltered. However, removal of the $\frac{a}{2}[111]$ loop is more difficult, requiring interaction only with other $\frac{a}{2}[111]$ dislocations. However, once dislocations break free of the subgrain boundaries, they appear to move individually; channeling is not required.

A recent paper concludes that hardening cannot be simply accounted for by the formation of small loops decorating dislocations present prior to irradiation.[5] Precipitation is likely to play a role. In that work, images in $\vec{g}$=200 contrast revealed very fine structure, interpreted as very fine

precipitation. The present results do not reveal this fine uniform precipitation. A possible explanation lies in irradiation temperature differences, the present results for specimens at 327ºC and the earlier results at 250ºC (to a high dose at 302ºC). The hardening phase in F82H is probably more stable at lower temperatures. However, given the expected increase in strength following irradiation to 5 dpa at 330ºC, post-irradiation deformation studies on specimens expected to be available shortly at 5 dpa should be of great interest.

Conclusions

Miniature sheet specimens of F82H have been examined following irradiation to 2.7 dpa at 327ºC in order to study post-irradiation deformation behavior. It is found that

1) Deformation in irradiated specimens is highly localized so that TEM specimens prepared more than 1 mm from the fracture surface usually showed no effects of deformation.
2) Surface slip steps created during postirradiation deformation are poorly defined similar to unirradiated Fe-9Cr specimens, indicating that channel deformation did not control.
3) Effects of irradiation are identified. Fine structure, probably consisting of small dislocation loops, formed around dislocations in martensite lath boundaries.
4) Hardening is attributed to interaction of sub-grain boundary dislocations with the irradiation induced loops. However, the hardening is insufficient to cause channel deformation.

FUTURE WORK

This work will be continued when specimens irradiated to 5 dpa are available.

REFERENCES

[1] D. S. Gelles, M. L. Hamilton, and R. Schaeublin in Effects of Radiation on Materials: 20th International Symposium, ASTM STP 1405, S. T. Rosinski, M. L. Grossbeck, T. R. Allen, and A. S. Kumar, Eds., ASTM West Conshohocken, PA (2001) 523.

[2] H. Lohner, *SIWAS-09*, Irradiation of Steel Specimens at Ambient Temperature - Project R268-09 Irradiation Report, JRC report P/F1/01/01, JRC Petten, 2001, The Netherlands.

[3] D. S. Gelles, S. Ohnuki, K. Shiba, Y. Kohno, A. Kohyama, J. P. Robertson, and M. L. Hamilton, in DOE/ER-0313/25 (1999) 143.

[4] J. Rensman, J. fan Hoepen, J. B. M. Bakker, R. den Boef, F. P. van den Broek and E. D. L. van Essen, "Tensile Properties and Transition Behavior of RAFM Steel Plate and Welds Irradiated up to 10 dpa at 300ºC," submitted for publication in the proceedings of ICFRM-10.

[5] R. Schaeublin, D. Gelles and M. Victoria, "Microstructure of irradiated Ferritic/martensitic steels in relation to mechanical properties," submitted for publication in the proceedings of ICFRM-10.

LONG-TERM HIGH TEMPERATURE OXIDATION BEHAVIOR OF ODS FERRITICS -- B. A. Pint and I. G. Wright (Oak Ridge National Laboratory)

To be published in the Journal of Nuclear Materials as Proceedings of the 10th International Conference on Fusion Reactor Materials, October 2001, Baden-Baden, Germany.

EXTENDED ABSTRACT

Four oxide dispersion strengthened (ODS) Fe-(13-14 at.%)Cr- ferritic compositions were exposed in air and air with 10 vol.% water vapor for up to 10,000 h at 700°-1100°C. At 700°-800°C in air, the reaction rates were very low for all of the alloys compared to stainless steels (types 310 and 347). At 900°C, a dispersion of Y_2O_3 in Fe-14%Cr-0.9%W (labeled FCW-Y), compared to a dispersion of Al_2O_3 (labeled FCW-Al), showed a distinct benefit in improving the oxidation resistance, due to a reactive element effect, Figure 1. However, a Y_2O_3-dispersed alloy with only 13%Cr (labeled FCW-YT) failed after 7,000 h at 900°C due to its smaller Cr reservoir, which is depleted by the formation of the Cr_2O_3 surface oxide. The absence of Ti and W in one alloy appeared to result in a thinner reaction product after oxidation at 800°C. One composition (FCW-Y) was exposed in 10% water vapor at 800° and 900°C and in air at 1000°C and 1100°C. In the presence of water vapor, volatilization of CrO_3 or $CrO_2(OH)_2$ occurred, resulting in mass loss (Figure 1) and increased metal wastage due to the continuous loss of the reaction product. A significant increase in the rate of attack also occurred for the higher temperature exposures in air. Overall, it appears that the corrosion-limited operating temperature in air of these relatively low Cr content alloys is below 900°C.

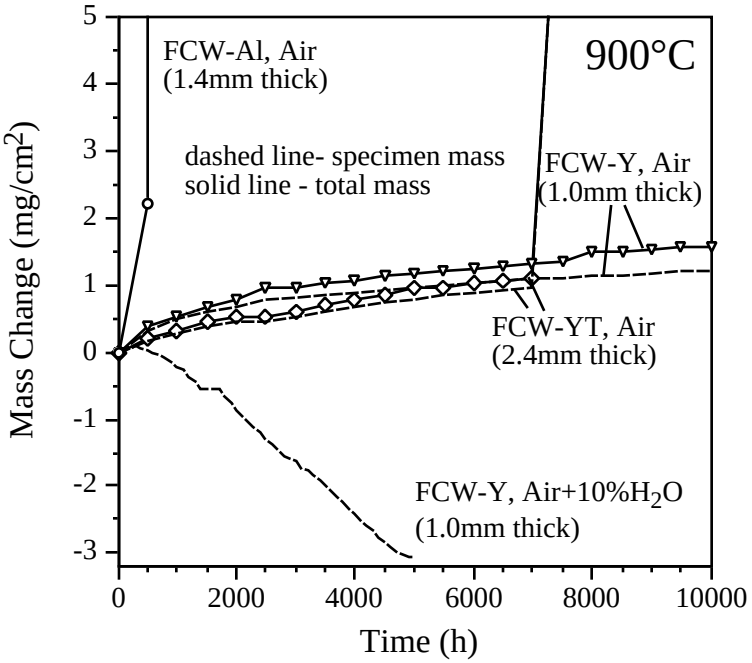

Figure 1. Total (solid lines) and specimen (dashed lines) mass gains measured at 900°C in air and air with 10% water vapor. The specimen thickness is shown for each. The addition of water vapor to the test resulted in mass losses for FCW-Y compared to exposure in air.

FERRITIC/MARTENSITIC STEELS—OVERVIEW OF RECENT RESULTS—R. L. Klueh (Oak Ridge National Laboratory), D. S. Gelles (Pacific Northwest National Laboratory), S. Jitsukawa (Japan Atomic Energy Research Institute), A. Kimura (Kyoto University), G. R. Odette (University of California at Santa Barbara, B. van der Schaaf (NRG) and M. Victoria (Paul Scherrer Institute)

Paper was presented at the 10th International Conference of Fusion Reactor Materials, October 14-19, 2001, Baden-Baden, Germany, and it will be published in the conference proceedings in the *Journal of Nuclear Materials*

Extended Abstract

Because of their swelling resistance and excellent thermal properties, reduced-activation ferritic/martensitic steels are presently considered the primary structural material for future fusion power reactors. However, there have been questions concerning the feasibility of their use, and to more rapidly address possible problems, an international collaboration involving Europe, Japan, and the United States began in 1992 under the auspices of the International Energy Agency (IEA). The collaboration involves work on large heats of the reduced-activation ferritic/martensitic steels F82H (7.5Cr-2WVTa) and JLF-1 (9Cr-2WVTa) that were produced in 1993, with the first steel plates for testing being delivered to the collaborating parties in 1994.

The testing phase for the large heats of F82H and JLF-1—especially for the unirradiated properties—is nearing completion. These steels have been well characterized to establish recommended procedures for heat treatment and welding, and data have been obtained on a range of mechanical and physical properties. A database has been developed based on the work that has been completed, and that database is available to the international community. In addition to determining the baseline data for the large heats of F82H, this steel was included in over twenty neutron irradiation experiments that were conducted in the High Flux Isotope Reactor (HFIR) in the U.S., in the Japan Research Reactor (JRR-4) and the Japan Materials Test Reactor (JMTR) in Japan, and the High Flux Reactor (HFR) in The Netherlands [10]. The results for the large heat of F82H were in general agreement with results for other experimental heats of 7-9Cr-WV-type reduced-activation steels that show improved properties over conventional Cr-Mo steels. Studies are still in progress to determine the effect of irradiation on a range of properties for base metal and weldments.

There is still uncertainty on the possible effect of transmutation helium on the fracture properties of the steels when irradiated in a fusion neutron environment. Simulation techniques (ion implantation or ^{54}Fe, Ni, and B doping) with their inherent uncertainties are the methods presently available to study helium effects, and these techniques are being used to further our understanding of this potential problem. Each of these simulation techniques has been used in the past few years to study the effect of helium.

In one experiment, F82H doped with ^{10}B and natural boron were irradiated in HFIR at 400ºC to 52 dpa to produce 30, 60, and 330 appm in the steels. There was a large effect of helium, as the steels containing 60 and 330 appm He showed a swelling of about 1.2%, compared to about 0.52% for the steel with 30 appm.

Besides the simulation techniques, the PIREX and the Swiss Spallation Neutron Source (SINQ) facilities were used to simultaneously produce helium and displacement damage by irradiation with protons. Low-temperature nucleation of bubbles at temperatures as low as 217ºC were observed. It is at these temperatures where observations of a helium effect on the impact properties have been observed in the simulation experiments.

This uncertainty with helium makes the need for a 14 MeV neutron source urgent for future materials studies.

Alloy development for fusion has now moved beyond the F82H and JLF-1, and the European and Japanese fusion programs have determined new compositions and processing schedules for the 7-9 Cr class of reduced-activation steel. Based partially on the work performed in the IEA collaboration, the European Union has developed specifications for a new martensitic steel, EUROFER 97, which has been produced and is now being evaluated. Data has been obtained on tensile, creep, and impact behavior, and the results indicate that the EUROFER 97 has properties similar to those of F82H.

The ferritic/martensitic steels presently being considered are limited to ≈600ºC. Higher temperature operation for higher efficiency fusion plants will require further development of the steels if they are to be used. One attractive route to such materials are the oxide dispersion-strengthened (ODS) ferritic/martensitic steels. That option is being pursued in Europe, Japan, and the United States, and progress is being made in solving some of the problems associated with these materials.

MICROSTRUCTURAL EXAMINATION OF LOW ACTIVATION FERRITIC STEELS FOLLOWING IRRADIATION IN ORR - D. S. Gelles (Pacific Northwest National Laboratory)*

OBJECTIVE

The objective of this effort is to determine the effects of irradiation on microstructure in low activation ferritic steels following irradiation at temperatures of 400°C and below in order to better understand swelling, microstructural evolution and irradiation hardening behavior in this alloy class at low irradiation temperatures.

SUMMARY

Microstructural examinations are reported for a series of low activation steels containing Mn following irradiation in the Oak Ridge Reactor at 330 and 400°C to ~10 dpa. Alloy compositions included 2% Cr, 9% Cr and 12% Cr steels with V to 1.5% and W to 1.0%. Results include compositional changes in precipitates and microstructural changes as a function of composition and irradiation temperature. It is concluded that temperatures in ORR are on the order of 50ºC higher than anticipated.

PROGRESS AND STATUS

Introduction

The post-irradiation tensile test response has been reported for a series of reduced activation alloys containing manganese following irradiation in the Oak Ridge Reactor (ORR) at 60, 200, 330, and 400°C to ~10 dpa,[1] and shear punch behavior of irradiated TEM disks that were irradiated under effectively identical conditions.[2] The alloys include 2% Cr alloys with V additions, and 9% and 12% Cr alloys containing Mn with V and W additions (Table 1). These alloys have been studied extensively prior to and following irradiation in the Fast Flux Test Facility in order to understand microstructural evolution in low activation alloys to high dose.[3-6] An alloy design concept involved substitution of Mn for Ni in order to control austenite stability. Unfortunately, subsequent experiments demonstrated that Mn additions resulted in unexpected Chi-phase precipitiation. However, as Mn is formed by transmutation from Fe in a fusion environment, studies of effects of Mn on irradiation effects in low activation alloys is pertinent. Recent improvements in specimen preparation technique now allow preparation of electron transparent foils from 1 mm diameter disks created during shear punch testing.[7] Smaller samples reduce magnetic and radioactivity effects allowing, for example, more effective determination of precipitate compositions. Therefore, this report is intended to describe microstructural examinations of the shear punch specimens, in order to provide understanding of the effects of irradiation on strength at temperatures below 400°C.

Experimental Procedure

Compositions and material identification codes for specimens irradiated in the ORR-MFE 6J and 7J tests are provided in Table 1. Specimens were of standard TEM geometry, 3 mm in diameter x 0.20 mm. The 6J test accumulated a midplane fluence of 2.4 x 10^{22} n/cm^2 (total) or 8.8 x 10^{21} n/cm^2 (E>0.1 MeV) and the 7J test accumulated a fluence of 2.7x 10^{22} n/cm^2 (total) or 9.5 x 10^{21} n/cm^2 (E>0.1 MeV).[8,9] This corresponds to damage levels of 6.6 - 6.8 and 7.1 - 7.3 dpa, respectively, variations corresponding to lower or higher chromium levels. Predicted helium levels are 2.1 to 2.3 appm for both tests, with variations due to higher or lower chromium levels,

* Pacific Northwest National Laboratory (PNNL) is operated for the U.S. Department of Energy by Battelle Memorial Institute under contract DE-AC06-76RLO-1830.

respectively. Specimens in 6J, designed to operate at 330°C, included the two digit location code LB, and specimens in 7J, designed to operate at 400°C, included the two digit location code LH, so that each specimen for examination is identified with a unique four digit code defining both material and irradiation conditions.

Specimen preparation procedures for 1 mm samples were similar to those described previously,[3] except that initial success rates were not as good as previously described. A solution was to use 3 mm stainless steel support rings of approximately the same thickness as the irradiated disks so that the gluing operation left the 1 mm disk flat in the support ring. Note that it was possible to obtain extra 1 mm disks for examination from the outer ring of the original 3 mm, so that a given TEM disk can provide 7 opportunities for a good specimen.

Examinations were performed on a JEOL 1200EX for microstructural features and on a JEOL 2010F for precipitate composition information. Precipitate particles were chosen for analysis close to the edge of the foil in order to minimize compositional effects from the surrounding matrix. Measurements employed Oxford instruments ISIS software in STEM mode. A typical run involved capturing an image, selecting points for analysis including nearby matrix and hole count for each image and storing the acquired spectra for later analysis. It should be noted that despite the shift to 1 mm samples, effects of magnetism and background radioactivity remained. The ^{54}Mn radioactivity signal was found to be prominent enough so that it had to be subtracted to accurately determine compositions, but because of differences in effective count rate with varying dead times, it was not possible to reproducibly determine Mn levels. As a result, the background subtraction was performed in order to obtain a level for Mn comparable to the starting composition, assuming in effect, that Mn did not segregate to precipitates. However, the most useful parameters defining carbide compositions are considered to be the V/Cr and W/Cr ratios.

Table 1. Identification codes and compositions for TEM specimens irradiated in the ORR-MFE 6J and 7J tests.[1]

ID code	Heat # or alloy name	Composition (w/o)					
		Cr	V	W	Mo	C	Mn
P3	V02262	2.25	0.5			0.1	
P4	V02263	2.25	1.0			0.1	
P5	UC-19	2.25	1.5		0.2	0.1	0.3
RB	V02268	9	0.3	1.0		0.1	2.5
P6	V02264	9	0.5			0.1	
P9	V02266	9	0.5			0.1	2.0
P7	V02265	9	1.3			0.2	1.0
RE	V02269	12	0.3	1.0		0.1	6.5
RA	V02267	12	1.0			0.1	6.5

Results

The results of this study will be divided into four sections. First, microstructural results for low Cr, intermediate Cr and higher Cr alloys will be presented successively and then results of precipitate compositional analysis will be provided.

Low Cr

The 2% Cr alloys were found to contain both a fine dislocation structure and fine precipitates following irradiation at 330ºC. Following irradiation at 400ºC, the structures were similar but on a coarser scale. No void swelling was found following irradiation at either temperature. Examples of the microstructures are shown in Figures 1 to 3. For each specimen, a series of two

micrographs is provided, generally taken of the same area near an (011) orientation, the one on the left using $\bar{g} = 01\bar{1}$ with $\bar{g}$ horizontal, and the one on the right using $\bar{g} = 200$ with $\bar{g}$ vertical. This configuration allows straightforward differentiation of a<100> Burgers vectors that should appear as strong horizontal images in 200 contrast. For example, from Figure 1, it can be concluded that most of the dislocations are probably of $\frac{a}{2}$<111> character. Figure 1 contains insets using 200 dark field contrast in order to emphasize that the smaller features have quite different contrast from the dislocation structure, indicating the presence of precipitates as small as 4 nm following irradiation at 330ºC and ~8 nm at 400ºC. Similar structure on a denser scale is found with increasing V content. (Note that images for specimen P4LB show a thicker area.) In specimen P4LH, it was possible to demonstrate that the fine precipitate often appears as square platelets on (100) planes. Therefore, precipitates appear to increase in number density with increasing V content.

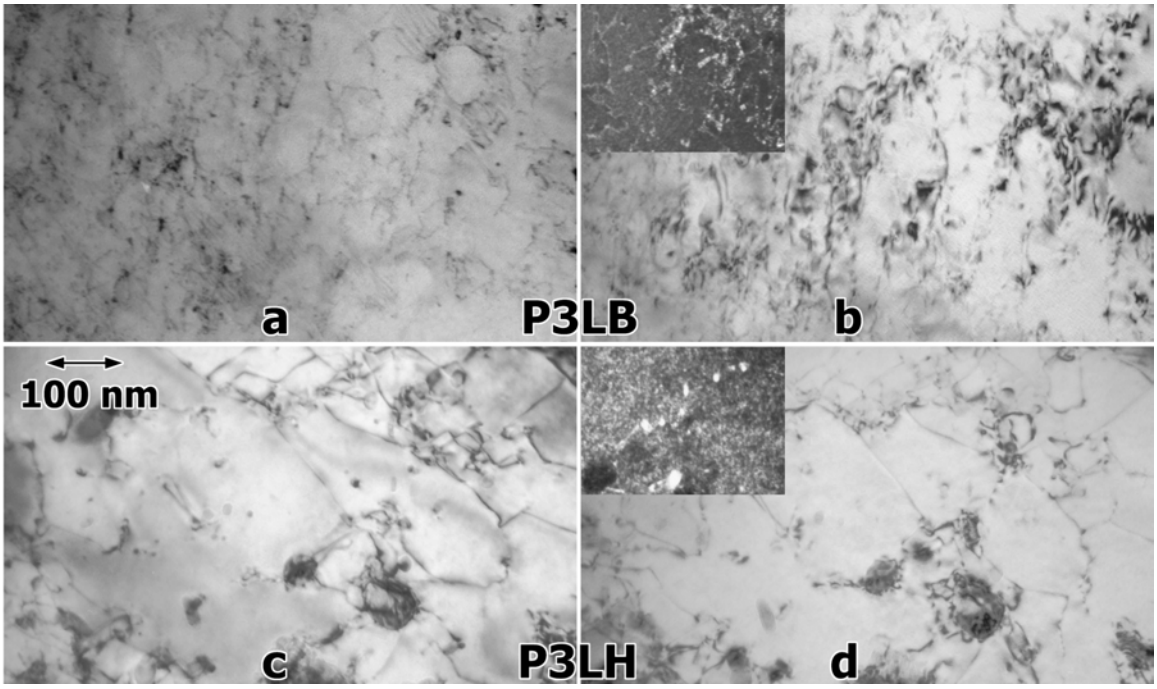

Figure 1. Microstructures in 2Cr-0.5V following irradiation at 330 and 400ºC.

Intermediate Cr

Alloys containing 9% Cr were also generally found to contain both a fine dislocation structure and fine precipitates following irradiation at 330ºC. Behavior observed in condition P9LB was atypical in that the dislocation structure was found to be quite coarse. This may indicate a specimen mix-up. Alternatively, additions of Mn may discourage precipitation when V levels are low. The structures following irradiation at 400ºC showed little evidence of precipitation apart from the large carbides probably remaining from preirradiation heat treatment. Again, no void swelling was found following irradiation at either temperature. Examples are provided in Figures 4 through 7. In all cases, an example following irradiation at 330ºC is given but only two examples of behavior at 400ºC are included. Note that the orientation for Figure 7 is close to (001).

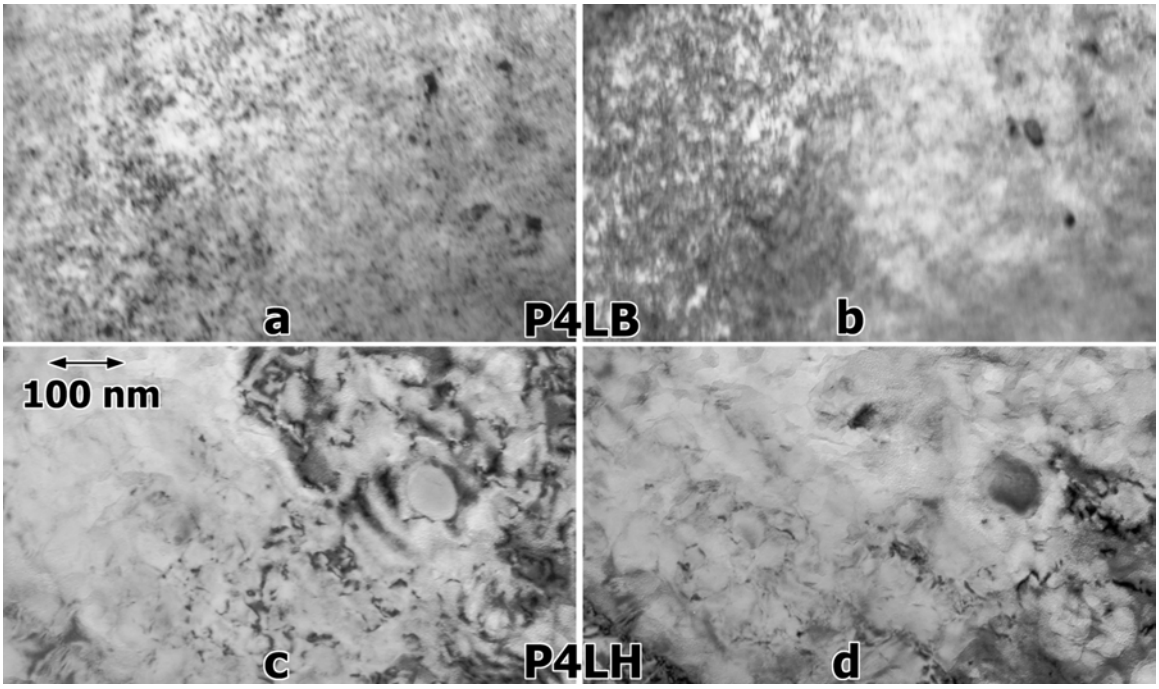

Figure 2. Microstructures in 2Cr-1V following irradiation at 330 and 400ºC.

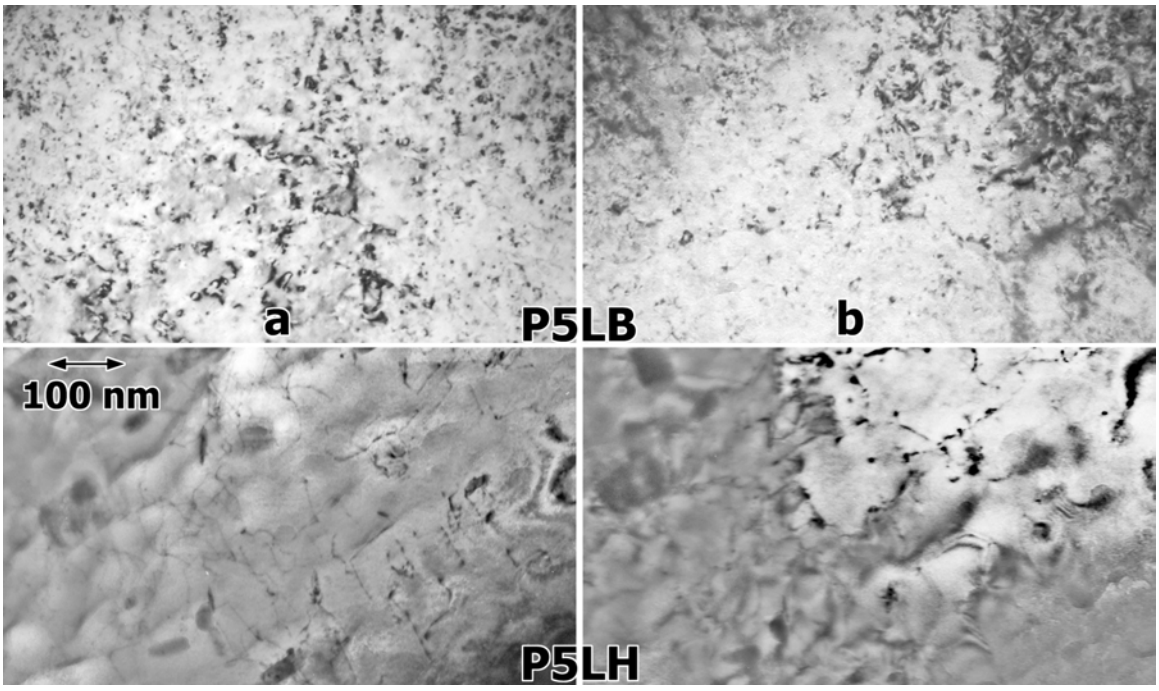

Figure 3. Microstructures in 2Cr-1.5V-0.3Mn-0.2Mo following irradiation at 330 and 400ºC.

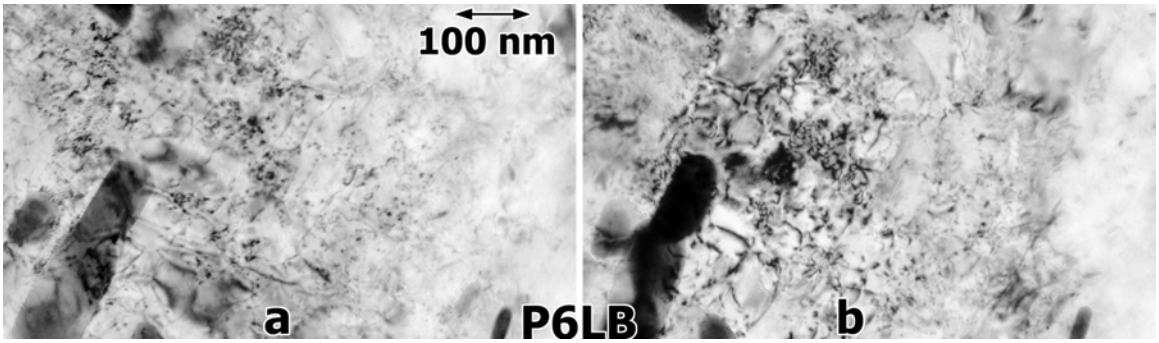

Figure 4. Microstructures in 9Cr-0.5V following irradiation at 330ºC.

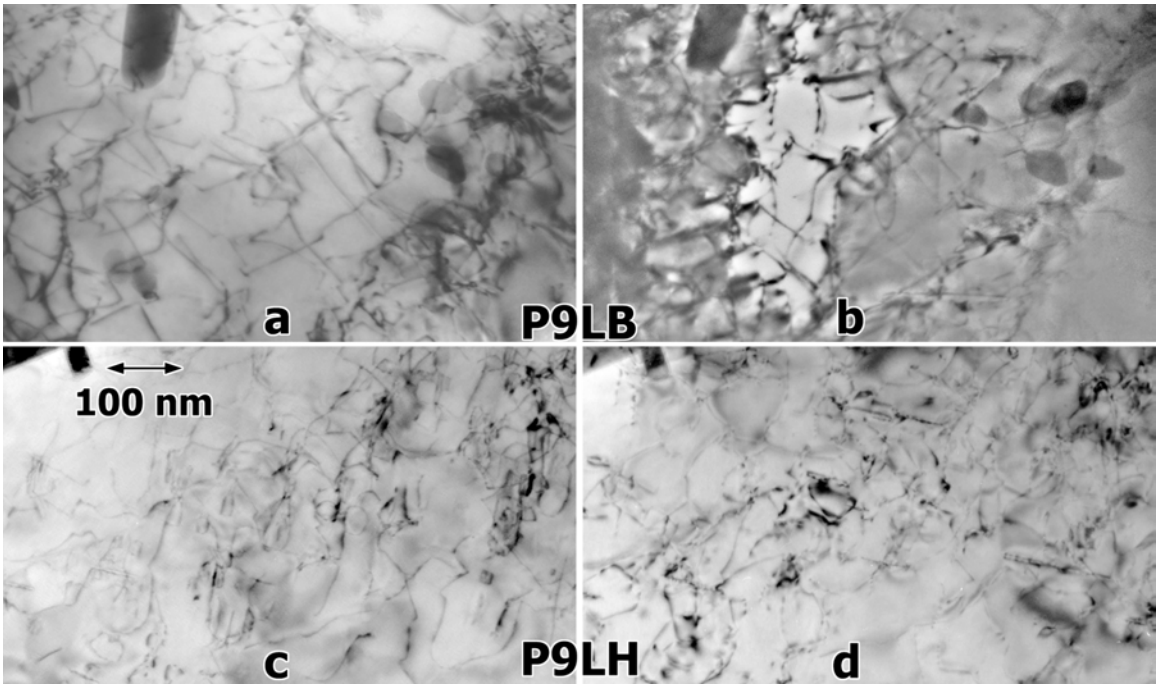

Figure 5. Microstructures in 9Cr-0.5V-2Mn following irradiation at 330 and 400ºC.

Higher Cr

The 12% Cr alloys were found to respond to irradiation somewhat differently than the low and intermediate Cr alloys. The difference in dislocation density was smaller as a function of irradiation temperature (lower at low temperatures and higher at higher temperatures than for lower Cr alloys), and extensive precipitation was found following irradiation at 400ºC. However, again no void swelling was observed. Examples are provided in Figures 8 and 9. The precipitation found following irradiation at 400ºC can be seen in Figures 8c and 9d (provided at higher magnification) and is typical of α', the Cr-rich bcc phase.

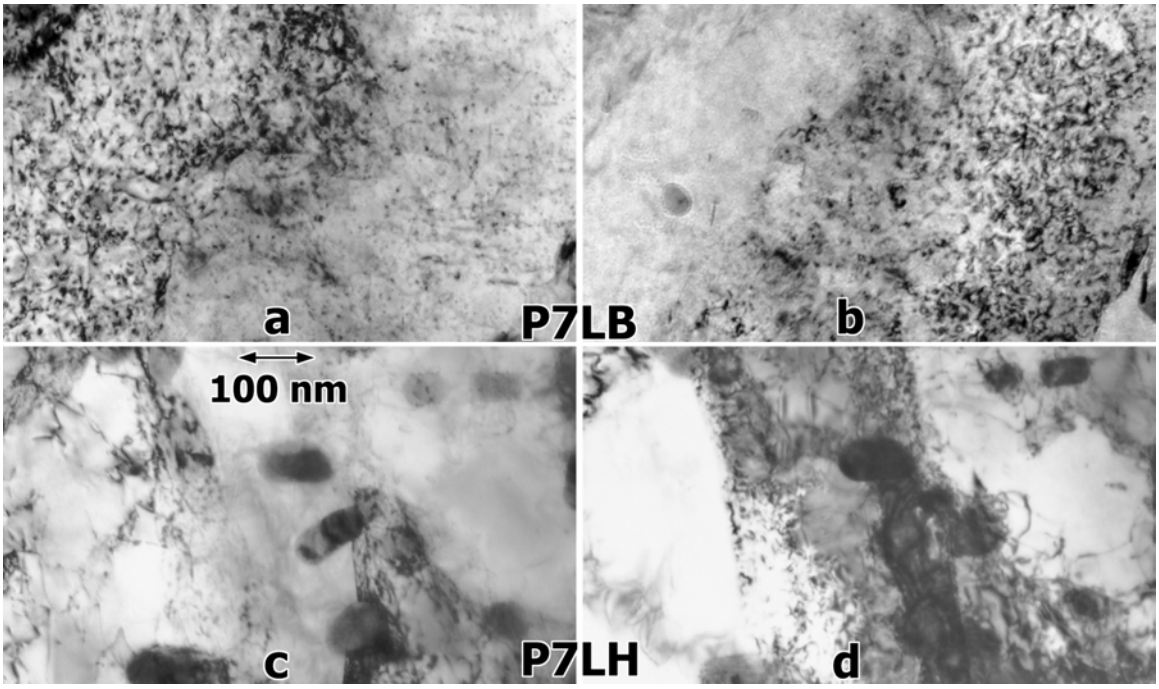

Figure 6. Microstructures in 9Cr-1.3V-1Mn following irradiation at 330 and 400ºC.

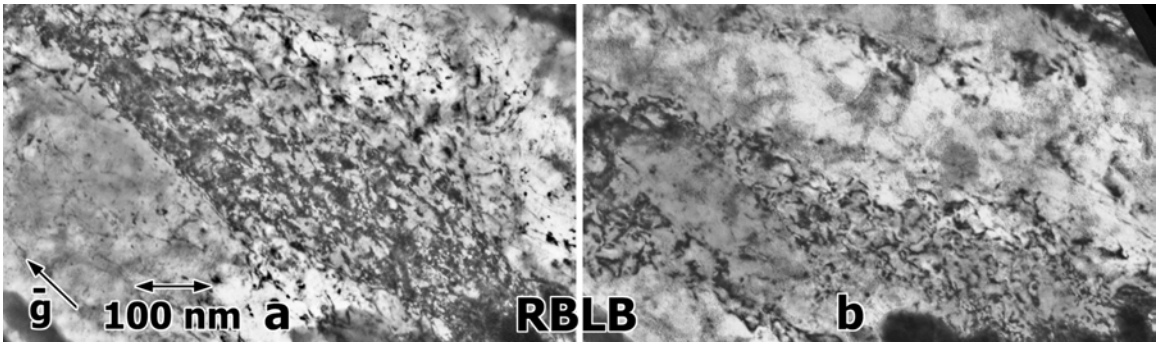

Figure 7. Microstructures in 9Cr-1W-0.3V-2.5Mn following irradiation at 330ºC.

Precipitate compositions

Compositions for precipitate particles in foils of each specimen were measured on at least 20 particles near or overhanging foil edges. This included both irradiation conditions, irradiated at 330 and 400ºC, and results are provided in Table 2. The compilation in Table 2 tends to emphasize maximum observed levels of V and Cr (and therefore lowest levels of Fe), ignoring determinations where levels were lower, on the assumption that higher levels of Fe corresponded to inclusion of matrix information. However, the V/Cr and W/Cr ratios reported include particles with higher levels of Fe. Wide variations can be noted, and examples where matrix determinations do not appear to be reasonable have been included (see RELH for example).

Of particular note are inclusion of results for α' in RALH and a phase with high Fe noted for P4LB. Compositional measurements of α' demonstrate high levels of Cr, as anticipated. Such

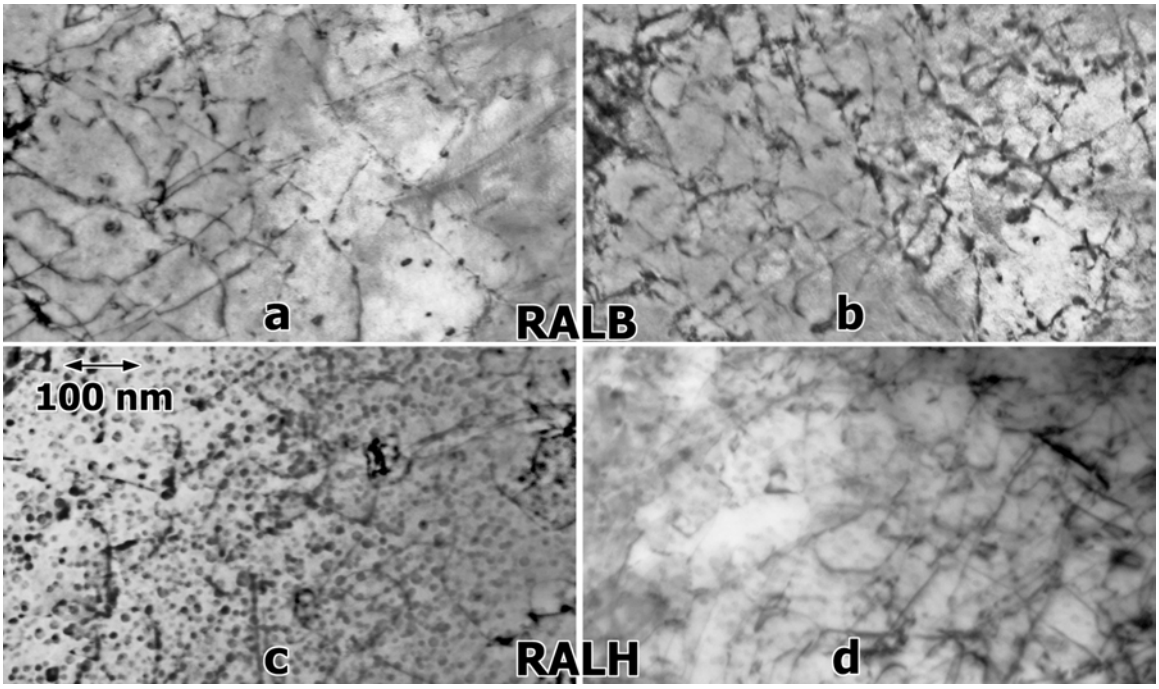

Figure 8. Microstructures in 12Cr-1V-6.5Mn following irradiation at 330 and 400ºC.

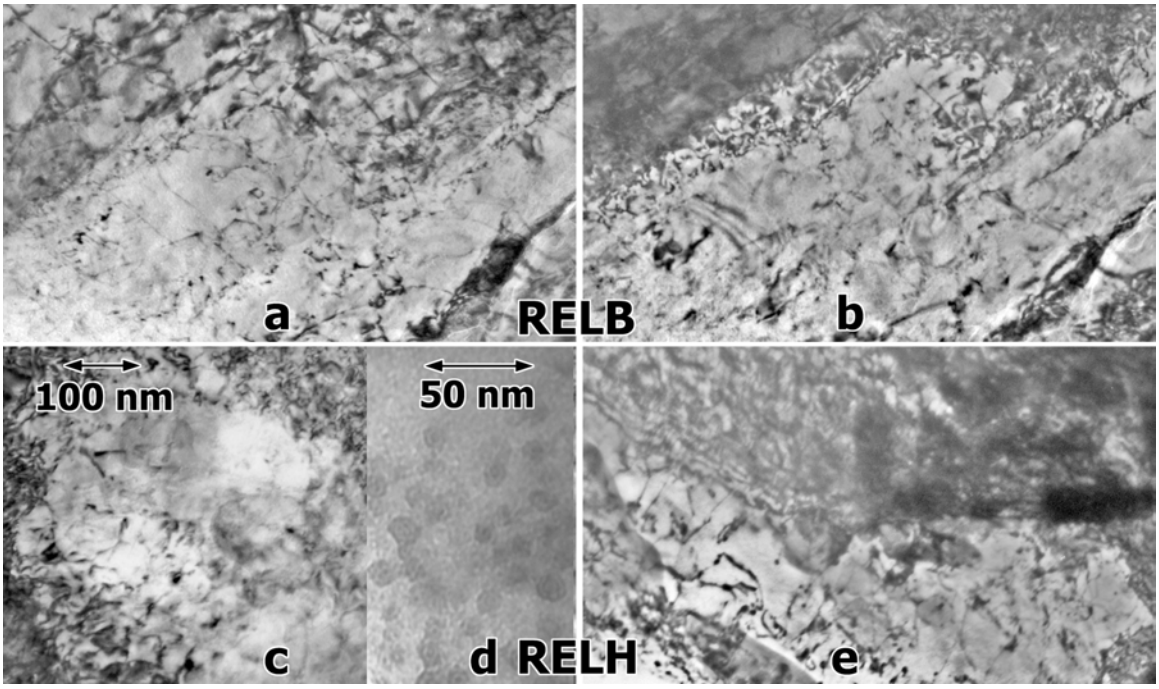

Figure 9. Microstructures in 12Cr-1W-0.3V-6.5Mn following irradiation at 330 and 400ºC.

measurements are rare. These measurements were made in TEM mode for particles that happened to hang over the edge of the foil, apparently because the electropolishing conditions left them unaffected. An example of similar microstructure found in condition RELH is inset in Figure 9. Also of note is that the phase in P4LB with high Fe cannot be heavily matrix-

contaminated MC because Cr levels are too high but it does not match the phase called M_7C_3. Although, the identity of this phase is not yet apparent, it provides an explanation for behavior, as will be discussed.

Table 2. Precipitate compositions in wt%.

Code	Metal comp.	Fe	Cr	Mn	V	W	V/Cr:W/Cr	Ident.
P3LB	Fe-2.25Cr-.5V	47-50	42-45	0	3.6-8.1	-	.07-.18	M_7C_3
"	"	12-21	10-11	0	68-78	-	6-7.9	MC
"	"	97	2.4	0	.5	-	.27	Matrix
P3LH	"	46-50	45-51	.3	3.2-5.7	-	.06-.13	M_7C_3
"	"	45-49	6-12	.3	50-80	-	5.3-8.7	MC
"	"	97-98	1.7-2.0	.3	.05-.76	-	.03-.20	Matrix
P4LB	Fe-2.25Cr-1V	85-90	5.7-11	0	3.5-4.9	-	.4-1.2	MC
"	"	12-36	4.5-18	0	51-81	-	7-14	?
"	"	94-95	3.5-4.0	0	1.0-1.7	-	.4-.5	Matrix
P4LH	"	12-29	25-41	0	35-41	-	.8-1.8	MC
"	"	97	2.5	0	.7	-	.27	Matrix
P5LB	Fe-2.25Cr-1.5V-.3M .2Mo	73-94	3.0-6.9	0.3	2.5-20	-	1.5-2.5	M_7C_3
"	"	7-30	4.8-5.1	0.3	65-87	-	13-16	MC
"	"	94-96	3.0-3.5	0.3	1.1-2.5	-	.3-.6	Matrix
P5LH	"	20-26	65-71	0.3	8.4-10	-	.12-.15	M_7C_3?
"	"	88-90	9-12	.3	0.8-1.9	-	.08-.12	Matrix?
P6LB	Fe-9Cr-.5V	22-35	57-67	0	7.3-11	-	.11-.17	$M_{23}C_6$
"	"	84-91	8.4-15	0	.1-.6	-	.05-.08	Matrix
P9LB	Fe-9Cr-.5V-2Mn	na	na	na	na	-	na	na
P9LH	"	19-34	59-74	2.0	4.7-5	-	.06-.09	$M_{23}C_6$
"	"	85-86	9	2.0	.1-.2	-	.01-.04	Matrix
P7LB	Fe-9Cr-1.3V-1Mn	20-34	62-72	1.0	2.5-7.8	-	.06-.16	$M_{23}C_6$
"	"	15	15	1.0	69	-	4.2	MC
"	"	89-90	8.8-9.5	1.0	.16-.33	-	.02-.06	Matrix
P7LH	"	18-29	61-69	1.0	7.8-11	-	.13-.17	$M_{23}C_6$
"	"	87-89	9.6-10	1.0	.9-1.3	-	.05-.12	Matrix
RALB	Fe-12Cr-1V-6.5Mn	28-64	39-62	6.5	1.7-5.7	-	.08-.13	$M_{23}C_6$
"	"	80	11.9	6.5	.7	-	.06	matrix
RALH	"	5-31	60-94	6.5	1.2-3.8	-	.02-.04	α'
"	"	24	65	6.5	4.7	-		$M_{23}C_6$
"	"	82	11.1	6.5	0.6	-	.07	matrix
RBLB	Fe-9Cr-1W-.3V-2.5	28-34	49-57	6.5	1.1-1.5	7.5-10	.02:.12	$M_{23}C_6$
"	"	41	45	6.5	5.3	2.6	.11:.06	σ?
"	"	83	9.5	6.5	0.4	0.8	.04:.09	Matrix
RBLH								
RELB	Fe-12Cr-1W-.3V-6.5Mn	19-42	46-70	6.5	.8-2.9	1.5-9.8	.04:.1	$M_{23}C_6$
"	"	76-78	14	6.5	.1-.3	1.4-3	.01:.10	Matrix
RELH	"	23-29	59-61	6.5	6.0-9.9	.2-.9	.15:.01	$M_{23}C_6$
"	"	83-86	7.7-8.7	6.5	.7-1.1	.06-.19	.11:.02	Matrix?

Discussion

The results of this investigation follow previously observed trends from this alloy series.[3-6] Identical specimens have been previously studied following irradiation in the Fast Flux Test Facility (FFTF) at 420ºC to doses from 7.7 to 200 dpa. In general, fine precipitation was found in the 2% Cr alloys following irradiation, assumed to be of MC (V_4C_3) type. Also, evidence for α' was apparent in 12% Cr alloy microstructures. Precipitate compositions were provided for extracted precipitates following irradiation at 520ºC to 14.5 dpa that are in agreement with the present results except that M_7C_3 was not found in 2Cr alloys (due to the higher temperature) and W levels were higher in alloys containing W following irradiation at 520ºC.

However, significant differences can be identified. As noted, no voids were observed following irradiation in ORR whereas a few voids were identified in FFTF irradiated V-9Cr-1V-1Mn (corresponding to condition P7) after 7.7 dpa at 420ºC. Also, dislocation structures appeared different, with more a<100> Burgers vectors evident in FFTF irradiated specimens. Finally, α' precipitation 12% Cr alloys was finer following irradiation in FFTF (~10 nm) than in ORR (~20 nm). As temperature control was believed to be more accurate in FFTF than in ORR (as it was based on direct reading thermocouples in contact with sodium coolant), it is anticipated that the irradiation temperature in the ORR 7J test is closer to 450ºC. This temperature deference along with effects of flux variation can be expected to explain unexpected swelling and dislocation differences between FFTF and ORR. The temperature of the ORR 6J capsule is expected to be significantly below 420ºC because the 6J microstructures are much finer than those from FFTF irradiation at 420ºC, but no comparable irradiation tests are available to determine if it also ran hotter than expected.

An objective of this work was to compare microstuctural observations with mechanical properties response for identical conditions. A compilation of the mechanical properties is duplicated in Table 3 from reference 2. As to be expected, higher irradiation temperatures produced coarser microstructures and lower strengths. Differences were not as great for 12% Cr alloys, explainable based on the distribution of α' and its effect on dislocation density. The α' precipitation formed after irradiation of 12% Cr alloys at 400ºC, whereas other alloys only showed coarse carbide structures following irradiation at the higher temperature. The 9% Cr alloys contained the simplest microstructures and showed the weakest behavior. The behavior for 2% Cr alloys was more complex however. The microstructural trends in the 2% Cr alloys showed increasing precipitation with increasing V. However, the mechanical properties showed maximum strength at 0.5V, minimum hardening at 1.0V and intermediate hardening (but failure before yielding in tensile testing) at 1.5V. Therefore, microstructural studies do not directly explain behavior. Perhaps an explanation lies in the observation of somewhat different precipitates in P4, i.e. the unidentified phase with higher Fe concentrations. Alternatively, more detailed examinations may be required to find structure on a finer scale, such as was done for F82H to explain hardening at low temperatures.[10]

Conclusions

A series of low activation alloys that were irradiated as TEM disks in the ORR have been examined by TEM following shear punch testing. Small 1 mm specimen geometries simplified microstructural examinations and compositional analyses but did not eliminate problems. In general, observed behavior reflected previous observations of these alloys following irradiation in FFTF. However, dislocation structures differed due to more coarse structure and less a<100> development, no void swelling was found, and α' was coarser. In part, these differences are ascribed to higher than expected temperatures in the 7J test.

Table 3. Shear punch and uniaxial tensile test results on low activation steel specimens following irradiation in ORR.[2]

ID TEM/Tensile	Dose (dpa)	Irr Temp (°C)	Test Temp (°C)	Effect.Yield Shear (MPa)	Effect.Max. Shear (MPa)	YS (MPa)	UTS (MPa)	UE (%)	TE (%)
P3LB/TE11	7.1	330	22	680	888	1367	1412	0.8	5.8
P3LH/TE13	7.1	400	22	320	462	1198	1230	0.8	6.9
P4LB/	7.1	330	22	580	694				
P4LH/	7.1	400	22	405	506				
P5LB/TZ11	7.1	340	22	650	717	1014	1014	0	0
P5LH/TZ15	7.1	400	22	305	423	661	700	1.4	8.6
RBLB/TR11	7.2	330	22	480	567	885	893	0.4	8.4
RBLH/TR15	7.2	400	22	260	458	576	673	6.2	16.6
P6LB/TM11	7.2	330	22	480	620	879	883	0.3	9.6
P7LB/TN11	7.2	330	22	500	613	917	933	0.6	8.9
P7LH/TN13	7.2	400	22	410	555	504	618	7.4	20.1
P9LB/TP11	7.2	330	22	430	537	960	971	0.5	8.1
P9LH/TP13	7.2	400	22	400	546	565	643	5.1	17.8
RELB/TU11	7.3	330	22	530	650	1009	1066	1.4	7.8
RELH/TU15	7.3	400	22	420	581	755	888	5	10.2
RALB/TL11	7.2	330	22	480	587	970	1004	3	10.8
RALH/TL13	7.3	400	22	400	553	719	846	7.1	15.3

FUTURE WORK

The effort is expected to shift to acquisition and testing of the ORR specimens further irradiated in HFIR.

REFERENCES

[1] M. L. Hamilton and D. S. Gelles, DOE/ER-0313/26 (1999) 102.

[2] R. M. Ermi, M. L. Hamilton, D. S. Gelles and A. M. Ermi, DOE/ER-0313/29 (2000) 103.

[3] D. S. Gelles and M. L. Hamilton, DOE/ER-0045/13 (1985) 128.

[4] D. S. Gelles and M. L. Hamilton, DOE/ER-0045/16 (1986) 131.

[5] D. S. Gelles in Reduced Activation Materials for Fusion Reactors ASTM STP 1047, R. L. Klueh, D. S. Gelles, M. Okada and N. H. Packan, Eds., ASTM, Philadelphia (1990) 113.

[6] D. S. Gelles, DOE/ER-0313/15 (1994) 156.

[7] S. Ohnuki, K. Shiba, Y. Kohno, A. Kohyama, J. P. Robertson, M. L. Hamilton and D. S. Gelles in Microstructural Processes in Irradiated Materials, MRS Symposium Proceedings Volume 540 (1999) 603.

[8] L. R. Greenwood, DOE/ER-0313/6 (1989) 23.

[9] L. R. Greenwood, DOE/ER-0313/8 (1990) 34.

[10] R. Schaeublin, D. S. Gelles and M. Victoria, “The Microstructure of Irradiated Ferritic/Martensitic Steels in Relation to Mechanical Properties,” presented at ICFRM-10, to be published.

TENSILE AND CREEP PROPERTIES OF AN OXIDE DISPERSION-STRENGTHEND FERRITIC STEEL—R. L. Klueh, P. J. Maziasz, D. T. Hoelzer, N. Hashimoto (Oak Ridge National Laboratory), I. S. Kim, and K. Miyahara (Nagoya University)

Paper was presented at the 10th International Conference of Fusion Reactor Materials, October 14-19, 2001, Baden-Baden, Germany, and it will be published in the conference proceedings in the *Journal of Nuclear Materials*

Extended Abstract

For increased efficiency in a fusion plant, the operating temperature must be increased above the maximum temperature (550 to 600ºC) for the conventional 9-12% Cr ferritic/martensitic steels. One possibility for doing this and still maintaining the advantages of ferritic steels (enhanced swelling resistance and thermal properties) is the use of oxide dispersion-strengthened (ODS) steels.

Two ODS steels from Kobe Steel Company, Japan, were investigated at Oak Ridge National Laboratory and Nagoya University. Nominal compositions of the two ODS steels were Fe-12Cr-0.25Y_2O_3 (designated 12Y1) and Fe-12Cr-3W-0.4Ti-0.25Y_2O_3 (12YWT). Previous work, which included optical microscopy, transmission electron microscopy, and atom probe field ion microscopy studies, indicated that the 12YWT contained a high density of extremely fine Y-Ti-O clusters, compared to much larger oxide particles in 12Y1. Tensile and creep properties of the two steels were obtained for the steels to determine the effect of the different microstructures on properties.

Tensile behavior of the two steels was determined over the range of room temperature to 900ºC and compared to the reduced activation 9Cr-2WVTa steel for tests to 700ºC. The yield strength of the 12YWT was superior to that of the 12Y1 and the 9Cr-2WVTa over the entire temperature range, which is consistent with the difference in the microstructures (the high number density of small particles in the 12YWT). Because of the much larger and less evenly distributed oxide particles in the 12Y1, the yield stress of this steel is only higher than that of the 9Cr-2WVTa steel below 550ºC, while the 12YWT continues to show excellent strength well above this temperature. As expected from the relative yield stress behavior, the elongation of the weaker 12Y1 exceeds that of the 12YWT. However, despite the higher strength, the 12YWT still has good ductility.

Creep and creep-rupture tests were conducted at 600-850ºC. The creep strength of the 12YWT exceeded that of the 12Y1. Larson-Miller parameters for the 12YWT and 12Y1 steels were compared with parameters for MA956 and MA957, two commercial ODS ferritic steels, and the 12YWT had the best creep-rupture properties. For tests at 800ºC, the creep-rupture strength of the 12YWT is also superior to that of the V-4Cr-4Ti alloy, another potential material for fusion applications.

The microstructure of the 12YWT creep specimen that failed after 14,500 h at 850ºC was examined by TEM and SEM. The TEM showed a high density of dislocations along with a clear depiction of the elongated grain structure of the material that is developed by the processing. Observations by SEM on polished specimens further elucidated the elongated grain structure of the as-processed material. The crept specimen showed indications of the elongated grain structure, but in addition, indications of recrystallization were observed. Such evidence of recrystallization was still only apparent in isolated regions, indicating that recrystallization was in its initial stages for a specimen in creep at 850ºC for 14,500 h. No unstressed specimens have been thermally aged to determine the role of stress in the recrystallization

It must be emphasized that even though the 12YWT steel displays these excellent properties, ODS steels for fusion are still at an early development stage, similar to the vanadium alloys.

Neither of these materials is at a stage of development comparable to conventional and reduced-activation ferritic/martensitic steels, for which the technology (i.e., steel processing, final fabrication, welding, etc.) is advanced to the point that a fusion plant could be constructed. Some of the problems still to be solved for ODS steels include: the elimination of the elongated grain structure (deriving from the way the steels are processed) that produces anisotropic behavior in the mechanical properties, the production of large section sizes, and the joining of ODS steels in a large structure. Finally, there is the question of irradiation resistance, for which very little information is available.

IRRADIATION CREEP AND MECHANICAL PROPERTIES OF TWO FERRITIC-MARTENSITIC STEELS IRRADIATED IN THE BN-350 FAST REACTOR – S .I. Porollo, Yu. V. Konobeev,and A. M. Dvoriashin (State Scientific Center of Russian Federation, (The Institute of Physics and Power Engineering, 249020 Obninsk, Russia) N. I. Budylkin, E. G. Mironova, M. V. Leontyeva-Smirnova, and A. G. Loltukhovsky (State Scientific Center of Russian Federation, A. A. Bochvar All-Russia Research Institute of Inorganic Materials (VNIINM), Moscow, Russia) and F. A. Garner (Pacific Northwest National Laboratory)*

OBJECTIVE

The objective of this effort is to determine the behavior of several ferritic-martensitic steels when exposed to high fluence neutron irradiation, and to compare the results with those of similar Western steels.

SUMMARY

Russian ferritic/martensitic steels EP-450 and EP-823 were irradiated to 20-60 dpa in the BN-350 fast reactor in the form of pressurized creep tubes and small rings used for mechanical property tests. Data derived from these steels serves to enhance our understanding of the general behavior of this class of steels. It appears that these steels exhibit behavior that is very consistent with that of Western steels. Swelling is relatively low at high neutron exposure and confined to temperatures <420°C, but may be camouflaged somewhat by precipitation-related densification. The irradiation creep studies confirm that the creep compliance of F/M steels is about one-half that of austenitic steels, and that the loss of strength at test temperatures above 500°C is a problem generic to all F/M steels. This conclusion is supported by post-irradiation measurement of short-term mechanical properties. At temperatures below 500°C both steels retain their high strength ($\sigma_{0.2}$=550-600 MPa), but at higher test temperatures a sharp decrease of strength properties occurs. However, the irradiated steels still retain high post-irradiation ductility at test temperatures in the range of 20-700°C.

Introduction

Ferritic-martensitic (F/M) steels are widely used as structural materials of various fission reactors in Russia and other former Soviet states. In particular, EP-450 steel is the reference structural material for hexagonal wrappers of the BN-600 fast reactor subassemblies. The main advantages of F/M steels are their high resistance to swelling, low rate of irradiation creep and rather low activation [1, 2]. The high irradiation resistance of F/M steels therefore encourages their use as structural materials for fusion reactors.

In this paper the results are presented of irradiation creep studies and short-term mechanical properties of two F/M steels, EP-450 (0.12C-13Cr-2MoVNbB) and EP-823 (0.16C-12Cr-MoWSiVNbB), irradiated up to 60 dpa in the BN-350 fast reactor at temperatures in the range 390-520°C. Data derived from these steels also serves to enhance our understanding of the general behavior of this class of steels.

Experimental Details

The chemical composition and final heat treatment of thin-wall cladding tubes (6.9 mm outer diameter, 0.4 mm wall thickness) made from EP-450 and EP-823 F/M steels are shown in Table 1. Two types of samples were constructed from these tubes and were used in the experiment: pressurized creep tubes (see Figure 1), and ring specimens of 2 mm in length cut from the tubes for measurement of mechanical properties. The creep tubes were filled with argon of 99.998% purity through a needle valve located in the large plug end to produce hoop stresses σ_h ranging from 0 to 294 MPa at the irradiation temperature.

* Pacific Northwest National Laboratory (PNNL) is operated for the U.S. Department of Energy by Battelle Memorial Institute under contract DE-AC06-76RLO-1830.

Table 1. Chemical composition of EP-450 and EP-823 F/M steels.

Steel	Content, wt %														
	C	Si	Mn	S	P	Cr	Ni	Mo	Nb	Ti	Al	V	B	N_2	Others
EP-450	0.14	0.20	0.31	0.009	0.017	12.95	0.20	1.54	0.47	-	-	0.22	0.004	-	-
	Heat treatment: solution treated 1050°C, 1s + aged 850°C, 5s.														
EP-823	0.18	1.05	0.60	0.008	0.012	11.40	0.70	0.67	0.20	0.03	0.03	0.40	0.004	0.04	W= 0.65 Ce= 0.01
	Heat treatment: normalization 1050°C, 15 min + tempering 740°C, 1 h.														

Figure 1. Argon-pressurized creep tubes irradiated in BN-350 reactor. All dimensions are given in mm.

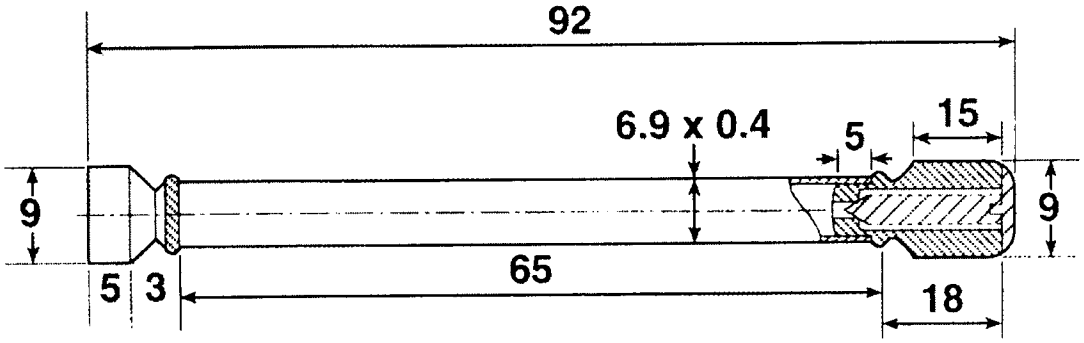

The creep tubes were irradiated in the BN-350 fast reactor (Kazakhstan) for 9430 h in two experimental assemblies located in the fifth row of the low enrichment zone. Each of the two assemblies operated over a different temperature range (390-410 and 480-520°C), with the temperature calculated based on prior measurements. At the core midplane this corresponds to a maximum total neutron fluence of 1.9×10^{23} n/cm^2 (1.36×10^{23} n/cm^2 ($E>0.1$MeV)) or 60 dpa (NRT) for both assemblies. The tubes were placed in perforated cylindrical baskets of 76 mm diameter in direct contact with flowing sodium. In both assemblies the EP-450 tubes were located at three axial levels: basket #4 at 0 to +100 mm, basket #10 at +300 to +400 mm, and basket #15 of +650 to +750 mm, all measured from the core midplane. EP-823 tubes were located only in basket #4 of both assemblies, reaching 380 and 490°C.

Using short fuel pins placed in the bottom part of the assemblies allowed heating of the baskets to their operating temperature. The irradiation conditions for each basket are shown in Table 2. Concurrent with the reactor tests, several tubes fabricated from EP-450 and EP-823 steels were tested outside the reactor for 9800 h at temperatures of 400°C and 500°C and at the same levels of hoop stress.

Table 2. Irradiation conditions for creep tubes in the BN-350 fast reactor.

basket #	4	10	15
assembly #1 $T_{irr.}$, °C	390±10	400±10	410±10
assembly #2 $T_{irr.}$, °C	480±10	500±10	520±10
ϕt, 10^{23}n/cm^2 E>0	1.90	1.42	0.60
ϕt, 10^{23}n/cm^2 E>0.1 MeV	1.36	1.02	0.45
dpa	60	45	20
σ_h, MPa	0; 98; 196; 294	0; 98; 196; 294	0; 98; 196; 294

Ring specimens of 2 mm length for measurement of mechanical properties were irradiated in flowing sodium at 490±10°C to 50 dpa in only one assembly in basket #9, located at +260+300 mm. After irradiation, the tube surfaces were cleaned in 50% ethanol–water solution and the diameter was measured using a micrometer. The diameter of each creep tube was measured at the tube middle and also at the distance of 15 mm from each end of the tube for two orientations differing by a 90° rotation around the tube axis. The irradiation creep strain ε^{ic} was determined as the difference between the total diametral strain and the diametral strain due to swelling, determined by the strain of stress-free tubes. The irradiation creep modulus B_{ic} was determined from the following expression:

$$B_{ic} = \varepsilon^{ic}/0.75\sigma_h(\text{dpa}).$$

It should be noted that this modulus is a composite creep rate, containing transient creep, creep in the absence of swelling (defined as the creep compliance B_0) and the swelling–enhanced creep component, usually defined as DS_{dot}, where D is the creep-swelling coupling coefficient, and S_{dot} is the swelling rate. Unfortunately, there may also be some precipitation-related strains included as well.

The mechanical characteristics for both irradiated and non-irradiated ring specimens were measured using a shielded tensile testing machine at the test temperatures ranging from 20 to 700°C. The aging time at given temperature was 10 min for unirradiated specimens and 20 min for irradiated ones. Two or three separate specimens were tested at a given temperature.

Results

The thermal creep tests of surveillance tubes at 500°C for 9800 hours demonstrated that thermal creep strains in EP-450 could reach several percent, while those at 400°C were much smaller.

All irradiated creep tubes had no visible defects and were still gas-tight. The measured total diametral strain, irradiation creep strain and the irradiation creep moduli for EP-450 and EP-823 steels are shown in Tables 3 and 4. At 390°C the creep characteristics for these steels are essentially equal. At 480°C the irradiation creep strain is distinctly larger in EP-823. In Table 3 it can be seen that stress-free swelling of EP-450 has two possible temperature maxima, located at ~400°C and ~500°C. Interestingly, two temperature maxima, located at ~425°C and ~510°C have been observed in Ref. [3] for pure iron irradiated in DFR to 30 and 23 dpa at a dose rate higher by one order of magnitude.

Table 3. Irradiation creep characteristics for EP-450 steel.

σ_h, MPa	390°C/60 dpa			400°C/45 dpa			410°C/20 dpa		
	$\Delta d/d$, %	$\varepsilon_{ic.}$, %	B_{ic}, 10^{-6} Mpa^{-1} $\times dpa^{-1}$	$\Delta d/d$ %	$\varepsilon_{ic.}$, %	B_{ic}, 10^{-6} MPa^{-1} $\times dpa^{-1}$	$\Delta d/d$ %	ε_{ic}, %	B_{ic}, 10^{-6} MPa^{-1} $\times dpa^{-1}$
0	0.26	0	0	0.41	0	0	0.14	0	0
98	0.59	0.33	0.7	0.43	0.02	0.06	0.14	0	0
196	1.25	0.99	1.1	0.76	0.35	0.5	0.34	0.20	0.3
294	1.77	1.51	1.1	1.05	0.64	0.6	0.40	0.26	0.3
σ_h, MPa	480°C/60 dpa			500°C/45 dpa			520°C/20 dpa		
	$\Delta d/d$, %	ε_{ic}, %	B_{ic}, 10^{-6} MPa^{-1} $\times dpa^{-1}$	$\Delta d/d$ %	ε_{ic}, %	B_{ic}, 10^{-6} MPa^{-1} $\times dpa^{-1}$	$\Delta d/d$ %	ε_{ic}, %	B_{ic}, 10^{-6} MPa^{-1} $\times dpa^{-1}$
0	0	0	0	0.22	0	0	0	0	0
98	0	0	0	0.29	0.07	0.2	0.29	0.29	2.0
196	0.29	0.29	0.3	0.36	0.14	0.2	0.36	0.36	1.2
294	0.58	0.58	0.4	0.94	0.72	0.7	0.58	0.58	1.3

Table 4. Irradiation creep characteristics for EP-823 steel.

σ_h, MPa	390°C/60 dpa		
	$\Delta d/d$,%	$\varepsilon_{i.c.}$, %	B_{ic}, 10^{-6} MPa^{-1} $\times dpa^{-1}$
0	0.20	-	-
98	0.64	0.44	1.0
196	0.92	0.72	0.8
294	1.08	0.88	0.7
σ_h, MPa	480°C/60 dpa		
	$\Delta d/d$,%	$\varepsilon_{i.c.}$,%	B_{ic}, 10^{-6} Mpa^{-1} $\times dpa^{-1}$
0	0	0	0
98	0.09	0.09	0.2
196	0.14	0.14	0.2
294	1.85	1.85	1.4

The mechanical characteristics of EP-450 and EP-823 steels, both before and after neutron irradiation at 490±10°C to 50 dpa, are shown in Figures 2-5. The strength properties of EP-450 before and after irradiation at 490°C to 50 dpa do not differ significantly, and radiation-induced loss of elongation is only significant at higher test temperatures (Figures 2, 3). Neutron irradiation of EP-823 steel resulted in significantly more hardening and somewhat greater loss of ductility across a wider temperature range (Figures 4, 5). At test temperatures above 500°C a sharp decrease of strength was observed for these two steels in both the initial and irradiated conditions.

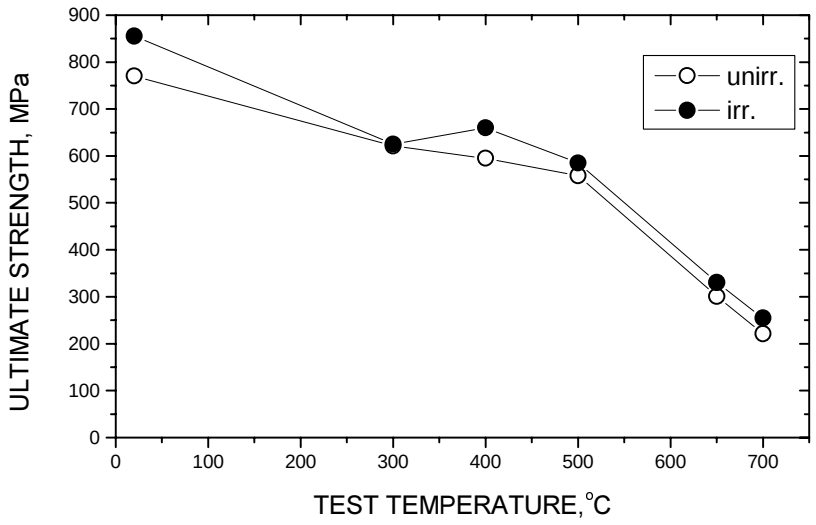

Figure 2. Ultimate strength for the EP-450 type steel as a function of test temperature after irradiation to 50 dpa at 490°C.

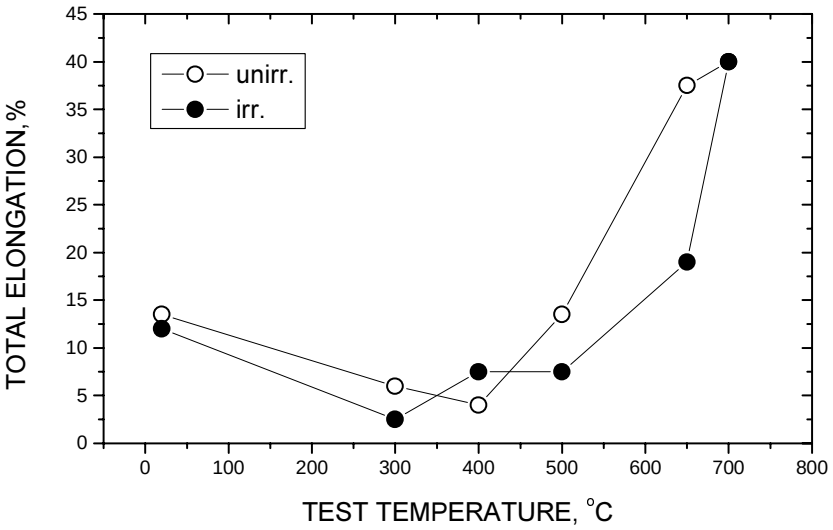

Figure 3. Total elongation for the EP-450 type steel as a function of test temperature after irradiation to 50 dpa at 490°C.

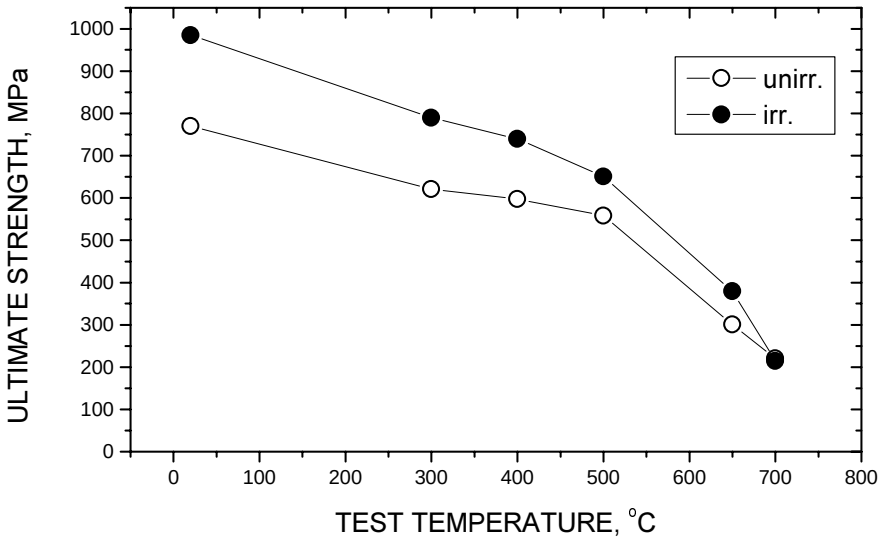

Figure 4. Ultimate strength for the EP-823 type steel as a function of test temperature after irradiation to 50 dpa at 490°C

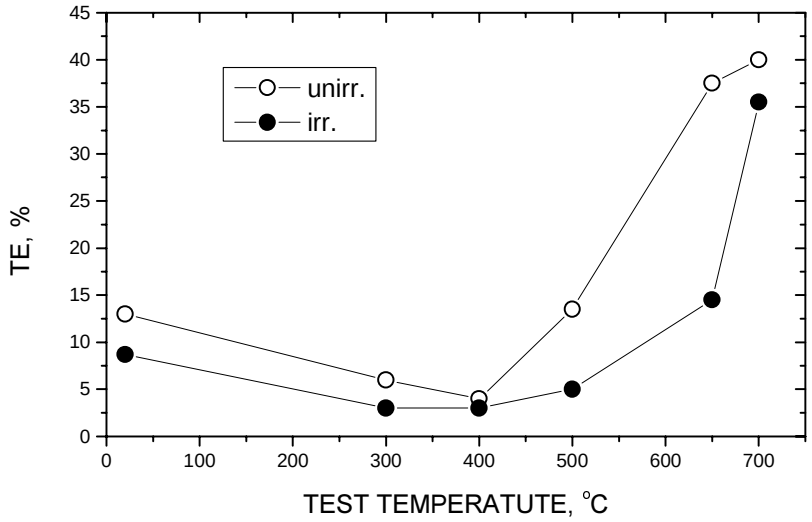

Figure 5. Total elongation for the EP-823 type steel as a function of test temperature after irradiation to 50 dpa at 490°C.

Discussion

Swelling of EP-450, as indicated by positive strains in the diameter of the unstressed tubes, appears only in the 390-420°C range, consistent with the reported behavior of other F/M steels. The maximum swelling appears to be ~1.2% at 400°C and 45 dpa, providing that the zero-stress strains do not include any contributions from precipitation. In the more limited

irradiation matrix of EP-823, there also appears to be some swelling on the order of ~0.6% at 400°C, but not at 500°C.

The temperature and stress dependencies of the irradiation creep modulus of EP-450 steel are shown in Figure 6. The rather low modulus observed at 98 MPa appears to signal the presence of negative strains arising from precipitate-related densification, also observed in some other F/M steels. It is also seen that at hoop stresses of 98, 196 and 294 MPa the modulus exhibits a flat minimum within the temperature range 410-480°C, with the modulus not exceeding 0.4×10^{-6} $(MPa\times dpa)^{-1}$ at the higher stress levels in this temperature range. There appears to be no significant swelling at these temperatures.

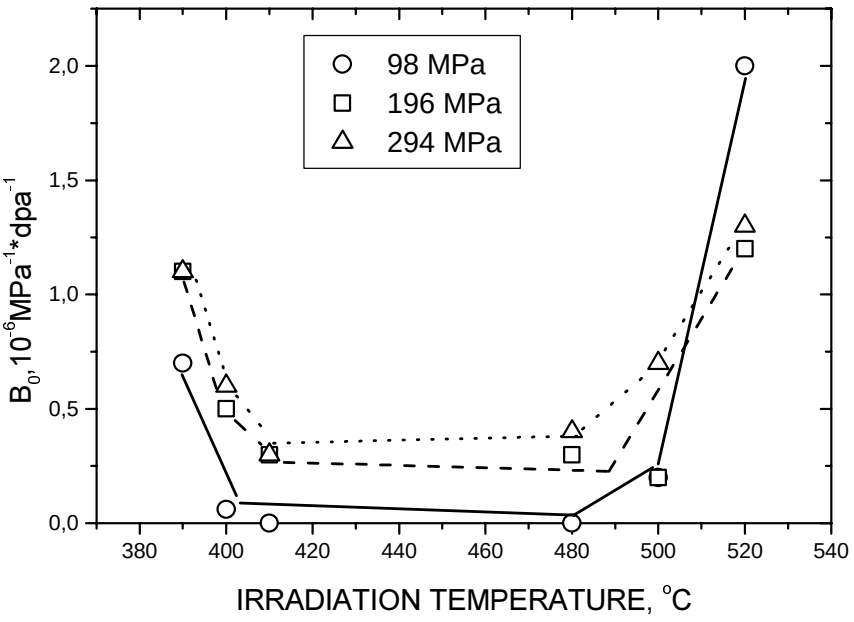

Figure 6. Creep compliance for the EP-450 type steel versus the irradiation temperature for three stress levels.

This low modulus value is one-third to one-half that routinely observed in austenitic steels (4) and is also consistent with moduli measured on other F/M steels in the absence of swelling, as summarized by Toloczko and Garner, who note that the creep compliance B_0 is on the order of 0.5×10^{-6} $(MPa\times dpa)^{-1}$ in HT9, 9Cr-1Mo and other F/M steels, especially when densification is not operating (5-9).

The observation of moduli larger than this value at temperatures below 410°C reflects the onset of the DS_{dot} contribution of irradiation creep. Since swelling in F/M steels has been observed to be enhanced by applied stress (5), it is assumed that a similar stress-dependency may be operating in this experiment. When added to the apparent densification proceeding in this steel, this complicates a separation of the B_0 and DS_{dot} contributions. Toloczko and Garner have earlier shown that the creep-swelling coupling coefficient of F/M and austenitic steels are essentially equal, unlike the difference observed in B_0 (7).

It is thought to be particularly significant that the EP-450 and EP-823 steels exhibited very consistent creep behavior at both 390 and 500°C, even though there are substantial differences in composition. This tends to confirm once again that the B_0 component of

irradiation creep is relatively insensitive to composition and starting state within a given alloy class, as observed in both austenitic and F/M steels (4, 8, 9).

With increasing irradiation temperature to 520°C the irradiation creep modulus EP-450 increases to 2×10^{-6} $(MPa\times dpa)^{-1}$. A similar temperature dependence of the irradiation creep modulus of EP-450 steel has been found in measurements of hexagonal wrappers of sub-assemblies in BN-600 fast reactor [10] and in the studies of Toloczko et al. on HT9 (8,9). An increase of the irradiation creep modulus of EP-450 at irradiation temperatures higher than 500°C is thought to be due to decreases in its strength characteristics in this temperature region, and the onset of greater-than-linear creep, as was also observed in HT9 (8,9). The relatively large strains observed at 500°C in the thermal control specimens supports this interpretation.

Measurements of short-term mechanical properties of EP-450 steel have revealed that irradiation hardening of this steel is relatively insignificant at the irradiation temperature of 500°C. This observation is in agreement with data obtained earlier in examination of EP-450 fuel pin cladding after irradiation in BN-350 [11]. For EP-823 steel the radiation-induced increase of ultimate strength is slightly higher (225 MPa). With increasing test temperature a sharp decrease of ultimate strength from 600 MPa at 500°C to 200 MPa at 700°C is observed in both steels. Similar behavior is observed in most other F/M steels.

Conclusions

The Russian ferritic/martensitic steels EP-450 and EP-823 have served as structural components in various fission reactors and may serve in future fusion devices. Data derived from these steels also serves to enhance our understanding of the general behavior of this class of steels. It appears that these steels exhibit behavior that is very consistent with that from Western steels. Swelling is relatively low at high neutron exposure and confined to temperatures <420°C, but may be camouflaged somewhat by precipitation-related densification. These irradiation creep studies confirm that the creep compliance of F/M steels is about one-half that of austenitic steels, and that the loss of strength at test temperatures above 500°C is a problem generic to all F/M steels.

Measurements of short-term mechanical properties for irradiated steels have shown, that at test temperatures below 500°C both steels retain their high strength ($\sigma_{0,2}$=550-600 MPa), but at higher test temperatures a sharp decrease of strength properties occurs. However, the irradiated steels still retain high ductility at test temperatures in the range of 20-700°C.

ACKNOWLEDGEMENTS

The Civilian Research and Development Foundation under Grant RE2-2224 sponsored the Russian portion of this work. The Office of Fusion, U.S. Department of Energy provided support for the U.S. portion of this research under contract DE-AC06-76RLO 1830 with Battelle Memorial Institute.

REFERENCES

[1] V. S. Khabarov, V. D. Dmitriev, A. M. Dvoriashin, V. V. Romaneev, E. A. Medvedeva, “Mechanical properties and microstructure of neutron-irradiated ferritic-martensitic steel, used as wrapper material for the BN-350 and BN-600 fast reactor”, Proceedings of International Conference“ Fast reactor core and fuel structural behavior ”, Inverness, 4-6 June 1990, p.p. 263-267.

[2] A. G. Ioltukhovski, et. al., “Material science and manufacturing of heat-resistant reduced-activation ferritic-martensitic steels for fusion”, Journal of Nuclear Materials, 283-287 (2000), 652-656.

[3] E. A. Little and D. A. Stow “Void swelling in iron and ferritic steels. II. An experimental survey”, Journal of Nuclear Materials, 1973, Vol. 87, No. 1, pp. 25-39.

[4] F. A. Garner, Chapter 6: "Irradiation Performance of Cladding and Structural Steels in Liquid Metal Reactors," Vol. 10A of Materials Science and Technology: A Comprehensive Treatment, VCH Publishers, 1994, pp. 419-543.

[5] M. B. Toloczko, F. A. Garner, and C. R. Eiholzer, "Irradiation Creep and Swelling of the U.S. Fusion Heats of HT9 and 9Cr-1Mo to 208 dpa at ~400°C," J. of Nucl. Mater., 212-215 (1994) 604-607.

[6] M. B. Toloczko and F. A. Garner, "Irradiation Creep and Void Swelling of Two LMR Heats of HT9 at ~400°C and 165 dpa", J. of Nucl. Mater., 233-237 (1996) 289-292.

[7] M. B. Toloczko and F. A. Garner, "Variability of Irradiation Creep and Swelling of HT9 Irradiated to High Neutron Fluence at 400-600°C", Effects of Radiation on Materials: 18th International Symposium, ASTM STP 1325, R. K. Nanstad, M.. Hamilton, F. A. Garner and A. S. Kumar, Eds., American Society of testing and Materials, 1999, pp.765-779.

[8] M. B. Toloczko, F. A. Garner and C. R. Eiholzer, “Irradiation Creep of Various Ferritic Alloys Irradiated at ~400°C in the PFR and FFTF Reactors”, J. of Nucl. Mater., 258-263 (1998), pp. 1163-1166.

[9] M. B. Toloczko, B. R. Grambau, F. A. Garner and K. Abe, “Comparison of Thermal Creep and Irradiation Creep of HT9 Pressurized Tubes at Test Temperatures from ~490°C to 600°C”, Proceedings of Symposium on Effects of Radiation on Materials, 20th International Symposium, ASTM STP 1405, S. T. Rosinski, M. L. Grossbeck, T. R. Allen, and A. S. Kumar, Eds., American Society for Testing and Materials, West Conshohocken, PA, 2002, pp. pp. 557-569.

[10] L. V. Zabudko, I. N. Kravchenko, O. S. Korostin, A. N. Ogorodov, “Analysis of the BN-600 reactor subassemblies operating experience”, Proc. of Inter. Conf. “ Fast reactor core and fuel structural behavior ”, Inverness, 4-6 June 1990, p.p. 289-292.

[11] A. M. Dvoriashin, V. D. Dmitriev, V. S. Khabarov, “The Effect of Neutron Irradiation on the Microstructure and Tensile Properties of 1Cr13Mo2NbVB Steel”, Effects of Radiation on Materials: 15th International Symposium, ASTM STP 1125, R. E. Stoller, A. S. Kumar, and D. S. Gelles, Eds., American Society for Testing and Materials, Philadelphia, 1992, pp. 1180-1189.

EFFECT OF CHROMIUM, TUNGSTEN, TANTALUM, AND BORON ON MECHANICAL PROPERTIES OF 5-9Cr-WVTaB STEELS—R. L. Klueh, M. A. Sokolov (Oak Ridge National Laboratory), and D. J. Alexander (Los Alamos National Laboratory)

Paper was presented at the 10th International Conference of Fusion Reactor Materials, October 14-19, 2001, Baden-Baden, Germany, and submitted for publication in the *Journal of Nuclear Materials*

Extended Abstract

The reduced-activation ferritic/martensitic steels use tungsten and tantalum as substitutes for molybdenum and niobium in the Cr-Mo steels that the reduced-activation steels replaced as candidate materials for fusion reactor applications. Studies were made to determine the effect of the composition of these elements on the properties of the steels. Chromium variations were also studied. Boron has a long history of use in steels to improve properties, and the effect of boron was also examined. Such information will be of use if the properties of the reduced-activation steels are to be optimized.

The effect of Ta, W, B, and Cr composition in Cr-2WV reduced-activation steels was investigated in the normalized-and-tempered (tempered at 700 and 750ºC) condition. Steels with 5, 7, and 9% Cr were examined, to determine the effect of increasing tungsten from 2 to 3%, changing tantalum from 0 to 0.1%, and changing boron from 0 to 0.013%. The effect of W, Ta, and B was investigated for the 5Cr steel, W and B for the 7Cr steel, and Ta and B for the 9Cr steel.

The following are the nominal compositions of the heats of steel used in this experiment:

(1) Fe-5Cr-2W-0.25V-0.1C (designated 5Cr-2WV),
(2) the 5Cr-2WV with 0.5% Ta (5Cr-2WVTa1),
(3) the 5Cr-2WV with 0.1% Ta (5Cr-2WVTa2),
(4) an Fe-5Cr-3W-0.25V-0.1C (5Cr-3WV),
(5) the 5Cr-3WV with 0.05% Ta (5Cr-3WVTa1),
(6) the 5Cr-3WVTa1 with 0.005% B (5Cr-3WVTa1B1),
(7) the 5Cr-3WVTa1 with 0.013% B (5Cr-3WVTa1B2),
(8) an Fe-7Cr-2W-0.25V-0.05Ta-0.1C (7Cr-2WVTa),
(9) an Fe-7Cr-3W-0.25V-0.05Ta-0.1C (7Cr-3WVTa),
(10) the 7Cr-2WVTa with 0.005% B (7Cr-2WVTaB),
(11) Fe-9Cr-2W-0.25V-0.1C (9Cr-2WV), and
(12) the 9Cr-2WV with 0.07% Ta (9Cr-2WVTa).

Results of the study are summarized as follows:

Tantalum Effect: Ta had a positive effect on strength and DBTT of the 5Cr and 9Cr steels. The USE was not affected by Ta for either steel.

Tungsten Effect: 3% W instead of 2% W in the 5Cr steels had no effect on strength in the absence of Ta. For 0.05% Ta, there was little effect after the 700ºC temper, but there was a positive effect when tempered at 750ºC. 3% W improved the DBTT for the 5% Cr steel after a 750ºC temper and had a slight effect on the 7% Cr steel after a 700ºC temper. The USE was unaffected by W in the 5Cr and 7Cr steels.

Boron Effect: B had no favorable effect on the properties of the 5 and 7% Cr steels but did favorably affect the strength and impact properties of 9Cr-2WVTa.

Chromium Effect: The 5Cr-2WVTa and 9Cr-2WVTa steels with 0.05% Ta appeared to be near the optimum composition for the compositions examined. After tempering at 750ºC, there was no

difference in the strength and ductility of the 5Cr-2WVTa and 9Cr-2WVTa, and they were superior to 7Cr-2WVTa. A composition of 7.5-9Cr-2WVTa has been accepted in the literature as best for future fusion applications. If the apparent minimum in strength between 5 and 9% Cr is an accurate representation, then steels with at least 9% Cr should be used. For the 5Cr-2WVTa, 7Cr-2WVTa, and 9Cr-2WVTa steels, the 5Cr-2WVTa had a clear advantage. The DBTT and USE of this steel after tempering at 700ºC are as good or better than those of the 7Cr-2WVTa and 9Cr-2WVTa tempered at 750ºC. Since 9Cr-2WVTa needs to be tempered at 750ºC for adequate toughness, the 5Cr-2WVTa steel may have advantages in both strength and impact toughness in the unirradiated condition.

4.0 COPPER ALLOYS

OVERAGING OF OUTOKUMPU CuCrZr AT 600°C - D. J. Edwards (Pacific Northwest National Laboratory)* and B.N. Singh (Risø National Laboratory)

OBJECTIVE

The objective of this work is to study the effect of overaging on the microstructure of CuCrZr, its effects on mechanical properties, and how it affects performance under neutron irradiation.

SUMMARY

An attempt is being made to alter the starting microstructure of CuCrZr to produce a microstructure that is not as sensitive to overageing under irradiation as the prime aged condition. Different overageing conditions (600, 700 and 800°C for 4 hours) have been examined in an earlier report, and in this report shorter overageing times at 600°C have been examined. Overageing times of 1 and 2 hours resulted in a microstructure that is similar in overall precipitate size and density to that of the oxide dispersion in GlidCop Al25. These samples will be included in future irradiation experiments to examine the effects of irradiation on the mechanical and physical properties.

PROGRESS AND STATUS

Introduction

Precipitation strengthened CuCrZr is a copper alloy being considered for use in fusion reactor devices due to its thermal and electrical conductivity coupled with reasonable strength and fracture toughness [1-6]. Other alloys such as the oxide dispersion strengthened GlidCop Al25 and the precipitation strengthened CuNiBe, the highest strength alloy by a wide margin, have also been evaluated. These latter two alloys lack the required mechanical properties at irradiation temperatures above ~250°C due to a transition in how they begin to fail. For example, in the extreme case the CuNiBe alloy loses all semblance of ductile failure and fails by brittle intergranular cracking along the grain boundaries at very low stresses. In contrast to this behavior, the CuCrZr alloy remains ductile throughout the same temperature range and maintains reasonable fracture toughness.

While CuCrZr can be heat treated to reasonable strength levels, precipitate stability becomes a serious issue when the irradiation temperature exceeds ~280°C [4]. At this irradiation temperature and higher, the fine-scale precipitate microstructure begins to overage due to enhanced diffusion and cascade dissolution of the precipitates. The coarsening of the precipitates degrades the strength to unacceptable levels, and if the temperature and dose are high enough, can eventually lead to swelling. Part of the problem lies in the small size of the precipitates as related to the volume of a displacement cascade. The precipitates in a prime aged CuCrZr are typically on the order of a 1-4 nm in average size, smaller than or on the order of the size of the displacement cascades formed during neutron irradiation. The small size of the precipitates allows ballistic dissolution to dissolve some of the precipitation and place solute back in solution. As the irradiation temperature increases, the dissolution and enhanced diffusion under irradiation lead to precipitate coarsening in CuCrZr. The variables involved are complex and not completely understood, but phase stability (oxide particles versus lower temperature intermetallic phases as an example) as a function of irradiation temperature can play an important role in how the dispersion changes with irradiation conditions.

* Pacific Northwest National Laboratory (PNNL) is operated for the U.S. Department of Energy by Battelle Memorial Institute under contract DE-AC06-76RLO-1830.

One approach to improve the stability of the microstructure during irradiation is to alter the starting precipitate size and density with the hope of achieving a balance between the radiation-induced dissolution of the precipitates and the subsequent redistribution of solute. A starting point would be to recognize that the ODS GlidCop alloy possesses an oxide dispersion that is extremely stable under irradiation up to temperatures of 450°C at very high doses. The average size of these particles is around 7 nm with a density of ~10^{22} m^{-3}, about an order of magnitude lower than in the prime aged CuCrZr [7]. The oxide particles are thermally stable up to high temperatures, which likely won't be the case for the precipitates in the CuCrZr. However, a coarser distribution of precipitates in the CuCrZr may achieve a microstructure more resistant to changes under irradiation, or at least postpone any serious degradation in mechanical and physical properties.

To that end, an experiment has been initiated wherein different ageing treatments have been explored to alter the starting microstructure of the CuCrZr. The preliminary analysis of the microstructure has been reported in an earlier semi-annual report [7]. Ageing conditions of 850, 700 and 600°C for 4 hours were given to samples of CuCrZr. The highest ageing temperature essentially left the material in a solution annealed condition with only a few large inclusions present in the microstructure. Both the 700 and 600°C ageing treatments however, produced a very coarse distribution of blocky precipitates with an average size of ~40 and 20 nm respectively. The density of these precipitates was on the order of 0.7 x 10^{21} m^{-3} for the 700°C treatment and 1.5 x 10^{21} m^{-3} for the 600°C treatment. The average sizes of particles represent a size distribution considerably more coarse than the precipitates that are present in the ODS alloy GlidCop Al25. Shorter ageing times were therefore given to the CuCrZr to further explore the possibility of producing a dispersion similar in density and size to that of the GlidCop.

In the following brief report, the results of overageing at 600°C for 1 and 2 hours will be presented. These results will be compared to the results obtained for the 4-hr aging treatments.

Experimental

Tensile specimens fabricated from Outokumpu CuCrZr (produced by Outokumpu Oy) were given three separate heat treatments to study the effect of overageing on the microstructure and mechanical properties. The heat treatments are listed below in Table 1. All heat treatments were done in vacuum (<10^{-4} torr). The microstructure was examined by transmission electron microscopy using a JEOL 2000FX.

TABLE 1 Heat treatments used to study overaging in Outokumpu CuCrZr

Prime Aged (PA): Solution annealed at 960°C / 3 hrs / WQ + aged 460°C / 3 hrs / WQ
600°C treatment: PA + 600°C / 4hrs / WQ
600°C treatment: PA + 600°C / 2hrs / WQ
600°C treatment: PA + 600°C / 1hrs / WQ

Results and Discussion

The overageing at 600°C for 1 and 2 hours produced a different precipitate distribution compared to the 4 hour overageing treatment reported earlier [1]. Micrographs are shown in Figure 1 giving examples of the different microstructures produced by the 3 different ageing times. The size distributions shown in Figure 2 illustrate the differences as a result of the shorter overageing times. The 1 and 2-hr treatment yielded a size distribution with a noticeably smaller average size and a narrower distribution than that produced in the 4-hr treatment. The shorter overageing times yield a size distribution similar to that of the GlidCop Al25. Grain boundary

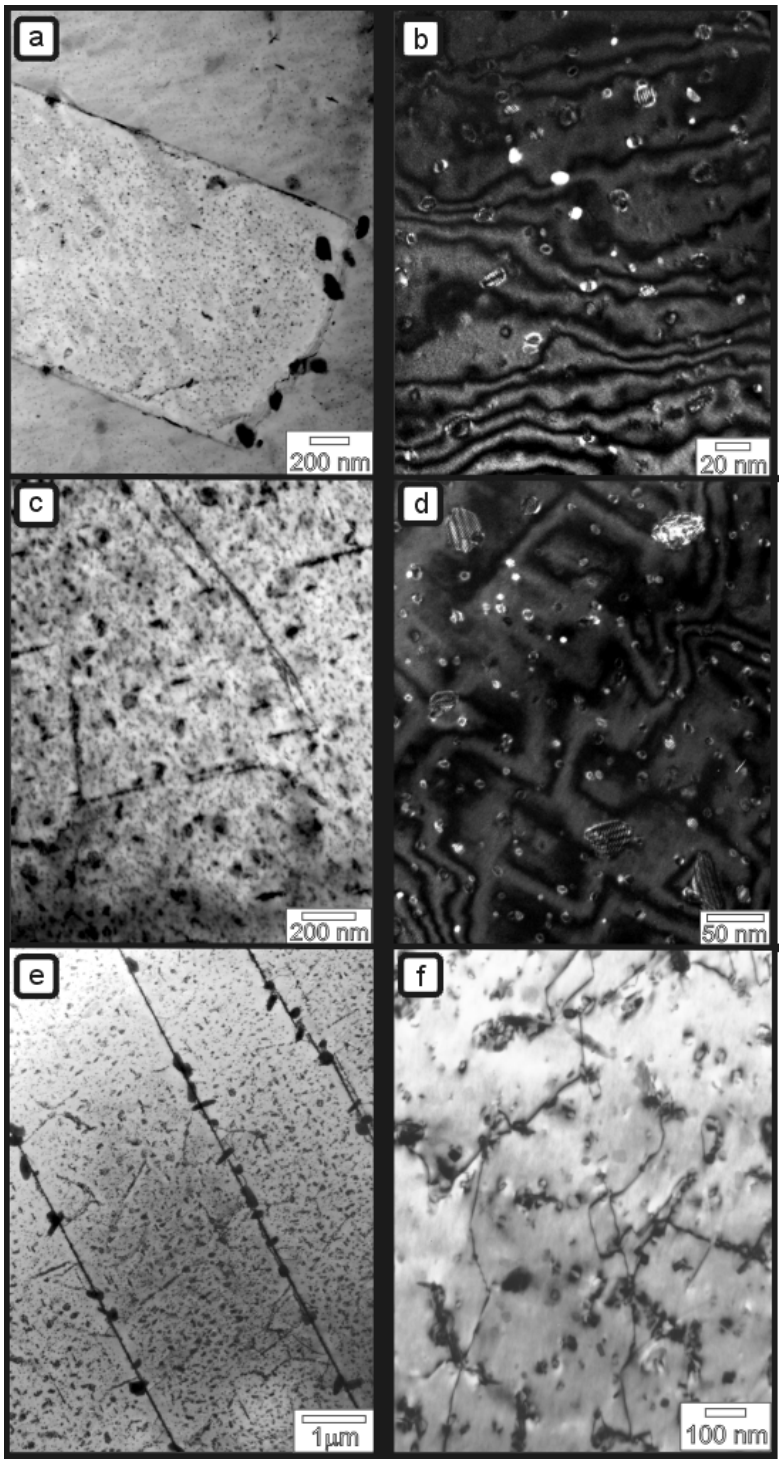

Figure 1. Comparison of the precipitate microstructure after overageing at 600°C for 1, 2 and 4 hours. The micrographs in (a) and (b) are for the 1-hr treatment, (c) and (d) are for the 2-hr treatment, and (e) and (f) are for the 4-hr treatment shown in the previous report [7].

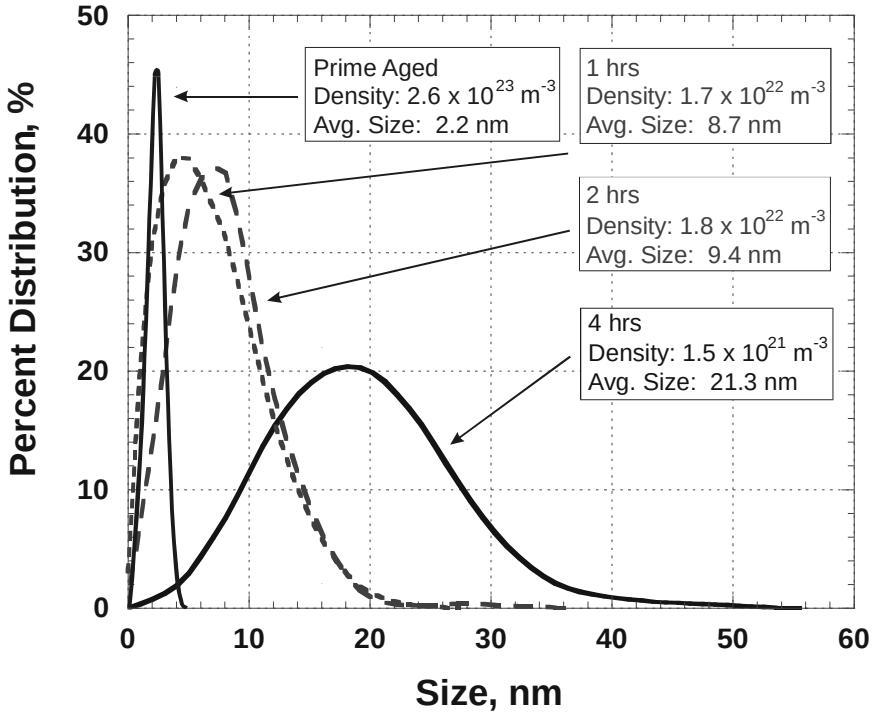

Figure 2. Size distributions are shown for the CuCrZr in the prime aged condition and after being overaged for 1, 2 and 4 hours. Note that the 1 and 2-hr treatments produce a size and density similar to that measured for the GlidCop Al25 alloys in the unirradiated condition (average size ~7 nm, density ~10^{22} m^{-3}).

precipitation and denuding along these areas occurred in all overageing conditions. Precipitation was also found to occur along annealing twins as shown in Figures 1a and 1e.

FUTURE WORK

Further work is necessary to characterize the precipitate types that have formed in the different aging treatments. Samples of the unirradiated material will be shipped to PNNL to be characterized in the 2010 Field Emission Gun ATEM. Tensile testing and electrical resistivity measurements will be conducted at Risø on the unirradiated samples to determine the effect of the aging treatments and how it relates to the observed microstructure. Samples will also be included in future irradiation experiments to study the effect of irradiation on the microstructure, mechanical and physical properties.

ACKNOWLEDGEMENTS

The present work was partly funded by the European Fusion Technology Programme. The authors wish to thank B. F. Olsen, N.J. Pederson and J.L. Lindbo. DJ Edwards would like to thank Risø National Laboratory for the support and assistance during his visit. His work was also partly supported by the U.S. Department of Energy under contract DE-AC06-76RLO 1830 with the Battelle Memorial Institute at the Pacific Northwest National Laboratory.

REFERENCES

1. S. A. Fabritsiev, A. S. Pokrovsky, S. J. Zinkle, D. J. Edwards, J. Nucl. Mater. 233-237 (1996) 513.

2. B. N. Singh, D. J. Edwards, M. Eldrup and P. Toft, Effect of Bonding and Bakeout Thermal Cycles on the Properties of Copper Alloys Irradiated at 350°C, Risø-R-971 (EN), Risø National Laboratory, Roskilde, Denmark, September (1997).

3. D. J. Edwards, B. N. Singh, P. Toft, and M. Eldrup, J. Nucl. Mater. 258-263 (1998) 978.

4. A. F. Rowcliffe, S. J. Zinkle, J. F. Stubbins, D. J. Edwards, and D. J. Alexander, J. Nucl. Mater. 258-263 (1998) 183.

5. S. J. Tähtinen, M. T. Pyykkönen, B. N. Singh and P. Toft, Proceedings of the 19th International Symposium on the Effects of Radiation on Materials, ASTM STP 1366, eds. M. L. Hamilton, A. S. Kumar, S. T. Rosinski and M. L. Grossbeck, (2000), p. 1243.

6. D. J. Edwards, J. W. Newkirk, F. A. Garner, M. L. Hamilton, A. Nadkarni and P. Samal, Proceedings of the 16th International Symposium on the Effects of Radiation on Materials, ASTM STP 1175, eds. A. S. Kumar, D. S. Gelles, R. K. Nanstad and E. A Little, (1993), p. 1041.

7. D. J. Edwards and B. N. Singh, Fusion Materials Semiannual Progress Report for Period Ending June 30, 2000 pp. 176-182.

5.0 REFRACTORY METALS AND ALLOYS

No contributions.

6.0 AUSTENITIC STAINLESS STEELS

No contributions.

7.0 MHD INSULATORS, INSULATING CERAMICS AND OPTICAL MATERIALS

An In-situ Calcium Oxide Coating on Vanadium Alloys in Liquid Lithium-Calcium*

J.-H. Park, K. Natesan, and D. L. Smith (Argonne National Laboratory)

OBJECTIVE

The objective of this task is to develop in-situ stable coatings at the liquid metal/structural-materials interface in a fusion device, with emphasis on coatings that can be converted to an electrically insulating film to prevent adverse currents generated by the magnetohydrodynamic force from passing through the structural walls. The thermodynamics and kinetics of oxygen and calcium interactions in the vanadium alloy/lithium system are being investigated to define the system parameters required for in-situ formation of a CaO coating on vanadium alloys. In addition, other potential coating candidates, such as Y_2O_3 and AlN, are being examined.

SUMMARY

Calcium oxide coatings were produced on oxygen-charged vanadium alloys (V, V-10Cr, V-1Ti, V-4Cr-4Ti, and V-5Cr-5Ti) by exposure to liquid Li that contained 2.8 at.% Ca. The thickness of in-situ-formed CaO layers was larger in the samples with higher oxygen charging. In the experimental conditions used, the thickness of the grown CaO films was 8-30 μm. For the CaO coating on V-4Cr-4Ti, the measured ex-situ dc-electrical conductivity was 3.0×10^{-10} to 1.0×10^{-8} $ohm^{-1}cm^{-1}$ in an Ar environment in the temperature range 200-500˚C.

INTRODUCTION

One of the most challenging areas for magnetic fusion reactors (MFR) is developing plasma-facing systems that can withstand high surface heat fluxes and neutron wall loads. Several electrically insulating oxides, such as binary oxides (CaO, BeO, MgO, Y_2O_3), ternary perovskite ($CaZrO_3$), spinel ($MgAl_2O_4$), and nitrides (AlN), have promise as coatings on a V alloy for application in liquid-lithium MFR-blanket systems. We have chosen the development of in-situ CaO film deposition on the vanadium alloys for the following reasons: CaO is thermodynamically stable in liquid Li, has the highest electrical resistivity desirable for a thin film, forms in-situ, and has potential for healing of defects (microcracks, open pores, etc.)[1,2] Based on its high thermodynamic stability, CaO can be formed in-situ to heal most of the defects in the insulator coatings that may arise in service.

The main reaction can be stated as Ca + O = CaO, where Ca dissolves in liquid Li and then reacts with O near the surface of V alloys to form CaO. The CaO layer grows based on the inward ambipolar diffusion of Ca^{2+} ion and the two electrons through the CaO layer to react with the O in the V alloys at the CaO/V interface. The O accepts two electrons to form O^{2-} ions, and reacts with Ca^{2+} ions to form CaO. As a result, the CaO layer is dynamically adhesive, and O levels decrease in the V alloys. It is expected that the reaction rate of will increase under neutron fluency. Additionally, CaO has low activation with neutron bombardment. Both Li and Ca-Li as liquid metals do not interact heavily with V alloys.

The present study involves in-situ CaO film fabrication at 600 and 700°C in 2.8 at.% Ca-Li on vanadium metal and the alloys V-10Cr, V-1Ti, V-4Cr-4Ti, and V-5Cr-5Ti. We have investigated step-by-step procedures for O charging and homogenization, and determined O-migration profiles before and after Ca-Li exposure in O-charged V alloys. This reporting period our work focused on the V-4Cr-4Ti alloy with CaO coating.

EXPERIMENTAL DETAILS

Samples of V-4Cr-4Ti were prepared in a rectangular shape (2 x 1 x 0.1 cm) with a 1 mm-diameter hole for the attachment. Samples were vacuum-annealed at 1000°C for 2 h, then heated at 710°C in Ar-O_2 to reach a proper amount of O charge, then O homogenized in a vacuum-sealed (quartz) cell for 17 h at 750°C. Details are given in our previous reports.[1-3]

Several samples were arrayed together, then dipped into a Ca-Li vessel at 600°C for times between 50 and 747.5 h. The sample tree was raised above the liquid-Ca-Li level and shaken to minimize residual Ca-Li around the samples. The excessive Ca-Li was dissolved in methanol to investigate the surface and cross section by scanning electron microscopy (SEM), X-ray diffraction (XRD), and energy dispersive spectroscopy (EDS). Ex-situ electrical conductivity measurements were performed for the samples exposed in 2.8 at.% Ca-Li after removal of the residual Ca-Li around the sample in the alcohol. For these measurements, metallic gallium was used as electrodes on two platinum discs in the top and bottom positions (see Fig. 1). Liquid gallium on the coating was not wet at room temperature, but the gallium was well adhered on the platinum discs for the electrical conductivity measurement. However, when the CaO-coated V alloys were placed between two gallium electrodes and a spring load applied, the excessive gallium extruded out around the sample-platinum edge. This excess gallium was removed before the entire stack was inserted into the measuring assembly. The electrical conductivity measurements were performed in 99.996% Ar at 25°C ≤ T ≤ 500°C, and the supplied current, i, was ≤ 1 x 10^{-6} A. Our instrumentation limit was an input impedance of 1 M-ohm and voltage range of 10 V.

DISCUSSION

During O charging, a blue surface layer of thin vanadium oxide appeared. However, with O homogenization, the sample surface became shiny metallic looking. It can be assumed that surface oxygen entered into the V alloy by solid-state diffusion. For the EDS analysis, O in the V-alloy system causes a problem if the vanadium (or Ti and Cr) concentration is too high. Since the oxygen k-energy level and the V-(Cr-Ti) l-energy level are too close for separation in the EDS analysis, determination of O is possible only when the vanadium concentration is low in comparison with oxygen. In the near future, we plan O analysis of the V alloy by secondary ion mass spectroscopy (SIMS).

According to cross-sectional EDS analysis and SEM photomicrographs, the thickness of the adhered CaO layer formed at 600°C for 120 h on V-4Cr-4Ti alloy is 8 μm. The SEM view and back-scattered electron image revealed a uniform thickness of the in-situ-formed CaO film on the V alloy. While performing the EDS analysis, we found that the interface area had a somewhat higher O concentration than that in the overall CaO layer. This higher O concentration is quite understandable because calcium reacts with the oxygen provided by the V alloy. This trend is promising for in-situ formation of CaO layers on the V alloys because the higher O concentrations mean that higher electrical resistivity is expected.

Figure 2 shows the XRD patterns for (a) physical vapor deposition (PVD) of CaO on O-charged V-4Cr-4Ti and in-situ formation of CaO on (b) V-4Cr-4Ti at 700°C for 50 h, (c) V-1Ti at 600°C for 120 h, and (d) V-5Cr-5Ti at 600°C for 120 h, (For items b-d, the O-charged V alloys were exposed to molten 2.8 at.% Ca-Li.) The results indicate that the PVD CaO coating is generally pure CaO, whereas the in- situ CaO coatings are structurally not similar to that developed by PVD, irrespective of the substrate composition. Presumably, an amorphous CaO film was formed in-situ in the liquid Li-Ca environment. Additional ongoing effort will examine the causes for this difference.

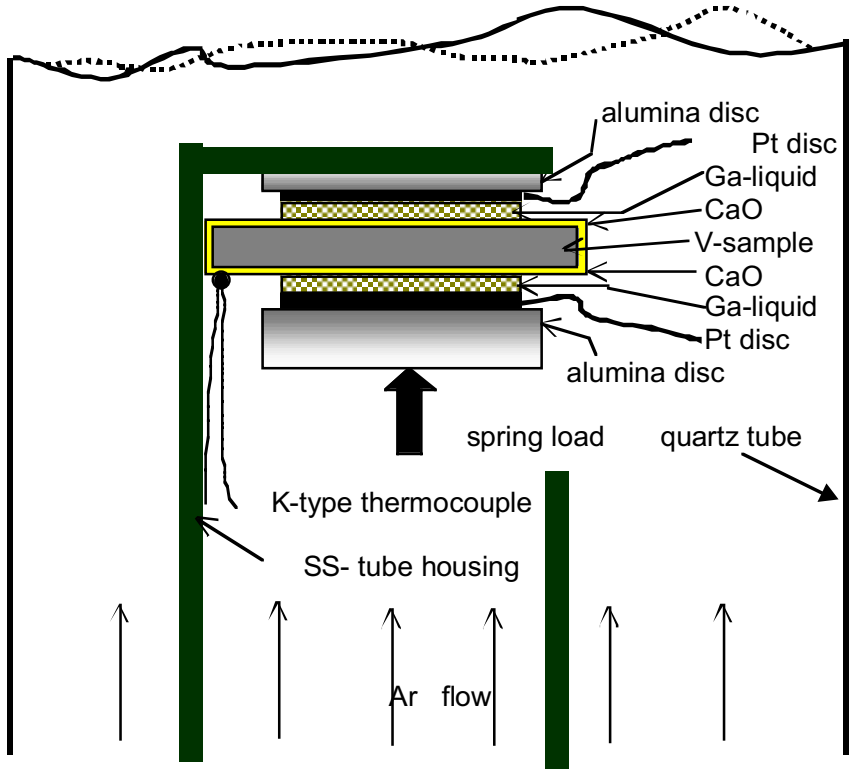

Fig. 1. Experimental setup used for resistance measurements on in-situ CaO coatings.

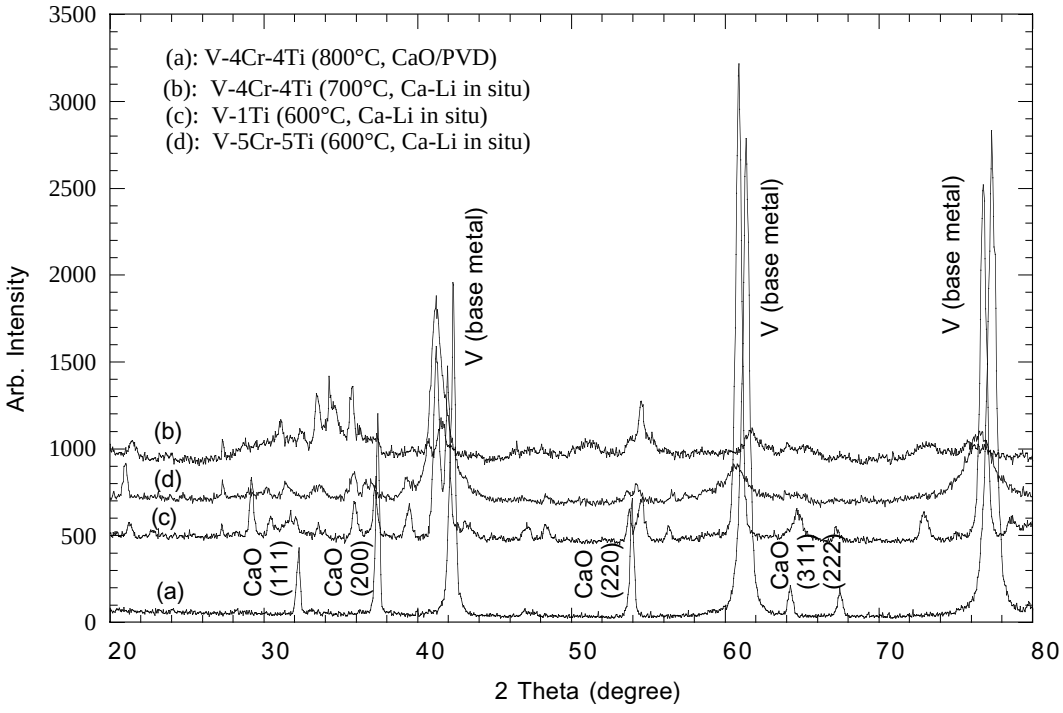

Fig. 2 XRD patterns for (a) PVD/CaO on O-charged V-4Cr-4Ti, and in-situ CaO on (b) V-4Cr-4Ti at 700°C for 50 h, (c) V-1Ti at 600°C for 120 h, and (d) V-5Cr-5Ti at 600°C for 120 h. For patterns b-d, the O-charged V alloys were exposed in-situ to 2.8 at.% Ca-Li.

The in-situ grown film contains Li based on our previous SIMS work. Lithium is oxidized when exposed to oxygen, carbon dioxide, or moisture by the reaction, $2Li + 1/2\ O_2 = Li_2O$, $2Li + 1/2O_2 + CO_2 = Li_2CO_3$, or $2Li + 1/2\ O_2 + H_2O = 2LiOH$, respectively. The generated Li ion is highly mobile in the solid state. Therefore, the Li ion under an electric field becomes very sensitive to field polarity and will be polarized through the film layer. When polarized, the Li makes an open circuit and follows a strong dc dry-battery behavior. Figure 3a shows the polarization behavior for a switching polarity with 10-s intervals. Figure 3b shows the temperature and iR-drop (dc i = ±1 μa) potential monitored as a function of time during the conductivity measurement of the CaO coating on oxygen-charged V-4Cr-4Ti.

Figure 4 shows the electrical conductivity and resistivity vs. reciprocal temperature for the sample prepared initially from oxygen charged V-4Cr-4Ti, followed by exposure to 2.8 at.% Ca-Li at 600°C for 50 h. These measurements were made after the excess Ca-Li had been dissolved from the CaO-coated samples using gallium metallic electrodes supplying a switching polarity of 1 μA (dc) in flowing 99.996% Ar. Figure 5 shows the measured dc-electrical conductivity for the CaO coating along with literature data. The electrical conductivity measured in an Ar environment at temperatures of 200-500˚C ranged from 3.0×10^{-10} to 1.0×10^{-8} $ohm^{-1}cm^{-1}$ for the in-situ CaO coating on V-4Cr-4Ti, and these values are comparable with earlier data.[5,6]

FUTURE DIRECTIONS

Planned future activities include the following:

1. In-situ electrical resistance measurements on the in-situ CaO coatings in a Li-Ca environment.

2. Development and characterization of other insulator coating candidates, such as Y_2O_3, and AlN.

CONCLUSIONS

In-situ CaO coatings were produced on oxygen-charged V-4Cr-4Ti alloy by exposure of the alloy to liquid Li that contained 2.8 at.% Ca. The adhered CaO layer was 8 μm. The dc-electrical conductivity of the coating measured in an Ar environment in the temperature range of 200-500˚C was 3.0×10^{-10} to 1.0×10^{-8} $ohm^{-1}cm^{-1}$.

REFERENCES

1. J. H. Park, K. Natesan, and D. L. Smith, “Calcium oxide coating on vanadium alloys in liquid lithium,” Paper Presented at the Mat. Res. Soc. Meeting, Boston, MA, Nov. 2001, to be published.

2. J.-H. Park and T. F. Kassner, “CaO insulator coatings and self-healing of defects on V-Cr-Ti alloys in liquid lithium system,“ J. Nucl. Mater. 233-237, 476-481 (1996).

3. J.-H. Park, “Intermetallic and electrical insulator coatings on high-temperature alloys in liquid-lithium environments,“ in *Elevated Temperature Coatings: Science and Technology I*, eds., N. B. Dahotre, J. M. Hampikian, and J. J. Stigilich, pp. 227-240 (1995).

4. J.-H. Park and W. D. Cho, “Evaluating electrically insulating films deposited on V-4% Cr-4% Ti by reactive CVD,“ Fusion Materials Semiannual Progress Report for Period Ending Dec. 31, 1996, DOE/ER-0313/21, pp. 52-56 (1996).

5. N. A. Surplice, “The electrical conductivity of calcium and strontium oxides,“ Brit. J. Appl. Phys., 17, 175-180 (1966).

6. B. J. Hopkins, and F. A. Vick, “Thermionic and related properties of calcium oxide,“ Brit. J. Appl.Phys., 9, 257-264 (1958).

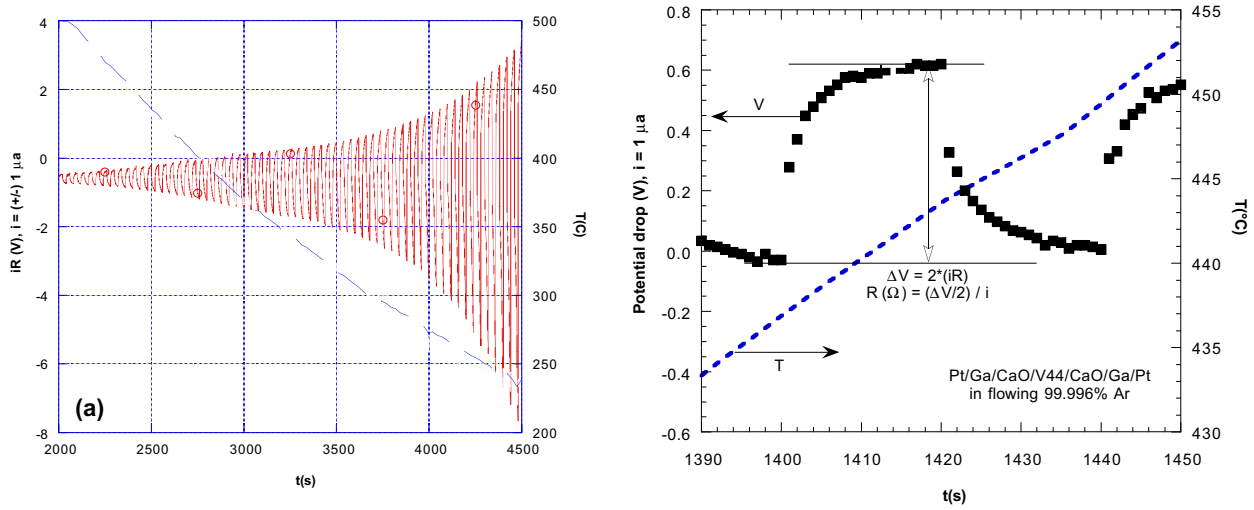

Fig. 3. Temperature and iR-drop potential monitored as a function of time during conductivity measurement for the O-charged V-4Cr-4Ti with CaO coating.

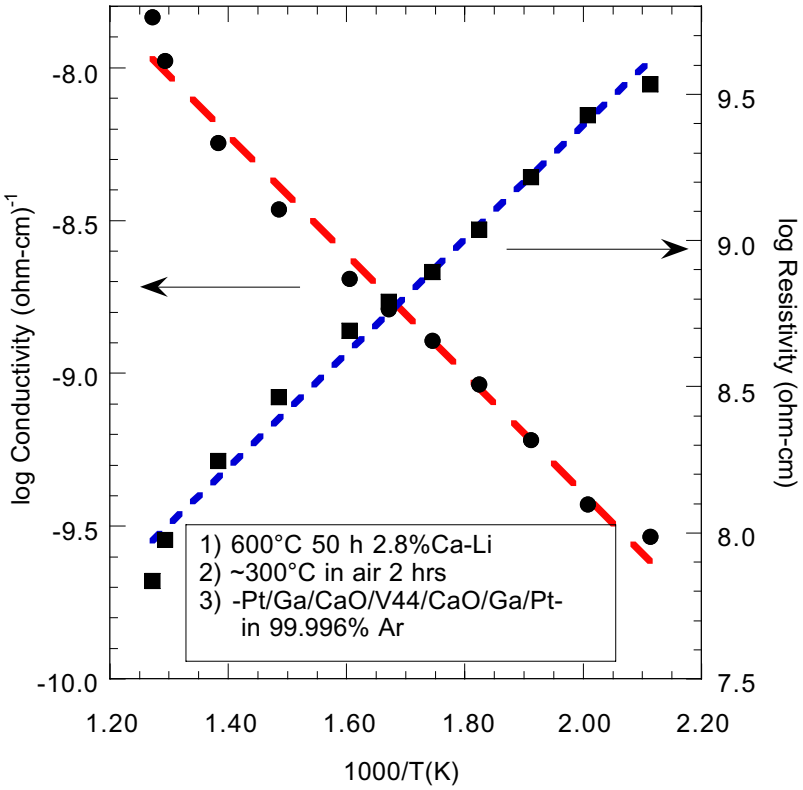

Fig. 4. Electrical conductivity and resistivity vs. 1000/T for the O-charged V-4Cr-4Ti after exposure in 2.8 at.% Ca-Li at 600°C for 50 h.

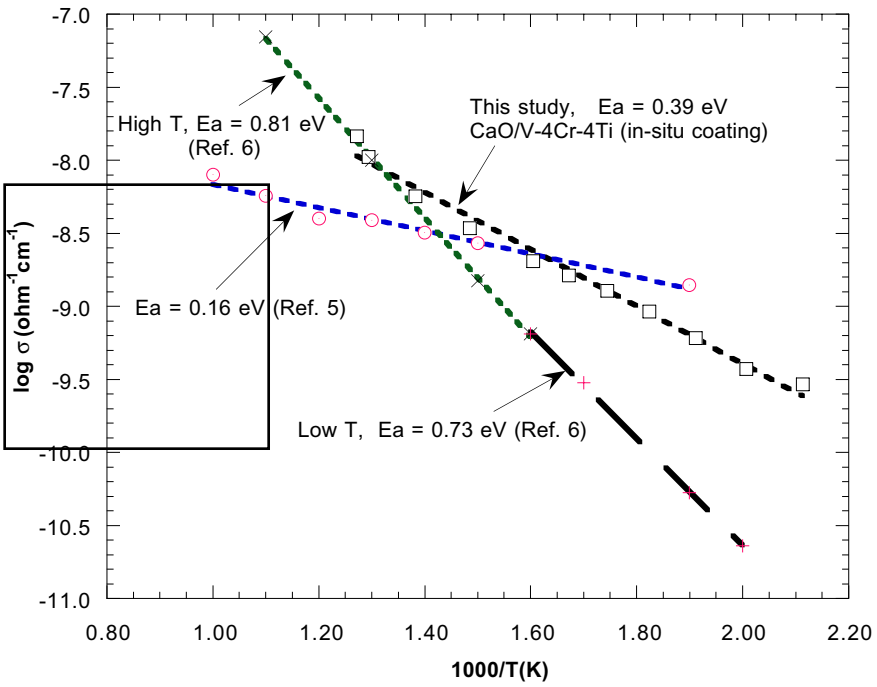

Fig. 5. Temperature dependence of electrical conductivity of in-situ CaO coating along with data on bulk CaO from literature (E_a = activation energy).

TEMPERATURE LIMITS ON COMPATIBILITY OF INSULATING CERAMICS IN LITHIUM* -- B. A. Pint, J. H. DeVan and J. R. DiStefano (Oak Ridge National Laboratory)

*dedicated to the memory of J. H. DeVan

To be published in the Journal of Nuclear Materials as Proceedings of the 10th International Conference on Fusion Reactor Materials, October 2001, Baden-Baden, Germany.

EXTENDED ABSTRACT

Calcium oxide and aluminum nitride are candidates for electrically insulating coatings in a lithium-cooled fusion reactor. Bulk specimens of single crystal CaO and polycrystalline AlN+0.04wt.%Y were exposed to lithium in 1000h isothermal capsule tests at 500°-800°C to determine the maximum temperature at which acceptable compatibility is likely. A large increase in mass loss of AlN was observed between 600° and 700°C. At 700°C, the amount of dissolution was reduced when a Mo capsule, which is a less stable nitride former, was used instead of a vanadium alloy test capsule, Figure 1. High mass losses for single crystal specimens of CaO were observed after exposure at 600°C. In this case, changing to a Mo test capsule or adding Ca or O to the lithium did not consistently show a beneficial effect. At 700°C, neither doping the Li with Ca or O significantly altered the high mass losses. These results suggest that CaO may be limited to exposure temperatures of less than 600°C but AlN may be able to operate above 600°C. Because some designs call for operating temperatures of 750°C, other insulator materials, such as Er_2O_3 and Y_2O_3, also are being evaluated. Preliminary results show promise for these oxides after exposure at 800°C, Figures 1 and 2.

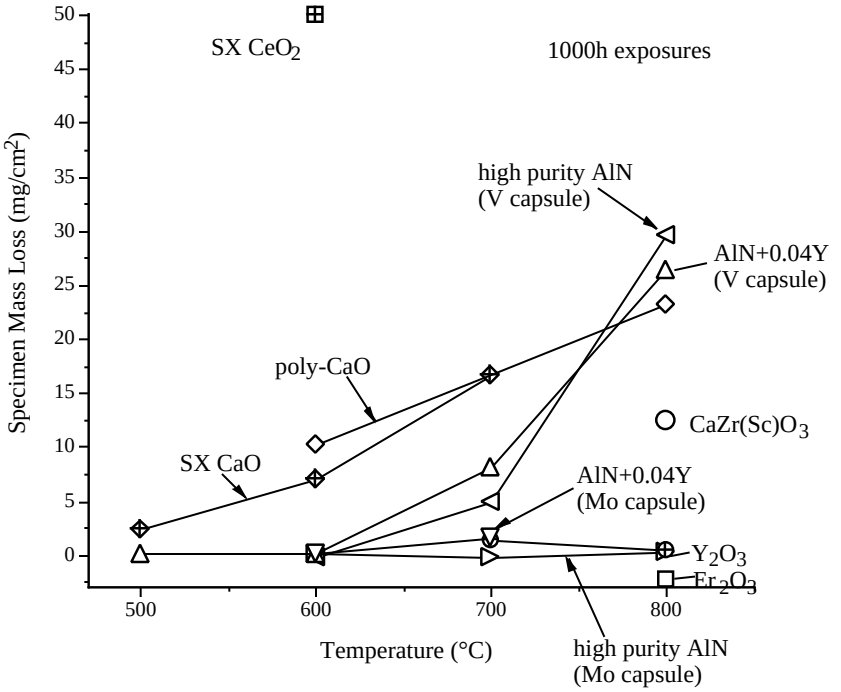

Figure 1. Mass losses for some other oxide materials compared to the data for AlN and CaO after 1000h at various temperatures. The results from poly-crystalline CaO are from previous work.

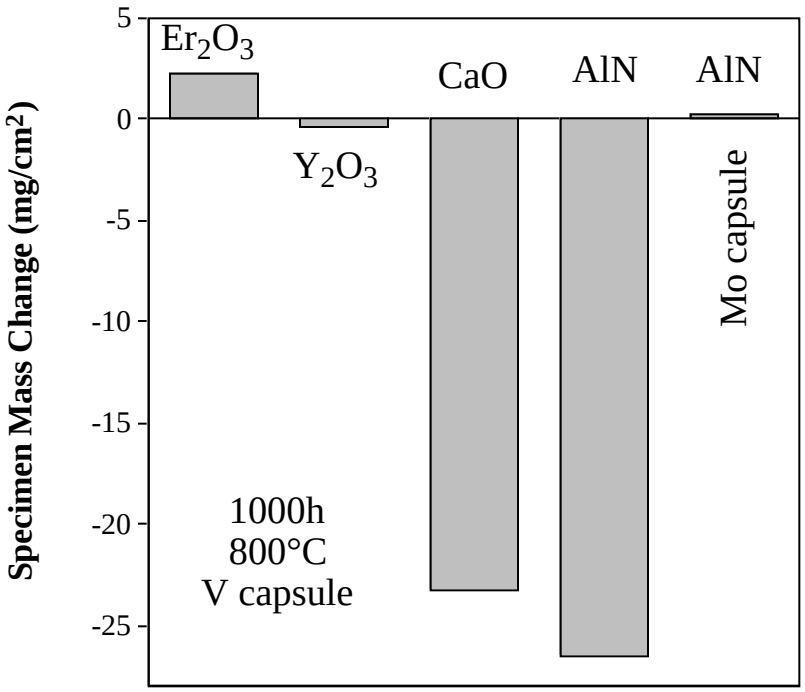

Figure 2. Mass changes for bulk specimens after 1000h at 800°C with V alloy capsules and no additions to the lithium. When AlN was tested in a Mo capsule, there was a slight mass gain instead of a large mass loss with a V alloy capsule.

THERMAL CONDUCTIVITY OF NATURAL AND ISOTOPICALLY ENRICHED DIAMOND - EFFECT OF NEUTRON IRRADIATION

D.P. White, Department of Physics, Merrimack College, N. Andover, MA 01845

OBJECTIVE

The objective of this work is to study the influence of defects produced by neutron irradiation on the thermal conductivity of diamond.

SUMMARY

Studies on the temperature dependence of the thermal conductivity of isotopically enriched (0.1% ^{13}C) diamond [1-5] have determined the form for the intrinsic scattering phonon relaxation times in diamond. In addition, low temperature thermal conductivity measurements and infrared spectra of lightly neutron-irradiated type IIa natural diamond [6] have determined the size and concentration of extended regions of disordered carbon responsible for phonon scattering. These results have been used to model the thermal conductivity changes expected in neutron irradiated diamond at higher temperatures, from 100 to 1000K. It was found that upon irradiation to a fluence of 4.5 X 10^{22} neutrons m^{-2} the thermal conductivity of natural diamond went from 2200 to 370 W/mK at 300K while the thermal conductivity of diamond with a 0.1% concentration of ^{13}C went from 3000 to 370 W/mK at 300K.

PROGRESS AND STATUS

Introduction

Electron cyclotron resonance heating (ECH) is a major candidate for plasma heating in ITER [7-11]. One of the milestones is the development of a 170Ghz, 1MW, continuous wave (CW) gyrotron. The development of a ceramic window capable of power transmission at these levels is critical. Sapphire and silicon nitride were not able to sustain CW operation at these levels [7,8] and thermal runaway occurred in these materials above ~170kW. Recent work has concentrated on diamond as it has a small dielectric loss tangent [7-11] and high thermal conductivity [1-5,12]. It is important to characterize the effect of neutron irradiation on the thermal conductivity of diamond, as this will have a direct influence on the final temperature of the window during CW operation of the gyrotron. In tests of diamond windows on 170Ghz gyrotrons [8,9] it was found that these windows could fulfill the requirements for CW transmission in the megawatt range. The thermal conductivity of the windows used in these tests was estimated to be about 1800 W/mK by comparing experimental results with numerical simulations. It is expected that upon neutron irradiation the thermal conductivity will be degraded [6,13-14] and thus the performance of these windows will be affected.

Theory

The thermal conductivity was calculated using the Callaway method [15]. This method takes into account the effects of intrinsic three-phonon normal (N) processes. These processes do not create thermal resistance directly but affect the thermal resistance by transferring phonons from frequencies where they are not scattered to frequencies where scattering is more efficient. The Callaway expression for the temperature dependent thermal conductivity, extended to take into account the differences in the transverse and longitudinal modes [1,3] is

$$K(T) = K_1(T) + K_2(T) \tag{1}$$

where,

$$K_1(T) = \frac{k^4 T^3}{6\pi^2 \hbar^3} \sum_{j=1}^{3} \frac{1}{v_j} \left(\int_0^{\theta_j / T} \tau_{cj} J_4(x) dx \right) \tag{2}$$

and

$$K_2(T) = \frac{k^4 T^3}{6\pi^2 \hbar^3} \sum_{j=1}^{3} \frac{1}{v_j} \frac{\left(\int_0^{\theta_j / T} \frac{\tau_{cj}}{\tau_{nj}} J_4(x) dx \right)^2}{\int_0^{\theta_j / T} \frac{\tau_{cj}}{\tau_{nj} \tau_{rj}} J_4(x) dx}. \tag{3}$$

The sum is over transverse and longitudinal modes, k is the Boltzmann constant, T is the absolute temperature, $\hbar$ is Plank's constant divided by 2π, v is the phonon velocity, $x = \hbar\omega / kT$, ω is the phonon angular frequency, and $J_4 = x^4 e^x (e^x - 1)^{-2}$. The relaxation times are defined as follows, the resistive relaxation time τ_r is given by, $\tau_r^{-1} = \sum_i \tau_i^{-1}$, where the sum is over all resistive scattering processes including intrinsic umklapp (U) processes, isotope scattering, extended defect scattering, etc.. The N process relaxation time is τ_n and τ_c is the combined relaxation time given by, $\tau_c^{-1} = \tau_r^{-1} + \tau_n^{-1}$.

Natural diamond has a Carbon-13 concentration of 1.1% and it is known that the thermal conductivity of isotopically enriched diamond is greatly increased over a wide temperature range compared to natural diamond particularly at the peak of the thermal conductivity curve. In order to explain the large increase (originally much larger than expected [16]) in terms of isotope scattering it was necessary to include the effects of N processes [5]. Subsequent analyses of the thermal conductivity of enriched diamond have included N processes. Wei et. al. [1] used the Callaway expression to fit experimental thermal conductivity data on diamond with the natural isotope concentration and isotopically enriched (0.1% ^{13}C) diamond over a wide temperature range (100-1000K). From this analysis they determined forms for the intrinsic phonon relaxation times. They found the U-process relaxation time to be,

$$\tau_u^{-1} = 4.7 \times 10^2 x^2 T^3 e^{\frac{-670}{T}} \tag{4}$$

and the N-process relaxation time to be,

$$\tau_n^{-1} = 1.49 x T^4 . \tag{5}$$

Olson et. al. [2] and Morelli et. al. [6] find similar expressions for the U-process relaxation time.

Morelli et. al. [6] measured the thermal conductivity of neutron irradiated diamond at low temperatures from 5-300 K. They determined that neutron irradiation caused phonon scattering by extended regions of disordered carbon. The size and concentration of these defects were

determined from curve fitting to their low temperature experimental data. They also found that the size and concentration thus determined correlated with those determined from infrared spectra. In addition they also saw an increase in the amount of simple point defect scattering (vacancy scattering) after neutron irradiation.

This information on intrinsic relaxation times and on neutron irradiation induced have been used here to determine the effect of neutron irradiation on the thermal conductivity of both isotopically enriched diamond and of diamond with the natural isotope concentration. To do this the phonon relaxation times were substituted into the Callaway expression, Eqs. 1-3.

The relaxation time due to isotope point defect scattering is given by [5,17],

$$\tau_{isotope}^{-1} = \frac{c(1-c)}{(12+c)^2}\Omega\frac{1}{4\pi v^3}\left(\frac{k}{\hbar}\right)^4 T^4 x^4 \qquad (6)$$

where c is the isotope concentration and Ω is the atomic volume. The relaxation time due to point defect vacancy scattering is given by [17-19],

$$\tau_{vac}^{-1} = 9c_v\Omega\frac{1}{4\pi v^3}\left(\frac{k}{\hbar}\right)^4 T^4 x^4 \qquad (7)$$

where c_v is the vacancy concentration. The relaxation time for extended defects is given by [3,6,20],

$$\tau_{ext}^{-1} = \frac{\rho v\pi a^2}{4} \text{ if } \frac{akTx}{v\hbar} > 1 \qquad (8)$$

$$\tau_{ext}^{-1} = \frac{\rho\pi a^6}{4v^3}\left(\frac{k}{\hbar}\right)^4 T^4 x^4 \text{ if } \frac{akTx}{v\hbar} < 1$$

where ρ is the extended defect volume density and a is the radius of the extended defect, assumed spherical. Extended defects scatter long wavelength phonons as point defects (Rayleigh scattering) and geometrically (boundary scattering) for short wavelength phonons.

Morelli et. al. [6] performed four irradiations with the following results.

Table I. Size and concentration of extended defects for various neutron fluences along with vacancy concentration necessary to produce point defect scattering in excess of that seen in unirradiated sample. F is the neutron fluence. Data from Ref. 6.

F (neutrons m^{-2})	ρ (m^{-3})	a (m)	c_v (per atom)
0	0	0	0
$3.0X10^{20}$	$4.5X10^{22}$	$8X10^{-10}$	$4.7X10^{-5}$
$1.2X10^{21}$	$1.9X10^{23}$	$8X10^{-10}$	$8.8X10^{-5}$
$6.0X10^{21}$	$1.0X10^{24}$	$8.5X10^{-10}$	$1.15X10^{-4}$
$4.5X10^{22}$	$5.6X10^{25}$	$5.5X10^{-10}$	$1.7X10^{-4}$

These values were used in the relaxation times above and used in the Callaway expression to calculate the thermal conductivity of diamond.

Results

The results of the calculations described above are displayed in the plot in Figure 1. The results for the irradiated isotopically enriched diamond are not shown as they fall on top of the natural diamond curves.

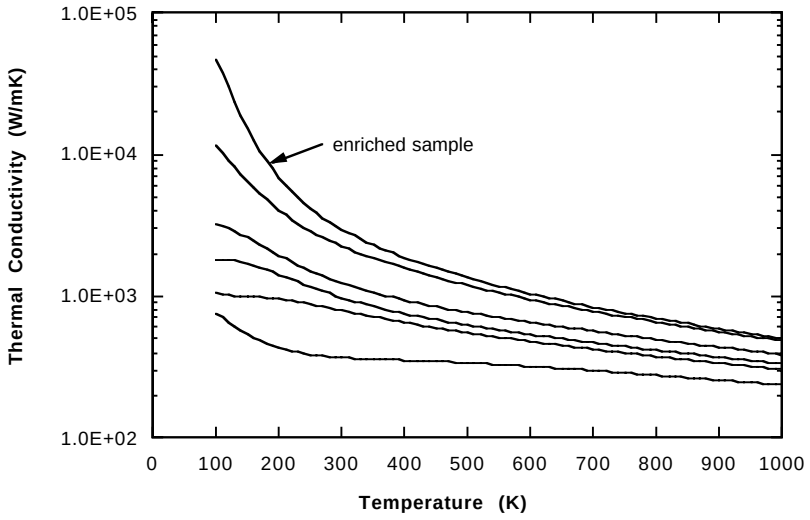

Figure 1. The thermal conductivity of diamond as a function of temperature. The upper curve is for unirradiated isotopically enriched diamond (0.1% ^{13}C). The other curves are for diamond with the natural isotope concentration of 1.1% in the same order as in Table 1.

CONCLUSIONS

From the data presented in Fig. 1 it is shown that the thermal conductivity of diamond is substantially degraded upon neuron irradiation. The decrease in the thermal conductivity of the isotopically enriched diamond is particularly pronounced and any advantage gained in terms of higher thermal conductivity is quickly eliminated upon neutron irradiation. An example of the decrease in thermal conductivity which occurs upon neutron irradiation, it was found that upon irradiation to a fluence of 4.5×10^{22} neutrons m^{-2} the thermal conductivity of natural diamond went from 2200 to 370 W/mK at 300K while the thermal conductivity of diamond with a 0.1% concentration of ^{13}C went from 3000 to 370 W/mK at 300K. This factor of 6 reduction in the case of natural diamond and the factor of 8 reduction in the case of the enriched diamond have implications in the design of ECH gyrotron windows.

FUTURE WORK

Future work will involve including other defect types into the calculations. With the model developed here it will be possible to determine the effect of each new type of defect on the thermal conductivity.

ACKNOWLEDGMENTS

The author is happy to acknowledge that this research was partially supported through a grant from the U.S. Department of Energy, Grant number DE-FG02-01ER54627 and through a course load reduction grant from the Faculty Development Grant Committee of Merrimack College.

REFERENCES

1. Lanhua Wei, P.K. Kuo, R.L. Thomas, T.R. Anthony, and W.F. Banholzer, Phys. Rev. Lett. 70, no. 24 (1993) 3764.
2. J.R. Olson, R.O. Pohl, J.W. Vandersande, A. Zoltan, T.R. Anthony, and W.F. Banholzer, Phys. Rev. B 47, no. 22 (1993) 14850.
3. J.E. Graebner, S. Jin, J.A. Herb, and C.F. Gardinier, J. Appl. Phys. 76, no. 3 (1994) 1552.
4. R. Berman, J. Phys. Chem. Solids 59, no. 8 (1998) 1229.
5. R. Berman, Phys. Rev. B 45, no. 10 (1992) 5726.
6. Donald T. Morelli, Thomas A. Perry, and John W. Farmer, Phys. Rev. B 47 (1993) 131.
7. K. Sakamoto, ITER EDA Newsletter vol. 8 (1999) 3.
8. K. Sakamoto, A. Kasugai, M. Tsuneoka, K. Takahashi, T. Imai, T. Kariya, and Y Mitsunaka, Rev. of Sci. Instru. 70, no. 1 (1999) 1.
9. O. Braz, A. Kasugai, K. Sakamoto, K. Takahashi, M. Tsuneoka, T. Imai, and M. Thumm, Int. J. of Infrared and Millimeter Waves 18, no. 8 (1997) 1495.
10. R. Heidinger, A. Ibarra, and J. Molla, J. Nucl. Mater. 258-263 (1998) 1822.
11. R. Heidinger, R. Spörl, M. Thumm, J.R. Brandon, R.S. Sussmann, C.N. Dodge, in Conf. Digest, 23rd International Conference on Infrared and Millimeter Waves, edited by T.J. Parker and S.R.P. Smith, Colchester, Essex UK, Sept. 7-11, (1998) 223.
12. J.E. Graebner, M.E. Reiss, L. Seibles, T.M. Hartnett, R.P. Miller, and C.J. Robinson, Phys. Rev. B 50, no. 6 (1994) 3702.
13. R. Berman, E.L. Foster, and H.M. Rosenburg, in Defects in Crystalline Solids –Report'54 Bristol Conference, edited by A.C. Strickland, The Physical Society, London (1954) 321.
14. D.T. Morelli, T.A. Perry, J.W. Vandersande, and C. Uher, Phys. Rev. B 48, no. 5 (1993) 3037.
15. J. Callaway, Phys. Rev. 113 (1959) 1046.
16. T.R. Anthony, W.F. Banholzer, J.F. Fleischer, L. Wei, P.K. Kuo, R.L. Thomas, and R.W. Pryor, Phys. Rev. B 42 (1990) 1104.
17. P.G. Klemens, in Thermal Conductivity, edited by R.P. Tye (Academic Press, NY) (1969).
18. P.G. Klemens, Nucl. Instr. and Meth. 229 (1984) 204.
19. D.P. White, J. Appl. Phys. 73 (1993) 2254.
20. J.W. Vandersande, Phys. Rev. B 15 (1977) 2355.

8.0 BREEDING MATERIALS

No contributions.

9.0 RADIATION EFFECTS, MECHANISTIC STUDIES, AND EXPERIMENTAL METHODS

On the Mechanism of Formation and Growth of <100> Interstitial Loops in Ferritic Materials

Jaime Marian, Brian D. Wirth

Chemistry and Materials Science Directorate, Lawrence Livermore National Laboratory, P. O. Box 808, L-353, Livermore, CA 94550

and

R. Schäublin

CRPP, Fusion Technology-Materials, École Polytechnique Fédérale de Lausanne, CK-5232, Villigen PSI, Switzerland

Abstract

We propose a comprehensive mechanism for the formation and growth of <100> interstitial loops in α-Fe. This mechanism, which involves the formation of <100> junctions in the direct reaction between mobile <111> loops, reconciles long-standing experimental observations of these defects in irradiated ferritic materials with recent atomistic simulations of collision cascades and defect cluster properties in Fe, in which highly-mobile <111> clusters are seen to be the dominant feature. The <100> junctions, although metastable, grow into visible <100> loops as a consequence of the high kinetic barrier associated with rotation into <111> configurations and a very low mobility. Finally, the atomic character of 100 and $\frac{1}{2}\ 111$ loops is investigated with molecular dynamics simulations and the atomic configurations are used to calculate the defect image contrast through direct simulation of TEM images. The simulated images are subsequently compared with actual TEM micrographs of irradiated ferritic materials. Excellent agreement between the experiments and the simulations is found, allowing for a direct identification of the nature and structure of interstitial loops. Hence, this work provides one of the necessary links to unify simulation with experiments in α-Fe and ferritic alloys subject to high-energy particle irradiation.

Introduction

Ferritic steels and alloys represent a technologically important class of materials that are widely used for structural purposes in current nuclear fission reactors and proposed as candidate materials for plasma-facing first wall structures in future fusion energy facilities. Predicting their in-service performance requires understanding the accumulation of defects and evolution of the microstructure under the severe irradiation conditions found in these environments.

It is well established that examination of ferritic alloys by transmission electron microscopy (TEM) following low dose irradiation (<0.1 displacement per atom, dpa) by neutrons or heavy ions does not reveal any visible damage. However, as the irradiation dose increases above ~1 dpa, a significant population of prismatic dislocation loops, presumably of interstitial type, is experimentally observed. In contrast to other *bcc* alloys, such as Mo and V, the dislocation loops consist of Burgers vectors, b=<100> and b=<111>, in almost equal proportions, rather than predominantly <111> . While this result has been known for nearly 40 years [1-6] the mechanisms responsible for the presence of <100> loops in ferritic alloys are not yet well understood.

A comparison of the dislocation loop energy based on continuum elasticity estimates (elastic energy proportional to Gb^2, where G is the shear modulus), indicates that <111> loops are energetically favored and thus, the observation of <100> loops in α-Fe and other ferritic alloys has remained a puzzle. In 1965, Eyre and Bullough [7] proposed a mechanism by which <100>, as well as <111>, dislocation loops could form from an aggregate of <110> self-interstitials through shear reactions of the type:

$$\frac{1}{2}[110] + \frac{1}{2}[00\bar{1}] \rightarrow \frac{1}{2}[11\bar{1}]$$
$$\frac{1}{2}[110] + \frac{1}{2}[\bar{1}10] \rightarrow \frac{1}{2}[010] \qquad \text{(1 and 2)}$$

Again, consideration of the dislocation energy of the two reactions reveals a puzzle as to why <100> loops would form rather than <111>. Additionally, the Eyre and Bullough mechanism is predicated on the formation of platelets of self-interstitial atoms (SIA) with Burgers vector b=<110>, which corresponds to a faulted dislocation loop. However, the high stacking fault energy of *bcc* materials discounts the formation and stability of faulted loops and, thus, one can safely conclude that the Eyre and Bullough mechanism is not plausible to describe the formation of <100> interstitial loops in ferritic alloys.

Indeed, recent molecular dynamics (MD) simulations of self-interstitial cluster geometry using Finnis-Sinclair, embedded atom-type and long-range pair potentials reveal that stable interstitial cluster configurations for size from n>2 consist of aggregates of <111> -oriented, rather than <110>, split dumbbells [8-10]. Clusters of <111> self-interstitials have very high mobility for one-dimensional (1D) motion along <111> directions up to very large sizes (n>100). As well, MD simulations of displacement cascade evolution have consistently revealed the formation of SIA clusters with <111> orientations, which again exhibit high mobility [11,12]. Here we provide a mechanism for the formation and growth of <100> dislocation loops that reconciles the long-standing experimental observation of these defects in irradiated ferritic materials with recent MD studies of <111> cluster stability, their production in displacement cascades and high mobility in one dimension.

In this report, we first describe in detail the energetics of <111> and <100> interstitial dislocation loops, then propose a mechanism for <100>-loop nucleation, which involves the direct interaction of migrating <111> loops, and, finally, a growth mechanism for <100> loops to reach TEM visible sizes. An additional objective of this work is to investigate the correlation between dislocation loops produced by MD simulations and their observation in TEM by generating equivalent, conventional TEM (CTEM) images and assessing experimental limitations in the observation of small defect clusters. The weak beam technique [13] seems most appropriate in the case of small defects such as these, as it provides an improved spatial resolution and signal-to-background ratio over the usual bright/dark field mode of imaging in TEM, as well as a framework for direct comparison with actual experimental micrographs. Thus, by using a *virtual* electron microscope, this work tries to partially bridge the gap that exists between multiscale modeling and experiments within the study of radiation damage effects in metals.

Results

Loop energetics

Clearly, an energetics analysis based exclusively on isotropic, continuum elastic energy considerations (Gb^2) is insufficient to describe the loop interaction dynamics, as it ignores important contributions such as loop shape, angle between the habit plane and the Burgers vector,

and anisotropy effects. An analysis of the energetics of <111> and <100> loops that takes into account all such contributions is attained by way of fully-atomistic, MD relaxations at low temperatures, followed by a conjugate-gradient energy minimization to obtain the configuration-dependent loop energies. The configurations of interest for b=<100> loops are those with {110} and {100} habit planes (corresponding to the closest-packed and perfect edge configurations). In terms of loop shape, the minimum-energy configurations correspond to loop sides oriented along the close-packed directions in each habit plane, i.e. rhombic <100>{110} loops and square or rectangular <100>{100} loops (the most stable configuration for <111> loops has been reported to be hexagonal-shaped <111> {110} [9,10]. All atomistic results have been obtained with the MDCASK code [14] in which the Finnis-Sinclair-type potentials for Fe derived by Ackland et al. [15] have been implemented.

Figure 1 presents the three corresponding formation energy curves, obtained through a fit to the MD data (also shown) using the continuum elasticity expression for the self-energy, E_l, of a prismatic dislocation loop as given by Hirth and Lothe [16]:

$$E_l = \frac{NL\mu b^2}{4\pi(1-\nu)}\left(\ln\left(\frac{L}{\rho}\right) + C\right) \qquad (3)$$

Here N is the number of sides of the loop, L is the side length, μ and ν the shear modulus and Poisson's ratio, b is the Burger's vector magnitude and ρ and C represent the dislocation core cutoff radius and a constant that includes the dislocation core energy. Using the elastic constant values calculated from the α-Fe potential used here and values of ρ=b/4 and ρ=b for the cutoff radii of <111> and <100> loops, we obtain core energies of 0.38 and 1.10 eV/Å, respectively. The value for <111> loops is consistent with results reported in the literature [9,17] while, to our knowledge, the core energy value for the <100> dislocation loops represents the first calculation reported to date. The high value for both the dislocation loop core radii and core energy for <100> loops suggests the existence of large tensile forces around the core region of the loop, which diminishes the validity of a purely isotropic elastic analysis.

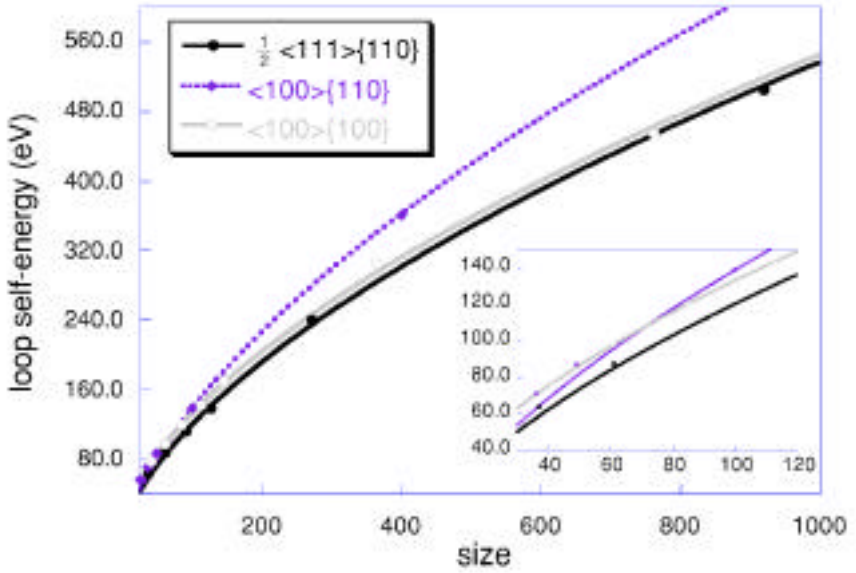

Figure 1:Dislocation loop energy as a function of size (number of constituent interstitials, n) for hexagonal <111>{110}, rhombic <100>{110} and square <100>{100} loops.

As seen in figure 1, <111> loops are the most stable configurations, consistent with previous continuum elasticity estimates, although the energy difference between <111> and <100>{100} configurations becomes very small (<10%) for larger loop sizes. Initially, <100> loops are more stable on {110} habit planes but, with increasing size, <100>{100} configurations become energetically favored, with a crossing around n~68. Presumably, this results from the reduction in dislocation segment length for <100> loops on {100} rather than {110} habit planes.

<100> loop formation

It has long been recognized that reactions between dislocations with Burgers vectors b=<111> can occur according to:

$$\frac{1}{2}[111] + \frac{1}{2}[1\bar{1}\,\bar{1}] \rightarrow [100] \qquad (4)$$

This can lead to the formation of <100> junctions and dislocation segments, which have been mainly observed in dislocation networks in Fe [18,19]. As well, such reactions between <111>-type loops can give rise to the formation of <100> loops. Indeed, Masters proposed such a mechanism in 1965 [1], yet discounted it due to a lack of observed loops with b=<111> in thin-film ion irradiation studies.

In order to shed light onto the formation of <100> loops, we have performed extensive MD simulations of interactions between <111> loops. One such interaction consisted of hexagonal and jogged hexagonal <111> loops with n=37 and 34, respectively, with intersecting glide prisms, akin to equation 4. Figure 2 shows a sequence of snapshots from the MD simulation at 1000 K. The two loops glide towards one another and collide, driven by the energy reduction that results when two loops condense into a single loop containing the same total number of interstitials. A [100] junction consisting of five SIAs on a (110) plane formed instantaneously following the collision (figure 2b). Notably, Osetsky et al., using a long-range pair potential, observed a similar reaction between interstitial clusters in α-Fe. However, the <100> junction was unstable and dissolved after a short time at 800 K [20].

The peculiarity of this interaction is that the glide direction of each loop is contained in the habit plane of the other interacting loop, and thus, once the loops collide, the dislocation segments of Burgers vector [111] can continue to glide within the loop of Burgers vector $[\bar{1}\,\bar{1}1]$. By reaction (4), this produces dislocation segments with Burgers vector [100] on both sides of the contact point. Given enough time, both <111> loops will gradually transform into a single entity with Burgers vector b=<100>. Therefore, we propose that <100> loops initially form as <100> junctions on {110} planes in collisions between <111> loops and grow outward until the defect boundaries are reached. As the <100> segments grow and the elastic energy density (stress) builds up, the cluster will eventually rotate onto {100} habit planes. A large number of cluster-interaction simulations involving different cluster shapes and sizes have been performed, and, in all cases, the main observation is that the intersecting loops need to be of approximately the same size, and possibly shape, to stabilize and grow <100>-type segments. When these constraints are not met, the smaller cluster always rotates into the <111> orientation of the larger cluster.

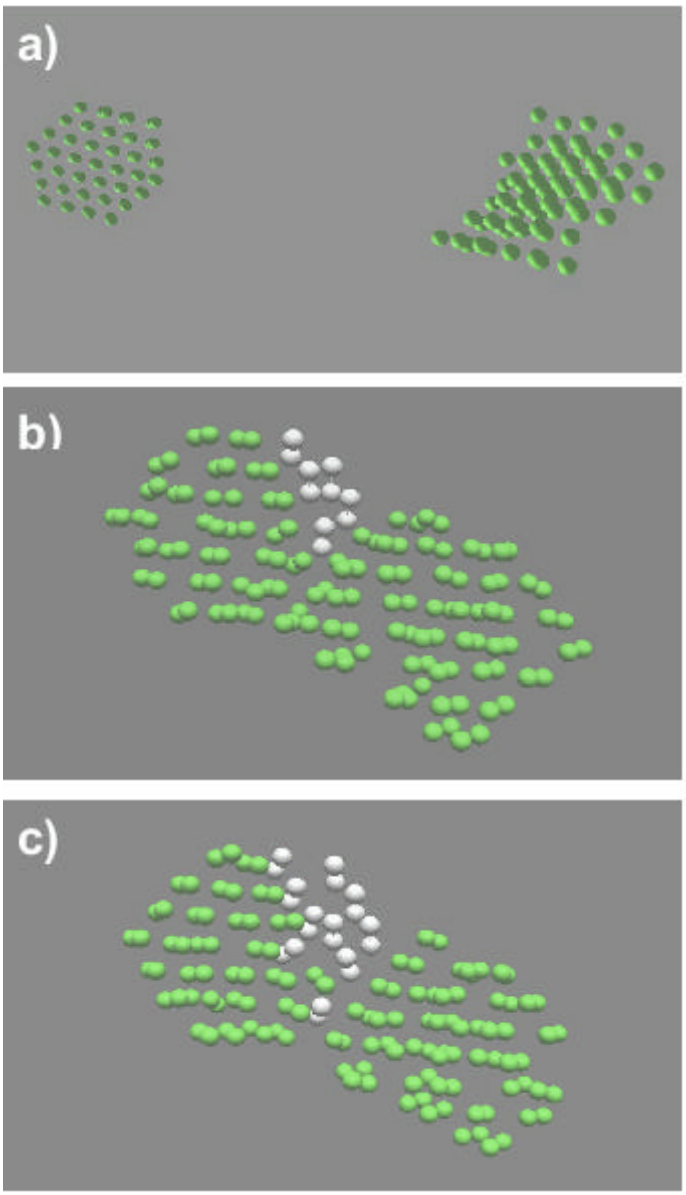

Figure2: Sequence of MD snapshots at (a) 0, (b) 120 and (c) 430 ps, of the interaction of two <111> loops with Burgers vectors appropiate to equation 4 at 1000 K. The loop on the left side of the image is a perfect, hexagonal 37-SIA cluster, while the one on the right is a 34-SIA jogged hexagonal loop. After forming a <100> junction following the loop collision, the junction expands throughout the resulting defect according to equations 5 and 6.

The high energies associated with having multiple dislocation segments within a loop make the propagation of the <100> segments a complex process at the atomic scale, since <111> dislocation segments no longer glide through perfect, close-packed directions but, instead, through a plane containing oppositely-oriented interstitials. Visualization of the MD simulations revealed that the <100> segments (best thought of as an array of akin self-interstitial atoms) propagate throughout the loop according to the following two-step reaction:

$$\frac{1}{2}[111]+\frac{1}{2}[00\bar{1}] \rightarrow \frac{1}{2}[110]$$
$$\frac{1}{2}[110]+\frac{1}{2}[1\bar{1}0] \rightarrow \frac{1}{2}[100] \qquad \text{(5 and 6)}$$

Thus, the interstitials reach their final [100] orientation by way of a modified Eyre-Bullough mechanism (modified reaction 1 and direct reaction 2). This is a thermally activated process by which SIAs at the <111>–<100> nodes, e.g with [111]-orientation, first undergo a partial $[00\bar{1}]$ shear into a metastable [110] configuration with an activation energy of ~0.5 eV. This produces large repulsive interactions with adjacent [100] dumbbells that force the metastable [110] dumbbell to further rotate into a more favorable configuration. This can be attained by the [110] dumbbell reversing its original trajectory back to the [111] orientation, or rotating into a [100] orientation through reaction 6, with an activation barrier of the order of 1.0 eV.

The nearly immediate formation of the <100> nucleus upon cluster collision is a consequence of the interaction process governed by equation 4 and driven by the energy reduction associated with forming a single cluster. The growth vs. shrinkage of the <100> junctions (loops) (equations 5 and 6) is governed by the interaction energy landscape, schematically shown in figure 3. The rate at which the growth of the [100] section is sampled (<111> to <110> to <100>) is favored with respect to its dissolution (inverse path), which, integrated over sufficiently long timescales, results in an effective <100>-loop transformation. For example, after 300 ps (figure 2(c)) five additional interstitials forming part of the $[\bar{1}\ \bar{1}\ \bar{1}]$ loop rotated into a [100] orientation and resided in that configuration during the entire simulation (1 ns). The direct rotation from a <111> to a <100> orientation, or vice-versa, can be neglected, since it requires energies in excess of 2.0 eV. This provides an explanation as to why, at moderate temperatures, the final configuration resulting from the interaction of two <111> loops consists of metastable <100> loops, rather than the slightly lower-energy <111> loops.

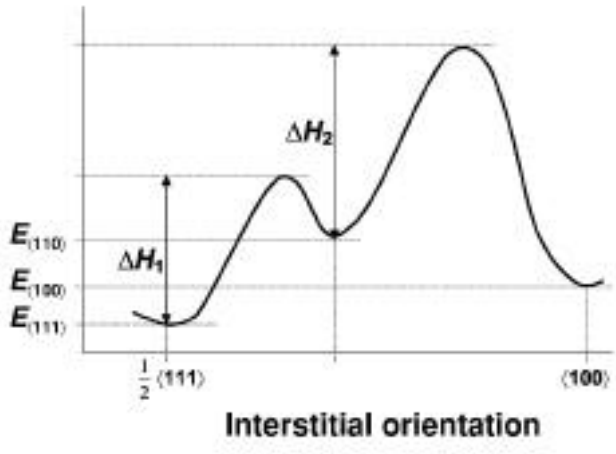

Figure 3: Schematic illustration of the energy landscape, projected along the reaction coordinate, for the propagation of <111> dislocation segments (best thought of as an array of individual SIAs) into <100> segments within the interacting <111> loops. The energy difference between each interstitial configuration is dependent upon loop size. ΔH_1 and ΔH_2 are of the order of 0.5 and 1.0 eV respectively.

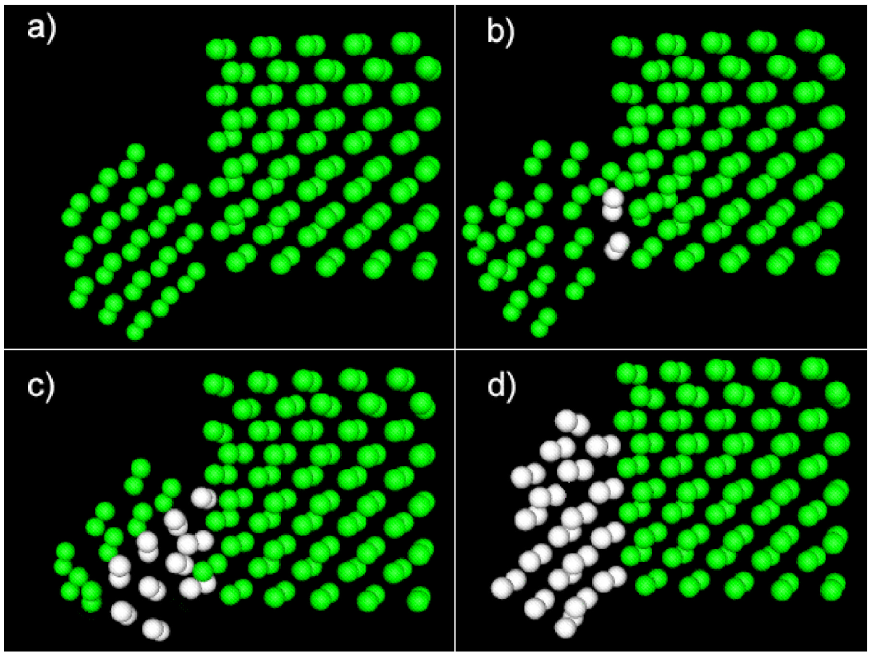

Figure 4: Sequence of MD snapshots at (a) 0.0, (b) 1.5, (c) 2.2 and (d) 3.5 ps, of the absorption of a hexagonal, 19-SIA [111](110) cluster by a square, 50-SIA [100](100) loop according to equation 7 at 100 K. Interstitials displayed in white are those belonging to the [111] cluster that have rotated to a [100] configuration.

<100> loop growth

The remaining point to consider is how <100> clusters grow to TEM observable sizes. Although intrinsically glissile owing to their pure-edge prismatic nature, the bcc crystal structure dictates that <100>{100} loops require a large jump distance. This results in a very high activation energy, computed to be >2.5 eV. Thus, once formed, <100> loops are essentially stationary, and can become a sink for mobile, cascade-produced <111> loops. Notably, MD simulations of interactions between <111>{110} and <100>{100} loops reveal <100> loop growth. Figure 4 shows one such interaction in which a 19-SIA <111> cluster is absorbed by a 50-SIA <100> square loop. Even though the lowest energy configuration corresponds to a 69-SIA <111> loop, the system follows the path of least resistance into a 69-SIA <100> loop through the following atomic reaction:

$$\langle 100\rangle + 2\left(\frac{1}{2}\langle 111\rangle\right) \rightarrow \langle 211\rangle \rightarrow \langle 100\rangle \qquad (7)$$

i.e. rotation of individual <111>-oriented interstitials in the presence of <100> SIAs into an intermediate metastable <211> configuration that rapidly rotates into a <100> orientation.

TEM image simulation, comparison with experiment

The CTEM images of the dislocation loops are simulated using the multislice method [21] to obtain their weak beam image at 200 kV. This is performed with the EMS software package [22]. The most relevant parameter in this type of simulation is the objective aperture size. Ideally, for CTEM, and more precisely for weak-beam image simulation, the sample should be more than 10-nm thick to avoid surface effects, and thinner than 80 nm to reduce anomalous absorption, which arises from inelastic scattering of the electrons, that would result in a blurry image [23].

Details on the main elements of the approach are given elsewhere [24]. The sample obtained from MD simulations is cut perpendicular to the electron beam direction in slices 0.2-nm thick. The sample is in all cases cut into 100 slices that are roughly 10 nm on a side and contain approximately 2000 atoms. The diffraction condition is selected by the beam direction, parallel to the cutting direction, in order to isolate the systematic row defined by the chosen diffraction vector **g**. In this work the diffraction vector was picked to be **g**=(200) and the diffraction condition was **g**(4.1**g**). The parameters used to obtain the images are similar to those of modern microscopes operated at an acceleration voltage of 200 kV.

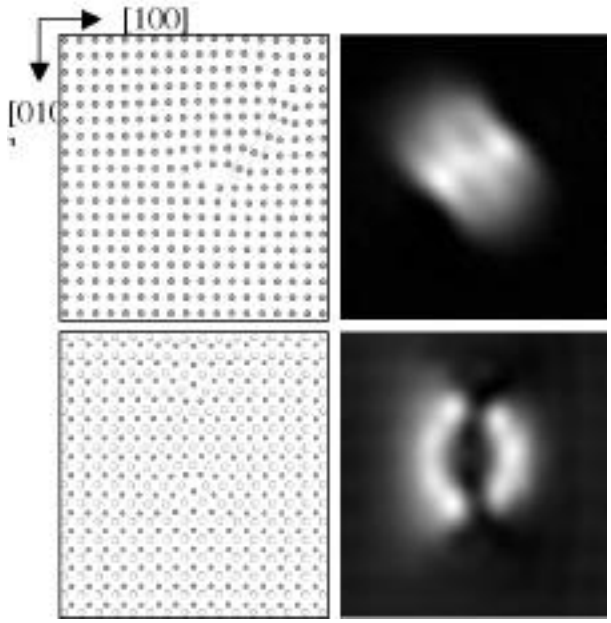

Figure 5: [001] view of the MD simulation box after relaxation of a $\frac{1}{2}[111]$ (top image) and a [100] (bottom) loop respectively. Next to each one of the atomistic images are the corresponding weak beam, **g**=(200), **g**(4.1**g**), CTEM simulated images.

Figure 5 shows the CTEM simulated images of a 91-SIA, hexagonal, $\frac{1}{2}\langle 111\rangle\{110\}$ loop and a 61-SIA, hexagonal, $\langle 100\rangle\{100\}$ loop, taken under the above conditions. A cut perpendicular to the [001] direction of the simulation box for each loop is also shown. The observed contrast in the images originates from the defect-induced displacement field. From the images, it is clear that the displacement field caused by the $\frac{1}{2}\langle 111\rangle$ loop is mostly circumscribed to the glide prism of the defect, while on the contrary, for the $\langle 100\rangle$ loop, the strain field has stereoscopic geometry and reaches outside the glide prism of the loop. This is likely a consequence of the larger dislocation core volume for $\langle 100\rangle$ interstitial loops, whereas the compressive stress caused by $\frac{1}{2}\langle 111\rangle$ loops is more easily accommodated along close-packed $\langle 111\rangle$ directions, with even small tensile regions appearing in between the main twin compressive lobes of the individual crowdions that constitute the cluster [25]. This means that the displacement field induced by the loops in the direction perpendicular to the Burgers vector is virtually non-existent, although this is not so clearly appreciated in the image of the $\frac{1}{2}\langle 111\rangle$ loop, since the diffraction vector is not parallel to the Burgers vector (**b**×**g**≠0). Another interesting feature is that while the $\langle 100\rangle$ loop clearly lies on two

consecutive *AB* (200) planes (to conserve the stacking sequence *ABAB*), the $\frac{1}{2}\langle 111\rangle$ rests on several $(1\bar{1}0)$ planes through kinks that are weakly distinguishable in the image. The double *bean* contrast observed in the $\langle 100\rangle$ image is characteristic of interstitial dislocation loops in metals, irrespective of their Burgers vector. This includes $\frac{1}{2}\langle 111\rangle$ clusters in Fe, as recognized in several experiments where $\frac{1}{2}\langle 111\rangle$ loops were observed edge-on (**b**×**g**=0) [26].

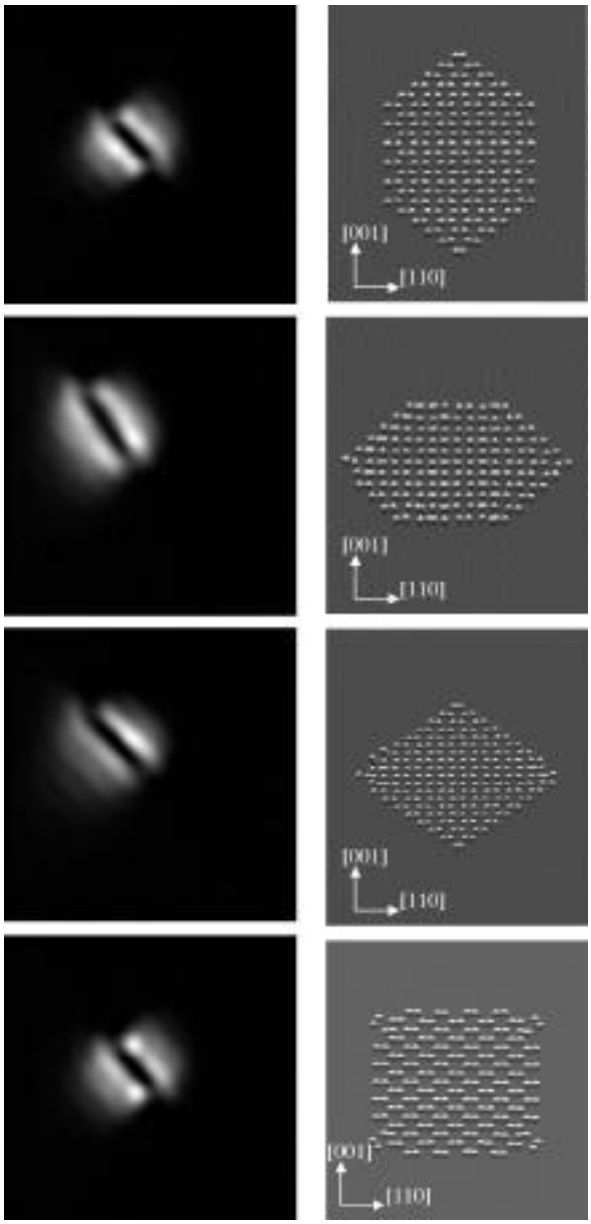

Figure 6: CTEM simulated images (left) of $\langle 100\rangle\{110\}$ loops with different sizes and shapes (right). The atomic configurations on the right are viewed from a $[1\bar{1}0]$ direction.

The shape of the dislocation loops does not seem to have a significant effect on the simulated images, although it significantly influences the loop self-energies. Figure 6 shows a series of 100 {110} loops of different sizes and their associated weak-beam images, which indicates that little information about the shape of the loops can be extracted using this set of CTEM imaging conditions. The images are qualitatively similar to that of the previous 100 {100} loop of figure 5, with the double-bean contrast clearly observed in all cases.

The results for loop energetics shown in figure 1 agree well with experiments [27,28] in that, for sizes larger than 65~70 SIAs, 100 loops are most stable on {100} planes. For the purpose of directly comparing the simulated images with actual TEM micrographs, an irradiated tempered martensite steel sample was analyzed in the microscope. Figure 7 shows an experimental TEM, weak beam, **g**(4.1**g**), **g**=(200) image of a F82H (Fe-9Cr) tempered martensite steel sample. The material was neutron irradiated at high dose rate and 302˚C, up to a total dose of 8.8 dpa in the HFR facility in Petten. The observed microstructure contains a number of features, most of which are defect clusters generated by the irradiation. The two insets displayed in figure 7 represent an 18-nm long, 937-SIA, rectangular, 100 {100} loop (A–bottom right) and a 4-nm, 91-SIA, hexagonal, 100 {100} loop (B–top left). Both loops exhibit characteristics that can be qualitatively recognized in the experimental micrograph, where two defects with similar size and contrast have been pointed out (A and B). These are interstitial dislocation loops with 100 Burgers vector and lying on {100} planes. We emphasize the excellent agreement between the simulations and the experimental observations.

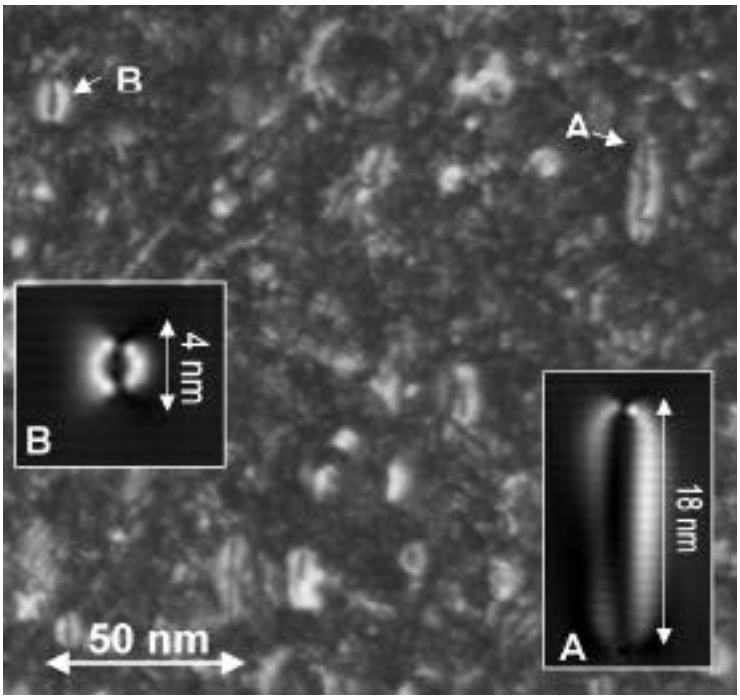

Figure 7: Experimental TEM weak beam image of a Fe-9Cr crystal irradiated with neutrons to a dose of 8.8 dpa at 302˚C. The two insets represent CTEM simulated images of (A) an 18-nm, rectangular [100] loop and (B) a 4-nm, hexagonal, [100] loop. A number of features can be observed in the TEM micrograph, among which two (A and B) interstitial loops with Burgers vector [100], sitting on {100} planes, can be identified. The agreement with the simulated loops in both contrast and shape is excellent.

Summary

In summary, based on extensive MD simulations of <111>–<111> and <100>–<111> interactions, we propose a comprehensive mechanism for the nucleation and growth of TEM visible <100> loops. This mechanism is consistent with both experimental observations and with the current understanding of interstitial cluster formation, diffusion and growth from atomistic simulations.SIAs produced in collision cascades initially aggregate as small <111> clusters. These clusters either rapidly migrate to system sinks or interact with each other. <100> nuclei form through the direct interaction of <111> clusters of comparable size via equation 4. The two interacting dislocation loops propagate through each other's habit plane according to reactions 5 and 6, resulting in the ultimate growth of the <100>{110} junction until the whole loop is transformed. The resulting loops are metastable with respect to <111>, but the energy differences can be quite small and the activation barrier to re-orient into <111> orientations quite large. With increasing size, n>68, <100>{110} loops re-arrange onto {100} habit planes. In this configuration, <100> loops are metastable and practically immobile, allowing for the absorption of other small <111> clusters via a direct-rotation mechanism (reaction 7) that allows <100>-loop growth up to TEM observable sizes.

Weak beam, CTEM images for a number of loops of different Burgers vectors, habit planes, sizes and shapes using **g**=(200) and **g**(4.1**g**) have been generated. Useful information about the induced strain field can be extracted from the CTEM simulated images in each case. The observed strain field of $\frac{1}{2}$ 111 loops remains mostly confined to the loop glide prism whereas that of 100 clusters extends beyond the limits of the prism, with the CTEM image conditions chosen. Loop shape does not have any significant impact on the simulated images, which all exhibit the well known, double-bean contrast of SIA loops.

Finally, qualitative agreement between the simulated images and actual experimental micrographs taken from one specific experiment of a Fe-9Cr sample is found to be excellent, which validates the use of this technique to identify the nature of interstitial clusters in irradiated ferritic materials.

The authors acknowledge many helpful discussions with Drs. W. Cai and V. Bulatov and are grateful to J. W. Rensman of the HFR facility at Petten, for providing the Fe-9Cr specimen for the TEM analysis. This work has been performed under the auspices of the U.S. Department of Energy and Lawrence Livermore National Laboratory under contract W-7405-Eng-48 and within the CSN-UNESA Coordinated Research Programme under contract P000531499.

References

[1] B. C. Masters, *Phil. Mag*. **11**, 881 (1965)
[2] B. L. Eyre and A. F. Bartlett, *Phil. Mag*. **11**, 261 (1965)
[3] B. L. Eyre and A. F. Bartlett, *J. Nucl. Mater*. **47**, 143 (1973)
[4] T. J. Bullough and B. L. Eyre, *Proc. R. Soc. Lond. A* **435**, 85 (1991)
[5] H. Kawanishi and E. Kuramoto, *J. Nucl. Mater*. **141-143**, 899 (1986)
[6] L. L. Horton and K. Farrell, *J. Nucl. Mater*. **122-123**, 687 (1983)
[7] B. L. Eyre and R. Bullough, *Phil. Mag*. **12**, 31 (1965)
[8] R. A. Johnson, *Phys. Rev.* **134**, 1329 (1964)
[9] B. D. Wirth, G. R. Odette, D. Maroudas and G. E. Lucas, *J. Nucl. Mater*. **276**, 33 (2000)
[10] Y. N. Osetsky, A. Serra, B. N. Singh and S. I. Gobulov, *Phil. Mag. A* **80**, 2131 (2000)
[11] R. E. Stoller, *J. Nucl. Mater.* **237**, 299 (1996)

[12] N. Soneda and T. Díaz de la Rubia, *Phil. Mag. A* **78**, 995 (1998)
[13] D. J. H. Cockayne, I. L. F. Ray and M. J. Whelan, *Phil. Mag.* A **20** (1969) 1265
[14] T. Díaz de la Rubia and M. W. Guinan, *Mater. Res. Forum* **174**, 151 (1990)
[15] G. J. Ackland, D. J. Bacon, A. F. Calder and T. Harry, *Phil. Mag. A* **75**, 713 (1997)
[16] J. P. Hirth and J. Lothe, *Theory of Dislocations, 2nd ed.* (Krieger Publishing Co., Malabar, FL, 1982)
[17] J. O. Schiffgens and K. E. Garrison, *J. Appl. Phys.* **43**, 3240 (1972)
[18] W. Carrington, K. F. Hale and D. McLean, *Proc. R. Soc. Lond. A* **259**, 203 (1960)
[19] S. M. Ohr and D. N. Beshers, *Phil. Mag.* **8**, 1343 (1963)
[20] Y. N. Osetsky, A. Serra and V. Priego, *J. Nucl. Mater.* **276**, 202 (2000)
[21] J. M. Cowley and A. F. Moodie, *Acta Crystallographica* **10** (1957) 609
[22] P. A. Stadelmann, *Ultramicroscopy* **21** (1987) 131
[23] W. M. Stobbs and C. H. Sworn, *Phil. Mag.* **24** (1971) 1365
[24] R. Schäublin, A. Almazouzi, Y. Dai, Y. N. Osetsky and M. Victoria, *J. Nucl. Mat* **276** (2000) 251
[25] J. Marian, B. D. Wirth, J. M. Perlado, G. R. Odette and T. Díaz de la Rubia, *Phys. Rev.* B **64**, 094303 (2001)
[26] A. E. Ward and S. B. Fisher, *J. Nucl. Mat* **166** (1989) 227
[27] D. S. Gelles, M. L. Hamilton and R. Schäublin, in *Effects of Radiation on Materials: 20th International Symposium, ASTM STP 1405*, S. T. Rosinski, M. L. Grossbeck, T. R. Allen and A. S. Kumar, Eds., American Society for Testing and Materials, West Conshohocken, PA, 2002
[28] E. A. Little, R. Bullough and M. H. Wood, *Proc. Royal. Soc. London* A **372** (1980) 565

NEUTRON-INDUCED SWELLING AND EMBRITTLEMENT OF PURE IRON AND PURE NICKEL IRRADIATED IN THE BN-350 AND BOR-60 FAST REACTORS - N. I. Budylkin, E**.** G. Mironova and V. M. Chernov Bochvar Institute of Nonorganic Chemistry, Moscow, Russia, V. A. Krasnoselov Research Institute of Atomic Reactors, Dimitrovgrad, Russia, S. I. Porollo Institute of Physics and Power Engineering, Obninsk, Russia, and F. A. Garner (Pacific Northwest National Laboratory)*

OBJECTIVE

The purpose of this effort is explore the differences in swelling and tensile properties that arise between two simple fcc and bcc metals when subjected to high fluence irradiation over a wide range of irradiation temperatures.

SUMMARY

Pure iron and nickel were irradiated to very high exposures in two fast reactors, BOR-60 and BN-350. It appears that both nickel and iron exhibit a transient-dominated swelling behavior in the range of 2 to $15x10^{-7}$ dpa/sec, with the shortest transient at ~500°C in nickel, but at <350°C for iron. It also appears that the duration of the transient regime may be dependent on the dpa rate.

When the two metals are irradiated at 345-355°C, it is possible to obtain essentially the same swelling level, but the evolution of mechanical properties is quite different. The differences reflect the fact that iron is subject to a low-temperature embrittlement arising from a shift in ductile-brittle transition temperature, while nickel is not. Nickel, however, exhibits high temperature embrittlement, thought to arise from the collection of helium gas at the grain boundaries. Iron generates much less helium during equivalent irradiation.

INTRODUCTION

Development of a comprehensive theory of the irradiation-induced nucleation and growth of voids in multi-component austenitic or ferritic-martensitic alloys is a challenging task, even after more than three decades following the first observation of void swelling. The construction of theoretical models is facilitated by experimental data developed from very simple systems without the complexity associated with segregation, precipitation or phase changes. Therefore data on the basic components of iron-base and nickel-base alloys such as pure metals (Fe, Ni) and simple binary Fe-Cr or ternary Fe-Cr-Ni model alloys are particularly useful. Pure metals in general exhibit void swelling at much lower doses than do even the simplest of model alloys, and therefore were addressed in this study.

While pure nickel has been irradiated a number of times to rather high neutron exposures [1-7], the data on pure iron is in general more limited in dpa level attained [8-14] and most of the data for both metals often cover rather narrow ranges of irradiation temperature. With respect to radiation-induced changes in mechanical properties, however, there are almost no data available for these metals.

This study focuses on the results of high dose (22-70 dpa) irradiations of pure iron and nickel in two fast reactors over a wide range of temperature, 345 to 650°C. Both swelling and mechanical property data were collected.

---

* Pacific Northwest National Laboratory (PNNL) is operated for the U.S. Department of Energy by Battelle Memorial Institute under contract DE-AC06-76RLO-1830.

Experimental Details

Two types of specimens were employed. The first were right circular cylinders of 6 mm in diameter and 28 mm length. The second were miniature tensiles also 28 mm long with gauge length of 15 mm and 3 mm diameter, with the grip ends also 6 mm in diameter. While both sets were measured to determine their density using hydrostatic weighing in CCl_4, the second set was subjected to tensile testing. The accuracy of density measurements before and after irradiation was ±0.2% and ±0.5%, respectively, reflecting the greater difficulty in remote measurement of radioactive specimens.

The nickel (99.95%) and iron (99.95%) specimens were annealed in sealed ampoules filled with pure argon for 60 minutes at 850°C and then water quenched. Some of the cylinder specimens were irradiated in the core of the BN-350 fast reactor and were in contact with flowing sodium at 500°C, reaching 50 dpa at 1.5×10^{-6} dpa/sec. The standard NRT model was used to calculate the displacement levels.

Another group of specimens were irradiated in contact with sodium coolant at temperatures ranging from 345-650°C and doses between 22-70 dpa. The irradiations were conducted in separate canisters in either the outer row of the BOR-60 reactor core or the first row of the reflector at dpa rates between $2.2\text{-}3.7 \times 10^{-7}$ dpa/sec. While most canisters were filled with cylindrical specimens, the iron tensile specimens were irradiated at 345°C to 58 dpa, and the nickel tensile specimens were irradiated at 355°C to 70 dpa. In most conditions iron and nickel were irradiated at identical dpa rates at a given temperature.

In most cases there was only one specimen per irradiation condition, but in three cases there were two specimens irradiated side-by-side, allowing a check on the reproducibility of the swelling process.

Tensile tests were conducted under argon gas at 1 mm/min at test temperatures ranging from 20-800°C.

Experimental Results

Figure 1 presents the swelling observed in pure nickel, showing an apparent peak swelling temperature at ~500°C. Figure 2a presents the majority of the swelling data plotted vs. dpa level, and shows that the temperature dependence of swelling is expressed primarily in the transient regime with a minimum transient at ~500°C. The temperature dependence of void swelling in nickel appears to arise primarily from the dependence of the transient regime of swelling on temperature, with the steady state swelling rate tending to increase to a value that is not strongly dependent on temperature.

Note that in both figures that irradiation at each temperature proceeds at a different dpa rate. Thus, there is the possibility that the apparent temperature dependence may actually result from the combined influence of two variables, especially at higher irradiation temperatures, as shown in Figure 2b.

Figure 3 presents a comparison of the higher fluence nickel data with the swelling data for pure iron. Note that with the possible exceptions of swelling at 345-355 and 650 °C, iron swells less than nickel. Even more importantly, however, is the observation that the peak swelling of iron occurs at some temperature below 350°C. Once again the temperature-flux dependence of swelling is exhibited in the duration of the transient regime of swelling, as shown in Figure 4.

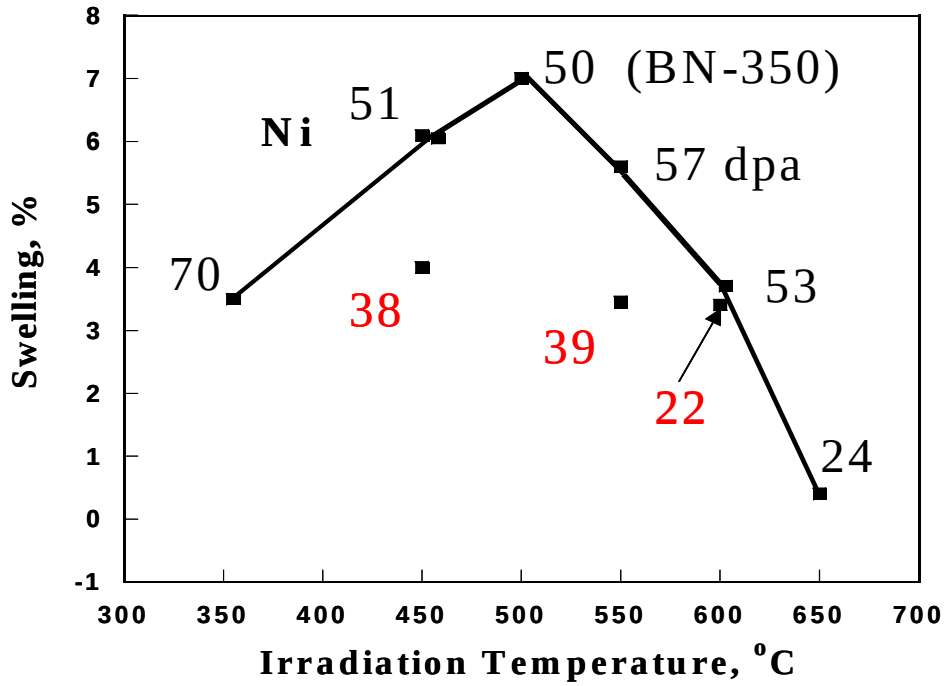

Figure 1. Swelling observed in pure nickel irradiated in BN-350 (500°C only) and BOR-60, plotted vs. irradiation temperature. Dpa levels are indicated for each data point. The two data at 51 dpa and 450°C indicate that the swelling is rather reproducible.

Figures 5a and 5b present the strength and ductility characteristics of pure nickel, both before and after irradiation to 70 dpa at 355°C. Before irradiation, annealed nickel is rather soft and ductile, with both strength and elongation decreasing with test temperature. Irradiation raises the strength and lowers the elongation in agreement with the behavior usually observed in irradiated metals.

Also as typically observed, the yield strength approaches the ultimate strength. Most importantly, the elongation falls to zero in the irradiated nickel when tested above ~500°C.

Figure 6a shows that pure iron at 58 dpa and 345°C exhibits trends in strength with temperature and irradiation similar to those of nickel, but the gap between unirradiated and irradiated properties is maintained until higher test temperatures.

Figure 6b shows quite a different behavior in the elongation of iron when compared to that of nickel. Although the elongation initially decreases with test temperature, above 400°C the elongation of unirradiated specimens increases strongly with test temperature. A similar behavior is seen in the irradiated specimens but only after the test temperature exceeds ~650°C. It is significant, however, that unlike the behavior of nickel the total elongation of irradiated iron remains at acceptable levels of 10-20% throughout the 20-800°C range.

Discussion

The temperature dependence of void swelling in both iron and nickel appears to arise primarily from the temperature and flux dependence of the transient regime of swelling, with the steady state swelling rate tending to increase to a value that is not as strongly dependent on temperature.

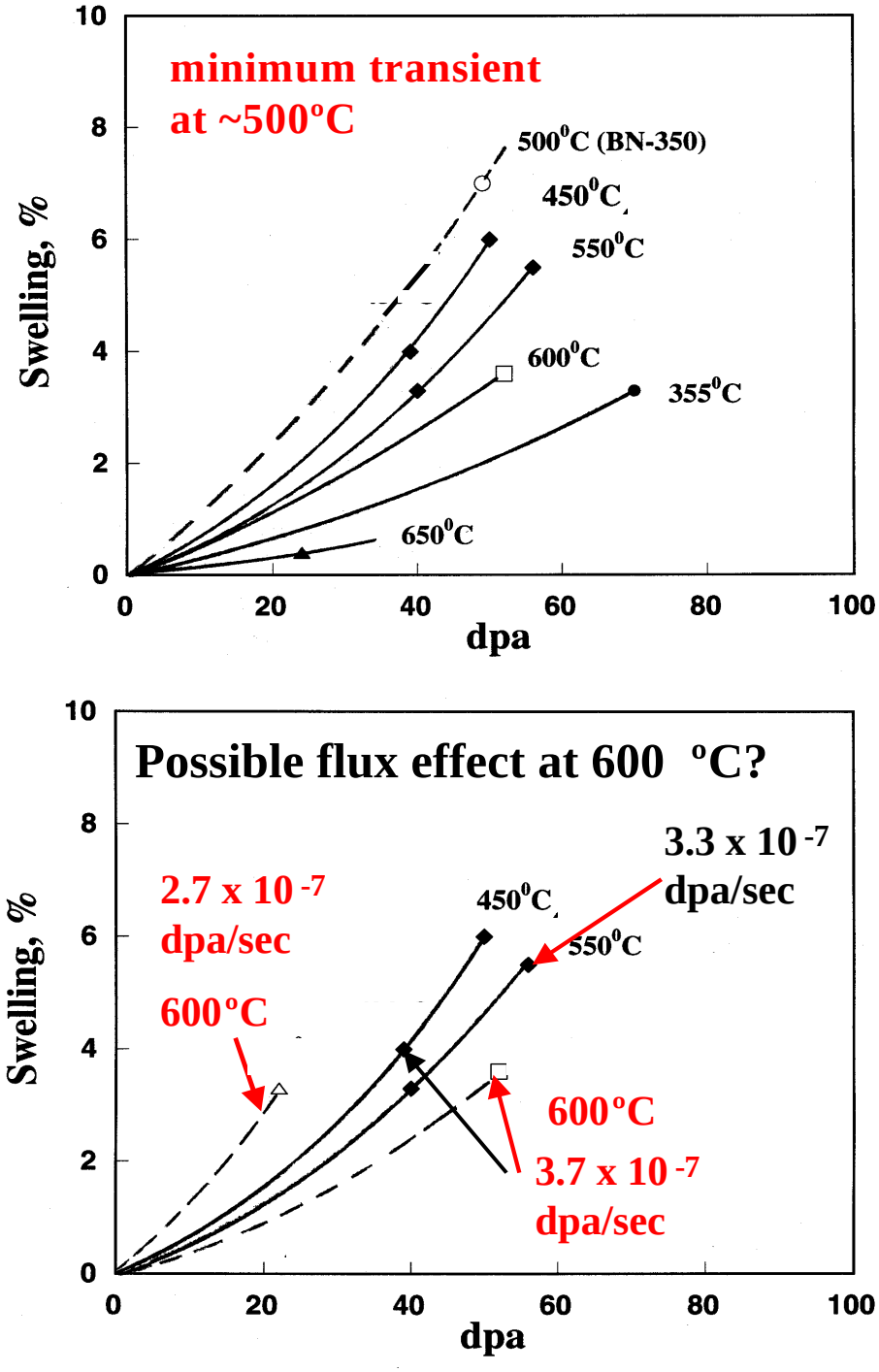

Figure 2. (top) Swelling observed in pure nickel, plotted vs. dpa for various temperatures. 2 (bottom) Swelling of a subset of irradiation conditions, indicating a possible influence of dpa rate on the duration of the transient regime, especially at 600°C.

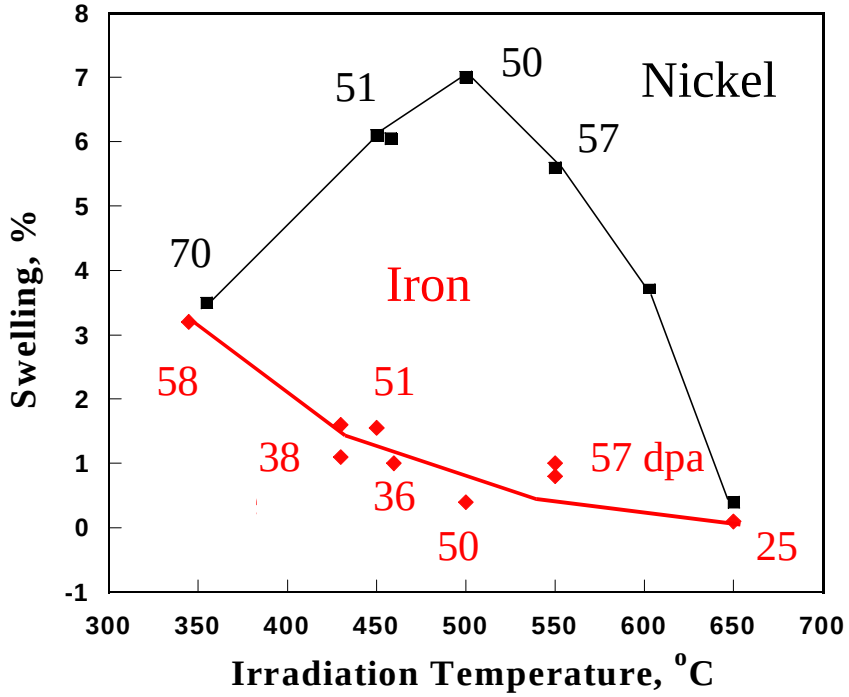

Figure 3. Comparison of the swelling of nickel and iron at comparable irradiation conditions. Dpa levels are indicated for each data point. Data pairs at 430 and 550°C indicate the reproducibility of swelling in this experiment.

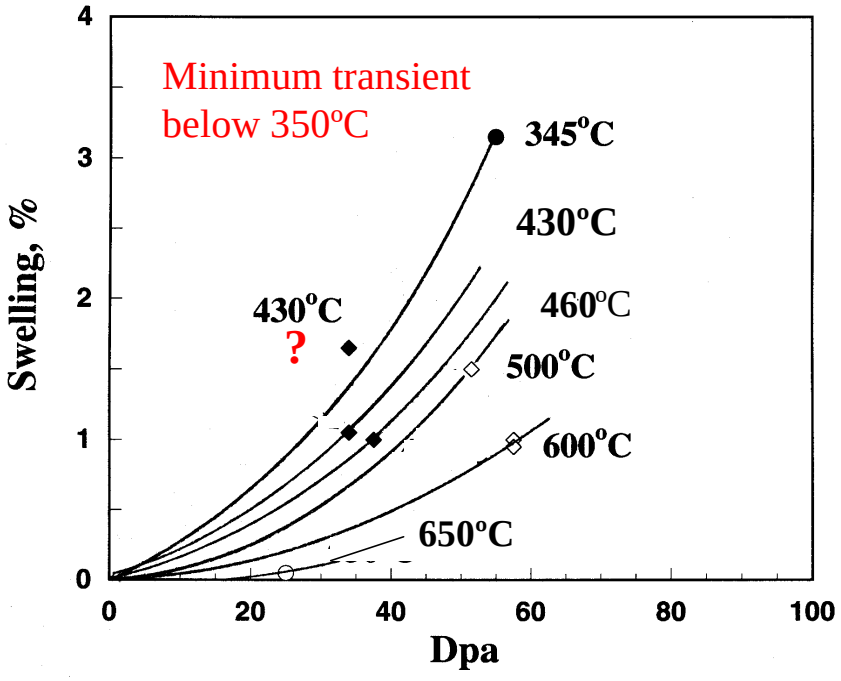

Figure 4. Swelling observed in pure iron, plotted vs. dpa for various temperatures.

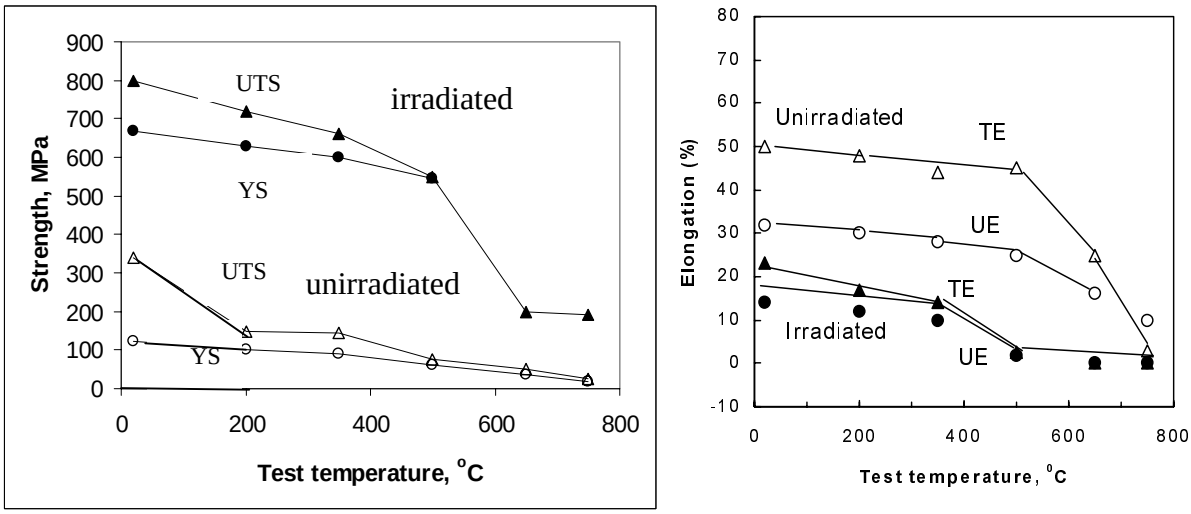

Figure 5. Strength and elongation characteristics vs. test temperature for both unirradiated and irradiated nickel (70 dpa, 355°C).

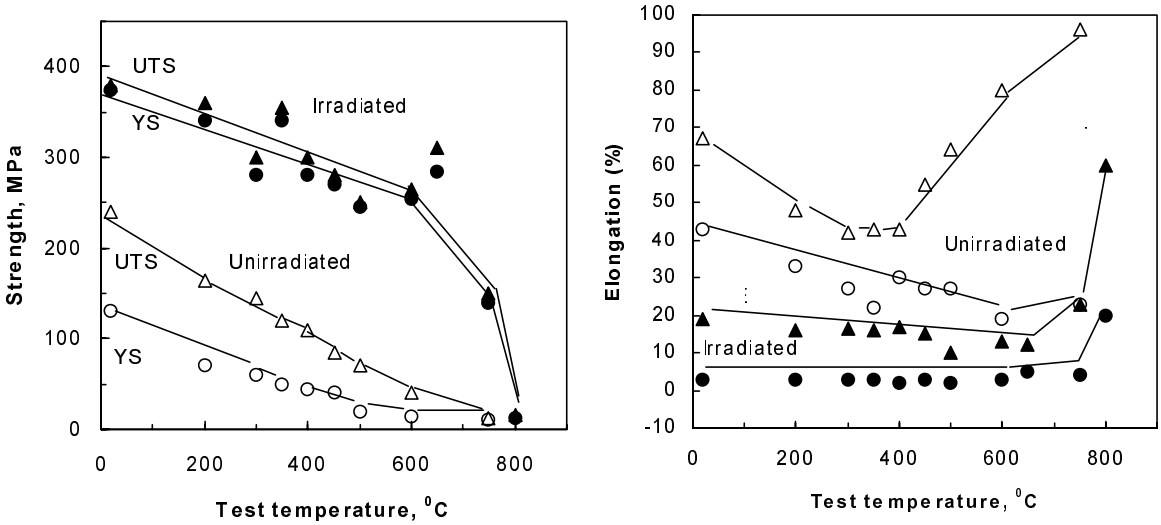

Figure 6. a) Strength and elongation characteristics vs. test temperature for both unirradiated and irradiated iron (58 dpa, 345°C).

It appears that above ~350°C nickel always swells more than iron at a given set of dpa rate and temperature, but it can not be stated with certainty that this statement is also true below 350°C.

The transient regime of swelling in nickel is clearly becoming longer with decreasing temperature below 500°C, while that of iron is clearly decreasing. It is thought to be quite likely that the peak swelling temperature (minimum transient) of iron has never been clearly observed because of the high inlet temperatures associated with fast reactors.

Data from other experiments at lower exposures has suggested that the peak swelling temperature of pure iron was in the range 400-425°C, but the higher exposure data from this experiment implies that such a conclusion reflected the combined influence of dpa rate and temperature on the duration of the transient regime.

The maximum swelling rate of pure nickel observed in this experiment appears to be on the order of ~0.2%/dpa but is still increasing with dpa. This value is well below the ~1%/dpa observed in other experiments [4,15,16]. It is significant to note that higher swelling rates were observed in experiments operating at lower displacement rates, producing significantly shorter transient regimes of swelling. Another paper addresses the effect of lower dpa rate to decrease the duration of the transient regime of swelling [17].

The maximum swelling rate observed in pure iron in this experiment is on the order of ~0.1%/dpa and still appears to be increasing with exposure. Recent estimates of the steady state swelling rate of pure iron and Fe-Cr binary model alloys range from 0.2%/dpa to 0.5%/dpa [9,12,18,19], considerably higher than earlier estimates.

The evolution of mechanical properties during irradiation is known to arise from all microstructural components, including voids, dislocations, loops and gas content, as well as the crystal structure of the metal. Although iron and nickel reached essentially the same swelling level at 345-355°C, their post-irradiation ductility behaved quite differently.

Iron exhibited significant hardening at 345°C, losing most of its uniform elongation, but still retaining 10-20% total elongation over the test temperature range. At higher test temperatures there was a partial recovery of ductility, however.

Nickel, however, exhibited high temperature embrittlement, having lost all ductility for test temperatures above 500°C. While nickel has a f.c.c. crystal structure and is therefore not prone to a DBTT shift, nickel does generate significantly more helium and hydrogen gas via transmutation, especially when compared to iron [20-21]. It is thought that collection of these gases, especially helium, at grain boundaries is facilitated at higher test temperatures, leading to grain boundary separation during tensile deformation. Unfortunately, it was not possible to examine the failure surfaces in this experiment, and this speculation cannot be confirmed.

Conclusions

When pure iron and nickel are irradiated side-by-side at a given set of dpa rate and irradiation temperature, it is possible to draw conclusions concerning their relative behavior with respect to void swelling and embrittlement.

It appears that both nickel and iron exhibit a transient-dominated swelling behavior in the range of 2 to 15×10^{-7} dpa/sec, with the shortest transient at ~500°C in nickel, but at <350°C for iron. It also appears that the duration of the transient regime may be dependent on the dpa rate.

When the two metals are irradiated at 345-355°C, it is possible to obtain essentially the same swelling level, but the evolution of mechanical properties is somewhat different. Both metals exhibit radiation hardening but the ductility losses are very different, especially at higher test temperatures, with partial recovery of ductility possible in iron. Nickel, however, exhibits high temperature embrittlement, thought to arise from the collection of helium gas at the grain boundaries. Iron generates much less helium during equivalent irradiation.

REFERENCES

[1] N. K. Vasina, I. P. Kursevitch, O. A. Kozhevmikov, V. K. Shamardin and V. N. Golovanov, J. Atomic Energy 59(1985) 256, in Russian.

[2] V. I. Scherbak, Fiz. Metal. Metalloved. 50 (1980) 1314, in Russian.

[3] G. Silverstre, A. Silvent, C. Regnard and G. Sainfort, J. Nucl. Mater. 57 (1975) 125.

[4] F. A. Garner, J. Nucl. Mater. 205 (1993) 98.

[5] J. F. Stubbins and F. A. Garner, J. Nucl. Mater. 191-194 (1992) 1295.

[6] J. F. Stubbins and F. A. Garner, Effects of Radiation on Materials: 17th International Symposium, ASTM STP 1270 (1996) 1038.

[7] T. M. Muroga and N. Yoshida, J. Nucl. Mater. 191-194 (1992) 1254.

[8] K. Farrell and J. T. Howston, J. Nucl. Mater. XXX (1970) 372.

[9] S. I. Porollo, A. M. Dvoriashin, A. N. Vorobjev and Yu. V. Konobeev, J. Nucl. Mater. 256 (1998) 297.

[10] L. L. Horton, J. Bentley and W. A. Jesser, J. Nucl. Mater. 108-109 (1982) 222.

[11] E. A. Little and D. A. Stow, J. Nucl. Mater. 87 (1979) 25.

[12] S. I. Porollo, A. M. Dvoriashin, Yu. V. Konobeev and F. A. Garner, J. Nucl. Mater. 283-287 (2000) 157.

[13] E. A. Little, Proc. International Conference on Materials for Nuclear Reactor Core Applications, Vol. 2, BNES, London, (1987) 47.

[14] N. P. Agapova, I. N. Ageev, N. I. Budylkin, E. G. Mironova and V. A. Krasnoselov, Proc. of Alushta '78 Conference on Reactor Materials Science, 1978, p. 297, in Russian.

[15] F. A. Garner, J. Nucl. Mater. 122-123 (1984) 459.

[16] F. A. Garner, A. M. Dvoriashin, S. I. Porollo and Yu. V. Konobeev, "Microstructure and Swelling of Neutron-irradiated Nickel and Nickel Binary Alloys", submitted to J. Nucl. Mater.

[17] F. A. Garner, M. L. Hamilton, B. H. Sencer, T. Okita, N. Sekimura, D. L. Porter, T. R. Allen and W. G. Wolfer, oral presentation in ICFRM-10.

[18] B. H. Sencer and F. A. Garner, J. Nucl. Mater. 283-287 (2000) 164.

[19] F. A. Garner, M. B. Toloczko and B. H. Sencer, J. Nucl. Mater. 276 (2000) 123.

[20] F. A. Garner, B. M. Oliver and L. R. Greenwood, J. of Nucl. Mater. 258-263 (1998) 1740.

[21] F. A. Garner, L. R. Greenwood and B. M. Oliver, Effects of Radiation on Materials: 18th International Symposium, ASTM STP 1325, (1999), 794.

THE EFFECTS OF ONE-DIMENSIONAL MIGRATION OF SELF-INTERSTITIAL CLUSTERS ON THE FORMATION OF VOID LATTICES - H. L. Heinisch (Pacific Northwest National Laboratory)* and B. N. Singh (Risø National Laboratory, Denmark)

(Summary of a paper presented at the Tenth International Conference on Fusion Reactor Materials, October 14-19, 2001, Baden-Baden, Germany. The paper will appear in the conference proceedings in J. Nucl. Mater.)

EXTENDED ABSTRACT

Void lattices in irradiated metals were first observed about 30 years ago [1], and while they have been the subject of many theoretical and experimental studies since then, no definitive theory of void lattice formation exists. Crowdion clusters having the property of three-dimensional diffusion in the material along paths consisting of segments of one-dimensional random walks are central to the Production Bias Model of void swelling [2], which has been shown to be quite successful in describing many aspects of microstructure evolution under cascade-producing irradiation. The rationale for the present investigation is that if a theory can explain void swelling, then it should also be compatible with the formation of void lattices. Thus, a key element of the Production Bias Model, the one-dimensional migration of crowdion clusters with occasional Burgers vector changes, was examined as a necessary condition for the formation of a void lattice.

Kinetic Monte Carlo computer thought experiments were performed with a simple model for the interactions of vacancy and SIA defects with voids in which the average length of the 1-D migration path segments of SIA clusters is the variable quantity. A cubic test cell containing an atomic-scale, face-centered cubic lattice was used. The cell contained spherical voids and mobile defect clusters, each defect being associated with a lattice site of the underlying crystal structure. The mobile clusters consisted of identically sized crowdion and vacancy clusters. Each crowdion cluster migrated in a 1-D random walk along a randomly chosen close-packed direction (<110>) on the fcc crystal lattice for exactly n_{dc} jumps before randomly choosing the close-packed direction for its next random walk of n_{dc} jumps. The vacancy clusters migrated by 3-D random walks on the fcc crystal lattice. The KMC modeling was used to investigate the role of 1-D migration and the effects of Burgers vector changes on the "shadow effect," whereby voids aligned along close-packed directions shield each other from 1-D migrating SIA defects, as postulated by Foreman [3] as a mechanism to select or preserve a void lattice. The strength of the shadow effect was investigated in a series of KMC experiments. A lattice of 256 uniform-sized voids in the test cell described above was supplemented by 256 additional voids of the same size placed at random positions within the cell. The cell was then "irradiated" with 50,000 crowdion clusters placed randomly in the cell and executing 1-D random walks along the close-packed directions, each for n_{dc} jumps before selecting a new Burgers vector direction. There were no mobile vacancy clusters in this experiment. Runs were done with different values of n_{dc}. Figure 1a shows the initial configuration looking down the [001] direction of the cubic volume. Figure 1b shows the same view after irradiation by the crowdion clusters with n_{dc}= 1 jump, the condition for "pure 3-D" migration. The lattice voids and random voids were attacked equally by the crowdion clusters. Figures 1c and 1d show the results for n_{dc} = 500 jumps and n_{dc} = 5000 jumps, respectively. The average 1-D path length for 500 jumps is about 0.85 times the nearest neighbor distance of voids in the lattice, while that for 5000 jumps is 2.7 times. The effect of shadowing is quite strong, even when the 1-D path length is of modest size.

KMC computer experiments were also performed to test the size stability, whether the voids grow or shrink, as a function of the value of n_{dc}. A lattice of 256 voids in a cell, as described above, was irradiated with equal numbers of crowdion clusters and vacancies. It was found that, under

---

* Pacific Northwest National Laboratory is operated for the U.S. Department of Energy by Battelle Memorial Institute under contract DE-AC06-76RLO 1830.

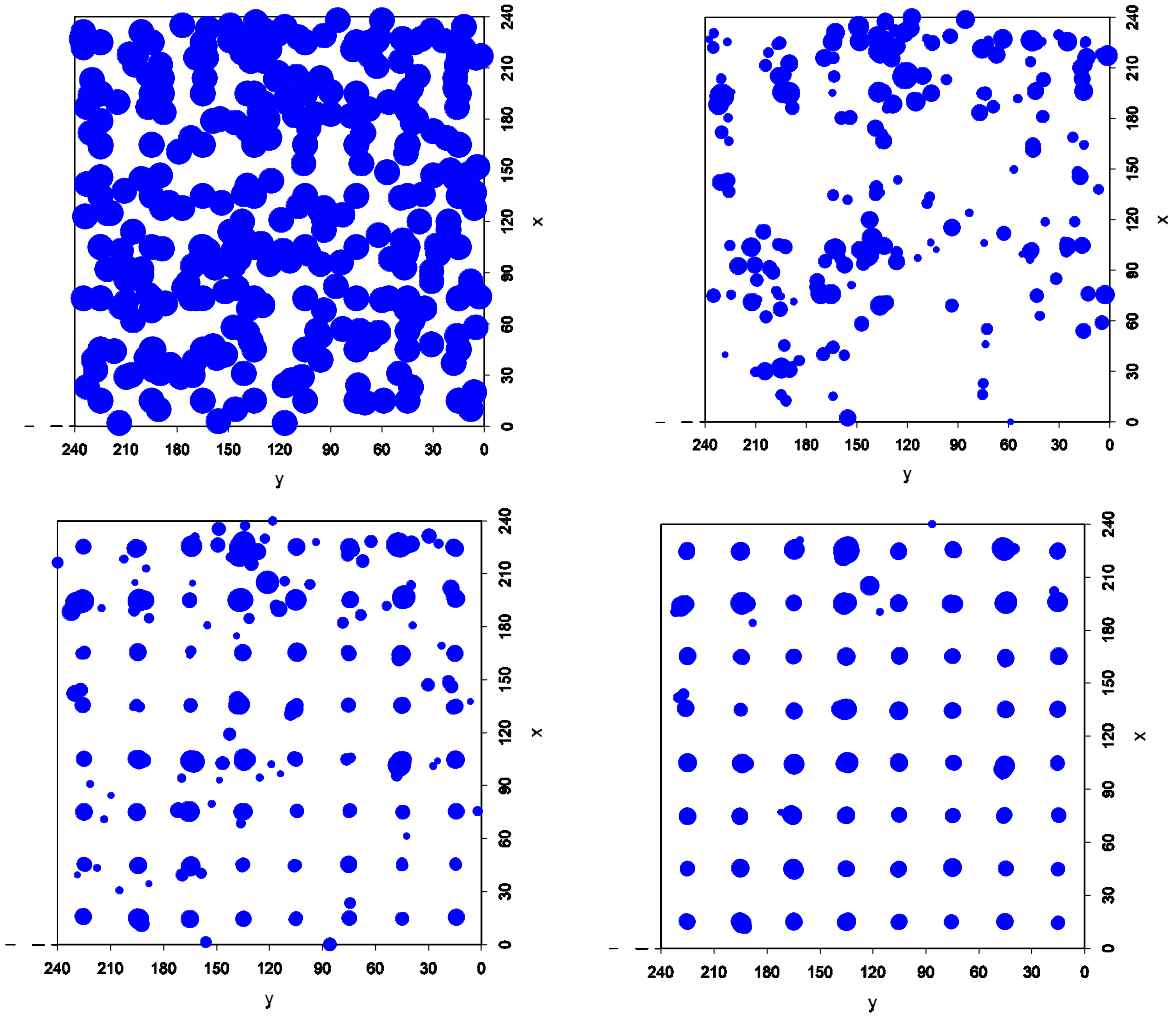

Figure 1. Looking down the [001] axis of a cubic cell a.) containing 256 voids in a lattice plus 256 randomly placed voids. b.) after "irradiation" by 50,000 interstitial clusters migrating on the crystal lattice with n_{dc} = 1 (3-D) c.) after "irradiation" by 50,000 interstitial clusters migrating on the crystal lattice with n_{dc} = 500 (1-D segments of average length L = 0.85 nearest neighbor distance of the void lattice) d.) after "irradiation" by 50,000 interstitial clusters migrating on the crystal lattice with n_{dc} = 5000 (1-D segments of average length L = 2.7 nearest neighbor distance of the void lattice). The sizes of the dots are scaled to the sizes of the remaining voids.

the condition of equal numbers of vacancies and interstitials available to interact with the voids, the size stability of voids in the lattice could be maintained when SIA clusters have 1-D path lengths on the order of the void lattice spacing.

Based on the results of these studies, the shadow effect is very strong, and it does not require 1-D path lengths significantly greater than the void lattice spacing for crowdion clusters to be effective in selecting a void lattice, relative to random voids. Of course, the shadow effect is much stronger if the crowdion clusters have longer 1-D path lengths, but under those conditions the fraction of crowdions available for interacting with the voids becomes much smaller. To maintain the void size under the long 1-D path length conditions requires that the available SIA in crowdion clusters must outnumber the available 3-D migrating vacancies by a large factor (about a factor of

7 in the example here). However, under the actual conditions in real materials, crowdion clusters with very long 1-D path lengths are probably rare. Thus, it should be possible to maintain a void lattice when the average 1-D path lengths of a significant fraction of crowdion clusters is on the order of the void lattice spacing. Further KMC computer experiments will be aimed at determining the conditions for void lattice formation.

REFERENCES

[1] J. H. Evans, Nature 229 (1971) 403.

[2] S. I. Golubov, B. N. Singh and H. Trinkaus, J. Nucl. Mater. 276 (2000) 78.

[3] A. J. E. Foreman, AERE-R-7135, Harwell (1972).

The Effect of Free Surfaces on Cascade Damage Production in Iron - Roger E. Stoller (Oak Ridge National Laboratory)

Extended Abstract

Our understanding of primary defect formation in irradiated materials has advanced as increased computational ability has permitted simulation methods such as molecular dynamics (MD) to explore larger atomic systems [1-9], leading to the expectation that more direct comparisons can be made between the simulations and experimental results. Perhaps the most influential body of experimental data on primary damage formation is that provided by experiments in which thin foils are irradiated by high-energy electrons and/or heavy ions [10-18]. In most cases, the experimental observations are carried out *in situ* by transmission electron microscopy. The results of MD simulations are also in general agreement with the data from these *in situ* irradiation experiments. For example, some material-to-material differences observed in the MD simulations, such as differences in in-cascade clustering between bcc iron and fcc copper, also appear in the experimental data [2,5,6]. However, the yield of large point defect clusters in the simulations is lower than would be expected from the thin foil irradiations, particularly for vacancy clusters. It is desirable to investigate the source of this difference because of the influence this data has on our understanding of cascade damage formation.

Previous theoretical [8,9] and experimental work [17,18] indicates that the presence of a nearby free surface can influence primary damage formation. Unlike cascades in the bulk, which produce vacancies and interstitials in equal numbers, the number of vacancies produced in the surface-influenced cascades can exceed the number of interstitials. This could lead to the formation of larger vacancy clusters and account the differences in visible defect yield between the results of MD cascade simulations conducted in bulk material and the thin-film, *in situ* experiments. The work reported in Refs. [8 and 9] has demonstrated the kinds of effects that can occur, but the magnitude of the effect has not been quantified in detail. Since displacement cascades are stochastic events, the quantitative impact of the free surface can only be determined by a systematic study with “enough” events to capture inherent statistical variations in their behavior.

A substantial database of atomic displacement cascades in iron has been developed [1-4] using the MD code MOLDY [19] and a modified version of the Finnis-Sinclair potential [20,21]. The database covers cascade energies from 0.1 to 100 keV and temperatures from 100 to 900K. This database provides an excellent basis for evaluating the effect of free surfaces. A cascade energy of 10 keV and a temperature of 100K was chosen for this initial study. For these conditions, the database contains two independent sets of cascades, 7 in a 128,000 atom cell and 8 in a 250,000 atom cell. An energy of 10 keV is high enough for some in-cascade clustering to occur, is near the plateau region of the defect survival curve, and initiates a limited degree of subcascade formation. In addition, the required size of the simulation cell, 250,000 atoms, is relatively small. This permits multiple cascades to be carried out in a reasonable timeframe.

The new simulations were carried out using the same MD code and interatomic potential discussed elsewhere [1-4,19-21]. A free surface was created by removing 5 layers of atoms from one surface of a $(50a_o)^3$ atom cell, containing 250,000 atom sites. In the course of the simulations, any atoms passing through free surface are frozen in place just above the surface. Periodic boundary conditions are otherwise imposed. Two sets of nine simulations were carried

out to evaluate the effect of the free surface on cascade evolution. In one case, all the PKAs selected were surface atoms, and in the other the PKA were chosen from the atom layer $10a_0$ below the free surface. Several PKA directions were used, with each of these directions slightly more than 10° off the [001] surface normal. The results of these simulations can be compared with the two sets of "bulk" cascades conducted previously in which cascades were initiated near the center of either $(40a_0)^3$ or $(50a_0)^3$ atom cells.

Figure 1 provides a representative example of a cascade initiated at the free surface. The peak damage state at ~1.1 ps is shown in (a) with the final damage state at ~15 ps shown in (b). The large number of apparent vacancies and interstitials in Fig.1 (a) is due to the pressure wave from the cascade reaching the free surface. With the constraining force of the missing atoms removed, this pressure wave is able to displace the near-surface atoms by more than $0.3\ a_0$, which is the criterion used to choose atom locations to be displayed. A similar pressure wave occurs in bulk cascades, making the maximum number of displaced atoms much greater than the final number of displacements. In contrast to the bulk cascades, the effect of the pressure wave persists longer in surface-influenced cascades, and may contribute to stable defect formation as discussed below.

The final displaced atom and vacancy positions obtained in each cascade were analyzed to determine the number of surviving point defects, the fraction of the point defects of both types contained in clusters, and the cluster size distributions. When compared to the bulk cascade database, several differences were observed. In Figure 2, number of surviving point defects has been normalized to the number of displacements calculated using the NRT standard [22]. The error bars represent the standard error of the mean values for each population, indicating that the differences observed are statistically significant. The two results for two independent sets of 10 keV bulk cascades are shown separately and as a combined data set. For a similar number (9) of cascades, the larger standard errors indicate greater dispersion for the surface-influenced cascades.

As shown in Figure 2, the number of stable defects increased for cascades initiated $10a_0$ below the surface. In this case, no atom sputtering was observed and the number of stable vacancies and interstitials was equal. This increase apparently arises from an effect of the pressure wave on in-cascade recombination in one of two ways (or some combination of the two). Either the final separation between vacancies and interstitials is somewhat greater in the surface-influenced cascades, or the surface relaxation leads to a smaller effective recombination radius. In the case of cascades initiated at the surface, the number of interstitials and vacancies is no longer equal. The number of vacancies continues to increase while the number of interstitials decreases. Interstitials are lost by two mechanisms; atoms are sputtered from the free surface and a few interstitials and small glissile interstitials are absorbed by the surface. The relative contribution of these two mechanisms in this set of 10 keV cascades has not yet been determined. This reduction in the number of interstitials and leads to a greater number of vacancies surviving since less recombination occurs.

Overall, the results of the current investigation can be summarized as follows:

1. stable vacancy production increases as the cascade initiation site approaches the surface
2. stable interstitial production increases and then decreases as the cascade initiation site approaches the surface

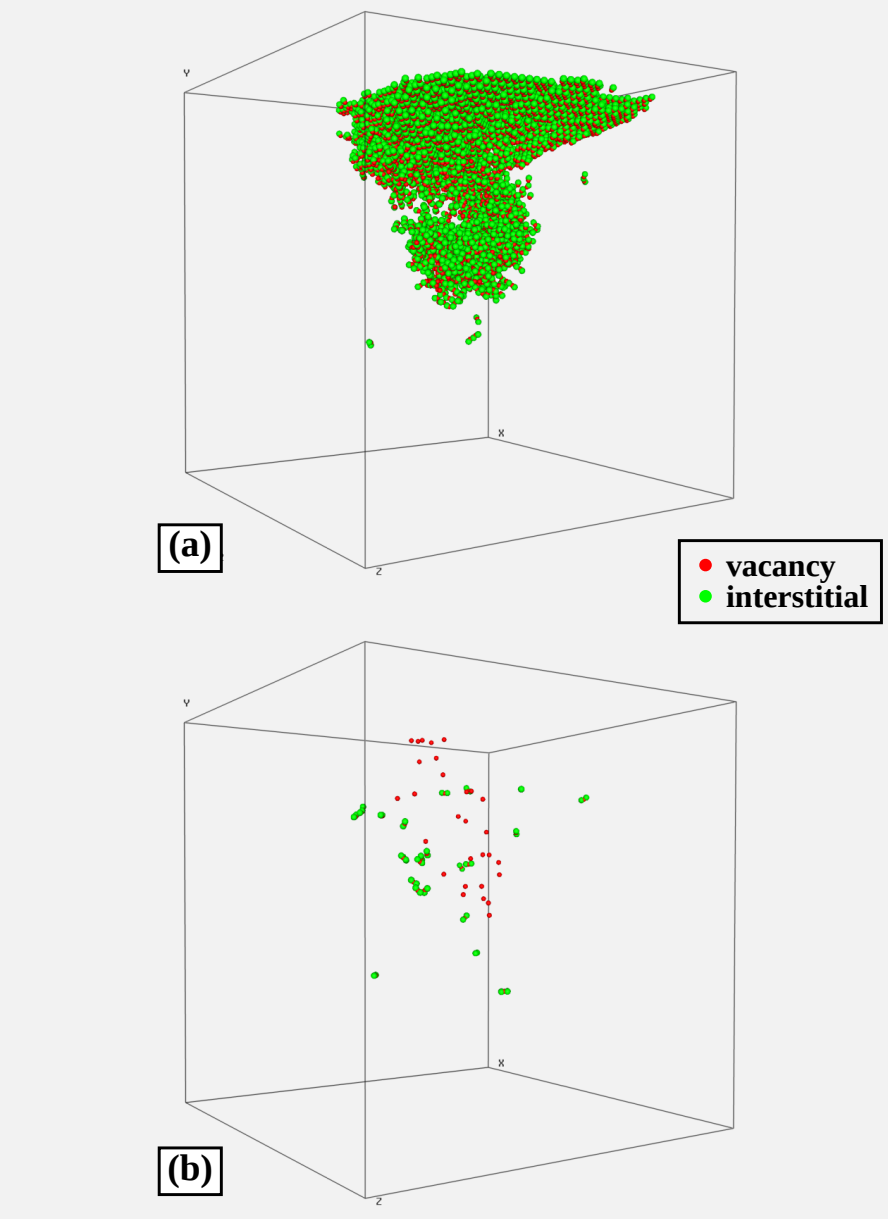

Figure 1. Typical 10 keV cascade with surface atom PKA; peak damage state is shown in (a) at ~ 1.1 ps and final damage state in (b) at ~15 ps.

3. for cascades initiated very near the surface, the number of stable vacancies exceeds the number of interstitials due to atom sputtering and the glide of some interstitials to the surface
4. the fraction of vacancies contained in clusters increases and cluster sizes increase for near-surface cascades
5. no significant change is observed for in-cascade interstitial clustering in near-surface cascades

None of the in-cascade clusters obtained in these simulations would be large enough to be visible in the transmission electron microscope. Thus, the results are trivially consistent with the

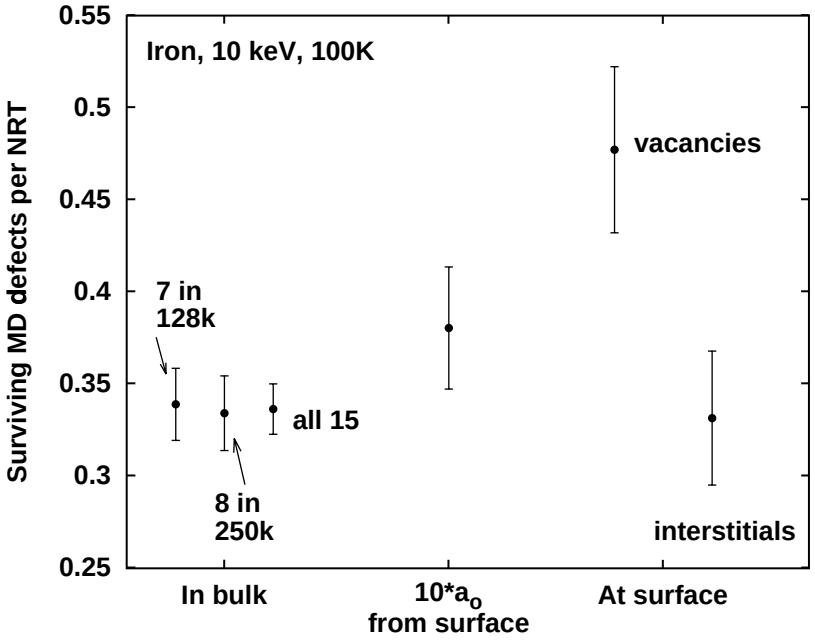

Figure 2. Average stable defect production in 10 keV cascades: two sets of bulk cascades, cascades initiated 10 a_0 below the free surface, and cascades initiated at the free surface.

very low defect yield (~0.001) observed experimentally, and the postulates that either cascade overlap [11,14] or very high damage energies [10,15] are required to obtain visible defects in iron. Therefore, further work is required to obtain the desired MD-based estimates for visible defect yield. The future work will focus on both higher energy simulations and higher temperatures; the conditions for which larger in-cascade clusters are formed in bulk cascades [4]. Somewhat larger numbers of simulations are also required to improve the statistics since near-surface cascades seem to exhibit more variability than bulk cascades. This is particularly needed to obtain statistically significant variations in the defect clustering parameters.

Acknowledgments

This research was also sponsored by the Division of Materials Sciences and Engineering, U.S. Department of Energy under contract DE-AC05-00OR22725 with UT-Battelle, LLC.

References

[1] R. E. Stoller and A. F. Calder, *J. Nucl. Mater*. 283-287 (2000) 746-752.
[2] W. J. Phythian, R. E. Stoller, A. J. E. Foreman, A. F. Calder, and D. J. Bacon, *J. Nucl. Mater.* 223 (1995) 245.
[3] R. E. Stoller, G. R. Odette, and B. D. Wirth, *J. Nucl. Mater.* 251 (1997) 49-69.
[4] R. E. Stoller, *J. Nucl. Mater.* 276 (2000) 22-32.
[5] D. J. Bacon, F. Gao, and Yu. N. Osetsky, *J. Nucl. Mater.* 276 (2000) 1-12.
[6] M. J. Caturla, N. Soneda, E. Alonso, B. D. Wirth, T. Diaz de la Rubia, and J. M. Perlado, *J. Nucl. Mater.* 276 (2000) 13-21.
[7] K. Nordlund and R. S. Averback, *J. Nucl. Mater.* 276 (2000) 194-201.
[8] M. Ghaly and R.S. Averback, *Phys. Rev. Let.* 72 (1994) 364.
[9] K. Nordlund, J. Keinonen, M. Ghaly and R.S. Averback, *Nature* 398 (1999) 48.

[10] M. L. Jenkins, C. A. English, and B. L. Eyre, *Phil. Mag.* 38 (1978) 97.
[11] I. M. Robertson, M. A. Kirk, and W. E. King, *Scripta Met.* 18 (1984) 317-320.
[12] C. A. English and M. L. Jenkins, *Mat. Sci. Forum* 15-18 (1987) 1003-1022.
[13] M. A. Kirk, I. M. Robertson, M. L. Jenkins, C. A. English, T. J. Black, and J. S. Vetrano, *J. Nucl. Mater.* 149 (1987) 21-28.
[14] J. S. Vetrano, M. W. Bench, I. M. Robertson, and M. A. Kirk, Met. Trans. 20A (1989) 2673-2680.
[15] M. L. Jenkins, M. A. Kirk, and W. J. Phythian, *J. Nucl. Mater.* 205 (1993) 160.
[16] T. L. Daulton, M. A. Kirk, and L. E. Rehn, *J. Nucl. Mater.* 276 (2000) 258-268.
[17] M. Kiritani, *Mat. Sci. Forum* 15-18 (1987) 1023-1046.
[18] T. Muroga, N. Yoshida, N. Tsukuda, K. Kitajima, and M. Eguchi, *Mat. Sci. For*um 15-18 (1987) 1097-1092.
[19] M. W. Finnis, “MOLDY6-A Molecular Dynamics Program for Simulation of Pure Metals,” AERE R-13182, UKAEA Harwell Laboratory, Harwell, UK, 1988.
[20] M. W. Finnis and J. E. Sinclair, *Phil. Mag. A* 50 (1984) 45-55 and Erratum, *Phil. Mag. A* 53 (1986) 161.
[21] A. F. Calder and D. J. Bacon, *J. Nucl. Mater.* 207 (1993) 25-45.
[22] M. J. Norgett, M. T. Robinson, and I. M. Torrens, *Nucl. Engr. and Design* 33 (1975) 50-54.

(Extended abstract of a paper to be published in the Journal of Nuclear Materials, presented at the 10th International Conference on Fusion Reactor Materials, Baden-Baden, Germany, October 2001)

DISPLACEMENT DAMAGE CROSS SECTIONS FOR NEUTRON-RRADIATED SILICON CARBIDE - H. L. Heinisch, L. R. Greenwood, W. J. Weber and R. E. Williford (Pacific Northwest National Laboratory)*

(Summary of a paper presented at the Tenth International Conference on Fusion Reactor Materials, October 14-19, 2001, Baden-Baden, Germany. The paper will appear in the conference proceedings in J. Nucl. Mater.)

EXTENDED ABSTRACT

Displacements per atom (DPA) is a widely used damage unit for displacement damage in nuclear materials. Calculating the DPA for SiC irradiated in a particular facility requires a knowledge of the neutron spectrum as well as specific information about displacement damage in that material. In recent years significant improvements in displacement damage information for SiC have been generated, especially the energy required to displace an atom in an irradiation event and the models used to describe electronic and nuclear stopping. Using this information, numerical solutions for the displacement functions in SiC have been determined from coupled integro-differential equations for displacements in polyatomic materials and applied in calculations of spectral-averaged displacement cross sections for SiC. This procedure has been used to generate spectrally averaged displacement cross sections for SiC in a number of reactors used for radiation damage testing of fusion materials, as well as the ARIES-IV conceptual fusion device. The table below lists the spectrally-averaged DPA cross-sections and DPA rates for SiC in several neutron environments.

Table 1. Spectrally averaged total DPA cross-sections, σ_{DPA}, in barns for SiC in several fission test reactors and a conceptual fusion reactor design incorporating SiC.

		σ_{DPA}, barns	
Reactor	Position	Fe	SiC
HFIR	PTP mid	191	158
ATR	midplane	302	260
HFR	C5	300	263
FFTF-MOTA	midplane	267	324
EBR-2	midplane	390	423
ARIES-IV	first wall	762	348

Table 2. Displacement damage rates in DPA per effective full power year (DPA/efpy) for SiC in several fission test reactors and a conceptual fusion reactor design incorporating SiC.

		DPA/efpy	
Reactor	Position	Fe	SiC
HFR	C5	12	11
ATR	midplane	14	12
EBR-2	midplane	25	27
HFIR	PTP mid	33	28
FFTF-MOTA	midplane	43	53
ARIES-IV	first wall	61	28

* Pacific Northwest National Laboratory (PNNL) is operated for the U.S. Department of Energy by Battelle Memorial Institute under contract DE-AC06-76RLO-1830.

10. DOSIMETRY, DAMAGE PARAMETERS, AND ACTIVATION CALCULATIONS

No contributions.

11. MATERIALS ENGINEERING AND DESIGN REQUIREMENTS

No contributions.

12. IRRADIATION FACILITIES AND TEST MATRICES

ASSESSMENT OF OPERATIONAL DIFFICULTIES EXPERIENCED IN RECENT HFIR INSTRUMENTED MATERIALS IRRADIATION EXPERIMENTS

K. R. Thoms, Oak Ridge National Laboratory, P. O. Box 2009, Oak Ridge, Tennessee 37831-8051

1. INTRODUCTION

Operational difficulties were experienced with some instrumented materials irradiation experiments performed in HFIR during the two-year period preceding the outage for the beryllium change out and reactor upgrades. While none of these problems posed hazards to either the reactor or personnel, some did result in premature termination of experiments, and in two cases resulted in unscheduled shutdowns of the reactor to remove the experiment. This paper will provide a detailed description of the operational problems, the investigations into the cause, and the proposed changes to prevent a recurrence of the problems.

2. DESCRIPTION OF OPERATIONAL DIFFICULTIES

The operational difficulties affected three different irradiation experiments (RB-10J, RB-13J, and RB-14J), and the operation of the junction boxes used to join the gas lines of the experiments to the gas lines of the instrumentation facilities. A schematic of how instrumented experiments are connected to the instrumentation facilities is shown in Figure 1. Typically, experiments are connected to the instrumentation facility during the outage preceding the beginning of irradiation, however, in some cases they may be connected a full cycle before irradiation begins. During every refueling outage all instrumented experiments are removed from the reactor and stored in the in-pool experiment storage facility while remaining connected to the instrumentation facility.

A chronology of events that relate to the operational difficulties is presented in Table 1. The following sections provide detailed information of the difficulties experienced with each experiment, or the junction boxes, roughly in the order of their occurrence.

2.1 RB-10J

The RB-10J experiment was the first HFIR materials irradiation experiment to utilize lithium filled subcapsules. Approval for installation in HFIR required that the lithium be contained within two monitored containments. The primary containment was made of all welded construction with the exception of two braze joints located a few inches above the

top of the primary containment vessel. The braze joints, forming part of the primary containment, were necessary to seal the two thermocouple assembly tubes (TCATs) that went into thermocouple wells in each of the lithium filled subcapsules. Additional braze joints, forming part of the secondary containment, were located in the lower bulkhead and a few inches above the lower bulkhead. All braze joints were completed in accordance with approved ORNL procedures. The arrangement of the subcapsules, the two containments, lower bulkhead, and critical braze joints is shown in Figure 2.

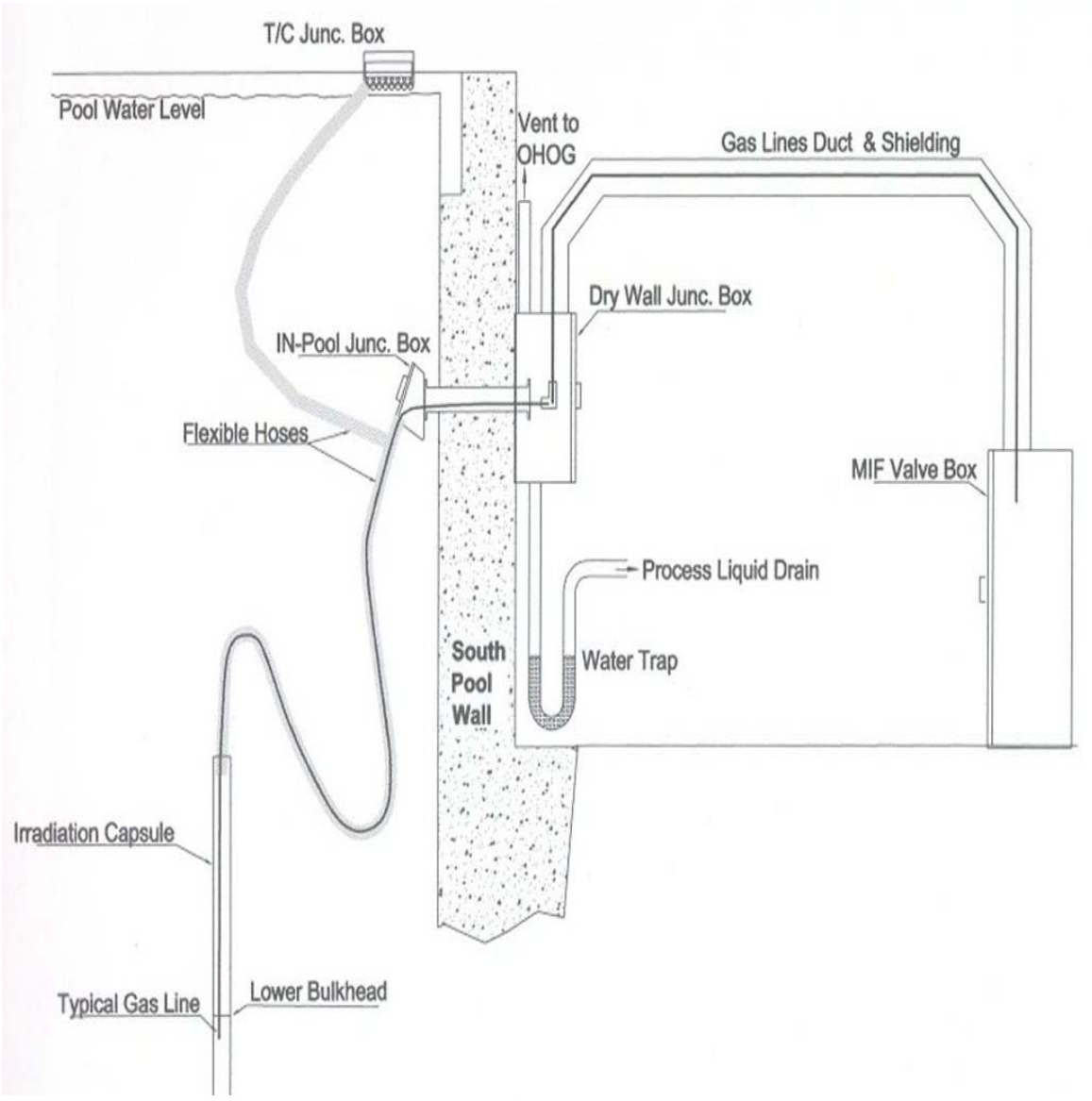

Figure 1. Schematic diagram of instrumented experiment installation

Table 1. Chronology of events relating to operational difficulties experienced with recent instrumented irradiation experiments.

July 22, 1998	Irradiation of RB-13J experiment started
October 13, 1998	Irradiation of RB-10J experiment started
October 23, 1998	A leak in the primary system of RB-10J is determined to be in the part of the primary system that is located within the test region of the capsule. The reactor is shutdown and RB-10J is removed from the reactor, but remains connected to the in-pool junction box
March 15, 1999	Irradiation of TRIST-TC1 experiment started
May 26, 1999	After reinstallation following the EOC 369 refueling outage RB-13J develops a leak making it impossible to maintain pressure in the capsule.
May 28, 1999	While developing an alternative mode of operation for RB-13J water is inadvertently permitted to partially fill the in-pool and dry-wall junction boxes. Experiments connected to the in-pool junction box include RB-10J, RB-13J, RB-14J, TRIST-TC1
June 3, 1999	RB-14J experiment started. RB-13J is not reinstalled in reactor, terminating the experiment after 8 of 10 planned cycles of irradiation.
June 27, 1999	TRIST-TC1 experiment is successfully completed
August 2, 1999	RB-13J and TRIST-TC1 are disconnected from facility
August 11, 1999	RB-10J experiment is re-started under a modified mode of operation
August 27, 1999	There are indications that a leak has developed in the secondary containment system of RB-10J. While the experiment is still operating within the approved conditions for operation, an administrative decision is made to shut down and remove the experiment. An administrative decision was also made to remove RB-14J.
January 27, 2000	Irradiation of RB-14J was resumed
May 12, 2000	RB-13J shipped to hot cells
June 6, 2000	After continuous increase in unexplainable moisture indications of two moisture monitors on the effluent of RB-14J, it was decided to terminate the irradiation after 7 of 10 planned cycles of irradiation
July 26, 2000	TRIST-TC1 shipped to hot cells
October 6, 2000	RB-10J and RB-14J are disconnected from facility
November 7, 2000	RB-14J shipped to hot cells
June 5, 2001	RB-10J shipped to hot cells

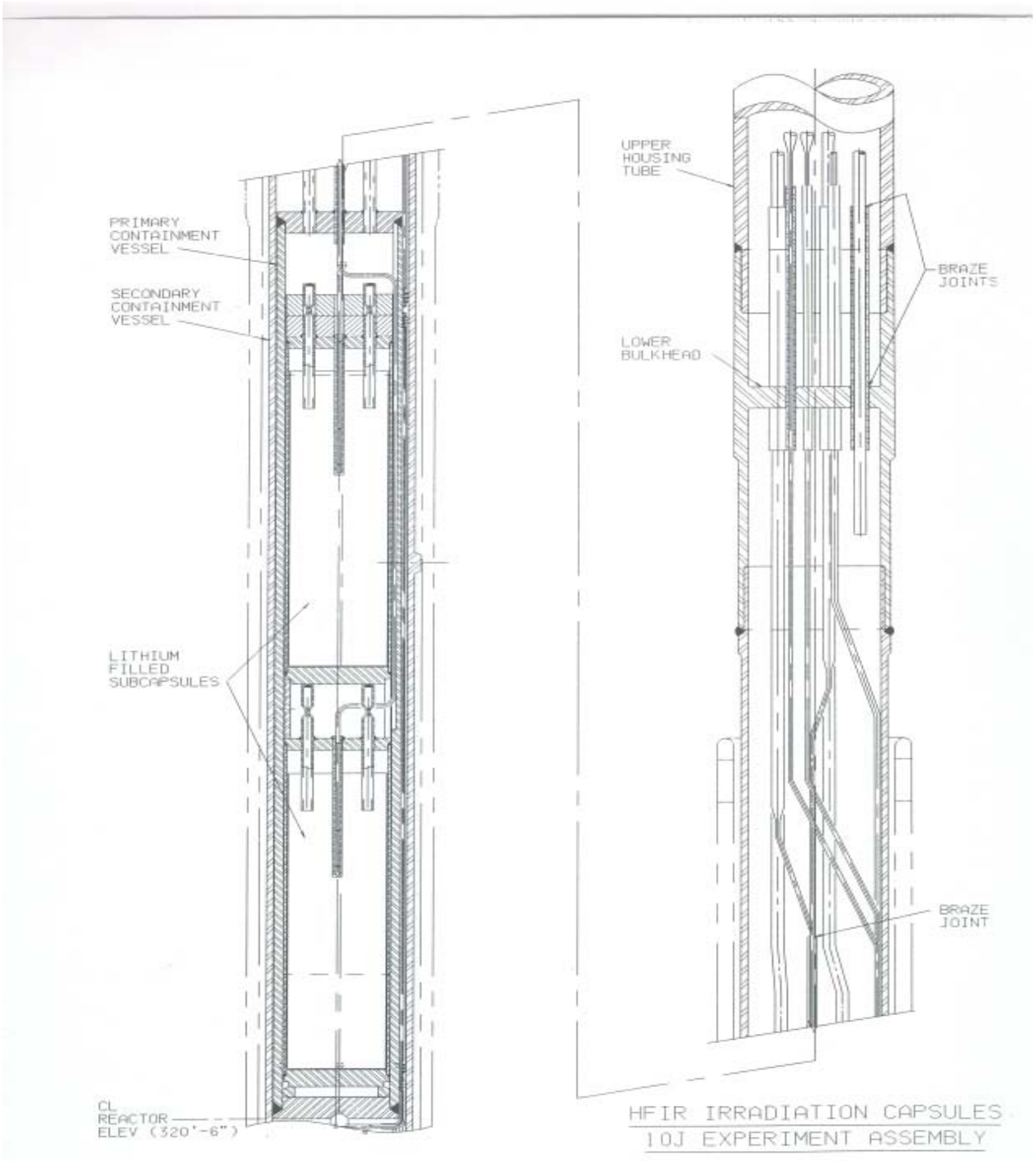

Figure 2. Arrangement of RB-10J from core midplane to above lower bulkhead

The initial mode of operation for RB-10J called for the primary containment to operate as a static gas (helium) system at 80 psig, while the secondary system was a continuously flowing mixed gas (helium and neon) operating at 30 psig. Irradiation began on October 13, 1998, and after about 10 days of normal operation the pressure in the primary system began to decrease indicating that a leak had developed somewhere in the primary containment. A series of tests were performed to try to determine the location of the leak, and at the conclusion of those tests it was apparent that the leak from the primary system was within the secondary containment in the region below the lower bulkhead. The primary suspect for the leak was one of the two brazes that seal the thermocouple assemblies into the primary system. Subsequent examination of these braze joints in the hot cell, discussed in detail in Section 3.1, confirmed that one had developed a leak.

In accordance with the experiment approval documentation, the leak required that the reactor be shut down and the experiment removed. This was done on October 23, 1998; the experiment was placed in the in-pool experiment storage facility while remaining connected to the instrumentation facility.

After modifying the mode of operation and performing additional safety analyses RRD and the RERC approved reinstalling the experiment in the reactor. Irradiation resumed on August 11, 1999. The mode of operation was changed to have the primary system operating statically at 470 psig and the secondary system operating as a mixed gas swept system at 490 psig. The existing very small leak between the primary and secondary systems now allowed small amounts of gas to leak from the secondary into the primary, and the difference between the inlet and outlet flow rates of the secondary system would serve as an indication of either an increase in the existing leak, or a leak in the secondary system. A total of about 150 standard cubic centimeters per minute (sccm) was being flowed through the secondary system and because of system dynamics the difference (outlet flow minus inlet flow) varied between +5 and -10 sccm. This pattern continued through the first nine days of operation, then began to decrease, reaching about -30 sccm after 15 days of operation. This was reviewed by RRD and the RERC and while both approved continued operation with some additional monitoring, an administrative decision was made to shut down the reactor and remove the experiment on August 27, 1999. After removal the experiment remained connected to the instrumentation facility until October 6, 2000. It was then disconnected from the instrumentation facility and moved to the spent fuel pool where it remained until June 5, 2001, when it was shipped to the hot cell.

2.2 RB-13J

The RB-13J experiment was an extremely complex experiment consisting of four specimen holder regions. Through the use of mixed gases (helium and neon) and electrical heaters the temperature of each region could be controlled independently. Five 1/16 in. gas lines supplied the temperature control gases and helium purge gas to the experiment. Tubing of sufficient length was not readily available at the time of assembly of the experiment and therefore couplings were used to join two lengths of 1/16-in. tubing for each of the five gas lines. The tubing was joined to the couplings by brazing in accordance with ORNL brazing procedure BPS-401.

The irradiation of RB-13J began July 22, 1998, and the performance proved to be outstanding for eight cycles. After the eighth cycle, during the EOC 369 refueling outage on May 17, 1999, the capsule was removed from the reactor and placed in the storage facility, as is done every refueling outage. On May 25, 1999, at approximately 11 p.m., the capsule was installed into the reactor in preparation for the ninth of ten planned cycles of operation. The following morning the capsule pressure was 0 psi, and there was no flow indicated through the capsule effluent line. This implied that a leak had occurred in the capsule.

After performing several tests and attempting to control the flows and pressure in the experiment using various techniques, it was surmised that there was a good possibility if irradiation was resumed, it would not be possible to control the temperatures as well has they had been up to that point. Because the customer preferred to accept the shortened irradiation time over the risk of less precise temperature control the irradiation of the experiment was terminated.

2.3 In-pool and dry-wall junction boxes

As stated in the above section, when it became impossible to maintain appropriate flow and pressure conditions in RB-13J, several alternative modes of operation were investigated. One of the options considered involved controlling the atmosphere inside the in-pool and dry-wall junction boxes. The historic method of operation of these facilities is to maintain an ordinary air atmosphere vented to the HFIR open hot off-gas (OHOG) system. It was thought that by maintaining a helium atmosphere at a slightly positive pressure, it might be possible to control temperatures in RB-13J well enough to continue irradiation. To assure that the proposed helium atmosphere would be

reasonably pure, a series of evacuation and back fill operations were performed to remove as much air as possible. At the time these operations were performed, there were four experiments connected to the in-pool junction box; RB-10J, RB-13J, RB14J, and TRIST-TC1.

The process of evacuating the boxes by pulling a partial vacuum apparently opened a leak in the in-pool junction box, which resulted in partially filling both boxes with pool water. The leak probably developed in one of two gaskets used in the in-pool junction box. While the boxes are designed to handle a small pool-water leak by venting it to the process liquid drain line, the valve to that line was closed to facilitate the evacuation and back fill process. Under normal conditions, water would be drained to the process waste line before it could reach a level that would allow it to enter the umbilical hoses that run between the in-pool junction box and the top of each experiment. However, because the valve to the process waste line was closed, the water level got high enough to fill the umbilical of the TRIST-TC1 experiment. While water was not visible in the umbilical hoses of the other experiments attached to the box, it was impossible to know for sure whether or not water had passed through the hoses and was in the solid pipe region of the experiments above the lower bulkhead.

Through a process of manipulating the TRIST-TC1 experiment and its umbilical hose, most of the water was removed and drained through the valve boxes. It was felt that while it was not desirable to have water in the region above the lower bulkheads of the experiments, the stainless steel components in this region would not be in jeopardy, and eventually all of the water would evaporate into the OHOG system.

After the decision was reached to not continue the operation of RB-13J, the operation of the junction boxes was returned to what it had been from their inception, i.e., simply vented to the OHOG.

2.4 RB-14J

The irradiation of RB-14J was begun on June 3, 1999. This was also a very complex experiment with four independently controlled regions using mixed gases (helium/neon or helium/argon) to control temperatures. The experiment operated as it was designed to, but because of the problems experienced with RB-10J, RB-13J, and some rabbit capsules, an administrative decision was made to temporarily terminate the irradiation on August 27, 1999, after about three cycles of irradiation. Following several internal reviews and additional safety analyses, approval was granted to reinstall the experiment, and irradiation was resumed on January 27, 2000.

After an additional three cycles of operation, erratic moisture indications began to be registered by the two moisture monitors on the capsule effluent gas system. These continued during the subsequent cycle, however, because it could not be determined for certain what the cause of the erratic moisture indications was, and because small amounts of mercury were found on one of the moisture probes, it was decided to permanently terminate the irradiation after seven of ten planned cycles of irradiation.

3. INVESTIGATION OF OPERATIONAL DIFFICULTIES

3.1 RB-10J

Because the leaks in both the primary and secondary containment systems of the RB-10J experiment were determined to be in the highly radioactive part of the experiment, all of the investigative work had to await moving the experiment into the hot cell. All instrumented experiments are shipped to the disassembly hot cell (building 3525) using the so-called Loop Transport cask, which is both a top- and bottom-loading cask. In preparation for shipment the cask is lowered into the HFIR pool water. The experiment is lowered into the cask through the top opening in such a manner that the top of the experiment is never placed below water. Once the experiment is inside the cask, the cask is raised out of the water and placed on the floor of the HFIR high bay area in a vertical position with the top ~4 ft. of the experiment protruding out the top of the cask. This top section of the experiment is cut off, a top is put on the cask, and the cask is drained and purged with dry air. The cask is then rotated to a horizontal position and mounted onto a truck for transport to building 3525.

The RB-10J experiment was shipped to the hot cell on June 5, 2001. Three days later the first steps were taken to perform a series of tests in the hot cell charging area prior to actually placing the experiment in the hot cell. With the cask still in a horizontal position, the bolts holding the top cover plug were loosened in preparation for removal of the top plug when about 1 liter of water came out of the plug onto the charging area floor. Health Physics personnel checked the water and found it to be contaminated, with the main activity due to Ag-110. The only source of Ag-110 was thought to be the silver brazes in the vicinity of the experiment lower bulkhead, and most likely the Ag-110 was leached into water that had probably been in the upper housing tube since water was allowed to enter the in-pool junction box two years prior to this.

Once the area was cleaned up, a series of pressurizations and leak tests were performed to (1) confirm that the leak between the primary and secondary systems was still there, and (2) make certain that there were no leaks in the thermocouple assembly tubes (TCATs). After both of these were confirmed the capsule was placed in the hot cell. The first braze joints to be examined were those just above the lower bulkhead. This was done by

cutting through the upper housing tube about an inch above the lower bulkhead and pulling the upper housing tube up far enough to see the tube-to-tube brazes and the bulkhead brazes. Then argon gas was used to pressurize the secondary containment vessel, but the leaks in these brazes were so large that only 40 psig was used, along with a soap check solution. Large leaks were observed in two of the tube-to-tube brazes above the lower bulkhead, and a videotape documentation of these leaks was made. These leaks were obviously much larger than they had been when the first indications of leaks in this system were observed in August of 1999.

To observe the two braze joints of the primary containment system, the secondary containment vessel was cut below the lower bulkhead and removed from the primary containment vessel. The entire primary containment vessel was leak tested by pressurizing the inside of the vessel to 100 psig and putting a soap solution over the entire vessel including all weld joints and the two braze joints. The only indication of a leak was at one of the braze joints, which showed a very small amount of foam after a few minutes, at which time the soap solution usually dried. As a more definitive test, the entire primary containment, still pressurized to 100 psig with argon, was submerged in water up to the cut below the lower bulkhead. In this test the only observed leak was a very small steady stream of bubbles coming from the braze joint that was determined to leak earlier with the soap solution method. This leak test was also recorded on videotape and is available for viewing.

To further determine the cause of the leaks in the braze joints both above the lower bulkhead and in the primary containment system, four braze joints were removed to make metallographic mounts. The four braze joints chosen were the two (one with a leak and one without) in the primary containment system, and two that leaked above the lower bulkhead. All four of these were tube-to-tube joints (or thermocouple-to-tube joints which are similar), and Figure 3 is a sketch showing the joint geometry and the features of an acceptable braze joint.

As can be seen in Figure 3, the braze material should wet the annulus between the two tubes and there should be a fillet where the inner tube enters the outer tube. To confirm the presence of good wetting of the annulus, the metallographic mounts of the braze joints where made by grinding the joint from the top to the point where the fillet was ground

away such that we could see the very top of the tube-to-tube annulus. The results of this process for the primary containment brazes is shown in Figure 4. The leaking joint is shown in plate 6179-07 (or LT), and the non-leaking joint is 6178-07 (or ST). It is quite obvious from Figure 4 that there was insufficient wetting of the annulus in both the leaking and non-leaking joint. For the non-leaking joint therefore, the fillet was apparently all that prevented that joint from also leaking. Similar metallographic mounts (shown in Figure 5) were made of the tube-to-tube braze joints above the lower bulkhead, and they show the same result.

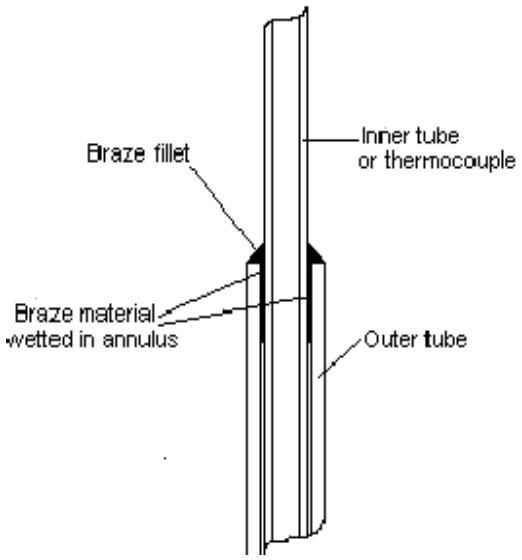

Figure 3. Typical geometry of an acceptable tube-to-tube braze joint

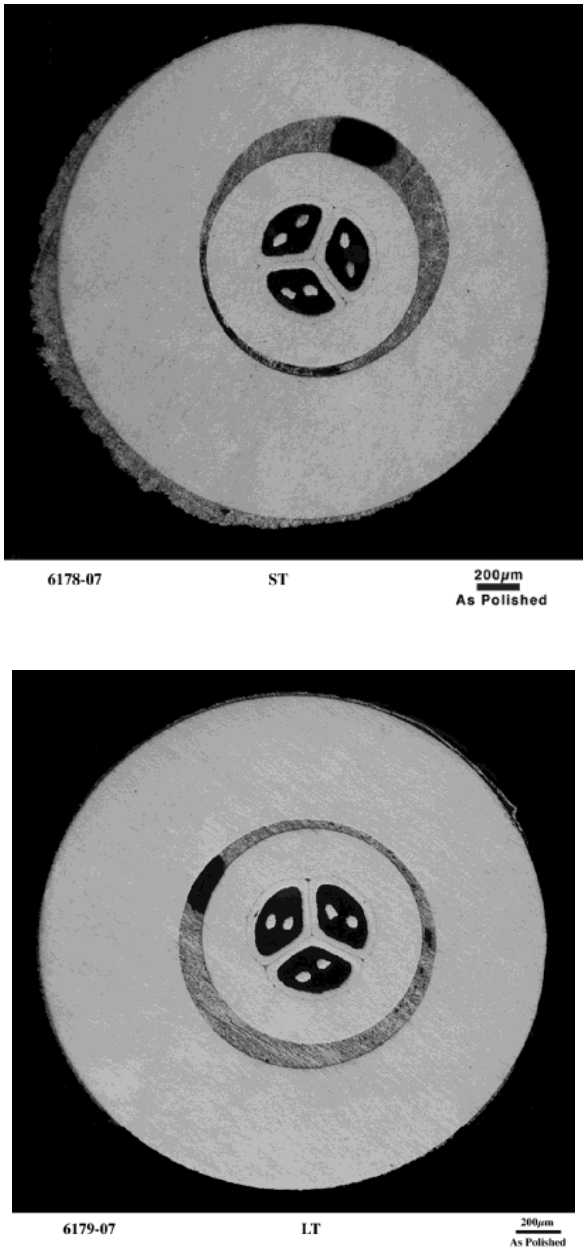

Figure 4. Micrographs of the two braze joints in the RB-10J primary containment system showing lack of penetration of braze material in annulus.

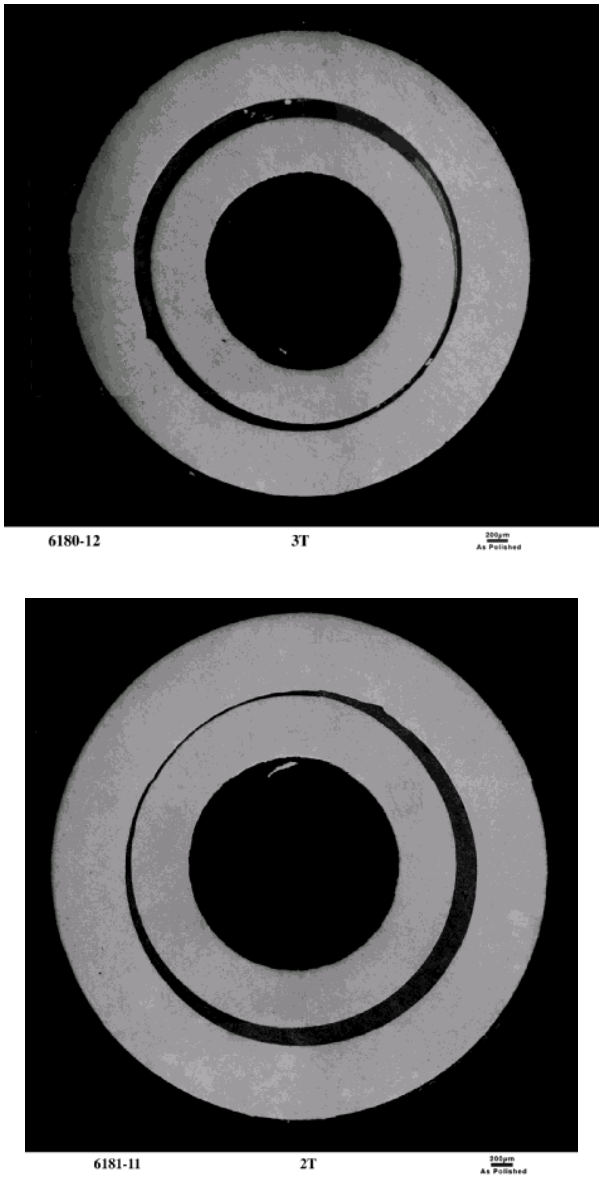

Figure 5. Micrographs of two braze joints just above the lower bulkhead in RB-10J also showing lack of penetration in the annulus

3.2 RB-13J

Tests performed on the RB-13J experiment when pressure could not be maintained in the capsule seemed to indicate that a leak had developed in one of the 1/16-in. gas supply lines. A primary suspect for the location of a leak was the brazed coupling-joint used to join two lengths of tubing for each of these lines. After the experiment was separated from the instrumentation facility and the umbilical hose, these joints were recovered, and

in one of them the tubing had pulled completely free of the coupling into which it had been brazed. The tube still had the braze fillet on it, but there was no braze material below the fillet, in the annulus between the tube and the coupling as there should have been. It was postulated that the manipulation of the experiment to return it to the reactor in preparation for another irradiation cycle put a strain on what was a poor joint and the tube was dislodged from the coupling. Experiments assembled after RB-13J used continuous lengths of 1/16-in. tubing and therefore do not have this braze joint.

3.3 In-pool and dry-wall junction boxes

The problem with getting water into the junction boxes was attributed to the pulling of a vacuum on the system, and probably dislodging either the flat gasket on the in-pool junction box cover, or the gasket between the junction box and the pool wall penetration flange. (It is also possible that the seals used on the bushings leading into the junction box developed leaks.) After the water was drained from the boxes they were pressurized to about 10 psig for several hours, then returned to their normal mode of operation, i.e., vented to the OHOG. A liquid level detector was added to the instrumentation monitoring the boxes, and no additional liquid has been detected to date.

3.4 RB-14J

The RB-14J experiment was sent to the hot cell about 5 months after irradiation was terminated. Prior to disassembly for specimen retrieval the upper housing tube was cut just above the lower bulkhead to facilitate examination of the braze joints in that region. While the braze joints themselves appeared to be satisfactory, there was an appearance of corrosion products on the tubes, with the concentration of these products seeming to be at the same elevation. This observation leads the author to postulate that water was present in the region just above the bulkhead and the corrosion products were deposited on the tubes from the level of the water upward. It is most likely then, that the erratic moisture monitor indications were a result of water above the lower bulkhead and poor braze joints. A photograph showing the appearance of the tubes in this region can be seen in Figure 6.

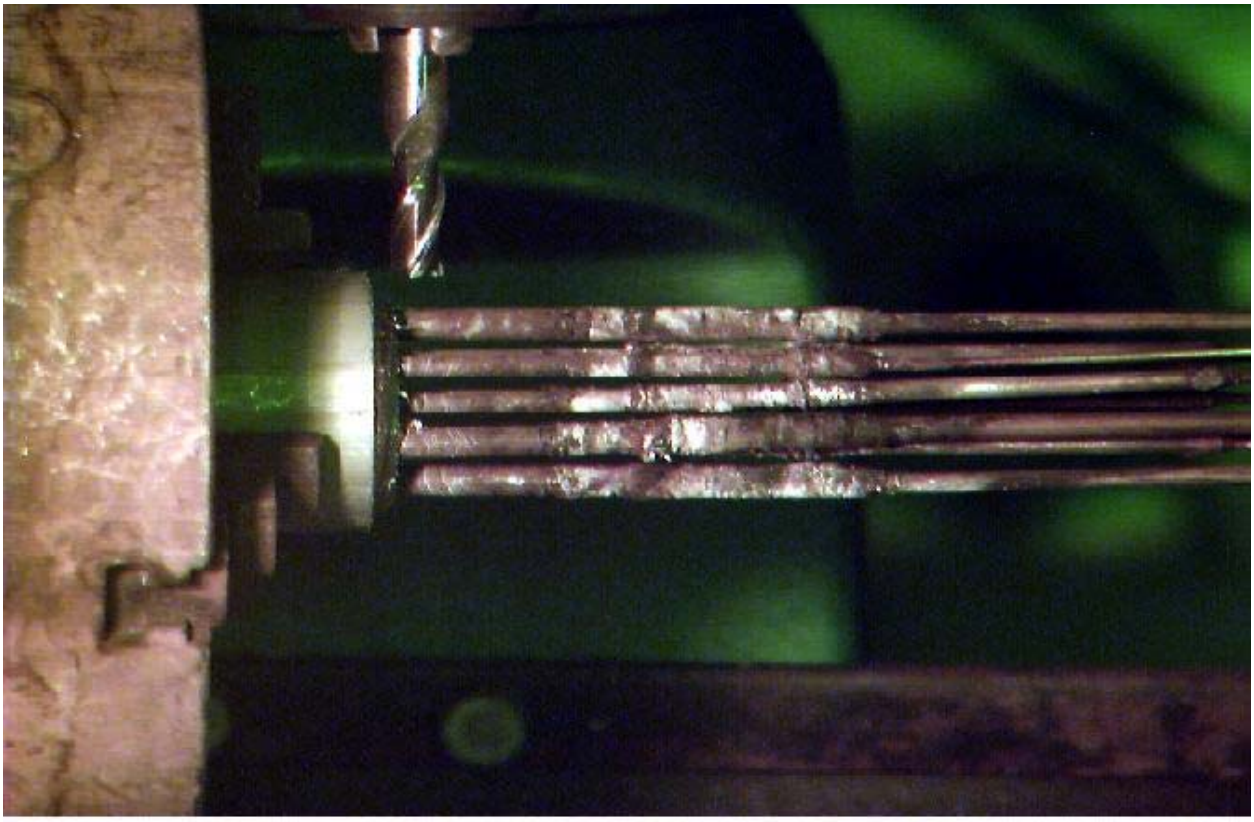

Figure 6. Photo of tubes in region above lower bulkhead in capsule RB-14J

4. CHANGES BEING IMPLEMENTED TO PREVENT RECURRENCE OF OPERATIONAL DIFFICULTIES

After reviewing all of the operational difficulties and investigations into causes of the problems, it appears that the problems can be attributed to poor braze joints, and having water in the region just above the lower bulkhead. To eliminate recurrence of these problems several changes will be incorporated in future irradiation experiments. The first involves a redesign of braze joints used in tube-to-tube brazes. Development of this new joint design is discussed in Section 4.1. Additional changes to be incorporated include relocating the lower bulkhead and changing the atmospheric environment in the region of the capsule between the lower bulkhead and the top of the reactor vessel head.

4.1 Braze joint design

As stated in Section 3.1, metallographic mounts of braze joints have shown that there has been insufficient wetting of braze material in the annulus of tube-to-tube joints. These brazes have passed inspections by passing a helium leak test, and a visual inspection in which the inspector examines the fillet at the top of the joint. However, inspection techniques have not been able to show the extent of braze metal penetration into, and wetting of, the annulus. The tubes and TCATs in these joints are fixed and therefore it is not possible to apply brazing flux in the annulus where it is needed to assure that a good joint can be completed. To avoid this problem a new joint design was necessary that (1) would not rely on being able get flux into the annulus between the two fixed tubes, and (2) could be inspected to assure that a good braze joint had been completed.

A proposed solution that was adapted was to place a sleeve over the original joint. It was decided to test both a tapered brazing sleeve, which would allow matching material wall thicknesses, and a straight brazing sleeve, which would allow heating the joint more uniformly. Figure 7 is a sketch of how such joints would appear in longitudinal cross section.

This design no longer relies on braze material wetting the annulus between the two tubes that are being joined. To demonstrate this technique, several sleeves 3/8 inches long were fabricated from stainless steel rod. The sleeves were drilled 3/16 inches into either end using drill sizes that were a few mils larger that the tubes in the joint. Flux was applied to the entire joint area and green stop-off was applied to the outside of the sleeve to prevent the braze metal from wetting around the sleeve. The sleeve was then slid down over the joint and onto the brazing flux and brazing flux was applied thoroughly to both ends of the sleeve. The braze was made by applying braze material to one end of the sleeve only, and letting the heat from the torch force the braze material to wet thru the sleeve and out the other end. The appearance of a fillet of braze material on the opposite end would be evidence of complete wetting of the annulus under the sleeve. Wetting of the annulus between the original tubes, where brazing flux could not be applied, would not be necessary. Following, in Figure 8, are pictures of braze joints that were completed in the manner described.

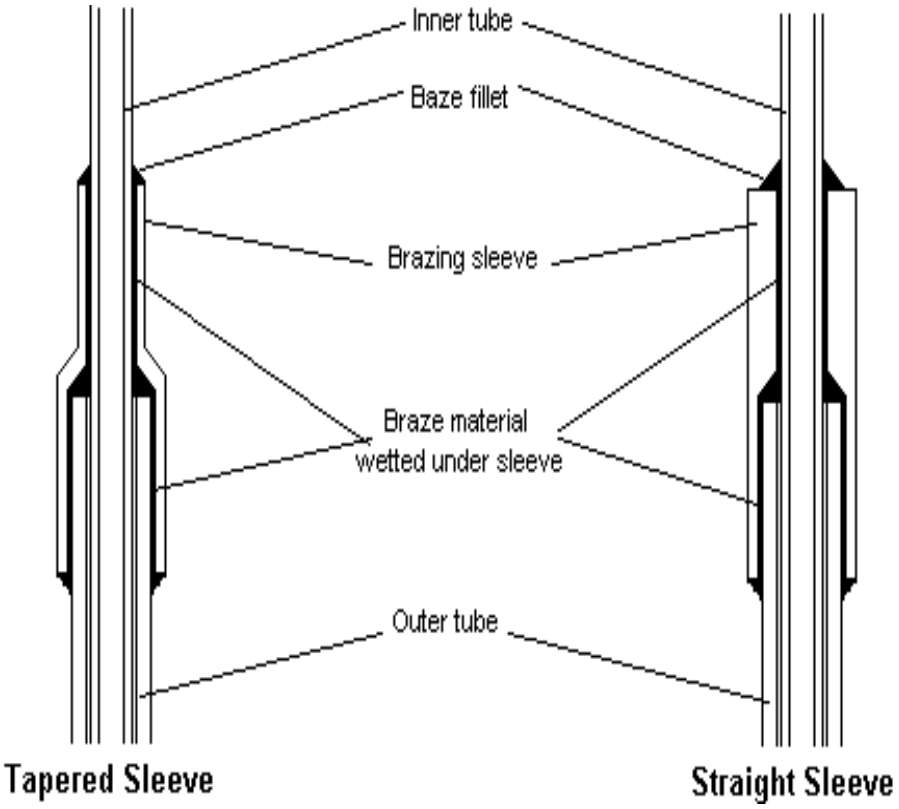

Figure 7. New joint designs for tube-to-tube brazes

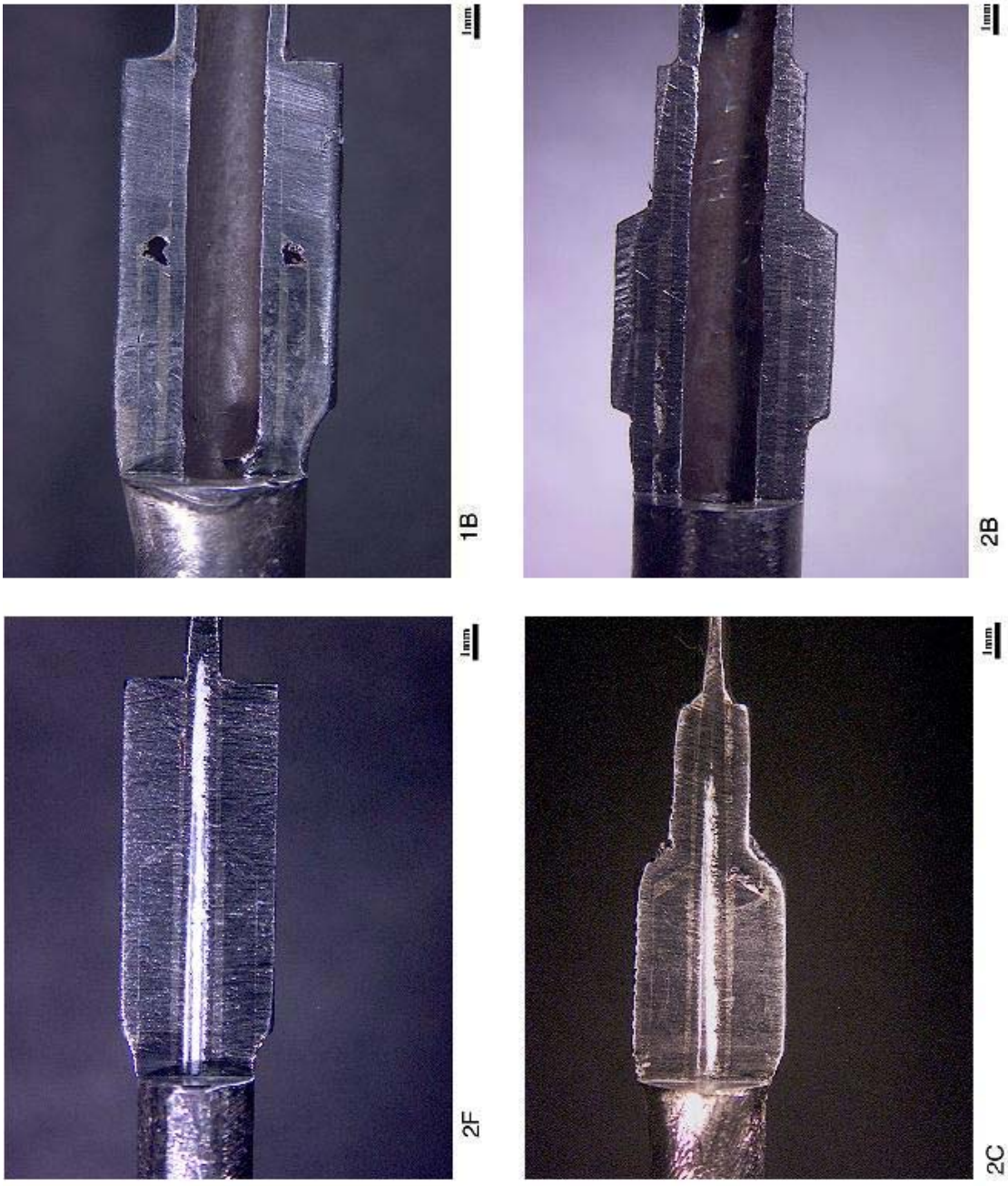

Figure 8. Photos through cross sections of test braze joints. Clockwise from upper left (1B) tube-to-tube with straight sleeve, (2B) tube-to-tube with tapered sleeve, (2C) thermocouple-to-tube with tapered sleeve, and (2F) thermocouple-to-tube with straight sleeve.

Two additional test brazes are shown in Figure 9 with parts of the joint identified.

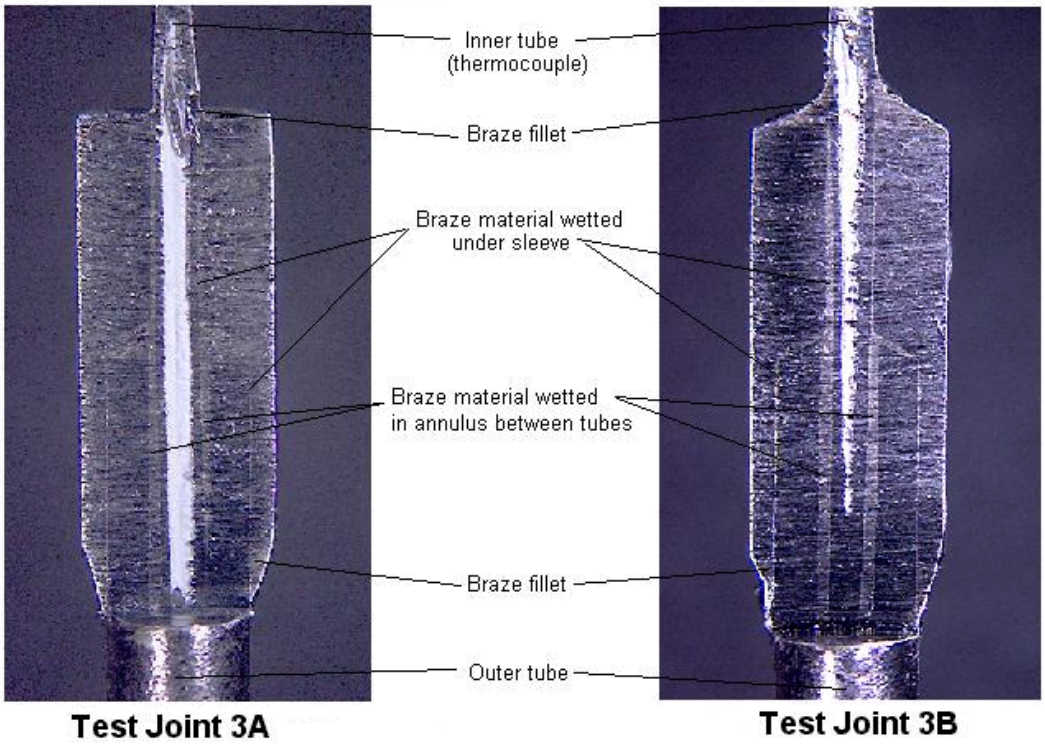

Figure 9. Two thermocouple-to-tube test brazes with straight sleeves

The photographs show that the brazing material not only wetted the annulus between the external sleeve and the tubes, but it also wetted the annulus between the tubes where the braze material was originally desired. A total of 12 such joints were prepared. After successfully completing the first six joints to prove wetting could be accomplished, 6 additional joints were completed, steamed cleaned, successfully helium leak tested, and sectioned to examine wetting of the joint.

It was concluded in these tests that application of brazing flux into the annulus between the tubes in the joint was not required in order to wet the annulus with braze material to produce an acceptable joint. It appears that the brazing flux and braze material will enter and wet the annulus for quite a depth if the joint is slowly and properly heated to drive the materials to the desired location. Unfortunately, there are no non-destructive methods to determine the depth of wetting of such braze joints. This makes the addition of the

external sleeve even more important. It was determined that with the additional sleeve and application of braze material to only one end, an acceptable joint would be obtained with wetting throughout the sleeve, as evidenced by the fillet of braze material on the end of the sleeve opposite where the material was added. Also, as an unexpected benefit, heating the joint properly to get the braze material to flow from one end of the external sleeve to the other forced the brazing flux and material to wet into the annulus where the braze material was originally desired. In other words, addition of the sleeve on the outside serves dual purposes. When wetted with braze material from one end of the sleeve to the other an acceptable braze seal can be obtained. Also if the joint is properly heated to force the braze material to wet under the entire sleeve, the braze material also will enter and wet the annulus where the braze seal was desired originally. The brazed sleeve on the outside is external evidence of what happens on the inside.

Based on this braze development project the following changes will be incorporated into the brazing procedure to be used for all braze joints in future materials irradiation experiments.

1. External sleeves (~ 3/8 in. long) will be used on all seals of tube-to-tube or thermocouple-to-tube joints.

2. Green stop-off will be painted on the outer surface of the sleeves to prevent braze material from reaching the other end by wetting the outer surface.

3. Brazing flux will be applied to the joint before sliding the sleeve into place, and once in place, flux will be applied to both ends of the sleeve.

4. The braze joint is to be heated thoroughly and slowly, allowing the brazing flux ample time to wet and prepare the metal surfaces before the braze material is applied.

5. The braze material is to be added only to one end of the sleeve and heat should be used to force the braze material thru the sleeve and out the other end forming a smooth fillet at both ends of the sleeve.

6. The completed braze joint will be cleaned with steam while under a pressure differential of about 15 psig to remove any residual flux from the joint.

7. The joint will be helium leak tested after it is steamed cleaned. If a leak is discovered the joint should be covered with brazing flux, heated to the remelt temperature, and additional braze material added if necessary. The repaired joint should be cleaned again using steam and pressure before the helium leak test is repeated.

4.2 Capsule design

While there was no evidence that either neutron damage or elevated temperature contributed to the braze failures, steps will be taken to reduce the possibility even further. The lower bulkhead will be moved up approximately 10 inches from where it was in these capsules, returning it to the location it was for other experiments that were run successfully for up to 22 HFIR cycles. This will significantly reduce the neutron flux and gamma heating rate at the location of the lower bulkhead and the brazes immediately above it. Also, this will allow any brazes below the lower bulkhead (e.g., the primary containment brazes in RB-10J), to be located in a region with lower neutron flux and gamma heating. They will now be made as high as possible, and steps will be taken to minimize the temperature that these brazes are subjected to during normal operation.

Additional gas lines (and still-to-be-determined instrumentation) will be added to the region between the lower bulkhead and the in-pool junction box to provide a means to (1) sweep the region with an inert gas, (2) determine if there is a leak in either the lower bulkhead or the tube-to-tube braze joints above the lower bulkhead, (3) determine if there is water on top of the lower bulkhead, and (4) remove any water that might accumulate on the lower bulkhead.

4.3 In-pool and dry-wall junction boxes

During the beryllium changeout outage the two gaskets used in the in-pool junction box were replaced. One of these gaskets was originally installed when the facility was built about 30 years ago. While the operation of these junction boxes will continue as before, the atmosphere in the solid lead tube portion of experiments that vents to the boxes, i.e., the region between the lower bulkhead and the top of the reactor vessel, will be controlled through a still-to-be-determined method. The liquid level detector installed after water had partially filled the boxes in May 1999 will become a permanent part of the junction box monitoring system. Other seals used in the in-pool junction box (e.g., O-ring seals on bushings and gasket seals on caps) will be closely examined and replaced if necessary.